The Control of a Back-to-back Power Converter for Small-Scale Reluctance Synchronous Generators in Grid-Connected Wind Turbine Systems

by

Joshua Cole Mitchell

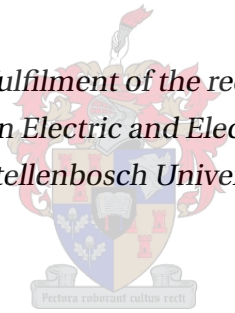

Thesis presented in partial fulfilment of the requirements for the degree of
Master of Science in Electric and Electronic Engineering
at Stellenbosch University

Department of Electric and Electronic Engineering,
University of Stellenbosch,
Private Bag X1, Matieland 7602, South Africa.

Supervisor: Prof. M.J. Kamper

March 2017

The financial assistance of the National Research Foundation (NRF) towards this research is hereby acknowledged. Opinions expressed and conclusions arrived at, are those of the author and are not necessarily to be attributed to the NRF.

Declaration

By submitting this thesis electronically, I declare that the entirety of the work contained therein is my own, original work, that I am the sole author thereof (save to the extent explicitly otherwise stated), that reproduction and publication thereof by Stellenbosch University will not infringe any third party rights and that I have not previously in its entirety or in part submitted it for obtaining any qualification.

Date: March 2017

Signed: J. C. Mitchell

Abstract

In this thesis several topics in the field of geared variable speed and fixed pitched wind turbine systems (WTS) are covered. The main focus is the layout of the power electronics and an alternative layout for small-scale WTS is introduced. This novel layout, implemented in both simulation and practice, is achieved by splitting the converters at their common DC bus and linking them through the wind turbine tower with a DC rated cable (DC-link). The grid-tie voltage source converter (VSC) is placed at ground level and the generator VSC is placed in the nacelle. DC bus voltage control is investigated in directly connected and DC-link-connected VSCs. Attention is paid to the DC bus dynamics, which is shown to be somewhat independent of the DC-link cable. Due to the strict standards for grid-tied WT and PV systems the control, design and implementation of an LCL-filter grid-tie VSCs is detailed in this research and was used extensively in the practical measurements to inject the generated power into the grid. Although this DC-link topology can work with any back-to-back VSC-connected generator topology, a reluctance synchronous generator (RSG), which has great potential for small scale systems, was used in this thesis. A non-linear current controller and an energy efficient, finite element method-based, maximum torque per ampere (MTPA) strategy was implemented, along with a hybrid saliency-based position sensorless control (PSC) technique to allow operation over the entire speed range without an encoder. PSC and encoder control of the RSG with an output du/dt LC-filter was also investigated. A non-linear wind turbine controller that can operate seamlessly in both under-rated and above-rated wind conditions was designed and implemented. This method uses maximum power point tracking (MPPT) and stall regulation to limit the systems power output without overloading the generator.

Opsomming

In hierdie tesis word verskeie onderwerpe i.v.m. geratte,wisselende gereelde windturbine sisteme (WTS) bespeek. Die hooffokus is die ontwerp van die elektronika en 'n alternatiewe ontwerp vir 'n kleinskaalse WTS word voorgestel. Hierdie nuwe ontwerp wat in die simulasie en die praktyk implementeer word, word moontlik gemaak deur om die omvormers by hulle gesamentlike gelykstroombus te splits en hulle deur middel van 'n gelykstroomkabel te verbind. Die netwerkgekonnekteerde kragbron-omvormer word op grondvlak geplaas, en die opwekker in die omhulsel. Die gelykstroom-busspanningsbeheer word ondersoek in die direkverbinde- en die gelykstroomverbinde omvormers. Aandag word geskenk aan die busdinamiek wat ietwat onafhanklik van die gelykstroomgeskakelde kabel is. Weens die streng standaarde vir die windturbines en die PV sisteme, word die beheer, ontwerp en implementering van die filter in netwerkgeskakelde omvormers in besonderhede beskryf en word dit gewoonlik gebruik om die opgewekte krag in die network in te spuit. Alhoewel hierdie gelykstroomskakel topologie met enige rug-aan-rug netwerkgeskakelde kragbron omvormer opwekker topologie kan werk, word 'n weerstands sinkroniese generator wat goeie potensiaal het in kleinskaalse sisteme in hierdie navorsing gebruik. 'n Nie-lineêre stroombeheerder en 'n doeltreffende (finite-element) metode met maksimum wringkrag per ampère strategie is geimplementeer, tesame met 'n (hybrid, saliency-based) sensorlose posisie beheer strategie om te verseker dat dit teen enige spoed sonder 'n enkodeerder kan werk. Sensorlose posisie- en enkodeerder beheer van die sinkroniese generator met 'n opbrengs du/dt filter is ook ondersoek. 'n Nie-lineêre windturbine-beheerder wat goed onder alle wind-toestande kan werk is ontwerp en geïmplementeer. Hierdie metode maak gebruik van maksimum kragpuntopsporing sonder om die opwekker te oorlaai.

Acknowledgements

I would like to express my sincere gratitude to the following people and organisations:

- Professor Maarten Kamper for his guidance and this opportunity to learn and further my career as an engineer.
- Julian Kulick and Christoph Hackl whose help was invaluable in producing this work and I would like to thank them for their friendship and guidance.
- Christoph Hackl for providing the opportunity for me to travel to Munich, Germany, for further research and for his hospitality.
- The NRF for providing me with the necessary funds to complete this degree, I am very grateful.
- Mr. Petrus Petsa, Andre Swart, Murry Juman, Kenan Cloetie, Armin Henning, Stephan Erasmus and J.p Du Plooy for all the invaluable help and guidance in the lab.
- Eduan Howard for designing the RSG rotor and his advice for testing and assembling it.

Publications

The work developed in this thesis on variable speed fixed-pitch small-scale wind turbine systems, reluctance synchronous generator torque control and back-to-back VSC DC-link control was presented at the IEEE international power electronics conference ECCE 2016 in Milwaukee, USA. The paper is titled:

- J. C. Mitchell, M. J. Kamper, and C.M. Hackl, "Small-scale reluctance synchronous generator variable speed wind turbine system with DC transmission linked inverters", IEEE international conference on power electronics, ECCE 2016.

Good feedback on this paper was received and has been deemed eligible for a journal application which is in progress. The collaboration with Munich University produced a second paper on the current control of the RSM in which professor Kamper and I co-authored. The paper is titled:

- C. M. Hackl, M. J. Kamper, J. Kullick, and J. Mitchell, Current control of reluctance synchronous machines with on-line adjustment of the controller parameters, IEEE International Symposium on Industrial Electronics (ISIE 2016), 2016.

Contents

List of Figures

List of Tables

Nomenclature

Indices

a, b, c	Phase axes.
s	Stator fixed reference frame.
g	Grid rotating reference frame.
dc	DC bus fixed reference frame.
m	Rotor synchronous reference frame (mechanical).
α, β	Stator axes (s-reference frame).
k	Rotor synchronous reference frame (electrical).
d, q	Direct and quadrature axes (k-reference frame).

Scalars are written in normal font, e.g., L, vectors ($\mathbb{R}^2$) are written in a small bold font e.g., $\boldsymbol{i}_{\mathrm{s}}^{k}$ and tensors or matrices ($\mathbb{R}^{2\times 2}$) are written in bold capitals, e.g., $\mathbf{T}_{\mathrm{c}}$. Subscripts identify the location of a physical quantity and superscripts identify the reference frame e.g., $\boldsymbol{L}_{\mathrm{s}}^{k}$ is the inductance,**L** of the stator, 's', in the synchronous rotating rotor reference frame, 'k',. Superscripts $^{\top}$ and $^{-1}$ are used to transpose vectors between reference frames using the Clarke and Park transformations $\boldsymbol{T}_{\mathrm{c}}$, $\boldsymbol{T}_{\mathrm{p}}$ and their inversions $\boldsymbol{T}_{\mathrm{c}}^{-1}$, $\boldsymbol{T}_{\mathrm{p}}^{-1}$.

$$\boldsymbol{T}_{\mathrm{c}} = \frac{2}{3}\begin{bmatrix} 1 & -\frac{1}{2} & -\frac{1}{2} \\ 0 & \frac{\sqrt{3}}{2} & -\frac{\sqrt{3}}{2} \end{bmatrix}, \boldsymbol{T}_{\mathrm{c}}^{-1} = \frac{3}{2}\begin{bmatrix} \frac{2}{3} & 0 \\ -\frac{1}{3} & \frac{\sqrt{3}}{3} \\ -\frac{1}{3} & -\frac{\sqrt{3}}{3} \end{bmatrix}$$

$$\boldsymbol{T}_{\mathrm{p}}(\phi) = \begin{bmatrix} \cos\phi & -\sin\phi \\ \sin\phi & \cos\phi \end{bmatrix}, \boldsymbol{T}_{\mathrm{p}}(\phi)^{-1} = \begin{bmatrix} \cos\phi & \sin\phi \\ -\sin\phi & \cos\phi \end{bmatrix},$$

Hence, $\boldsymbol{x}^{k} = \boldsymbol{T}_{\mathrm{p}}(\phi_{\mathrm{k}})^{-1}\boldsymbol{x}^{s} = \boldsymbol{T}_{\mathrm{p}}(\phi_{\mathrm{k}})^{-1}\boldsymbol{T}_{\mathrm{c}}\boldsymbol{x}^{abc}$ where $\boldsymbol{x}^{k} = (x^{d}, x^{q})^{\top}$, $\boldsymbol{x}^{s} = (x^{\alpha}, x^{\beta})^{\top}$, $\boldsymbol{x}^{abc} = (x^{a}, x^{b}, x^{c})^{\top}$, where $\boldsymbol{x}$ represents any vector or matrix.

Symbols

V	Voltage	V
i	Current	A
ψ	Flux-Linkage	Wb turns
R	Resistance	Ω
L	Linearised Inductance	[H]
M	Mutual Inductance	[H]
ϕ_k	Rotor electrical angle	[rad]
ϕ_m	Rotor mechanical angle	[rad]
θ_g	Grid electrical angle	[rad]
ω	Angular velocity	[rad/s]
n	Rotational speed	[r/min]
T	Torque	[Nm]
B_{eq}	Equivalent friction coefficient	$[Nm : s = rad]$
J_{eq}	Equivalent moment of inertia	$[kg : m2]$
ϕ_{pf}	power factor angle	degrees [°]
γ	Current angle	degrees [°]
g_r	Gear ratio	$[p.u.]$
r_T	blade radius	$[m]$
p	Pole pairs	$[p.u.]$
P	Power	W (Js^{-1})
v_w	Wind speed	$[s]$
c_p	Coefficient of performance	$[s]$
λ	Tip speed ratio	$[s]$
t	Time	$[s]$
T_s	Sampling period	$[s]$
f_s	Sampling frequency	$[Hz]$
T_{sw}	Switching period	$[s]$
f_{sw}	Switching frequency	$[Hz]$

Abbreviations

AC	Alternating Current
ADC	Analoge to Digital Converter
AHFI	Alternating High Frequency Iinjection
DAC	Digital to Analog Converter
DC	Direct Current
EM	Electro Magnetic
FEM	Finite Element Method
FOC	Field-Oriented Control
FPGA	Field Programmable Gate Array
FS	Fundemental Saliency
HAWT	Horizontal Axis Wind Turbine
HPF	High Pass Filter
IM	Induction Machine
LPF	Low Pass Filter
LUT	Look Up Table
MTPA	Maximum Torque Per Ampere
NA	Not Applicable
PCC	Point of Common Coupling
PI	Proportional Integral
PLL	Phase of Lock Loop
PMSG	Permanent Magnet Synchronous Generator
RPS	Rapid Prototyping System
RSG	Relutance Synchronous Generator
RSM	Relutance Synchronous Machine
RTAI	Real Time Application Interface
SCIG	Squirrle Cage Iinduction Generator
SI	Simulated Inverter
SPC	Sensorless Position Control
SSWT	Small Scale Wind Turbine
SVPWM	Space Vector Pulse Width Modulation
TCMF	Torque Calculated from Measured Flux
TSR	Tip Speed Ratio
VA	Volt Ampere
VSC	Voltage Source Converter
VSD	Voltage Source Drive
VSI	Voltage Source Inverter
WTS	Wind Turbine System

Chapter 1

Introduction

1.1 Background to Study

There are more than 200 small-scale wind turbine (SSWT) companies in 26 countries world wide, with just over a third of them situated in the U.S, the U.K and the Netherlands [2]. Conservative estimates indicate that the growth of the SSWT market is a steady rate of 20% (from 2015 to 2020) with a peak cumulative installed capacity of 2 GW by 2020 [3]. The power range classifying wind turbine systems (WTSs) as small-scale or otherwise is not definite in literature. The International Electro-technical Commission (IEC) defines small-scale WTS as 50 kW at a generated voltage less than 1000 VAC or 1500 VDC. However, in other sources and in this thesis, the small-scale capacity range is classified as 1-100kW [3].

SSWTs are particularly attractive to rural areas, which due to socio-economic or infrastructure factors, have no access to the national grid. These regions generally rely on diesel generators which have high operating costs (fuel, maintenance) and negatively impact the environment [4]. In these cases small-scale PV and WT systems can greatly benefit these communities. However, the initial capital cost of SSWTs is much higher than that of diesel generators and is likely a factor which influences the decision to use these systems. Other users who may benefit from the use of SSWTs include owners of small farms or small-holdings. Thus it is important to develop reliable technology with the highest possible energy yield to cost ratio.

WTSs can be characterised as variable-speed or fixed-speed. Fixed-speed systems achieve optimum rated power at a fixed wind speed, generally operate without the use of power electronics and are fixed directly to the grid [5]. Variable-speed systems are distinguished by the use of power electronics in the form of voltage source converters (VSC), can operate efficiently over a large wind speed range and are generally regarded as preferable to fixed-speed systems [6–8]. The power quality of variable speed turbines is also somewhat improved by the use of power electronics, which controls and filters

the injected grid power [9]. The necessary addition of power electronics does add reliability and maintenance issues as well as increased costs. A quantitative energy capture advantage of fixed-speed systems over variable speed systems is difficult to achieve as it depends greatly on the wind speed at a particular site. For instance a site with a greatly varying wind speed average will benefit more from a variable speed system than a fixed one.

Most small- to medium scale systems use variations of the permanent magnet synchronous generator (PMSG), do not require a gearbox, and generate AC power, which is rectified to charge batteries and are directly or indirectly grid-connected [2, 10, 11]. This is partly due to the fact that the PMSG has the highest efficiency, power factor, and power density [10, 12]. However, owing to the weight and cost of the permanent magnets the system is expensive to manufacture. For direct-connected WTS the PMSG is large and requires a fully rated power electronics converter [5].

As the output power of a system increases $\leq 10\,\text{kW}$ so does the feasibility of items such as gearboxes and power electronics, which opens the doors to other generator topologies such as the squirrel-cage induction generator (SCIG). The SCIG is a low maintenance, rugged, low cost, easy to manufacture machine. It may be directly connected or self-excited using power electronics, but suffers from a low efficiency as a result of the stator windings, which must handle both the active and reactive power produced for rotor excitation. The need for a gearbox reduces the efficiency of the system, increases its complexity and is a disadvantage for all geared topologies [13, 14].

The widely-used industry standard for medium- to large scale variable speed WTS is the doubly-fed induction generator (DFIG) equipped with a partially-rated converter $\approx$ 30% of the DFIG rated power and a multi stage gear box [15, 16]. Although cost effective, this system suffers from the use of slip rings and grid fault controllability issues [5]. Its use in small-scale systems is uncommon.

The reluctance synchronous machine (RSG) has shown promise in recent years with an efficiency and torque density comparable to that of the induction machine [17]. The synchronous reluctance generator (RSG) is also cheaper to manufacture than wound rotor synchronous generators, PMSGs, SCIGs and DFIGs, making it particularly well suited to SSWTs because of its low cost [18–20]. Its main drawbacks are a lower power factor [17], the need for complex (non-linear) control [21] and a position sensor for field-oriented control (FOC) [22]. However, the encoder can be avoided with the use of sensorless position control (PSC) techniques [23].

Today there are strict standards for grid-tied WT and PV systems which are in place to ensure the preservation of the grid's power quality. These standards require the VSC output power to be adequately controlled and filtered [24]. Either an LCL-filter or LC-filter must be used in order to meet these strict standards.

With regard to the mechanical design of SSWTs, towers are preferred, as roof-mounted turbines have very poor energy yield [25, 26]. Passive yaw is the most common feature in the sub-10 kW scale because the turbine can be redirected with the simple use of a tail vane. Although designs vary widely, a common topology is an up wind nacelle with variable pitch. Furling devices are typically avoided as they are expensive and have reliability issue. An electrical and/or mechanical braking system is usually installed to shut down the turbine in dangerous wind speeds [27–37]. The reliability of variable pitch is among the highest failure modes next to power electronics and should be avoid if possible [18].

Literature regarding the system layout for SSWTs is very limited. The available information from SSWTs companies [27–37], shows that the general practice is to locate the power electronics at ground level, however some prefer to place the entire power electronic system, transformer and grid filters in the nacelle. This is analogous to typical large-scale layouts [18]. A relatively new layout is investigated in this research. Although the layout is not seen in current SSWTs designs it has been used for large-scale systems. The proposed alternative is to split the converters at their common DC bus, one converter on the ground level and one in the nacelle. The advantage of this is that the DC bus voltage can be raised above that of AC grid or motor connection standards of 400 V, which allows the generator system to transfer power through the DC cable with minimal loss at all loads. However, increasing the DC bus voltage has some disadvantages such as increases IGBT switching losses, IGBT cost and an increase in the primary grid-side LCL-filter inductance.

DC bus power control is very well documented in many published papers [38]. However, the non-linear DC bus dynamics and non-minimum phase properties are mostly overlooked in the controller design. A number of methods have been developed to deal with this behaviour using VSCs (see [38] and references therein). Linearisation is the most common technique [24, 38], but there are more advanced methods such as state feedback [38] and model predictive strategies [39]. In [40], the non-linear DC bus dynamics and the control of bidirectional power flow for an airborne wind energy system are discussed in detail and will serve as basis for the later development of a stable bidirectional DC-link controller used for the back-to-back DC bus.

1.2 Problem Statement and Scope

The objective in this research is to identify an optimal power electronic layout for a small scale RSG, variable-speed, fixed-pitch, downwind, grid-connected wind turbine system. The techniques for variable-speed wind turbine control, RSG current and torque control, PSC, grid current control and DC bus voltage control are investigated and implemented in simulation and practice. Matlab Simulink and Stellenbosch's own finite

element-based machine design software, SEMFEM, are used extensively to simulate the system properties. Practical investigations are achieved through the use of SEW inverters, a real-time application interface (RTAI) implemented on a Linux based Pentium computer and various other machines and equipment available in the Stellenbosch University electrical machines laboratory. Establishing the controllability and feasibility of the RSG and a DC-linked power electronic layout is the main focus of this research.

1.3 Thesis Layout

The thesis structure consists of five chapters and five appendices organised as follows:

- In chapter one the introduction, project outline, scope and the thesis structure are presented.
- In chapter two the theoretical background for the various components in the proposed WTS is presented.
- In chapter three the theoretical background for the development and implementation of RSG current and torque control, RSG PSC, RSG current control with an LC-filter, grid-tie current control and DC bus voltage control are presented.
- In chapter four the simulated and measured results of the various theoretical models and practical implementations are presented.
- In chapter five the conclusions and recommendations based on the results detailed in chapter four are presented.
- In appendices A to E, space vector reference frame theory, the measurement equipment, electrical layouts, simulation models and the main algorithms used in this thesis are presented.

Chapter 2

Wind Turbine System Components: Literature and Theory

In this chapter the reader is introduced to the various concepts and mathematical frameworks, taken from literature, which are required for the control of the proposed small-scale variable speed RSG wind turbine. Firstly, the general aerodynamics of wind turbines, their control strategies and wind turbine emulators are reviewed. These are then followed by a derivation of the dynamic equations of the RSM, with special attention to the non-linear flux and inductance of the machine. Finally, a brief description of a VSC and its mathematical model is given.

2.1 Wind Turbine Theory

The aim in this section is to familiarise the reader with the theory on wind turbines in general and a narrowed focus on the theory and control of small-scale, variable speed, fixed pitch wind turbines. The implementation of these systems and how they are tested in other research projects is also presented.

2.1.1 Power Output from an Ideal Turbine

For horizontal axis wind turbines (HAWT) the kinetic energy of a thin sheet of air mass m, flowing at velocity v_w into the thin sheet, is given by (2.1), where U_{wind} is in Joules, A is the cross-sectional area in m^2 with segment thickness x in metres andρ is the air density in $\frac{kg}{m^3}$.

$$U_{wind} = \frac{1}{2}\rho A x v_w^2. \tag{2.1}$$

The available power in the wind, P_{wind}, is the time derivative of (2.1) that is:

$$\begin{aligned} P_{ideal} &= \frac{U_{wind}}{dt} \\ &= \frac{1}{2}\rho A v_w^2 \frac{x}{dt} \\ &= \frac{1}{2}\rho A v_w^3. \end{aligned} \tag{2.2}$$

This equation demonstrates two basic features of wind power. The first is that wind power increases with the third power of wind speed. Secondly, wind power is highly diffuse, requiring a large rotor to capture a substantial amount of power.

2.1.2 Power Output from Practical Turbines

The percentage of power extracted from a wind stream by a wind turbine is defined as the coefficient of performance, c_p [41]. It can be calculated if the wind power and mechanical power is known. The theoretical maximum of this value is known as the Betz limit which states that a maximum of 59.26% of the air stream energy can be converted into mechanical power. The coefficient of performance is determined by several factors; wind-speed, blade parameters and rotational speed of the turbine rotor [41]. As the rotor's rotational speed changes the relative wind velocities along the blade also change, thus the aerodynamic performance of the blade is altered and inevitably the efficiency of the turbine.

Figure 2.1a illustrates the relationship between the c_p, wind speed and the rotor speed. For design convenience, wind speed and rotational velocity are combined into one variable, the tip speed ratio (TSR), λ as explained in (2.4). This allows a single curve of c_p versus λ to be formulated as shown e.g. in fig. 2.1a: a simulated ideal 3.8 m diameter three-bladed turbine. From this curve all wind-speeds and rotational velocities for a given c_p can be calculated. Since the optimum TSR and c_p remain fixed, the optimum c_p, λ maximum power point remains constant at all wind speeds as seen in the simulated and measured power curves for a simulated and measured 3.8 m diameter turbine in figs. 2.1b and 2.1c respectively. The measured turbine data and 1.9 m blades were provided by Aero Energy and used as the basis for the further design of the other WTS components such as the gearbox and generator operating parameters and capacity.

$$P_w = \frac{1}{2}\rho A c_p v_w^3, \tag{2.3}$$

$$\lambda = \frac{r\omega_w}{v_w}. \tag{2.4}$$

where r is the rotor radius in m, ω_w is the rotor rotational velocity in $rad.s^{-1}$ and v_w is the upstream wind velocity in $m.s^{-1}$.

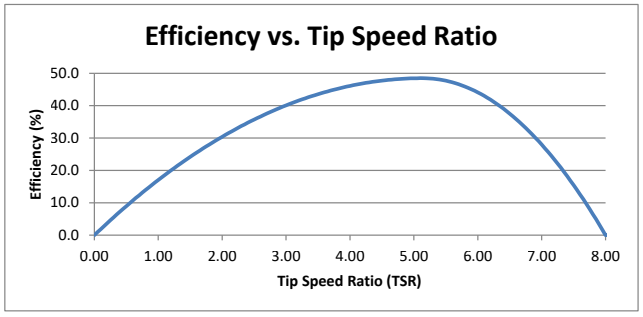

(a)

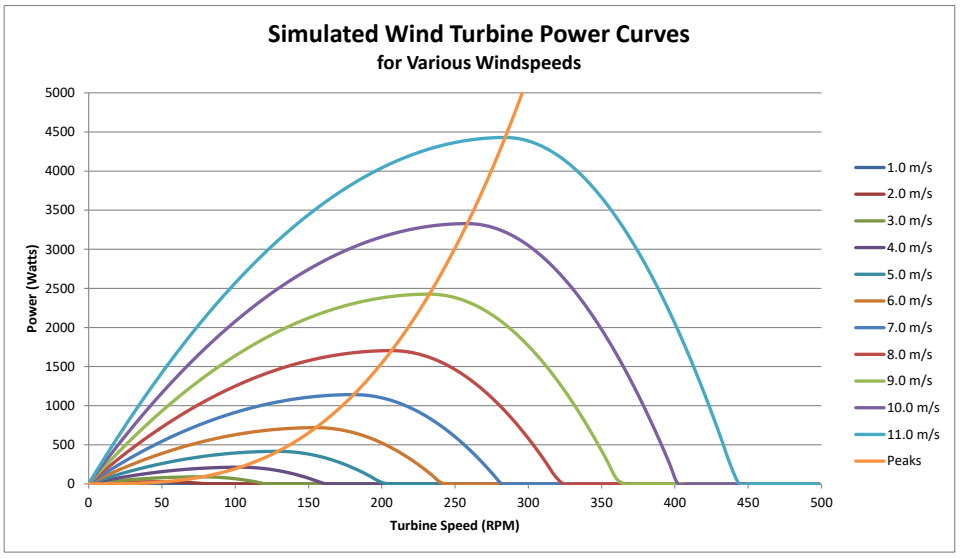

(b)

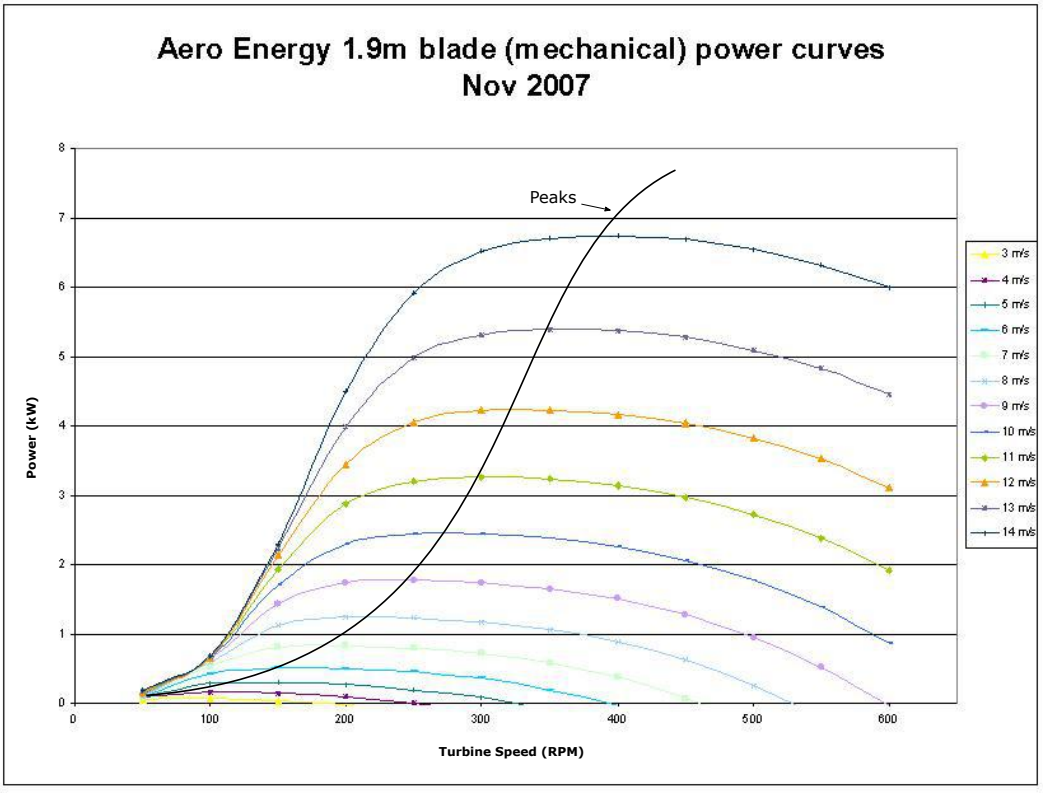

(c)

Figure 2.1: (a) Simulated c_p versus TSR. (b) Simulated wind power vs RPM at various wind speeds with optimum RPM power point curve for a 3.8 m diameter, turbine where the maximum power occurs at a tip speed ratio (TSR) of 5.14. (c) measured wind power vs RPM data for the 3.8 m turbine.

2.1.3 Aerodynamic Theory of Aerofoils and Wind Turbine Blades

The main mechanical element in all wind turbines is the blade. Wind turbine blades can be considered as rotating wing which generate, lift and drag in the same manner as aerofoils. The curved side (upper surface) of the aerofoil generates low air pressures while the underside wing generates high pressures. In terms of flow velocity, the flow is at a higher speed going over the upper surface and a lower speed on the lower surface. The result is a net lift force perpendicular to the direction of the flow of air. The variation of flow velocity is related to the shape and angle of attack of the aerofoil. The aerodynamics which govern untwisted wind turbine blades differs from that of an aeroplane wing, because the rotation of the blade changes the angle of attack along the length of the blade [42]. Figure 2.2a illustrates how a turbine blade aerofoil is positioned and its relative wind velocities [43]. The basic function of the aerofoil shape is to increase the acceleration in the plane of rotation. A component of the lift force allows this increased acceleration and a component of the drag force impedes it. As illustrated by fig. 2.2a, the wind velocity relative to the blade, W_w, called the apparent wind, is stronger than the incidence wind and v_w when at a favourable angle of attack. The apparent wind increases the angle of attack, thus increasing the drag, decreasing the lift force and increasing the axial thrust force, resulting in decreased efficiency. When the angle of attack is increased above a critical maximum value, as shown in fig. 2.2b, the air flow on the upper surface of the aerofoil stops sticking to the surface [44]. This is called flow separation and is caused by the inertia and viscous effects in the flow. The air rotates turbulently around the blade in an unbalanced vortex, causing the pressure on the upper surface to disappear and thus the lift force. The stall can also be caused by irregularities in the blade surface such as dents, icing, or insect marks, even at low angles of attack. Wind turbine designers take advantage of the stall condition in order to control the power output of the turbine and prevent the turbine from being damaged in high wind-speeds.

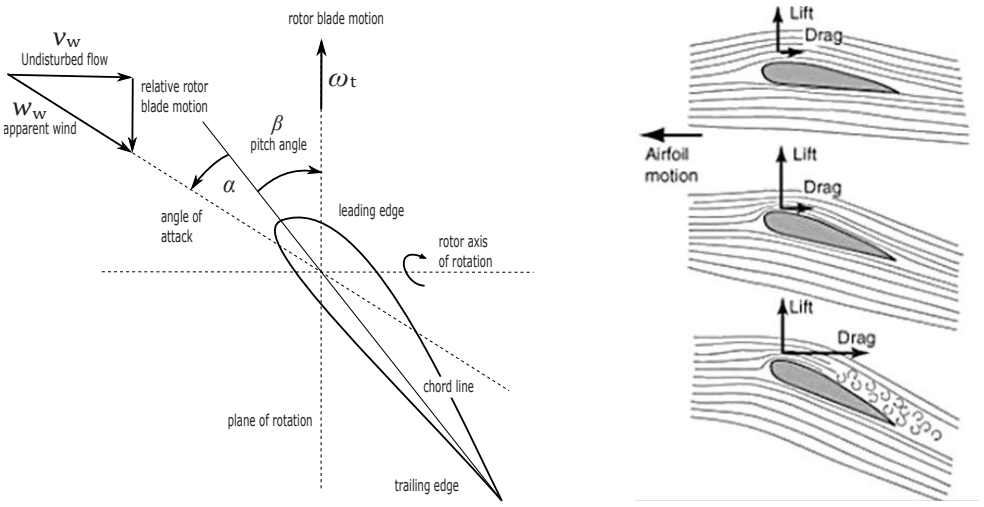

(a) (b)

Figure 2.2: (a) Nomenclature of a cross-sectioned turbine blade aerofoil, (b) flow separation of an aerofoil.

2.1.4 Wind Turbine System Layouts

There is a wide variety of variable speed WTS topologies available today, see fig. 2.3. Variable speed systems using power electronics dominate the small- and large scale markets [15]. Mechanically SSWTs can be quite diverse, with combinations of either fixed, hydrolic or electrically actuated pitch control. Yaw control is the ability of the turbine to manoeuvre into and out of the oncoming wind stream. Effectively the planar rotation of the nacelle. It can also be achieved actively with hydraulics or electric drives and passively with a tail vain or with a downwind turbine design. Most systems avoid furling devices (air brakes used to bring the turbine out of the direct wind stream) especially for units above 5 kW and instead electrically or mechanically brake the turbine. Drive train layouts consist of only four types: single-staged gearboxes, multi-stage gearboxes, direct drive or hybrids of all three systems, all of which generally require some form of power electronic converter to allow the speed of the generator to vary. For small-scale applications the most used topologies are the SCIG and the PMSG, with the PMSG almost exclusively used for systems ≤ 10 kW [27–37].

The drive train of a WTS is a complex system with many dynamic and flexible parts. The system can be reduced to a single-mass [45, 46], two-mass [47, 48] or three-mass system [49]. Two-mass systems are sufficient for this project as the drive train is small and the flexibility of each component can be neglected. Figure 2.4 illustrates the two-mass system comprised of the turbine rotor, a larger rotating disk-mass with inertia, J_w, damping factor B_w, and rotational speed ω_w, a smaller rotating mass as the generator

represented by $J_m, B_m\omega_{\mathrm{m}}$ and the gearbox ratio g_{r}. The shaft stiffness and inertia are negligible for a system of this size.

From the very limited information on power electronics layouts for SSWTs [50–54], it was found that almost all small- and large-scale systems utilise layout option three in fig. 2.5. Table 2.1 shows the advantages and disadvantages of each layout option. Although there is likely to be other systems which use layout two, no information on this type of system could be found other than the one used by Vestas on their large-scale off-shore 8 MW V164 WT, which is currently the largest wind turbine in the world [55].

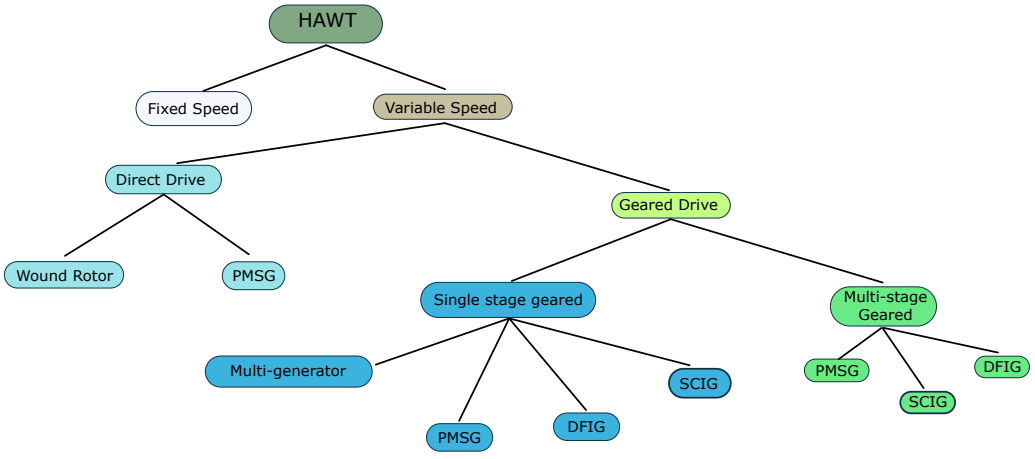

Figure 2.3: Various drive train and generator system topologies for large- and small-scale variable speed horizontal axis wind turbines (HAWTs).

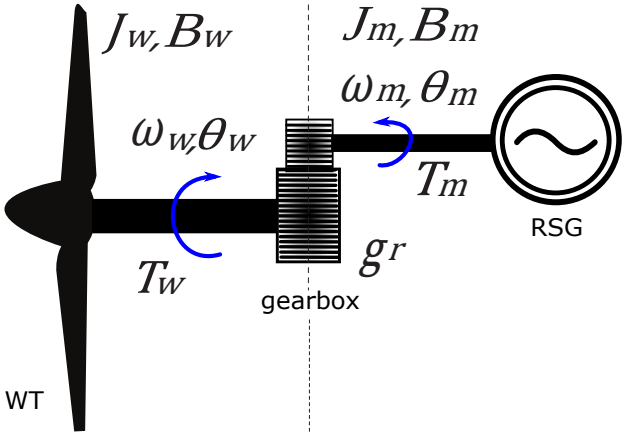

Figure 2.4: 2-mass model of a wind turbine drive train.

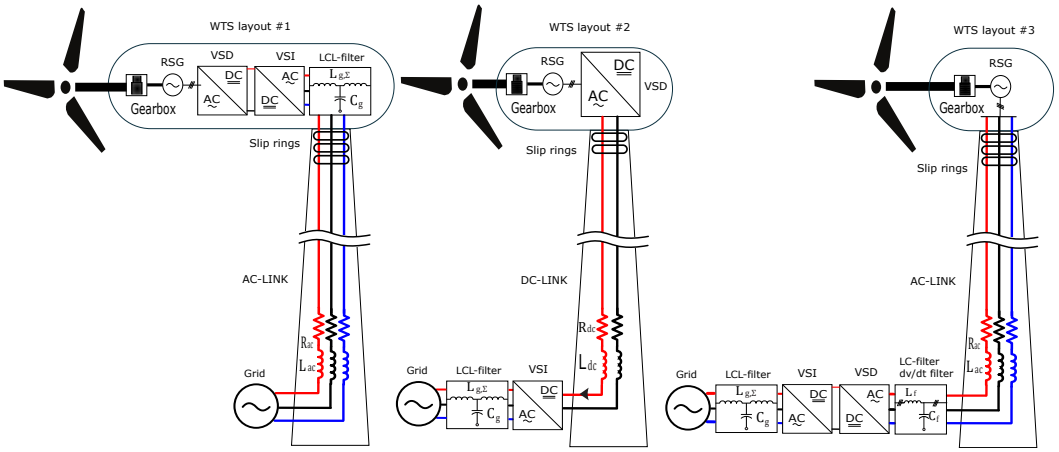

Figure 2.5: Power electronic layouts for variable speed systems.

Figure 2.6 is a per unit estimation of the cable transmission losses associated with each layout where the same generated power, cable diameter and length is used for all layouts. Layout three has the highest losses because of the lower power factor of the generator compared to that of layout one and two, which transfer power at unity power factor and DC respectively. The decrease in power factor results in an increase in current (for constant power, $P = VAcos(\phi)$ and thus an exponential increase in transmission losses. Layout two has only slightly higher efficiency than layout one because of the 600 V reference voltage, which can still be increased to further reduce transmission losses. A WTS utilising layout two is proposed in fig. 2.7, where several complicated mechanical structures are eliminated, such as the pitch control and yawing mechanisms.

Table 2.1: The advantages and disadvantages of three variable speed SSWTS power electronic layouts.

Layout	Advantages	Disadvantages
1	• encoder control is possible. • PSC is possible. • compact power electronics.	• not maintenance friendly. • largest and heaviest nacelle due to the LCL filter. • three terminal slip-rings required for AC-link. • 3 × AC-link cable transmission losses.
2	• encoder control is possible. • PSC is possible. • grid-tie VSC is maintenance friendly. • two terminal slip-rings required for DC-link. • highest transmission efficiency (DC-link) • nacelle weight and size reduction.	• VSD is not maintenance friendly. • slightly heavier nacelle.
3	• PSC is possible. • lightest, smallest nacelle configuration • power electronics, maintenance friendly	• three terminal slip-rings required for AC-link. • LC-filter is required [18]. • LC-filter losses. • encoder can be used but difficult to implement. • lowest transmission efficiency.

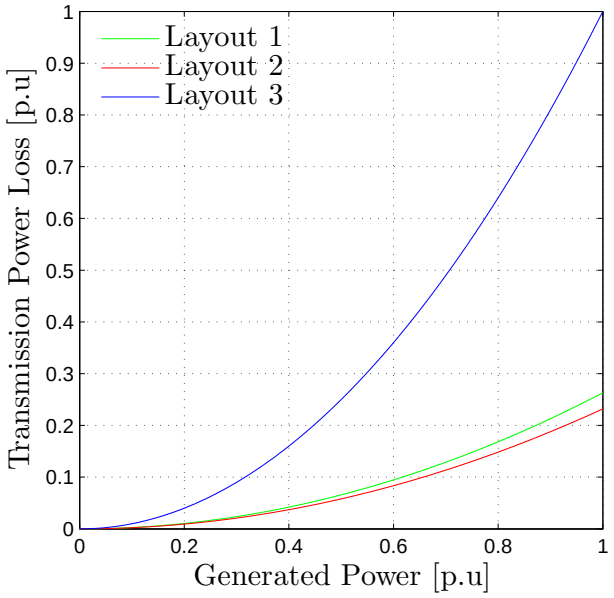

Figure 2.6: Per unit copper transmission loss estimations for the three layouts of variable speed systems. The grid and rated generator rms phase voltages are taken as 230 V and the DC-link as 600 V.

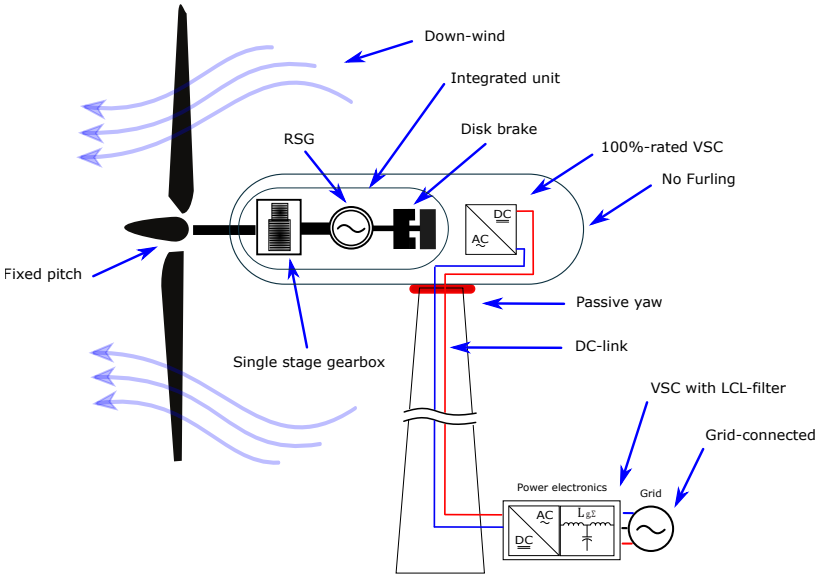

Figure 2.7: Downwind, fixed pitch, variable speed, passive yaw wind turbine with integrated single stage RSG gear box and disk brake.

2.1.5 Control of Fixed Pitch Variable Speed Wind Turbines

HAWTs can be characterised as variable-speed or fixed-speed systems. Fixed speed systems achieve optimum rated power at a fixed wind speed, generally operate without the use of power electronics and are fixed directly to the grid [5]. The major disadvantage of the fixed speed design is that the turbine will operate sub-optimally at wind speeds that do not correspond to the peak tip-speed ratio [5]. Variable speed systems are distinguished by the use of power electronics in the form of voltage source converters (VSC) and can operate efficiently over a large wind speed range.

The efficiency of a wind turbine can be indirectly controlled by controlling the tip-speed ratio and or the pitch angle. Larger scale turbines use pitch mechanisms to regulate the WTS power, but for small-scale WTSs a fixed-pitch topology is preferred as pitching systems are prone to reliability issues [56]. Maximum aerodynamic efficiency is achieved when the tip speed ratio λ is a held at its optimum value. In general WTSs use speed controllers, which need a wind speed estimate together with the measured turbine rotor speed to obtain the instantaneous tip speed ratio (TSR). From this control directives are issued to increase or decease the rotor speed for Maximum Power Point Tracking (MPPT) of the c_p value [24]. The relationship between wind-speed and output power can be described by a power curve, which is illustrated in fig. 2.8. Control directives are dependent on the four operating regions of the power curve that are described as follows.

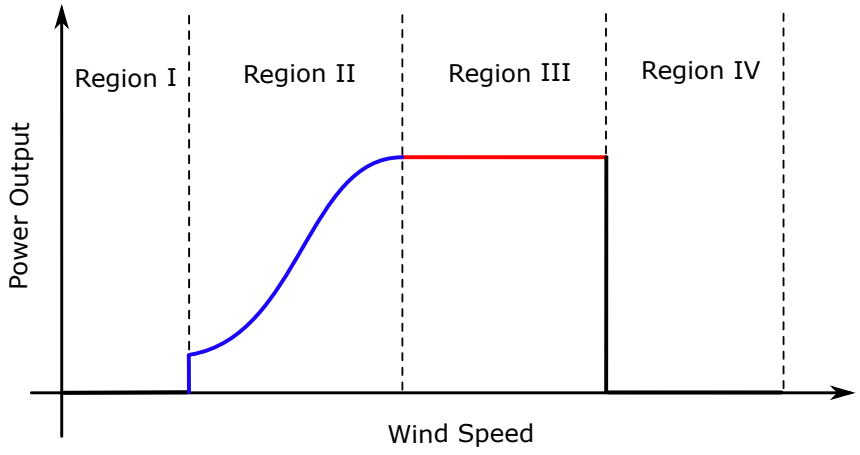

Figure 2.8: Power output versus wind speed for a variable speed wind turbine.

Region I: Wind speed below cut-in which defines the threshold below which it becomes economically unfeasible to run the turbine. The rotor is then placed in a free-rotating mode and no power is transferred into the grid. This region's control-directive is to monitor wind speed until suitable for operation, but requires constant rotation of

the turbine even below cut-in wind speeds, which can reduce bearing and gear box life faster than that of a system with an anemometer.

Region II: Wind speed is above cut-in wind-speed. This region's control-directive is to track the optimum c_p value to generate maximum power.

Region III: Wind speed is above rated conditions. This region's control-directive is to adjust its operating point to keep the maximum power at rated conditions. This can be done by either decreasing the rotor speed (decrease the TSR) to reduce lift on the blades or by increasing the rotor speed (increase the TSR) to stall the blades through turbulence. This is refereed to as soft stalling or passive stalling.

Region IV: At very high wind speeds the generator can no longer provide enough torque to slow the turbine rotor or control it effectively. At this point the machine can be damaged and must be shut down using a mechanical brake. During this region no power should flow into the grid.

Regions I and IV are straight forward to control. The rotor speed is simply monitored until limits are reached, at which point the system reacts by applying MPPT (region I $\longrightarrow$ region II) or braking (region II $\longrightarrow$ region IV).

Region II requires a more complex approach. On SSWTs it is beneficial to decrease the number of sensors in the design to reduce maintenance, mechanical complexity and cost. Elimination of a wind speed sensor can be achieved by deriving a non-linear dynamic controller from (2.7), by solving the common turbine power equation and eliminating the wind velocity term. Only the optimum tip speed ratio $\lambda^\star$ and $c_\mathrm{p}^\star$ of the turbine, normally provided from the blade supplier, are required. This method is particularly attractive when using PSC techniques because no encoder is required to measure rotor speed, thus further reducing the number of sensors required by the system [18]. Rearranging the TSR, (2.4) for wind speed, and substituting this into the wind power equation (2.3), we arrive at (2.5) which is dependent only of λ, ω_w and c_p, where r_T is the turbine radius. . Note that only generator rotor speed measurements, ω_m, can be made, thus to obtain the turbines rotor speed, ω_w, the gear box ratio g_r must be known.

$$\begin{aligned} P_w &= \frac{1}{2}\rho A c_\mathrm{p}(v_w)^3, \\ &= \frac{1}{2}\rho\pi r_T^2 c_\mathrm{p}(\frac{r\omega_\mathrm{m}}{g_\mathrm{r}\lambda})^3. \end{aligned} \tag{2.5}$$

Dividing by $\frac{\omega_\mathrm{m}}{g_\mathrm{r}}$ to obtain the turbine torque:

$$T_w(\lambda,\omega_\mathrm{m}) = \frac{1}{2}\frac{\rho\pi r_T^5 c_\mathrm{p}(\lambda)}{g_\mathrm{r}^2\lambda^3}\omega_\mathrm{m}^2. \tag{2.6}$$

The dynamic mechanical equation for the turbine rotor, gear box and generator is given as:

$$\frac{d}{dt}\omega_{\mathrm{m}} = \frac{1}{J_{tot}}\left[\frac{T_w(\lambda,\omega_{\mathrm{m}}))}{g_{\mathrm{r}}} - B_{tot}\omega_{\mathrm{m}} + T_{\mathrm{m},ref}(\omega_{\mathrm{m}})\right]. \tag{2.7}$$

where the total system inertia and damping as seen by the generator are $J_{tot} = \frac{J_w}{g_r^2} + J_m$, $B_{tot} = \frac{B_w}{g_r^2} + B_m$. Stiffness of the shaft is not included because it is negligible under the low torsional loading. The torque reference $T_{\mathrm{m},ref}(\omega_{\mathrm{m}})$ is the reaction torque delivered by the generator and is defined as (2.8). If the damping factor of the system is known, it can be used to subtract the damping torque from the torque reference which would otherwise cause a constant offset in c_{p}.

$$T_{\mathrm{m},ref}(\omega_{\mathrm{m}}) = \underbrace{-K_P^*\omega_{\mathrm{m}}^2 + \frac{B_{tot}}{g_{\mathrm{r}}}\omega_{\mathrm{m}}}_{\text{region II}}. \tag{2.8}$$

where K_P^*, defined in (2.9), is a fixed optimum constant irrespective of wind speed as identified by the inherent dynamics of the turbines efficiency from fig. 2.1b. Note that g_{r} is cubed due to the additional g_{r} in (2.7) as for the high speed side T_m.

$$K_P^* = \frac{1}{2}\frac{\rho\pi r_T^5}{g_r^3}\frac{c_{\mathrm{p}}(\lambda^*)}{\lambda^{*3}}. \tag{2.9}$$

For region III the torque reference must now act to limit the output power and stall the turbine. This can be done by either increasing the rotor speed to stall the rotor through turbulence or by decreasing the rotor speed and reducing the lift on the blades. Each method has its pros and cons. The former option, (2.10) allows the turbine to operate in the power regulated region for longer without overloading the generator. However, if the wind speed continues to increase the turbine will at some point reach dangerous rotor speeds and must be shut down. The latter option keeps the rotor at safe speeds, but can over load the motor quickly if the wind velocity is too great.

$$T_{\mathrm{m},ref}(\omega_{\mathrm{m}}) = \underbrace{\frac{P_{max}}{\omega_{\mathrm{m}}}}_{\text{region III}}. \tag{2.10}$$

A seamless transition between regions II and III is preferred. A hysteresis approach of changing between (2.10) and (2.8) does not allow for this because the power fluctuations are quite large and often cross the upper and lower hysteresis power band limits. If large hysteresis bands are used this method can also result in the WTS operating with (2.10) when in region II for prolonged periods of time, which decreases the power production of the WTS. The transition from (2.8) to (2.10) also produces large torque transients, which is not ideal for mechanical systems. The proposed solution is to have one dynamic equation which works for both regions. This can be done if region two is adjusted to operate

from a power reference rather than a torque reference. Multiplying (2.7) by $\frac{\omega_\mathrm{m}}{\omega_\mathrm{m}}$ leads to (2.11), which is the dynamic power version of the controller. If $P_{m,ref}$ is then limited to P_{max} the turbine can dynamically stall and MPPT without a hysteresis controller. Furthermore $P_{m,ref}$ still operates under the same principles as $T_{\mathrm{m},ref}$ as can be seen in (2.12).

$$\begin{aligned}\frac{d}{dt}\omega_\mathrm{m} &= \frac{\omega_\mathrm{m}}{\omega_\mathrm{m} J_{tot}}\left[\frac{T_w(\lambda,\omega_\mathrm{m})}{g_\mathrm{r}} - B_{tot}\omega_\mathrm{m} - T_{\mathrm{m},ref}\right], \\ &= \frac{1}{\omega_\mathrm{m} J_{tot}}\left[\frac{P_w(\lambda,\omega_\mathrm{m})}{g_\mathrm{r}} - B_{tot}\omega_\mathrm{m}^2 - P_{m,ref}\right]. \end{aligned} \tag{2.11}$$

$$P_{m,ref}(\omega_\mathrm{m}) = -K_P^*\omega_\mathrm{m}^3 + B_{tot}\omega_\mathrm{m}^2. \tag{2.12}$$

By imposing the restriction, $0 \leq |P_{m,ref}| \leq |P_{max}|$ on $T_{\mathrm{m},ref}$, the controller can operate seamlessly in both regions.

$$T_{\mathrm{m},ref}(\omega_\mathrm{m}) = \underbrace{\frac{P_{m,ref}}{\omega_\mathrm{m}}}_{\text{region II and II}}. \tag{2.13}$$

2.1.6 Wind Turbine Emulators

A static model, such as a step response, cannot capture realistic turbine behaviour which is based on a wind regime or the dynamics of the drive train, such as resonance and torque ripple [57]. It is for this reason that wind turbine emulators (WTEs) are used to rapidly test and develop wind turbine mechanical, electrical and control systems by correctly emulating the desired system dynamics. An example of the wind turbine emulator designed for this project is illustrated in fig. 2.9.

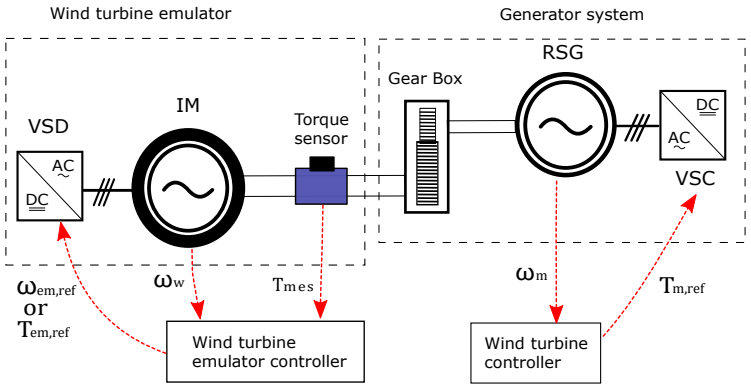

Figure 2.9: Layout of a closed-loop wind turbine emulator, incorporating speed or torque control in the emulator feedback loop.

An emulation system can include, but is not limited to variable wind speed, turbine inertia, wind shear, tower shadow, steady state characteristics, resonance and vibration [46, 58, 59]. Wind speed input data is determined by the nature of the test being facilitated. Real data or synthetic data can be used, but the controlled conditions of synthetic data are ideal for testing control systems and is the preferred choice of researchers [46, 58, 60–65]. Various wind models exist which can be used to develop synthetic time series data, as described by [48, 66]. Synthetic data allows for step changes or ramps in wind speed and steady state observations. Figure 2.10b is synthetic time series data provided by [48].

The selection of prime movers in literature is based on the difficulty and quality associated with its speed and torque control. DC machines are the easiest followed by other machines such as SCIM or PMSMS, which require FOC methods. Several researches [45, 46, 61–63] use the SCIM because its torque or speed can be controlled, using FOC or the commonly known volts hertz method, and is electrically actuated from an appropriate variable speed drive (VSD).

Depending on whether the prime mover (in this case an IM) is speed-controlled or torque-controlled, the modelling of the wind turbine dynamics are slightly different. Essentially the turbine emulator model must supply a reference torque $T_{em,ref}$ or speed $\omega_{em,ref}$ to the VSD. The simplest WTEs in literature rely on an open-loop control structure, [48, 67], whereas others utilise various sensors, torque and speed transducers, in a feedback loop (closed-loop control). Closed-loop structures are preferred for accuracy. Torque and speed feedback is the chosen control type for this project's emulator.

Torque-based emulators are the most commonly used because they allow the dynamics of the turbine to be manipulated more directly [62, 67]. The turbines aerodynamic torque at the rotor, $T_{w,em}$, is calculated from (2.14). The instantaneous TSR, $\lambda(v_w(n), \omega_w(t))$, is calculated using the turbine rotor speed and a discrete wind speed, $v_w(n)$, which is sampled from a LUT, fig. 2.10b. The instantaneous c_p is extracted from a c_p vs λ LUT, as in fig. 2.10a. The inertia and damping of the actual wind turbine can be included in the torque reference, $T_{em,ref}$, as shown in (2.15). This requires that the inertia of the IM be known so that it can be compensated for in the torque reference. Torque feedback using a torque transducer is then implemented to insure that the reference is achieved.

$$T_{w,em}(v_w(n), \omega_w) = \frac{\rho \pi r^3 c_p(\lambda) v_w(n)^2}{2\lambda(v_w(n), \omega_w(n))}. \tag{2.14}$$

$$T_{em,ref} = T_{w,em} - J_w \frac{d}{dt}\omega_w - B_w \omega_w + \underbrace{J_{IM} \frac{d}{dt}\omega_w + B_{IM}\omega_w}_{\text{dynamic IM compensation}}. \tag{2.15}$$

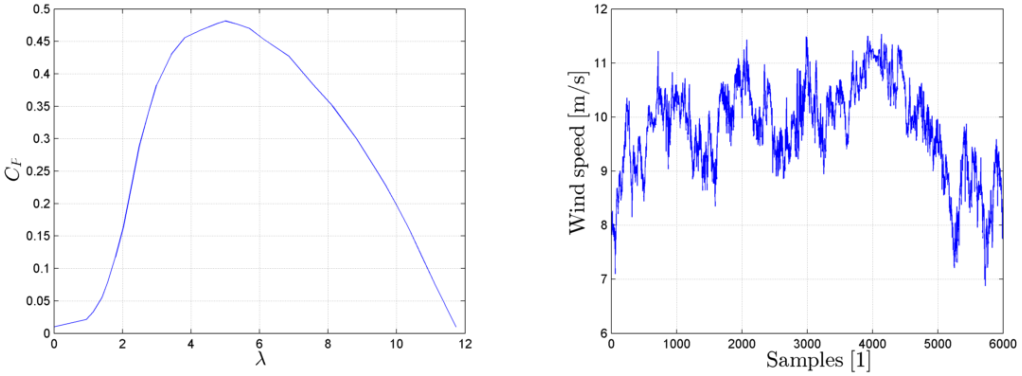

(a) c_p vs λ LUT. (b) Sampled wind speed.

Figure 2.10: The c_p vs λ LUT and 10 minutes of wind speed data sampled at 10 Hz which was used for the instantaneous aerodynamic torque calculation in the WTS emulator and Matlab simulations.

Speed control methods as described by [45, 48] emulate the turbine dynamics though manipulation of the turbines acceleration rather than the applied torque. The acceleration dynamics of the two-mass model from the low-speed-side is described by (2.16). For emulation purposes the inertia of the high speed side can be ignored since it is already inherent in the practical system and thus does not need to be compensated for in the speed reference. In general a VSD can be programmed to reach any reasonable speed set-point in a given time period (acceleration). If the time period is programmed to be much less than that of the turbine's time constant, the inertial dynamics of the IM are de-coupled and eliminated. However, the damping factor of the IM should still be compensated for in the speed reference, (2.17). Since the emulation algorithm is controlling the acceleration without any limits on the IM inertia or damping, it can accurately mimic the turbine's acceleration dynamics. A speed and torque measurement, ω_w, T_{mes} are required to determine the turbine's acceleration, where T_{mes} is the reaction torque applied by the generator. Estimations can also be used, but decrease overall accuracy. This instantaneous acceleration value is then discretely integrated/accumulated every sampling period to achieve the speed reference, $\omega_{em,ref}$, (2.17). In this case the integration method used is the forward Euler method, $x(n+1) = x(n) + K * T_s * u(n)$ with T_s as the fixed sampling frequency.

$$\frac{d}{dt}\omega_w = \frac{\left[T_w - B_w\omega_w - g_r\left(T_m + B_m\omega_w\right)\right]}{J_w + g_r^2 J_m}. \tag{2.16}$$

Note that in (2.17) the measured reaction torque is on the low-speed side. Figure 2.9 illustrates the basic layout of the speed controlled WTE. If the turbine mass and damping factors are not known they must be estimated. [68] provides some guidelines on how to achieve this based on blade lengths from 15 m to 80 m. The drive train damping factor is commonly taken to be as low as 0.05 p.u [58, 68].

$$\omega_{em,ref}(n+1) = \omega_{em,ref}(n) + \frac{1}{J_w T_s}\left[T_{w,em}(v_w(n), \omega_w(n)) - B_w\omega_t(n) - T_{mes}(n) + B_{IM}\omega_w(n)\right] \tag{2.17}$$

2.2 The Synchronous Reluctance Machine

In this section the reader is introduced to the theoretical model of the RSM. A brief background is initially given followed by general principles of the machines operation. The RSM's dynamic mechanical and electrical operation is then described mathematically using differential equations, vector notation and rotating reference frame methods. If the reader is unfamiliar with the Clark and Park transforms please refer to appendix A for further insight.

2.2.1 The RSM background

J. K Kostko first introduced the RSM in 1923 [69], but it is still neglected in industry due to misguided belief in its poor performance. In fact, with today's technology, advanced rotor designs and modern control techniques, the RSM is comparable and in some cases outperforms the IM ($\leq$ 200 kW range) [70]. A typical power factor for the RSM is 0.7 - 0.8, which is slightly lower than for an equivalent IM. In generator mode the power factor is significantly less due to core loss [71]. Although the PMSG still holds a slight advantage over the RSM in efficiency and power factor, the reliance on rare earth metals significantly increases cost and is environmental harmful [72].

The basic stator set-up of the IM and RSM are identical, as both require a rotating field. The main difference is found in the rotor design. Unlike the IM which has a laminated solid steel core with longitudinal conductive bars for eddy currents, the RSM has an almost solid laminated steel rotor, with air gaps placed in specific locations to provide saliency. It is the lack of circulating rotor currents that reduces the core and copper losses on the RSM and raises its efficiency above that of the IM.

Although FOC requires that the rotor position be known, typically achieved with an encoder, the RSM is particularly well suited to PSC techniques due to is saliency and anisotropy [23].

2.2.2 Design and Operation of the RSM

This research the fcus is on the control of a four pole, transversally laminated RSG, as shown in fig. 2.11. A customised rotor was developed by the Stellenbosch University Electrical Machines Laboratory PhD. student, Eduan Howard and specifically optimised to increase the power factor and torque, but using an identical stator to that of an IM to save time and cost. The air gaps in the rotor are designed to create high and low reluctance paths, which the Reluctance force acts on to align the rotor to its least reluctance path. Most of the energy in the machine is contained in the air gap, which is greatest when the gapped rotor section (q-axis) is aligned with the stator current vector, and the least when the solid section of the rotor (d-axis) is aligned with the stator current vector.

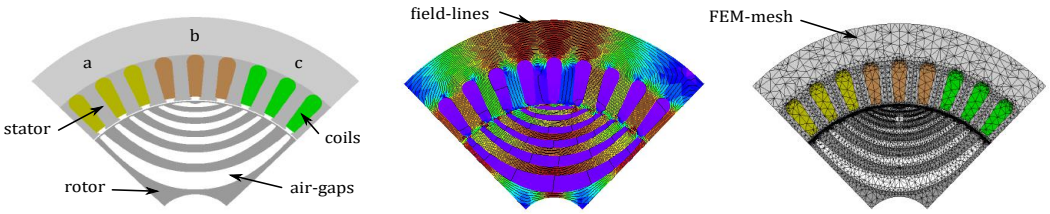

Figure 2.11: Quarter model of the RSM rotor designed by Stellenbosch University Electrical Machine laboratory PhD student, Eduan Howard.

The design of the RSM was conducted in SEMFEM, a machine modelling finite element-method (FEM) package, developed by Stellenbosch University, where various parameters can be extracted for analysis, simulation and control of the machine. Only a quarter of the model is needed for simulation because the machine has four symmetrical poles, however all possible rotor and stator angle combinations must be taken into account in the design and mapping of the machine's flux-linkage. This rotor was also designed with an axially skewed rotor (7°) to reduce torque ripple and thus required that five different finite element (FE) simulations be run for five segments of the rotor, $(-3.5^\circ, -1.25^\circ, 0^\circ, 1.25^\circ, 3.5^\circ)$. An average of all this data is then taken to achieve the final performance of the RSM, shown in fig. 2.12. The rotor laminations and shaft were assembled at the Electrical Machines Laboratory at the University of Stellenbosch and SEW in Cape Town (SA). Photos of the RSM laminations, integrated gearbox and rotor shaft are available in appendix B.2.4, as well as the CAD drawings for the redesign of the rotor shaft with a skewed key way.

2.2.3 The Stator and Rotating Reference Frame

The RSM can be represented as a three-phase electrical system using (2.18) or as an equivalent two-phase system by transformation to the stator reference frame ($\alpha\beta$ reference frame),(2.19), using the Clark Transformation, $\boldsymbol{T}_c$ (see appendix A).

$$\boldsymbol{u}_s^{abc} = R_s \boldsymbol{i}_s^{abc} + \frac{d}{dt}\boldsymbol{\psi}_s^{abc}\boldsymbol{i}_s^{abc}. \tag{2.18}$$

The stator voltage $\boldsymbol{u}_s^s$ is represented by (2.19).

$$\begin{aligned} \boldsymbol{u}_s^s &= \boldsymbol{T}_c \boldsymbol{u}_s^{abc}, \\ &= R_s \boldsymbol{i}_s^s + \frac{d}{dt}\boldsymbol{\psi}_s^s. \end{aligned} \tag{2.19}$$

where the magnitude and orientation of the stator flux $\boldsymbol{\psi}_s^s = \boldsymbol{\psi}_s^s(\boldsymbol{i}_s^s, \gamma)$ is directly and exclusively caused by the presence of stator currents, $\boldsymbol{i}_s^s$ and the current angle, γ, see fig. 2.13. The magnitude of the flux-linkage field will vary depending on these two quan-

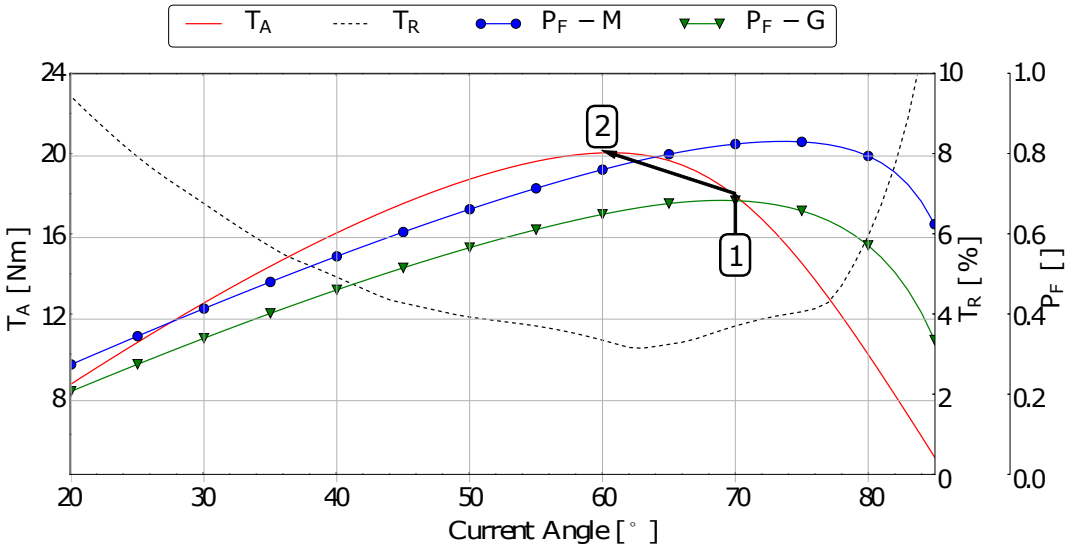

(a) Average torque, torque ripple and power factor versus current angle change with rotor at 7° skew angle.

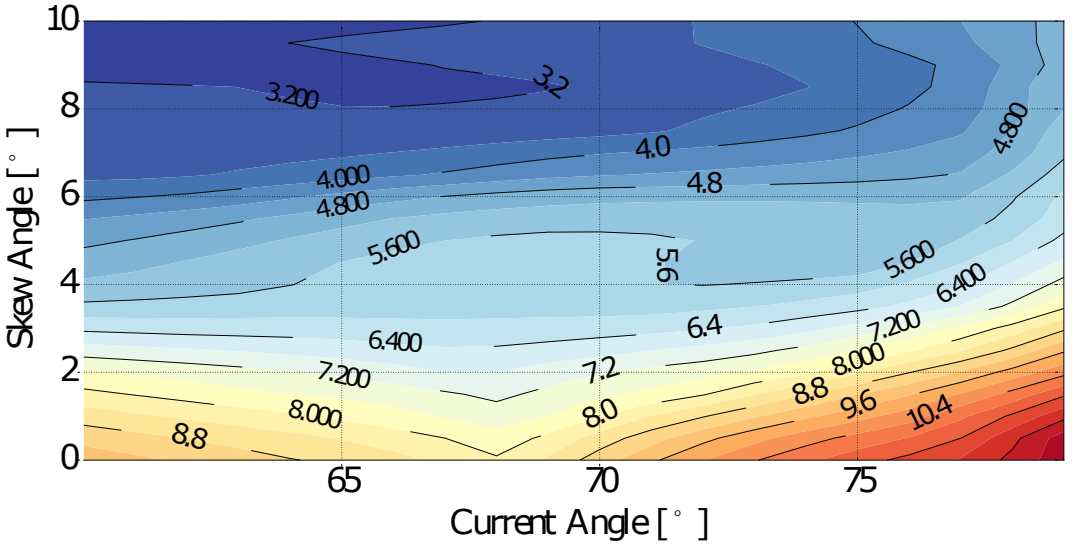

(b) Skew versus current angle with a torque ripple parameter.

Figure 2.12: FE generated results for the 3 kW RSM design by Eduan Howard.

tities and it is the variation in the field, through the rotor's cross-sectional solid and air-gapped areas, that causes torque to be generated as a result of the rotor's anisotropy.

Electromechanical torque in the stator reference frame is described by (2.20) where p is the pole number.

$$T_{\mathrm{m}} = p\frac{3}{2}(\boldsymbol{i}_{\mathrm{s}}^{s})^{T}\boldsymbol{J}\boldsymbol{\psi}_{\mathrm{s}}^{s}. \tag{2.20}$$

The Park Transformation is used to transform the model from the stationary reference frame to the synchronous rotating reference frame, as shown in fig. 2.13. This is allows the system to be represented by two static DC quantities, d and q, which are eas-

ier to control than α and β. Figure 2.14 illustrates the equivalent dq circuits of the RSM formulated from (2.28).

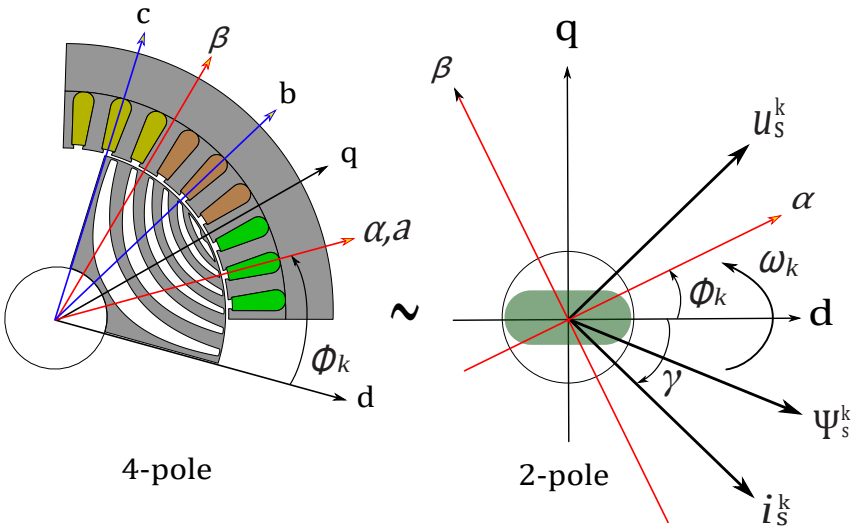

Figure 2.13: Current flux and voltage vectors in the dq-reference frame for generator mode.

$$\boldsymbol{u}_{\mathrm{s}}^{k} = \boldsymbol{T}_{\mathrm{p}}(\phi_{\mathrm{k}})^{-1}\boldsymbol{T}_{\mathrm{p}}(\phi_{\mathrm{k}})\left[R_{\mathrm{s}}\boldsymbol{i}_{\mathrm{s}}^{k} + \omega_{\mathrm{k}}\boldsymbol{J}\boldsymbol{\psi}_{\mathrm{s}}^{k} + \frac{d}{dt}\boldsymbol{\psi}_{\mathrm{s}}^{k}\right], \tag{2.21}$$

$$= R_{\mathrm{s}}\boldsymbol{i}_{\mathrm{s}}^{k} + \underbrace{\omega_{\mathrm{k}}\boldsymbol{J}\boldsymbol{\psi}_{\mathrm{s}}^{k}}_{EMF} + \frac{d}{dt}\boldsymbol{\psi}_{\mathrm{s}}^{k}). \tag{2.22}$$

From this transformation and derivation the back EMF speed voltage term, $\omega_{\mathrm{m}}(t)\boldsymbol{J}\boldsymbol{\psi}_{\mathrm{s}}^{k}(t)$ emerges. This term can be regarded as a disturbance and adequately compensated for by the controller because of the assumption that the rate of change of this speed voltage term during one sampling period is insignificant [21].

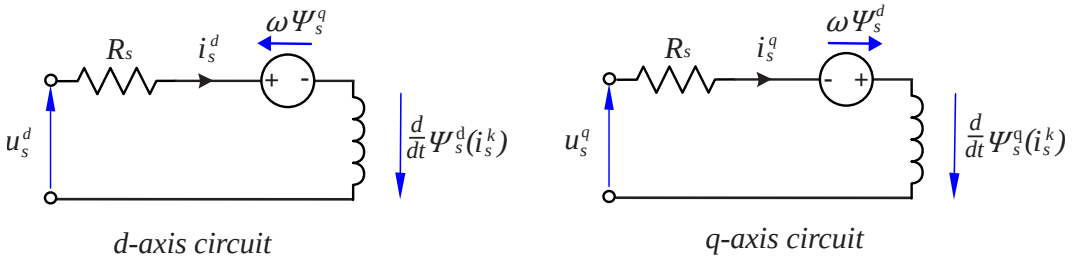

Figure 2.14: The equivalent circuit of the RSM in the dq reference frame. This circuit includes the magnetic saturation and cross-coupling between the d and q axis circuits. This model does not include core loss.

Electromechanical torque in the rotor reference frame is now described by

$$T_{\mathrm{m}} = p\frac{3}{2}(\boldsymbol{i}_{\mathrm{s}}^{s})^{T}\boldsymbol{J}\boldsymbol{\psi}_{\mathrm{s}}^{s}, \tag{2.23}$$

$$= p\frac{3}{2}\boldsymbol{i}_{\mathrm{s}}^{k}\boldsymbol{T}_{\mathrm{p}}((\phi_{\mathrm{k}})^{-1}\boldsymbol{J}\boldsymbol{T}_{\mathrm{p}}(\phi_{\mathrm{k}}))\boldsymbol{\psi}_{\mathrm{s}}^{k},$$

$$= p\frac{3}{2}(\boldsymbol{i}_{\mathrm{s}}^{k})^{T}\boldsymbol{J}\boldsymbol{\psi}_{\mathrm{s}}^{k}. \tag{2.24}$$

2.2.4 Magnetic and Cross Saturation

In reality the stator current ($\boldsymbol{i}_{\mathrm{s}}^{k}$) and flux linkage ($\boldsymbol{\psi}_{\mathrm{s}}^{k}$) dynamics of the RSM are highly non-linear, with significant saturation and cross-coupling occurring in both dq axes. If the flux-linkage and current relationship is taken to be strictly linear $\psi = i.L$, then the control response time and tracking error suffers greatly. Figure fig. 2.15 illustrates these saturation and cross-coupling effects with respect to stator current. The relationship between $\boldsymbol{\psi}_{\mathrm{s}}^{k}$ and $\boldsymbol{i}_{\mathrm{s}}^{k}$ is found either by carrying out practical tests on the machine or from FEM.

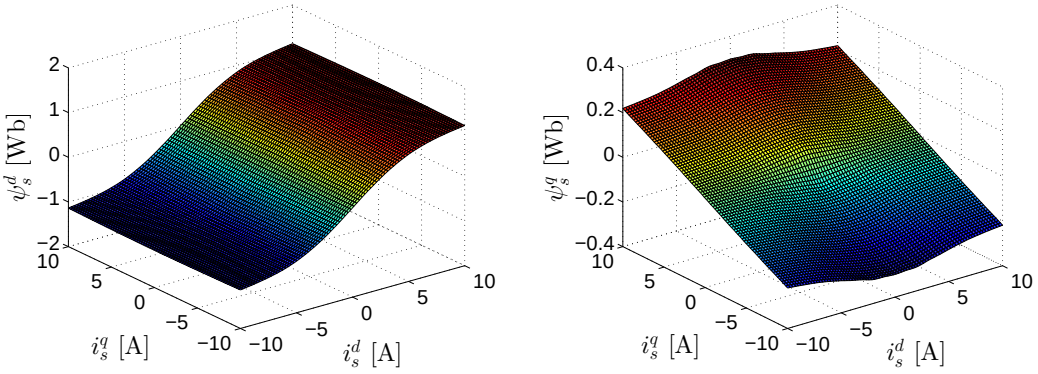

(a) d-axis flux-linkage (b) q-axis flux-linkage

Figure 2.15: Non-linear flux-linkages of the 3 kW RSG.

It can be seen that in the non-linear case the flux fields are time varying and depend on both currents, $\boldsymbol{i}_{\mathrm{s}}^{k} = (i_{\mathrm{s}}^{d}, i_{\mathrm{s}}^{q})^{T} \mapsto \boldsymbol{\psi}_{\mathrm{s}}^{k}(\boldsymbol{i}_{\mathrm{s}}^{k})$. Analytical methods to describe the flux-linkage dynamics are avoided by using the flux maps. However, in some cases the derivatives of the flux-linkages are required to formulate the inductances.

$$\frac{d}{dt}\boldsymbol{\psi}_{\mathrm{s}}^{k} = \frac{d}{dt}\boldsymbol{\psi}_{\mathrm{s}}^{k}(\boldsymbol{i}_{\mathrm{s}}^{k})) \qquad = \frac{\partial\boldsymbol{\psi}_{\mathrm{s}}^{k}(\boldsymbol{i}_{\mathrm{s}}^{k})}{\partial\boldsymbol{i}_{\mathrm{s}}^{k}}\frac{d\boldsymbol{i}_{\mathrm{s}}^{k}}{dt} \tag{2.25}$$

The non-linear inductance $L(\boldsymbol{i}_{\mathrm{s}}^{k})$ can be defined as the derivative of the flux-linkage by $L = \dfrac{\partial\boldsymbol{\psi}_{\mathrm{s}}^{k}(\boldsymbol{i}_{\mathrm{s}}^{k})}{\partial\boldsymbol{i}_{\mathrm{s}}^{k}}$, which represents the tangent at a specific operating point.

The symmetric and positive definite inductance matrix $\boldsymbol{L}_{\mathrm{s}}^{k}(\boldsymbol{i}_{\mathrm{s}}^{k}) \in \Re^{2x2}$ is defined as:

$$\begin{aligned}\boldsymbol{L}_{\mathrm{s}}^{k}(\boldsymbol{i}_{\mathrm{s}}^{k}) &= \frac{\partial \boldsymbol{\psi}_{\mathrm{s}}^{k}(\boldsymbol{i}_{\mathrm{s}}^{k})}{\partial \boldsymbol{i}_{\mathrm{s}}^{k}}, \\ &= \begin{bmatrix} \dfrac{\partial \psi_{\mathrm{s}}^{d}(\boldsymbol{i}_{\mathrm{s}}^{k})}{\partial i_{\mathrm{s}}^{d}} & \dfrac{\partial \psi_{\mathrm{s}}^{d}(\boldsymbol{i}_{\mathrm{s}}^{k})}{\partial i_{\mathrm{s}}^{q}} \\ \dfrac{\partial \psi_{\mathrm{s}}^{q}(\boldsymbol{i}_{\mathrm{s}}^{k})}{\partial i_{\mathrm{s}}^{d}} & \dfrac{\partial \psi_{\mathrm{s}}^{q}(\boldsymbol{i}_{\mathrm{s}}^{k})}{\partial i_{\mathrm{s}}^{q}} \end{bmatrix}, \\ &= \begin{bmatrix} L_{\mathrm{s}}^{dd}(\boldsymbol{i}_{\mathrm{s}}^{k}) & L_{\mathrm{s}}^{dq}(\boldsymbol{i}_{\mathrm{s}}^{k}) \\ L_{\mathrm{s}}^{qd}(\boldsymbol{i}_{\mathrm{s}}^{k}) & L_{\mathrm{s}}^{qq}(\boldsymbol{i}_{\mathrm{s}}^{k}) \end{bmatrix}. \end{aligned} \tag{2.26}$$

The self inductances are defined as L_{s}^{dd} and L_{s}^{qq} and the mutual inductance L_{s}^{dq} and L_{s}^{qd} where $L_{\mathrm{s}}^{dq} = L_{\mathrm{s}}^{qd}$, $L_{\mathrm{s}}^{dd} > 0$, $L_{\mathrm{s}}^{qq} > 0$, $L_{\mathrm{s}}^{dd} L_{\mathrm{s}}^{qq} - (L_{\mathrm{s}}^{dq})^2 > 0$. An example of the self and mutual inductance for only L_{s}^{dd} and L_{s}^{dq} is shown in fig. 2.16.

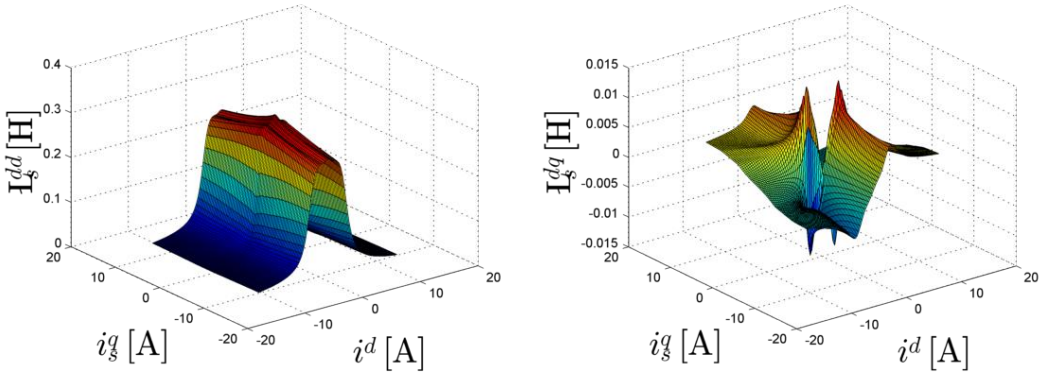

(a) L_{s}^{dd} inductance.

(b) L_{s}^{dq} inductance.

Figure 2.16: Examples of the self and mutual inductances of the the 3 kW RSG.

Using (2.26), (2.25) can be rewritten as (2.27).

$$\frac{d}{dt}\boldsymbol{\psi}_{\mathrm{s}}^{k} = \boldsymbol{L}_{\mathrm{s}}^{k}(\boldsymbol{i}_{\mathrm{s}}^{k})\frac{d}{dt}\boldsymbol{i}_{\mathrm{s}}^{k}. \tag{2.27}$$

The new definition of the flux derivative can be inserted into (2.22) to give:

$$\boldsymbol{u}_{\mathrm{s}}^{k} = R_{\mathrm{s}}\boldsymbol{i}_{\mathrm{s}}^{k} + \boldsymbol{L}_{\mathrm{s}}^{k}(\boldsymbol{i}_{\mathrm{s}}^{k})\frac{d}{dt}\boldsymbol{i}_{\mathrm{s}}^{k} + \omega_{\mathrm{k}} J \boldsymbol{\psi}_{\mathrm{s}}^{k}(\boldsymbol{i}_{\mathrm{s}}^{k}). \tag{2.28}$$

Eq. (2.22) can be further de-constructed into its component wise form, (2.29), which is more easily manipulated for controller design purposes in section 3.1.

$$\left.\begin{aligned} u_{\mathrm{s}}^{d} &= R_{\mathrm{s}} i_{\mathrm{s}}^{d} + L_{\mathrm{s}}^{dd}(\boldsymbol{i}_{\mathrm{s}}^{k})\frac{d}{dt} i_{\mathrm{s}}^{d} + L_{\mathrm{s}}^{dq}(\boldsymbol{i}_{\mathrm{s}}^{k})\frac{d}{dt} i_{\mathrm{s}}^{q} - \omega_{\mathrm{k}}(t)\psi_{\mathrm{s}}^{q}(\boldsymbol{i}_{\mathrm{s}}^{k}(t)), \\ u_{\mathrm{s}}^{q} &= R_{\mathrm{s}} i_{\mathrm{s}}^{q} + L_{\mathrm{s}}^{qq}(\boldsymbol{i}_{\mathrm{s}}^{k})\frac{d}{dt} i_{\mathrm{s}}^{q} + L_{\mathrm{s}}^{qd}(\boldsymbol{i}_{\mathrm{s}}^{k})\frac{d}{dt} i_{\mathrm{s}}^{d} + \omega_{\mathrm{k}}(t)\psi_{\mathrm{s}}^{d}(\boldsymbol{i}_{\mathrm{s}}^{k}(t)). \end{aligned}\right\} \tag{2.29}$$

2.2.5 Losses and Endwindings

Like any machine the RSM is subject to various losses, the majority of which is produced by the copper stator coils. However, some losses such as core loss are directly proportional to electrical frequency and will dominate at high speeds. Iron loss should be taken into account in more elaborate models of the RSM, however this was deemed beyond the scope of this project. Although copper and core loss affect the power factor and optimum current angle when under generator operation, it was beyond the scope of this project to implement losses in FEM. Figure 2.17 illustrates the core loss and shifting of the current vector, which results in an increased current angle and decreased power factor for generator mode. The power factor is represented by ϕ_{pf}, and i_m^k is the current seen by the RSG after the stator copper and core losses. $\boldsymbol{i}_{\mathrm{s}}^k$ is the applied or generated stator current.

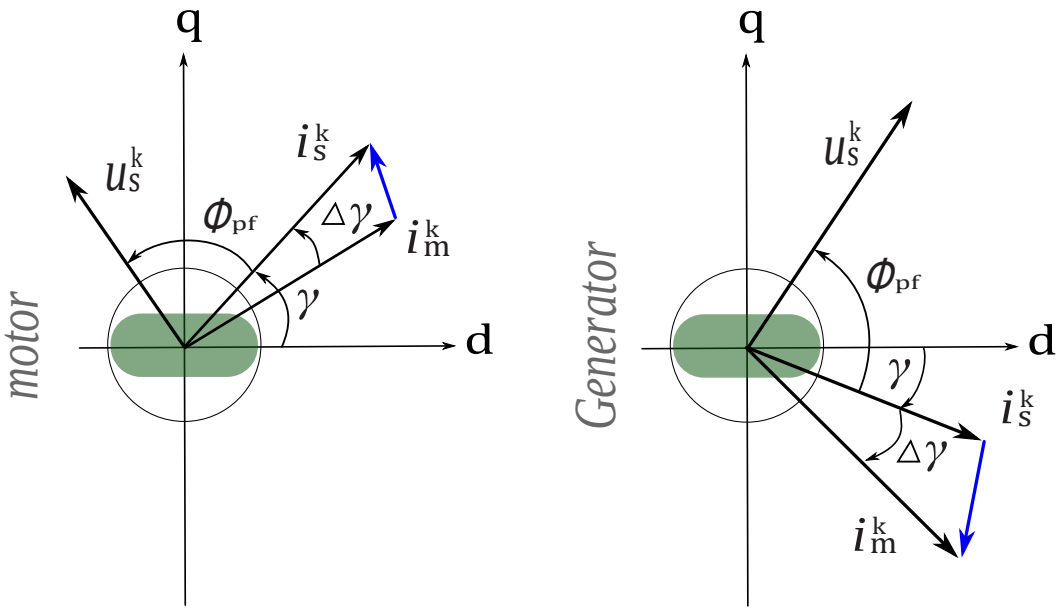

Figure 2.17: Phasor diagram of the power factor difference between motor and generator operation due to of the shift in the stator current vector as a result of core losses in the RSM.

2.3 Three-Phase Voltage Source Converters

As mentioned in section 2.1.4 and fig. 2.5, the VSC is an essential part of the intended variable speed WTS that is used to control the speed and torque of the RSG. VSCs are power electronic devices which convert a DC voltage source into a single-phase or multi-phase AC voltage source. VSCs have numerous applications, which extend beyond just variable frequency drives (VSDs) for AC motor speed control, to uninterruptible power

supplies, solar inverters and grid connected inverters [24]. Insulated-gate bipolar transistors (IGBT) are predominantly used in high voltage three-phase inverters instead of metal-oxide-semiconductor field-effect transistors (MOSFETs), which have higher on state losses at higher voltages.

The voltages present at the output of the VSC are not purely sinusoidal, but rather approximate the desired fundamental frequency by a series of high frequency pulses referred to as pulse width modulation (PWM). This approximation is done at every sampling instant, where the sampled value of the reference sinusoid single value is held over a fixed sampling period by adjusting the width of the pulse such that the mean value of the pulse over the entire period is equal to the sampled value [73]. With the addition of an output low-pass filter such as an LC, LR, or LCL filter, the high-order harmonics of the PWM signal can be filtered out leaving predominantly the fundamental harmonic.

[74] proposes a mathematical model for a three-phase inverter where the switches can be described by a switching vector, $\boldsymbol{s}^{abc} = (s^a, s^b s^c) = (U, V, W)$ with only two states, $\boldsymbol{s}^{abc} \in (0,1)$, and eight combinations $\boldsymbol{s}^{abc} \in (000, 001, 010, ..., 111)$. Stator phases are typically connected in wye, and thus can only supply line-to-line voltages, $u_{\mathrm{s}}^{abc,ltl}$ which are, according to (2.30), dependent on the DC bus voltage and switching states.

$$u_{\mathrm{s}}^{abc,ltl}(t) = u_{\mathrm{dc}}(t) \begin{bmatrix} 1 & -1 & 0 \\ 0 & 1 & -1 \\ -1 & 0 & 1 \end{bmatrix} \boldsymbol{s}^{abc}(t). \tag{2.30}$$

The DC link currents i_{dc} are defined by the phase current $\boldsymbol{i}_{\mathrm{s}}^{abc}$ and the switching vector in (2.31). Symmetric phase voltages $\boldsymbol{u}_{\mathrm{s}}^{abc}$ are governed by (2.32), to which the Clarke Transformation can be applied to achieve the space vector description of the stator voltage, (2.33).

$$i_{\mathrm{dc}}(t) = \boldsymbol{i}_{\mathrm{s}}^{abc}(t)^{\top} \boldsymbol{s}^{abc}(t), \tag{2.31}$$

$$\boldsymbol{u}_{\mathrm{s}}^{abc}(t) = \boldsymbol{T}_{\mathrm{v}}^{-1} u_{\mathrm{s}}^{abc,ltl}(t) \frac{u_{\mathrm{dc}}(t)}{3} \begin{bmatrix} 2 & -1 & -1 \\ -1 & 2 & -1 \\ -1 & -1 & 2 \end{bmatrix} \boldsymbol{s}^{abc}(t), \tag{2.32}$$

$$\boldsymbol{u}_{\mathrm{s}}^{s}(t) = \boldsymbol{T}_{\mathrm{c}} \boldsymbol{u}_{\mathrm{s}}^{abc}(t). \tag{2.33}$$

Conveniently the VSC can be simplified and represented by (2.34), a 1^{st}-order transfer function (PT1 system) with a time constant equal to the dead time period, T_{vsc}, of the switching devices (IGBTs). This is because the sampled values are modulated over one switching period T_{sw}), thus the output voltage $\boldsymbol{u}_{\mathrm{s}}^{abc}$ lags the reference signal $\boldsymbol{u}_{\mathrm{s},ref}^{abc}$ by one

switching cycle $\boldsymbol{u}_{\mathrm{s}}^{abc}(t) = \boldsymbol{u}_{\mathrm{s,ref}}^{abc}(t - T_{\mathrm{s}w})$ [74] .

$$\begin{aligned} F_{VSC}(s) &= \frac{\boldsymbol{u}_{\mathrm{s}}^{abc}(s)}{\boldsymbol{u}_{\mathrm{s,ref}}^{abc}(s)} \\ &= \frac{1}{1 + \frac{sT_{\mathrm{vsc}}}{1!} + \frac{s^2 T_{\mathrm{vsc}}^2}{2!}} \\ &\approx \frac{1}{1 + sT_{\mathrm{vsc}}} \end{aligned} \tag{2.34}$$

Figure 2.18 illustrates the basic layout of a VSC with a three-phase passive rectifier. Typically industrial VSDs come with back-end three-phase rectification so that the drive can be operated from three-phase mains. Passive rectification only allows power flow in one direction (to the drive). Most VSCs will have a separate DC input so that the DC-bus can be accessed directly, this is the case with the SEW Movi-drive VSCs which were used extensively in this project.

A VSC can also be configured in a back-to-back strategy, as shown in fig. 2.19. This topology can transfer power bi-directionally using active rectification on either end. Another added benefit of active rectification is that the DC bus voltage can be controlled, rather than being fixed at $\approx 560\,\mathrm{V}$. For a variable speed WTS a back-to-back VSC is necessary as it allows the voltage and frequency of the AC generator to be adjusted without influencing the grid. This topology also allows adequate grid filtering to be implemented, which will be discussed later on. The SEW Movi drives make control system development very easy. The drives are custom built to allow a user to input three high side PWM signals (TTL logic 5V) to control the states of each of the full-bridge legs, as well as providing isolated and filtered current and voltage measurements. The Movi drive takes care of any IGBT driver circuity issues such as dead-time or the correct charging and discharging of the IGBT gates. Perhaps the most important feature of these drives is the short circuit current protection, which can be set to any desired level using SEW software and will subsequently deactivate the IGBTs if triggered.

2.3.1 Modulation Methods

Space vector PWM (SVPWM) is a widely used PWM modulation scheme, which allows a more efficient use of the DC bus voltage than conventional sinusoidal PWM (SPWM) and is extensively used for FOC motor control by almost all of the literature resources in this project. SVPWM is achieved by the injection of a third harmonic and can produce about 15% higher output voltage [24, 75, 76]. The maximum allowable voltage from SPWM is $u_{max} = \frac{u_{\mathrm{dc}}}{2}$ and SVPWM is $u_{max} = \frac{u_{\mathrm{dc}}}{\sqrt{3}}$. Figure 2.21 shows the filtered fundamental line-to-line and phase voltages of SVPWM and SPWM generated in Matlab using a simulated inverter. Note the distinguishable feature of SVPWM with its third harmonic "bumps"

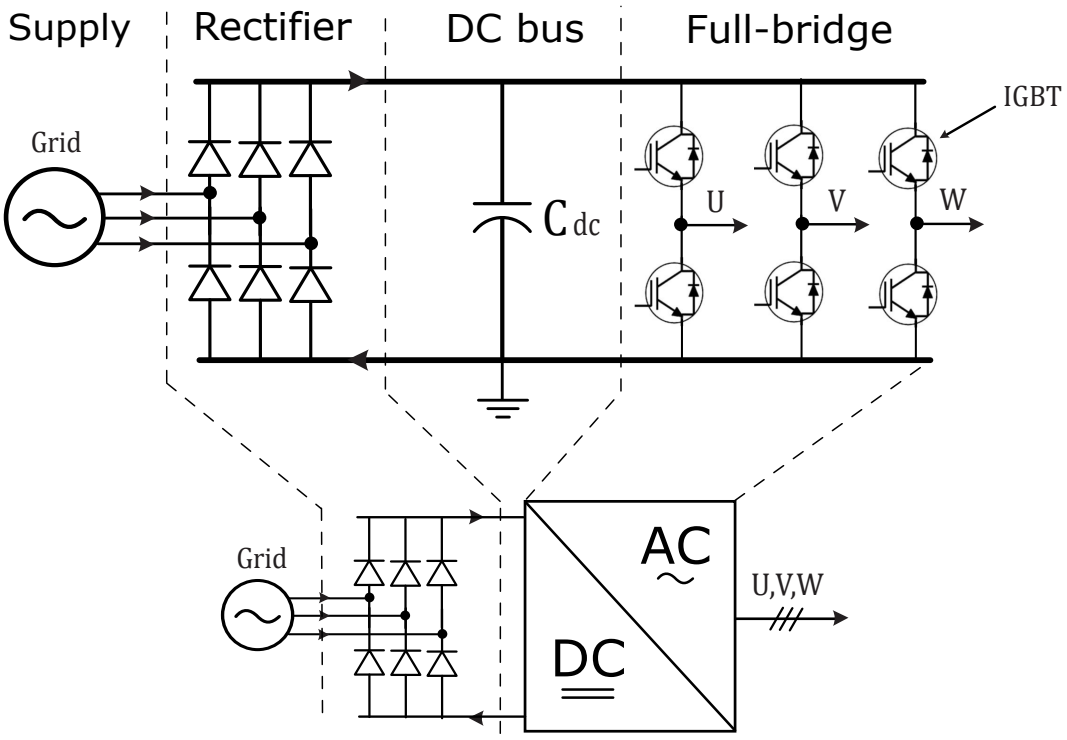

Figure 2.18: Lower and higher level diagrams of a full-bridge IGBT VSC with a three-phase passive rectifier for operation off a three-phase grid supply.

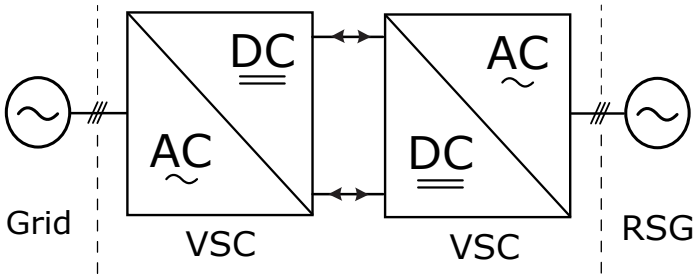

Figure 2.19: Higher level diagram of a back-to-back VSC, with bi-directional power flow.

which reduce its peak phase voltage amplitude. An in-depth review and implementation of SVPWM is available in appendix A.2.

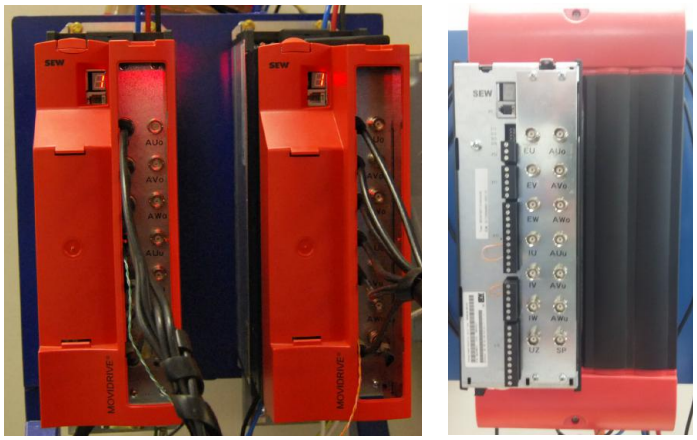

Figure 2.20: The custom-built SEW Movi-drive with PWM input and measurements output panel.

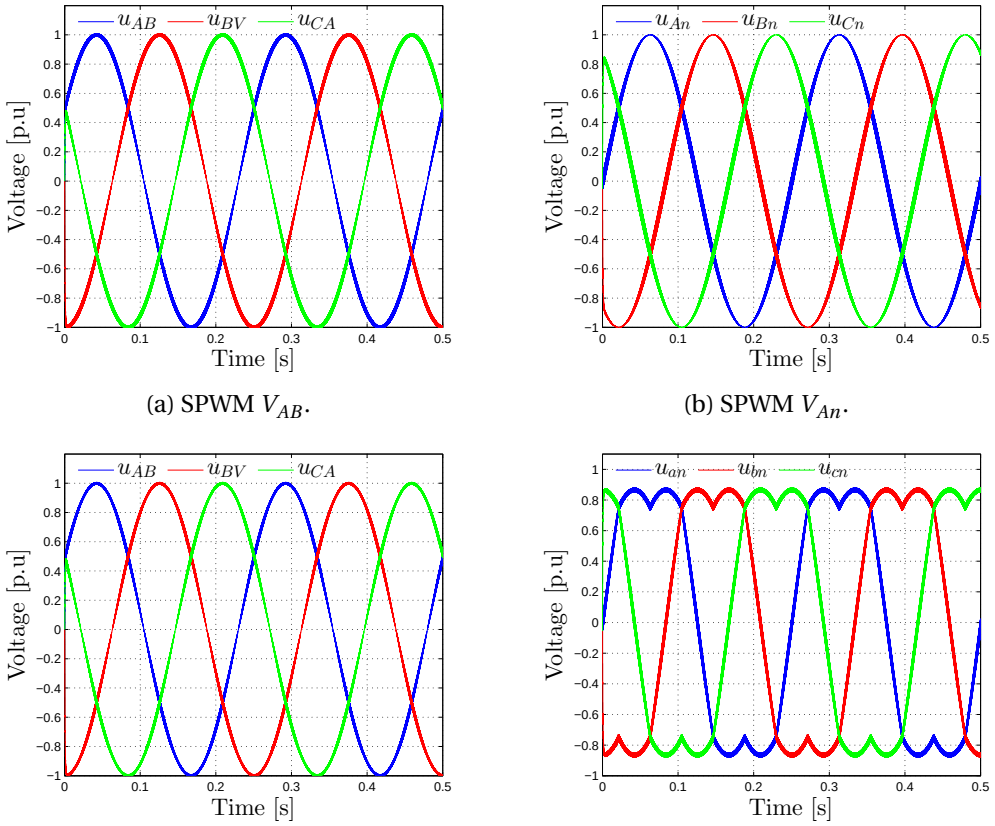

(a) SPWM V_{AB}.

(b) SPWM V_{An}.

(c) SVPWM V_{AB}.

(d) SVPWM V_{An}.

Figure 2.21: Simulink inverter model generated line-to-line and phase voltages of SPWM and SVPWM.

Chapter 3

RSG and Grid-Tie Control: Literature and Theory

In this chapter an overview of the theory required to control the RSGs is given with special attention paid to the cross-coupling effects and the non-linearity of the flux-linkages and inductances. A control model for the RSM is derived and a method for selecting PI controller gains on-line is presented. Open-loop torque control of the RSG using a maximum torque per ampere is then detailed. The theory and literature for two PSC techniques are also discussed in this chapter. An estimator-based FOC-method for operating the RSG, with PSC or an encoder, using an output LC-filter is given. Finally grid synchronization, grid current injection control and DC bus voltage control techniques are presented.

3.1 RSG Controller Design

To control the torque or speed of a RSG, the air gap flux-linkage space vector must be controlled precisely in magnitude and frequency to cause torque on the rotor. Thus, an essential part of RSM control is how the rotor angle is tracked. Without this angle there is no way for the Park Transformation to orientate the stator voltages in relation to the d-axis of the rotor. This is generally known as Field Orientated Control (FOC). Direct FOC methods track the rotor angle by means of a sensor whereas indirect methods estimate it using various PSC techniques, which are discussed in section 3.2.

Although direct torque control (DTC) is an alternative to FOC and is used extensively by some wind turbine companies, a clear distinction between which method is best suited to wind turbine systems has not yet been made [77]. The main advantages of DTC are its inherent PSC properties and dynamic performance, but it has several drawbacks such as the high sampling frequency, variable switching frequency and high torque pulsations [78].

Current control methods proposed by several authors were investigated, [21, 48, 70, 79–82] , all of which implement FOC, include inverter time delay and adaptive cross-coupling feed-forward compensation. PI controllers are predominantly used, some use fixed gain which limits the performance of the system whereas others use gain scheduling to match the non-linearities and improve controller response. Discrete controllers are developed in [48, 79, 82], but did not significantly improve the controller performance because the sampling and switching frequencies are very high. Gain scheduling was proposed by [48] which demonstrates a more responsive current controller than a fixed gain version.

The cascade control structure presented in fig. 3.1a is often preferred to simplify large complex systems by using nested controllers, and is common practice with the control of AC machines. It is important to make sure that the outer level controllers have lower bandwidths than the inner loops so as not to interfere with the inner loop dynamics. Feed-forward compensation is an effective way of eliminating disturbances which are coupled into a system's dynamics, as shown in fig. 3.1. If disturbances can be observed or measured they can be added to the controller output as compensation and the disturbance can then be neglected in the controller design. If done correctly the compensation will improve the system response time and eliminate steady state error [83].

Although the various current control strategies reviewed in the literature were eligible for use in this project, the main body of section 3.1 was created during collaboration with Munich University [21] . In this section a non-linear, on-line update control method is described. The control model for the linear case is explained first and then the model for the non-linear case. The overall control model is presented in fig. 3.1.

3.1.1 Linear Current Control

In the linear case the flux-linkage is directly related to the currents generated in the stator where the inductance matrix $\boldsymbol{L}_{\mathrm{s}}^{k}$ is constant over all current values.

$$\psi = \boldsymbol{i}_{\mathrm{s}}^{s}\boldsymbol{L}_{\mathrm{s}}^{k}. \tag{3.1}$$

In reality this approximation is fairly inaccurate because the current and flux relationship is actually highly non-linear due to magnetic-cross coupling and saturation. To simplify things it is easier to derive the current dynamics in the linear case and then manipulate the non-linearities at the end. A controller design equation (2.28) was formulated in section 2.2.4. Rearranging (2.28) into a state space form and solving for the

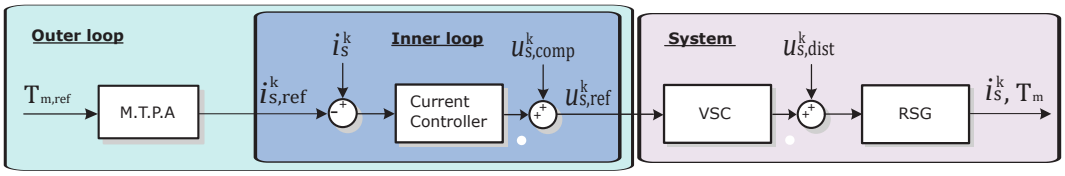

(a) Cascaded control structure of the RSG, showing feed-forward compensation.

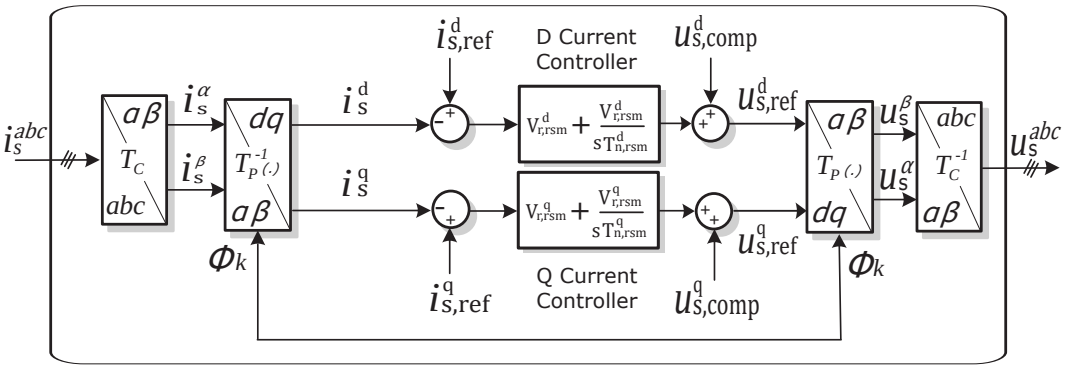

(b) Inner loop current control structure.

Figure 3.1: Overview of the cascade current controller design, with focus on the inner loop current control.

current derivatives leads to:

$$\left.\begin{aligned} \frac{d}{dt}i_s^d &= \frac{1}{L_s^{dd}}\left[u_s^d - R_s i_s^d + \omega_k \psi_s^q(\boldsymbol{i}_s^k) - L_s^{dq}\frac{d}{dt}i_s^q\right], \\ \frac{d}{dt}i_s^q &= \frac{1}{L_s^{qq}}\left[u_s^q - R_s i_s^q - \omega_k \psi_s^d(\boldsymbol{i}_s^k) - L_s^{qd}\frac{d}{dt}i_s^d\right]. \end{aligned}\right\} \tag{3.2}$$

Take note here that in the linear case all the inductance terms are constant. The cross coupling of the equations through $\frac{d}{dt}i_s^d(t)$ and $\frac{d}{dt}i_s^q(t)$ is now apparent. The cross-coupling terms can be eliminated by simultaneously solving the equations. The process is the same for the q-axis and thus only the d-axis arithmetic is done below.

$$\begin{aligned} \frac{d}{dt}i_s^d = \frac{1}{L_s^{dd}}&\left[u_s^d - R_s i_s^d + \omega_k \psi_s^q(\boldsymbol{i}_s^k)\right] \\ &- \frac{L_s^{dq}}{L_s^{qq}}\left[u_s^q - R_s i_s^q - \omega_k \psi_s^d(\boldsymbol{i}_s^k))\right] + L_\gamma \frac{d}{dt}i_s^d, \end{aligned} \tag{3.3}$$

where $L_\gamma = \dfrac{L_s^{dq}L_s^{qd}}{L_s^{qq}L_s^{dd}}$. Subtraction of the derivative term and division by $(1-L_\gamma)$ yields

$$\begin{aligned} \frac{d}{dt}i_s^d(1-L_\gamma) = \frac{1}{L_s^{dd}}&[u_s^d - R_s i_s^d + \omega_k \psi_s^q(\boldsymbol{i}_s^k) \\ &- \frac{L_s^{dq}}{L_s^{qq}}(u_s^q - R_s i_s^q - \omega_k \psi_s^d(\boldsymbol{i}_s^k))]. \end{aligned} \tag{3.4}$$

$$\frac{d}{dt}i_s^d = \frac{L_s^{qq}}{L_s^{qq}L_s^{dd} - L_s^{dq}L_s^{qd}}[u_s^d - R_s i_s^d + \omega_k \psi_s^q(\boldsymbol{i}_s^k) - \frac{L_s^{dq}}{L_s^{qq}}(u_s^q - R_s i_s^q - \omega_k \psi_s^d(\boldsymbol{i}_s^k))]. \tag{3.5}$$

The auxiliary inductances can be simplified to:

$$\left.\begin{aligned} L_{s,aux}^d &= \frac{L_s^{qq}L_s^{dd} - L_s^{dq}L_s^{qd}}{L_s^{qq}}, \\ L_{s,aux}^q &= \frac{L_s^{qq}L_s^{dd} - L_s^{dq}L_s^{qd}}{L_s^{dd}}. \end{aligned}\right\} \tag{3.6}$$

$L_{s,aux}^d$ and $L_{s,aux}^q$ are strictly positive due to the properties of the inductance matrix from section 2.2.4. The disturbance voltages are grouped to form:

$$\left.\begin{aligned} u_{s,\text{dist}}^d(\boldsymbol{i}_s^k, \omega_k, u_s^q) &= \omega_k \psi_s^q(\boldsymbol{i}_s^k) - \frac{L_s^{dq}}{L_s^{qq}}\left[u_s^q - R_s i_s^q - \omega_k \psi_s^d(\boldsymbol{i}_s^k)\right], \\ u_{s,\text{dist}}^q(\boldsymbol{i}_s^k, \omega_k, u_s^d) &= -\omega_k \psi_s^q(\boldsymbol{i}_s^k) - \frac{L_s^{qd}}{L_s^{dd}}\left[u_s^d - R_s i_s^d + \omega_k \psi_s^q(\boldsymbol{i}_s^k)\right], \end{aligned}\right\} \tag{3.7}$$

which leads to the final state space form for the linear system model:

$$\left.\begin{aligned} \frac{d}{dt}i_s^d &= \frac{1}{L_{s,aux}^d}\left[u_s^d - R_s i_s^d + u_{s,\text{dist}}^d(\boldsymbol{i}_s^k, \omega_k, u_s^q)\right], \\ \frac{d}{dt}i_s^q &= \frac{1}{L_{s,aux}^q}\left[u_s^q - R_s i_s^q + u_{s,\text{dist}}^q(\boldsymbol{i}_s^k, \omega_k, u_s^d)\right]. \end{aligned}\right\} \tag{3.8}$$

Even in this compact form the system is still coupled through $u_{s,\text{dist}}^d$ and $u_{s,\text{dist}}^q$. However, the equations can now be easily dealt with using disturbance compensation. The VSC and its subsequent converter delay of T_{dt} (see section 2.3) prevents perfect compensation from being achieved. An approximation has to be made which can be either dynamic or static.

$$F_C(s) = \begin{cases} -(1+T_{dt}) & \text{: ideal compensation,} \\ -V_C & \text{: static compensation with } V_C \leq 1, \\ -V_C\dfrac{1+T_{dt}}{1+T_s} & \text{: dynamic compensation with } T_s \ll T_{dt}, V_C \leq 1. \end{cases}$$

$$\boldsymbol{u}_{s,comp}^k(\boldsymbol{i}_s^k(t)) = \mathscr{L}^{-1}F_C(t)\boldsymbol{u}_{s,\text{dist}}^k(\boldsymbol{i}_s^k, \omega_k, \boldsymbol{u}_s^k),$$

$$\left.\begin{aligned} u_{s,comp}^d(\boldsymbol{i}_s^k, \omega_k, u_{s,ref}^q) &= -u_{s,\text{dist}}^d(\boldsymbol{i}_s^k, \omega_k, u_{s,ref}^q), \\ u_{s,comp}^q(\boldsymbol{i}_s^k, \omega_k, u_{s,ref}^d) &= -u_{s,\text{dist}}^q(\boldsymbol{i}_s^k, \omega_k, u_{s,ref}^d). \end{aligned}\right\} \tag{3.9}$$

However, for the simplification of the design process ideal compensation can be assumed if the sampling time T_s of the controller is sufficiently smaller than the inverter delay T_{dt}. This allows the transformation of (3.8)and (3.8) into their Laplace form.

$$\left.\begin{aligned} \frac{i_s^d(s}{u_s^d(s)}) &= \frac{\frac{1}{R_s}}{1+s\frac{L_{s,aux}^d}{R_s}}, \\ \frac{i_s^q(s}{u_s^q(s)}) &= \frac{\frac{1}{R_s}}{1+s\frac{L_{s,aux}^q}{R_s}}. \end{aligned}\right\} \tag{3.10}$$

Figure 3.2 shows that the system can be de-constructed into two consecutive first-order - PT1 elements which are combined into a single PT2 system, (3.11).

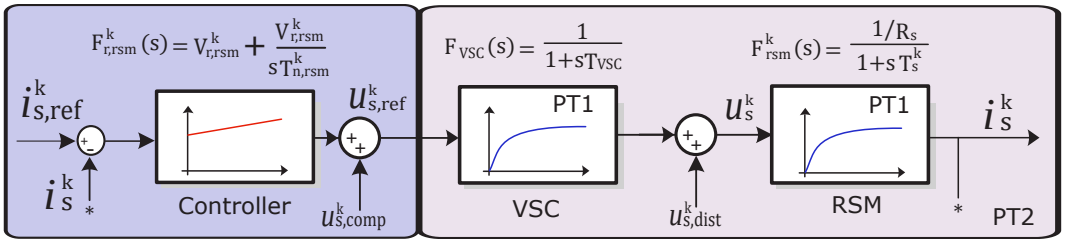

Figure 3.2: Closed loop control system for the RSM with feedfoward compensation. VSC and RSM represented as PT1 systems and the system as a PT2.

$$\frac{\boldsymbol{i}_s^k(s}{\boldsymbol{u}_s^k(s)}) = \frac{\frac{1}{R_s}}{(1+s\frac{\boldsymbol{L}_{s,aux}^k}{R_s})(1+sT_{vsc})}. \tag{3.11}$$

The dynamics of a PT2 system can be controlled satisfactorily with a PI-controller.

$$F_{r,rsm}(s) = V_{r,rsm}^k \frac{1+sT_{n,rsm}^k}{sT_{n,rsm}^k}. \tag{3.12}$$

Using the Modulus Optimum criterion [84, Sec. 7.1], the gain selection is chosen to maximise the bandwidth of the controller.

$$\left.\begin{aligned} \textbf{Gain: } V_{r,rsm}^k &= \frac{T_s^k R_s}{2T_{vsc}}, \\ \textbf{Time Constant: } T_{n,rsm}^k &= T_s^k. \end{aligned}\right\} \tag{3.13}$$

3.1.2 Non-linear Current Control

The non-linear model of the RSG is characterized by flux-linkage and inductance quantities which are non-linearly dependent on the stator current. These parameters are obtained using the flux map data calculated in FEM packages (see section 2.2.4) and stored in look-up tables (LUTs) for access during operation on the embedded system, as shown in fig. 3.3. Previous work has shown that flux map data is an accurate representation of the actual motor [81, 82, 85].

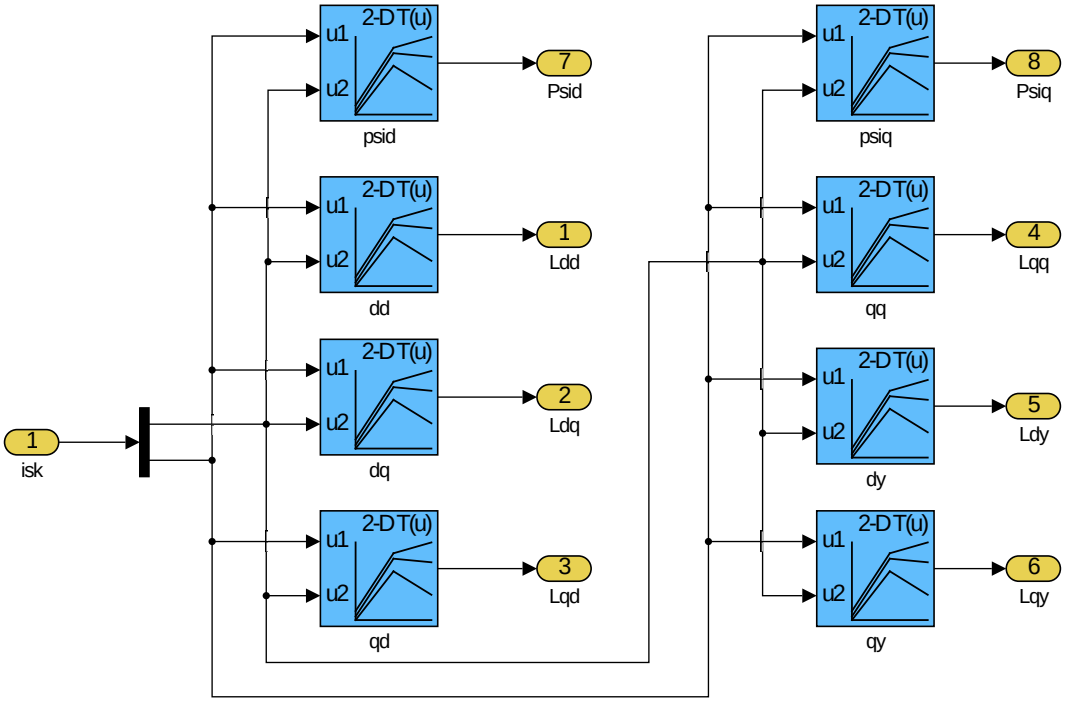

Figure 3.3: Look up table format showing self inductance L_s^{qq}.

For the non-linear case the current dynamics can be directly adapted to (3.10) with the current dependent inductances substituted in place of the static ones.

$$\left.\begin{aligned} \frac{\mathrm{d}}{\mathrm{d}t} i_s^d &= \frac{1}{L_{s,aux}^d(\boldsymbol{i}_s^k)} \left[u_s^d - R_s i_s^d + u_{s,\mathrm{dist}}^d(\boldsymbol{i}_s^k, \omega_k, u_s^q) \right], \\ \frac{\mathrm{d}}{\mathrm{d}t} i_s^q &= \frac{1}{L_{s,aux}^q(\boldsymbol{i}_s^k)} \left[u_s^q - R_s i_s^q + u_{s,\mathrm{dist}}^q(\boldsymbol{i}_s^k, \omega_k, u_s^d) \right]. \end{aligned}\right\} \tag{3.14}$$

where the current dependent auxiliary inductance terms are defined as:

$$\left.\begin{aligned} L_{s,aux}^d(\boldsymbol{i}_s^k) &= \frac{L_s^{qq}(\boldsymbol{i}_s^k) L_s^{dd}(\boldsymbol{i}_s^k) - L_s^{dq}(\boldsymbol{i}_s^k) L_s^{qd}(\boldsymbol{i}_s^k)}{L_s^{qq}(\boldsymbol{i}_s^k)}, \\ L_{s,aux}^q(\boldsymbol{i}_s^k) &= \frac{L_s^{dd}(\boldsymbol{i}_s^k) L_s^{qq}(\boldsymbol{i}_s^k) - L_s^{qd}(\boldsymbol{i}_s^k) L_s^{dq}(\boldsymbol{i}_s^k)}{L_s^{dd}(\boldsymbol{i}_s^k)}, \end{aligned}\right\} \tag{3.15}$$

and the disturbance terms as:

$$\begin{aligned} u^d_{\mathrm{s,dist}}(\boldsymbol{i}^k_\mathrm{s}, \omega_\mathrm{k}, u^q_\mathrm{s}) &= \omega_\mathrm{k}\psi^q_\mathrm{s}(\boldsymbol{i}^k_\mathrm{s}) - \frac{L^{dq}_\mathrm{s}(\boldsymbol{i}^k_\mathrm{s})}{L^{qq}_\mathrm{s}(\boldsymbol{i}^k_\mathrm{s})}\left[u^q_\mathrm{s} - R_\mathrm{s} i^q_\mathrm{s} - \omega_\mathrm{k}\psi^d_\mathrm{s}(\boldsymbol{i}^k_\mathrm{s})\right], \\ u^q_{\mathrm{s,dist}}(\boldsymbol{i}^k_\mathrm{s}, \omega_\mathrm{k}, u^d_\mathrm{s}) &= -\omega_\mathrm{k}\psi^d_\mathrm{s}(\boldsymbol{i}^k_\mathrm{s}) - \frac{L^{qd}_\mathrm{s}(\boldsymbol{i}^k_\mathrm{s})}{L^{dd}_\mathrm{s}(\boldsymbol{i}^k_\mathrm{s})}\left[u^d_\mathrm{s} - R_\mathrm{s} i^d_\mathrm{s} + \omega_\mathrm{k}\psi^q_\mathrm{s}(\boldsymbol{i}^k_\mathrm{s})\right], \end{aligned} \tag{3.16}$$

Thus as in the linear case the cross-coupling terms are compensated for by the following feed-forward disturbance compensation:

$$\left.\begin{aligned} u^d_{\mathrm{s},comp}(\boldsymbol{i}^k_\mathrm{s}, \omega_\mathrm{k}, u^q_{\mathrm{s},ref}) &= -u^d_{\mathrm{s,dist}}(\boldsymbol{i}^k_\mathrm{s}, \omega_\mathrm{k}, u^q_{\mathrm{s},ref}), \\ u^q_{\mathrm{s},comp}(\boldsymbol{i}^k_\mathrm{s}, \omega_\mathrm{k}, u^d_{\mathrm{s},ref}) &= -u^q_{\mathrm{s,dist}}(\boldsymbol{i}^k_\mathrm{s}, \omega_\mathrm{k}, u^d_{\mathrm{s},ref}). \end{aligned}\right\} \tag{3.17}$$

where the reference voltages $u^d_{\mathrm{s},ref}$ and $u^q_{\mathrm{s},ref}$ are used to approximate the applied voltages u^d_s and u^q_s, respectively. The simplified transfer function, (3.18), can be then formulated.

$$\frac{\boldsymbol{i}^k_\mathrm{s}(s)}{\boldsymbol{u}^k_{\mathrm{s},ref}(s)} = \frac{\dfrac{1}{R_\mathrm{s}}}{1+s\dfrac{\boldsymbol{L}^k_{\mathrm{s},aux}(\boldsymbol{i}^k_\mathrm{s})}{R_\mathrm{s}}}. \tag{3.18}$$

Taking into account the underlining VSC dynamics leads to (3.19).

$$\left.\begin{aligned} \frac{i^d_\mathrm{s}(s)}{u^d_{\mathrm{s},ref}(s)} &= \frac{\dfrac{1}{R_\mathrm{s}}}{1+sT^d_\mathrm{s}(\boldsymbol{i}^k_\mathrm{s})}\frac{1}{1+s\,T_{\mathrm{vsc}}}, \\ \frac{i^q_\mathrm{s}(s)}{u^q_{\mathrm{s},ref}(s)} &= \frac{\dfrac{1}{R_\mathrm{s}}}{1+sT^q_\mathrm{s}(\boldsymbol{i}^k_\mathrm{s})}\frac{1}{1+s\,T_{\mathrm{vsc}}}. \end{aligned}\right\} \tag{3.19}$$

Since the system time constants, $\boldsymbol{T}^k_\mathrm{s}(\boldsymbol{i}^k_\mathrm{s}) = \frac{\boldsymbol{L}^k_{\mathrm{s},aux}(\boldsymbol{i}^k_\mathrm{s})}{Rs}$, are functions of the $\boldsymbol{i}^k_\mathrm{s}$, the controller closed-loop poles must be shifted continuously by updating the controller parameters online, based on the actual current measurement (system state) to maintain stability and the optimum response times. A simple tuning rule to tune the parameters $V^k_{\mathrm{r,r}sm}$ (gain) and $T^k_{\mathrm{n,r}sm}$ (time constant) of the PI controllers is provided by the modulus optimum criterion [84, Sec. 7.1], provided that the inductance and flux linkage of the machine remain constant for the duration of the sampling period. The final control structure is illustrated in fig. 3.4 with the torque control block MTPA which will be discussed in the next section.

$$\left.\begin{aligned} \textbf{Gain: } V^k_{\mathrm{r,r}sm}(\boldsymbol{i}^k_\mathrm{s}) &= \frac{T^k_\mathrm{s}(\boldsymbol{i}^k_\mathrm{s})R_\mathrm{s}}{2T_{\mathrm{vsc}}} = \frac{L^k_\mathrm{s}(\boldsymbol{i}^k_\mathrm{s})}{2T_{\mathrm{vsc}}}, \\ \textbf{Time Constant: } T^k_{\mathrm{n,r}sm}(\boldsymbol{i}^k_\mathrm{s}) &= T^k_\mathrm{s}(\boldsymbol{i}^k_\mathrm{s}). \end{aligned}\right\} \tag{3.20}$$

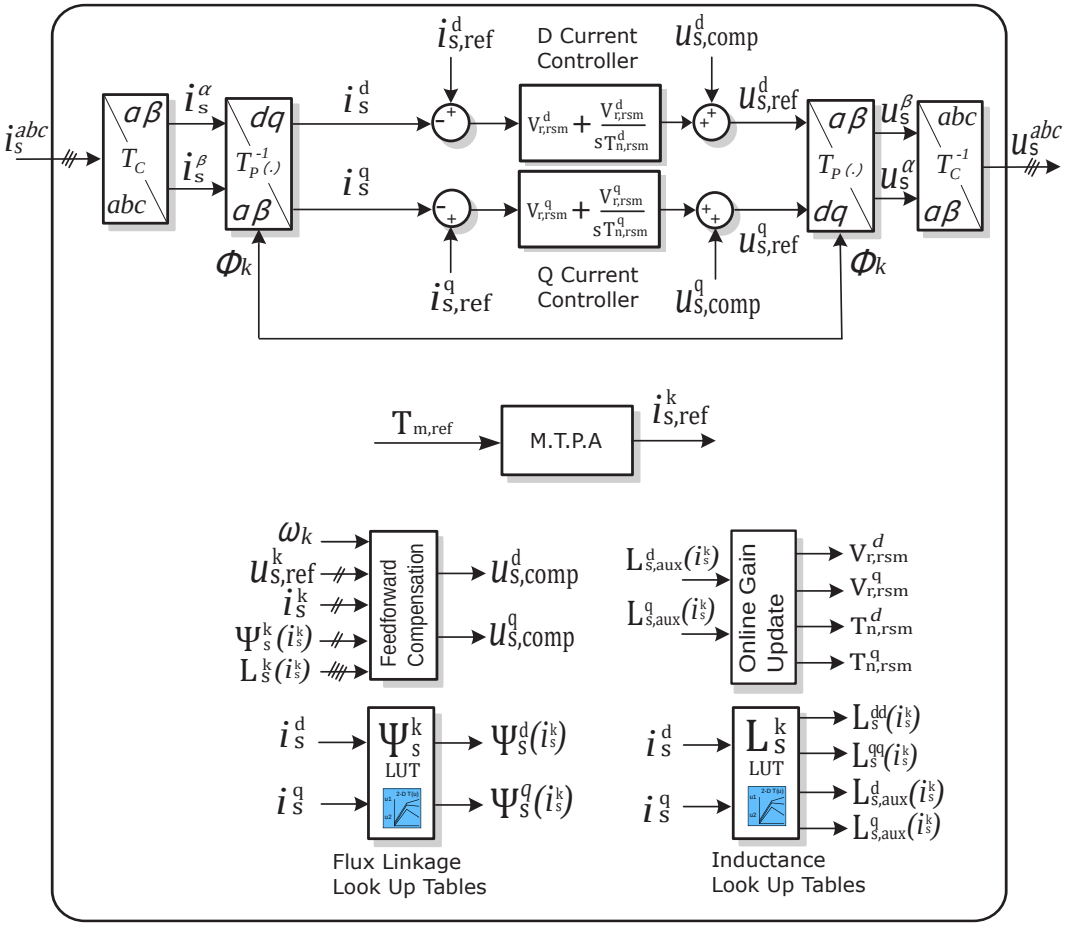

Figure 3.4: Non-linear current controller structure including MTPA.

3.1.3 Anti-wind-up limits

Integrator wind-up describes a scenario where a set-point cannot be reached e.g. due to insufficient output voltage, and the integral part of the PI controller continues to increase indefinitely. In reality there are limits to the output voltage of the VSC and the DC-bus, thus to prevent saturation of the VSC, appropriate limits must be set for the output of the PI controllers. In fig. 3.5 a basic form of anti-wind-up that limits the $u^d_{s,ref}$ and $u^q_{s,ref}$ vectors independently is shown. Although this method sufficiently stops the integrator wind-up it does nothing to prevent the distortion or realignment of the current vector when output saturation occurs. Continually assessing the output voltage vector and subsequently realigning it is computationally expensive, but should be implemented if the operating voltage limits of the VSC are frequency reached. Since the majority of the tests in this thesis were conducted in the operating range of the RSM, the basic anti-wind-up method was used.

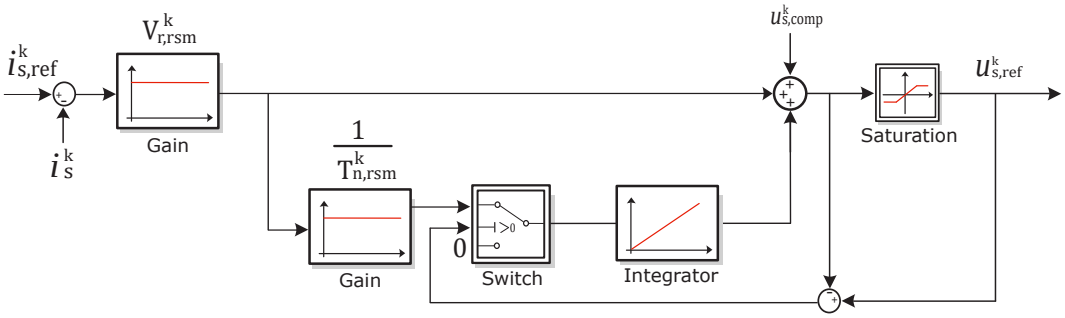

Figure 3.5: Non-linear PI controller, with anti wind-up.

3.1.4 Torque Control

In a cascaded control system the torque controller provides the current reference $\boldsymbol{i}^k_{s,ref}$ to the current controllers. It can be shown that since the underlying current controllers have a time constant $\boldsymbol{T}^k_s$ which can be considered small against the time constant of the mechanical system, the torque reference is assumed to be achieved with negligible delay. This reduces the open-loop torque control objective to obtaining an optimum current vector from the target torque $T_{m,ref}$. Machine specific torque limits and current limits must also be imposed on the torque controller to restrict the machine's operation range to safe rated values.

The machine specific FEM torque map, shown in fig. 3.6, is compiled into LUTs so that $T_m = T_m(i^d_s, i^q_s) \in \mathbb{R}^{n\times n}$. The map can be generated using flux-linkage data, and (2.24), the SEMFEM output torque can be used directly or a measured torque map can be used. Given $T_{m,ref}$, the torque controller objective is to locate the appropriate optimum current vector and deliver that as a reference to the current controllers. However, it can be seen from fig. 3.6 that the torque map is ambiguous, with many combinations of current vector qualifying for a given torque reference. Various control strategies which eliminate or exploit this ambiguity exist, such as maximum voltage per amp, maximum power factor per amp and the focus of this section, maximum torque per ampere (MTPA).

3.1.5 Maximum Torque per Ampere Control

In Maximum Torque per Ampere (MTPA) the control objective is to minimise the current magnitude for a given torque reference or maximise the torque for a given current reference. This creates an efficient means of operating the machine if it is assumed that the stator copper loss $P = \frac{3}{2}R_s|\boldsymbol{i}^k_s|^2[W]$ dominates all other losses in the machine. If the optimal current vector problem is approached analytically for a linear machine the results will show that the optimum current vector lies at 45°. In the non-trivial case, the non-linear nature of the machine prevents analytical solutions because no analytical

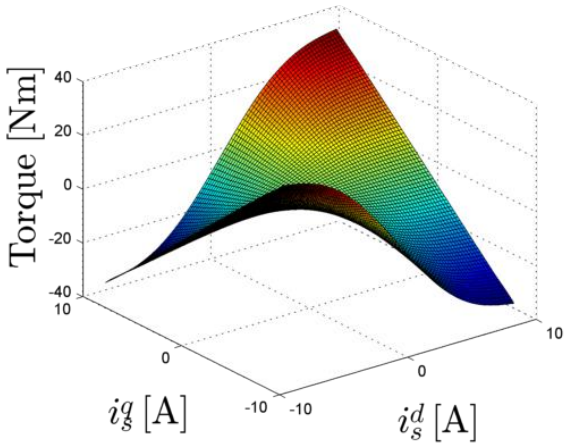

Figure 3.6: FEM generated torque map for the 3 kW RSM shown versus d/q-axis currents.

description of the flux linkages is available. Thus the current vectors are better dealt with numerically. Generic synchronous machine flux map-based torque control algorithms have been worked on extensively. [79] developed a MTPA method for a family of synchronous machines namely RSM, PMARSM, PMSM and IPMSM, which includes the speed and DC bus voltage. The torque control strategy is relatively straightforward and its practical implementation is computationally inexpensive, since the calculations are done in an off-line process, which relies on machine specific data from FEM and therefore includes non-linear effects such as saturation and cross-coupling. The current references are then extracted on-line using LUTs. Since the system in this project has a fixed DC bus voltage, a simpler MTPA current vs torque map strategy. This generic numerical strategy developed by [86], showed good simulated performance, but did not present any measured results. The algorithm extracts all points from the torque map $T_{\mathrm{m}}(|\boldsymbol{i}_{\mathrm{s}}^k|,\gamma)$. Cartesian co-ordinates are preferred over to polar ones, so that the optimum current magnitude $|\boldsymbol{i}_{\mathrm{s}}^k|$ and current angle γ are easier to analyse. Figure 3.7 illustrates the FEM-based polar co-ordinate MTPA map. Appendix D.0.3 contains the Matlab code used to solve the MTPA. Essentially all points, $T_{\mathrm{m}}(|\boldsymbol{i}_{\mathrm{s}}^k|,\gamma)$ in the map are compared until the point with the lowest current magnitude for the given torque point is found. This process is too computationally expensive to perform on-line and so an off-line solution is found, curve fitting is applied to the selected corresponding current magnitudes, current angles and torque references. Two 1D torque maps LUTs are then generated, one dependent on current magnitude and one dependent on current angle as shown in fig. 3.8.

$$i_s^k(i_{\mathrm{s}}^d, i_{\mathrm{s}}^q) = \begin{pmatrix} |i_s^k|(i_{\mathrm{s}}^d, i_{\mathrm{s}}^q) \\ \gamma(i_{\mathrm{s}}^d, i_{\mathrm{s}}^q) \end{pmatrix} = \begin{pmatrix} \sqrt{i_s^{d^2} + i_s^{q^2}} \\ atan2(i_{\mathrm{s}}^q, i_{\mathrm{s}}^d) \end{pmatrix} \tag{3.21}$$

The performance of the RSM is different in motor mode and generator mode. The most distinguishing feature is that in motor mode, the RSM will perform with a higher power factor at the terminals of the machine. This is because of the internal core loss as shown in fig. 3.9. Internally (after core loss) the power factor and current angle for the RSG and RSM are the same, however the core loss will cause the optimum current injection angle of the RSG to rise above that of the RSM. This deviation means that the MTPA scheme developed for an RSM cannot achieve the same results if applied to an RSG.

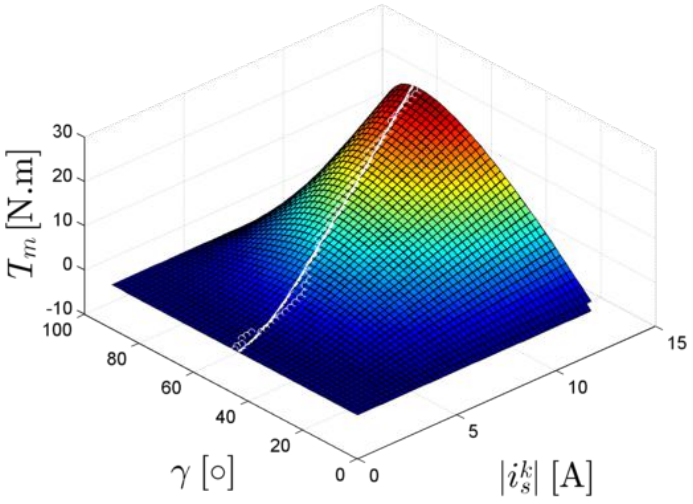

(a)

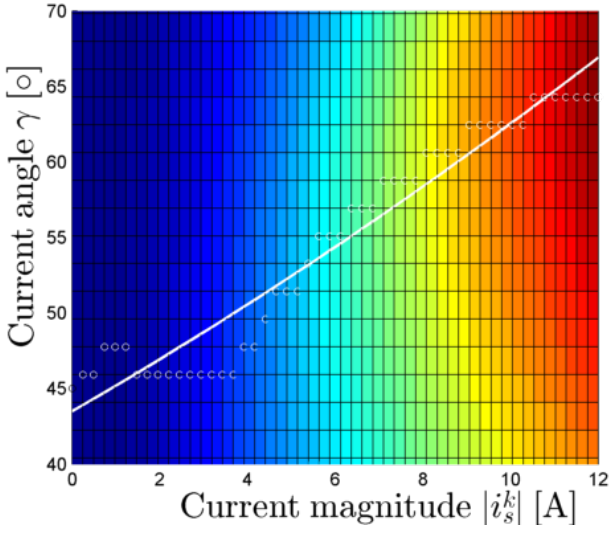

(b)

Figure 3.7: Two different views of the FEM-based MTPA map for the 3 kW RSM in motor mode. (a) 3-D torque map vs current angle and magnitude. (b) 2-D view of figure (a) to highlight the MTPA curve.

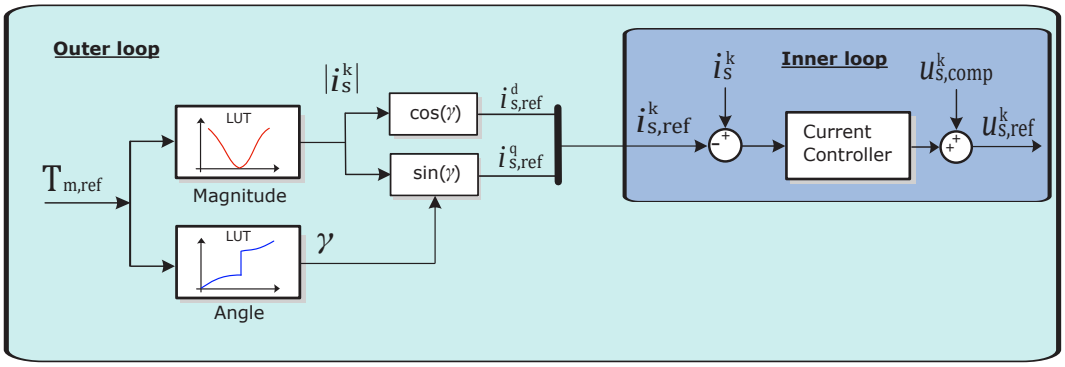

Figure 3.8: MTPA LUTs in the outer control loop.

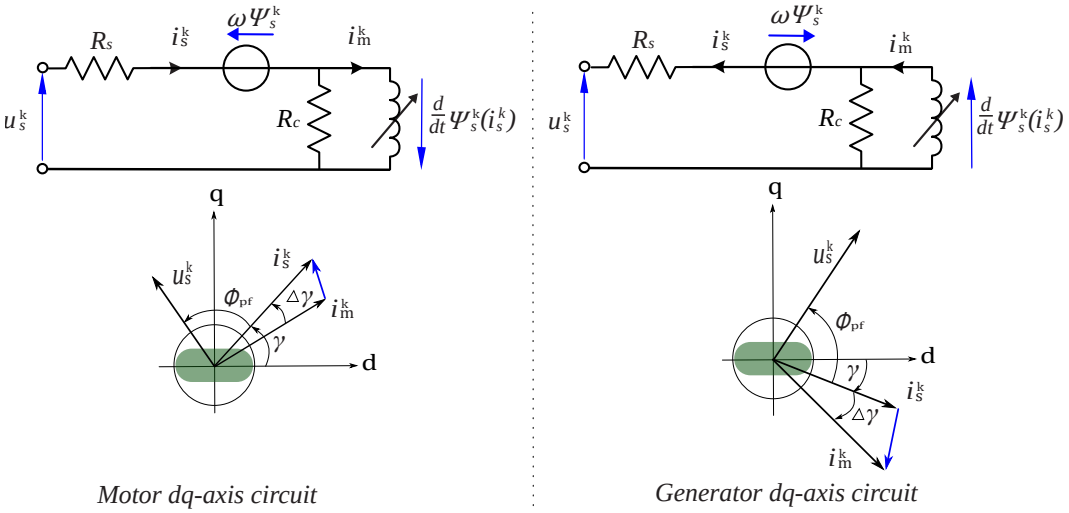

Figure 3.9: A RSM dq-circuit with internal core-loss and current angle diagrams for motor and generator mode.

3.2 Position Sensorless Control Techniques

Various hybrid position sensorless control (PSC) methods have been investigated to overcome the issue of rotor position sensors, such as an encoder [22, 23, 87–91]. PSC techniques typically utilise a machine's saliency properties or a machine's theoretical model in order to estimate the rotor angle. In synchronous machines the term saliency is commonly used to describe the angle dependent inductance of the machine or the ratio of the direct and quadrature inductances $L_d - L_q$ [92].

For machines with strong inductance saliency such as the RSM, saliency-based PSC methods (SB-PSC) are particularly well suited. SB-PSC methods such as Arbitrary injection method [88], and alternating high frequency injection (AHFI),[22, 79, 85] can generally run at all loads and speeds provided there is no heavy saturation, but due to the excitation voltage there is increased torque ripple, and additional DC bus voltage margins are required which limit the operating maximum speed [23]. Typically, SB-PSC methods are used at standstill and upto low speed.

Fundamental saliency and model based methods, which include all observer, back-EMF and flux-linkage-based models, and are typically used for PM synchronous machines because no stator currents are required to cause rotor flux, and operate from medium to high speeds [79, 93, 94]. The fundamental saliency method developed in [23], adapts well to the non-linearity of the RSM, provided saliency compensation is introduced. This method is also independent of current angle and makes other improvements to its previous works [89, 95, 96]. This method is only effective from 10% rated speed to above rated speeds, provided that there is a minimum quadrature stator current to keep the rotor saliency visible to the estimators.

A single PSC method which can operate effectively in the entire speed range of the RSM is yet to be published. Instead, two separate methods are combined to allow the machine to operate in the entire speed range. Several authors have published research on hybrid controllers which allow PSC methods to work together [22]. One such paper controls a permanent magnet synchronous machine with a speed dependent variable gain signum function that combines the outputs from the AFHI method and a speed-adaptive observer based model [97]. The PI gains of the PLL used in this method are also adjusted according to the signum function. Other methods proposed by [22] and [88] are based on a hysteresis effect where during acceleration of the machine a speed dependent changeover is used to switch between separate PLL's of the PSC methods. Hysteresis is then used to avoid unnecessary switching between PLL structures.

Although, theoretically the hybrid method presented here could be used with other combinations of fundamental and saliency based models, the scope of this work is restricted to the non-linear fundamental saliency (FS) method described by [23] and the simplified AHFI method proposed by [22].

3.2.1 Fundamental Saliency Method

In a linear machine with no saturation, the direct and quadrature inductance ratio is always constant and saliency is not load dependent. However, in the case of heavy saturation the difference between inductance saliency and fundamental saliency becomes apparent, as shown in fig. 3.10. The fundamental saliency maintains its magnitude at high load saturation, whereas the inductance saliency magnitude decreases and can cause the PSC method to fail [23]. In essence the fundamental saliency describes the flux magnitude per current as a function of current angle.

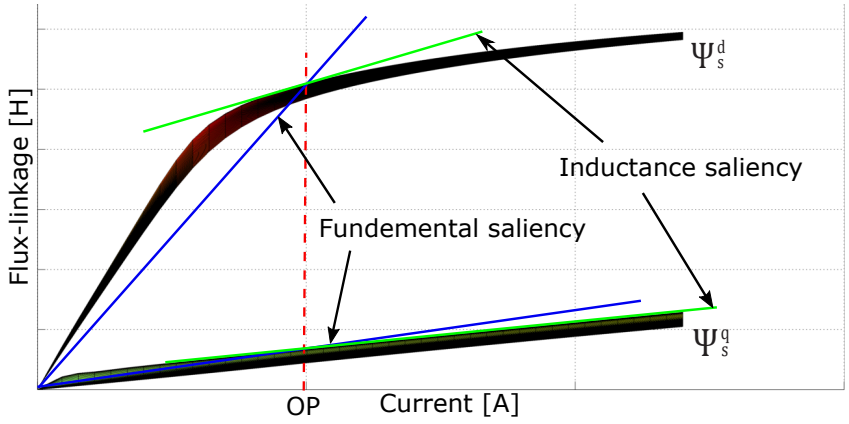

Figure 3.10: A comparison of operating points between fundamental and inductance saliency [23].

3.2.1.1 Linear Position Estimator

Consider the rotor flux linkage vector $\boldsymbol{\psi}_s^k(t)$ as a function of $\boldsymbol{i}_s^k(t)$ and its anisotropy (saliency), regardless of its linear or non-linear properties. It is assumed that $\boldsymbol{i}_s^k(t)$ has a linear relationship with the rotor flux $\boldsymbol{\psi}_s^k(t)$ and thus $\boldsymbol{\psi}_s^k(t)$ can be calculated using the secant inductance vector $\boldsymbol{L}_s^k(t)$. It is shown in [23] that the secant inductance vector $\boldsymbol{L}_s^k(t)$ can be calculated by taking the partial derivative of with (3.22) respect to time.

$$\boldsymbol{\psi}_s^s = \boldsymbol{\psi}_s^k(\boldsymbol{i}_s^s, \phi_k), \tag{3.22}$$

$$= \boldsymbol{T}_p \boldsymbol{\psi}_s^k \left(\boldsymbol{T}_p^{-1} \boldsymbol{i}_s^s \right). \tag{3.23}$$

$$\dot{\boldsymbol{\psi}}_s^s = \frac{\partial \boldsymbol{T}_p}{\partial \phi_k} \frac{d\phi_k}{dt} \boldsymbol{\psi}_s^k + \boldsymbol{T}_p \frac{\partial \boldsymbol{\psi}_s^k}{\partial \boldsymbol{i}_s^k} \frac{d\boldsymbol{i}_s^k}{dt}, \tag{3.24}$$

$$= \boldsymbol{L}_s^s \boldsymbol{i}_s^s + \boldsymbol{J}\omega \boldsymbol{\psi}_s^s - L_s^s \boldsymbol{J}\omega \boldsymbol{i}_s^s, \tag{3.25}$$

$$\text{with } \boldsymbol{L}_\text{s}^s = \boldsymbol{T}_\text{p}\boldsymbol{L}_\text{s}^k\boldsymbol{T}_\text{p}^{-1} \text{ and } \boldsymbol{L}_\text{s}^k = \frac{\partial \boldsymbol{\psi}_\text{s}^k}{\partial \boldsymbol{i}_\text{s}^k}. \tag{3.26}$$

The current derivative can then be formulated using Eq. (3.26)

$$\dot{\boldsymbol{i}}_\text{s}^s = L_s^{s-1}(\boldsymbol{u}_\text{s}^s - R_\text{s}\boldsymbol{i}_\text{s}^s - \boldsymbol{J}\omega\boldsymbol{\psi}_\text{s}^s + \boldsymbol{L}_\text{s}^s\boldsymbol{J}\omega\boldsymbol{i}_\text{s}^s). \tag{3.27}$$

The anisotropic properties of the rotor produce the constant magnitude inductance tensor, (3.28), and thus the secant inductance vector can be derived in the dq-reference frame [23], with the mutual inductances omitted.

$$\boldsymbol{L}_\text{s}^k = \begin{bmatrix} L_\text{s}^q & 0 \\ 0 & L_\text{s}^q \end{bmatrix}. \tag{3.28}$$

$$\begin{aligned} \boldsymbol{L}_\text{s}^s &= \boldsymbol{T}_\text{p}\boldsymbol{L}_\text{s}^k\boldsymbol{T}_\text{p}^{-1}, \\ &= \begin{bmatrix} L_\text{s}^q\cos^2(\phi_\text{k}) + L_\text{s}^q\sin^2(\phi_\text{k}) & (L_\text{s}^d - L_\text{s}^q)\sin(\phi_\text{k})\cos(\phi_\text{k}) \\ (L_\text{s}^d - L_\text{s}^q)\sin(\phi_\text{k})\cos(\phi_\text{k}) & L_\text{s}^q\sin^2 + L_\text{s}^q\cos 2(\phi_\text{k}) \end{bmatrix}. \end{aligned} \tag{3.29}$$

Introducing $\boldsymbol{L}_\Sigma$ the isotropic and $\boldsymbol{L}_\Delta$ rotating inductance terms in eqs. (3.30) and (3.31) respectively, the secant inductance from (3.29) can be rewritten as in (3.32).

$$\boldsymbol{L}_\Sigma = \frac{L_\text{s}^d + L_\text{s}^q}{2}, \tag{3.30}$$

$$\boldsymbol{L}_\Delta = \frac{L_\text{s}^d - L_\text{s}^q}{2}. \tag{3.31}$$

$$\boldsymbol{L}_\text{s}^k = \boldsymbol{L}_\Sigma\begin{bmatrix} 1 & 0 \\ 0 & 1 \end{bmatrix} + \boldsymbol{L}_\Delta\begin{bmatrix} \cos(2\phi_\text{k}) & \sin(2\phi_\text{k}) \\ \sin(2\phi_\text{k}) & \cos(2\phi_\text{k}) \end{bmatrix}. \tag{3.32}$$

Using (3.32), the isotropic $\boldsymbol{\psi}_\Sigma^s$ and circulating fundamental saliency $\boldsymbol{\psi}_\Delta^s$ flux linkage vectors are defined as:

$$\begin{aligned} \boldsymbol{\psi}_\text{s}^s &= \boldsymbol{L}_\Sigma\begin{bmatrix} 1 & 0 \\ 0 & 1 \end{bmatrix}\boldsymbol{i}_\text{s}^s + \boldsymbol{L}_\Delta\begin{bmatrix} \cos(2\phi_\text{k}) & \sin(2\phi_\text{k}) \\ \sin(2\phi_\text{k}) & \cos(2\phi_\text{k}) \end{bmatrix}\boldsymbol{i}_\text{s}^s, \\ &= \boldsymbol{\psi}_\Sigma^s + \boldsymbol{\psi}_\Delta^s. \end{aligned} \tag{3.33}$$

As demonstrated in fig. 3.11 the orientation of the rotor and the flux-linkage vector, $\boldsymbol{\psi}_\text{s}^s$, are dependent on the current vector which is parallel to $\boldsymbol{\psi}_\Sigma^s$, where as $\boldsymbol{\psi}_\Delta^s$ rotates with double the rotor speed, $2\omega_\text{k}$, at a constant magnitude. Note that in this case ϕ_k represents the angle between the measured stator-reference frame current vector, $\boldsymbol{i}_\text{s}^s$ and the rotating d-axis, and the entire reference frame is rotated onto $\boldsymbol{i}_\text{s}^s$ by $\boldsymbol{T}_\text{p}(\phi_\text{k})$.

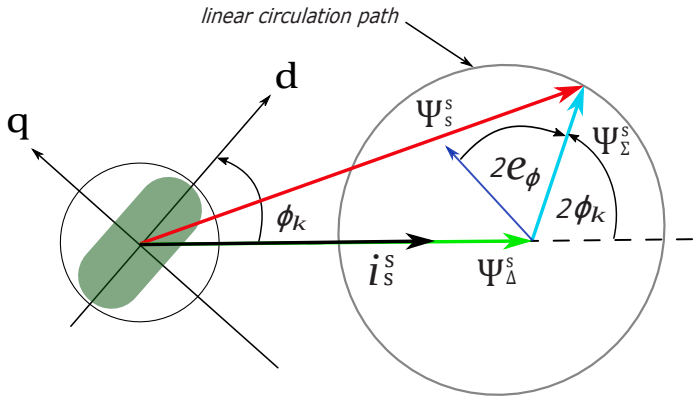

Figure 3.11: Linear flux-linkage orientation due to saliency [23].

In lament terms, the estimation of the rotor angle is acquired by extracting ϕ_k using estimates of the machine model and measured quantities. To achieve this, the term $\boldsymbol{\psi}_\Delta^s$ is estimated in two separate ways, compared and then passed through a phase lock loop(PLL) structure. The first estimation, (3.34):

$$\begin{aligned}\boldsymbol{\psi}_\Delta^s &= \boldsymbol{\psi}_s^s - \boldsymbol{L}_\Sigma \boldsymbol{i}_s^s, \\ &= \int \boldsymbol{u}_s^s - R_s \boldsymbol{i}_s^s dt - \boldsymbol{L}_\Sigma \boldsymbol{i}_s^s. \end{aligned} \tag{3.34}$$

where $\boldsymbol{\psi}_\Sigma^s$ is used to shift the rotating term to the origin provided that $\boldsymbol{L}_s^k$ is known. The second estimation of $\boldsymbol{\psi}_\Delta^s$ is done by taking the vector product of the $\boldsymbol{\psi}_\Delta^s$ and $\widehat{\boldsymbol{\psi}}_\Delta^s$ to determine the angle difference between the vectors. This difference is then used in (3.35) as the PLL feedback error signal which aligns the vectors by driving the error to zero.

$$\begin{aligned} e_{pll} &= \boldsymbol{\psi}_\Delta^s \boldsymbol{T}_p \boldsymbol{J} \widehat{\boldsymbol{\psi}}_\Delta^s, \\ &= |\boldsymbol{\psi}_\Delta^s||\widehat{\boldsymbol{\psi}}_\Delta^s| \sin(2e_{\phi_k}), \\ e_{\phi_k} &= \phi_k - \hat{\phi}_k. \end{aligned} \tag{3.35}$$

$$\widehat{\boldsymbol{\psi}}_\Delta^s = S(\phi_k)\boldsymbol{i}_s^s = \begin{bmatrix} \cos(2\phi_k) & \sin(2\phi_k) \\ \sin(2\phi_k) & \cos(2\phi_k) \end{bmatrix} \boldsymbol{i}_s^s. \tag{3.36}$$

In (3.36) the $\boldsymbol{L}_\Sigma^s$ is ignored since the length of a vector acts as a gain within a PLL. The gains of the PLL are set later on to assure correct bandwidth. Consequently the length of the vector $\boldsymbol{\psi}_\Delta^s$ in (3.34) also acts as a gain. Thus it is possible to mitigate the drift effect of the integrator by subtracting a drift compensation term $k_d \boldsymbol{\psi}_\Delta^s$ in the integral of Eq. (3.34). For low speeds the drift term is negligible and does not effect orientation.

$$\boldsymbol{\psi}_\Delta^s = \int \boldsymbol{u}_s^s - R_s \boldsymbol{i}_s^s - k_d \boldsymbol{\psi}_\Delta^s dt - \boldsymbol{L}_\Sigma \boldsymbol{i}_s^s. \tag{3.37}$$

The drift gain values are usually between 2 and 15 depending on switching frequency and machine parameters. If this gain value is too large the FS-PSC method will not track the magnetic axis of the machine correctly. For negative torque the magnetic axis should lag the rotor axis by a load dependent saliency shift angle (see Section 3.2.1.3) and vice versa. It is noted here that a reduction of saliency at low loads breaks the PLL because the error becomes so small. Oscillations start and cause further distortion to the estimated saliency. Thus a minimum stator current (machine dependent) is required to make the saliency visible, this is generally 20 % of rated current. A minimum speed is also required to keep the measured flux, $\boldsymbol{\psi}_{\Delta}^{s}$, visible and can be as low as 10 % rated speed.

3.2.1.2 Non-linear Position Estimator

The assumption made in the linear case above does not function well in practice as the RSM's current and flux relationship is highly non-linear due to saturation effects [23]. In fig. 3.12 it is shown that $\boldsymbol{\psi}_{\Delta}^{s}$ does not rotate within a circle, but rather traces a saturation dependent elliptical pattern. This consequently leads to an estimation error in the PLL scheme. Adapting the linear case is relatively easy provided that flux maps for the machine are available. To ensure stable operation of the method the centre of flux circulation must always be known. To do this $\boldsymbol{\psi}_{\Sigma}^{s}$ must now become a non-linear function of current, which can be achieved through the LUT described by (3.38).

$$\begin{aligned}\boldsymbol{\psi}_{\Sigma}^{s} &= \frac{\psi_{s}^{d}(|\boldsymbol{i}_{s}^{s}|,0)+\psi_{s}^{q}(0,|\boldsymbol{i}_{s}^{s}|)}{2}\frac{\boldsymbol{i}_{s}^{s}}{|\boldsymbol{i}_{s}^{s}|}, \\ &= \boldsymbol{\psi}_{\Sigma}^{s}(|\boldsymbol{i}_{s}^{s}|)\frac{\boldsymbol{i}_{s}^{s}}{|\boldsymbol{i}_{s}^{s}|}.\end{aligned} \tag{3.38}$$

3.2.1.3 Saliency Shift and Compensation

In the technical sphere of electrical machines, a saliency shift refers to the phenomenon whereby the magnetic axis of the machine moves away from the fixed rotor axis when under load. The fixed axis is defined as where d-axis is through the least reluctance path of the rotor. This displacement or shift is caused by saturation in the solid and air gapped rotor regions. In a linear case where saturation does not occur, the magnetic axis remains aligned [23, 79, 92].

In the non-linear case the effect can be reduced by mapping the error as a function of current and then adding this error to the final PLL error signal. This shift can be acquired in a number of ways. In[23] the shift is physically measured and a best fit curve is then formulated, where the data points can then be interpolated and stored in a LUT for use on-line. This type of saliency mapping can be done in practice on the machine

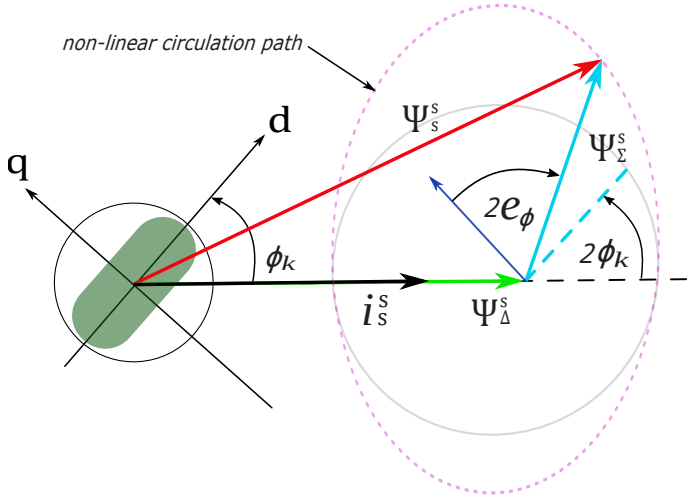

Figure 3.12: Non-linear flux-linkage orientation due to saliency. Coordinates are in the stator current reference frame.

using an encoder. However, if an encoder or the measurement equipment is not available or it is simply too time consuming to do this, the flux maps can be used to calculate the saliency shift. Figure 3.13 illustrates the resemblance between a FEM-based and a measured saliency shift compensation (SSC) map for a 9 kW RSM. A Matlab script used to formulate the saliency shift is provided in appendix D.0.5. The FEM-based SSC map can achieved in the following steps:

1. calculate $|\boldsymbol{\psi}_s^s|$, $|\boldsymbol{i}_s^s|$, $\phi_k = atan(i_s^q, i_s^d)$ and $\phi_s(\boldsymbol{\psi}_s^s) = atan(\psi_s^q, \psi_s^d)$.
2. calculate the current reference frame angle $\phi_f = \phi_k - \phi_s(\boldsymbol{\psi}_s^s)$, for all points in the map.
3. calculate the $\alpha\beta$ components of $\boldsymbol{\psi}_s^s$ map using ϕ_f.
4. calculate $\boldsymbol{\psi}_\Sigma^s$ as in (3.38).
5. calculate $\boldsymbol{\psi}_\Delta^s$ using $\boldsymbol{\psi}_\Delta^s = \boldsymbol{\psi}_s^s - \boldsymbol{\psi}_\Sigma^s \boldsymbol{i}_s^s$.
6. calculate the angle of the magnetic-axis using the components of $\boldsymbol{\psi}_\Delta^s$.
7. The angle between the magnetic axis and twice the current reference frame angle ϕ_k is the saliency shift.

The overall PSC structure is illustrated in fig. 3.14. Note that the inclusion of the saliency shift angle $C(\boldsymbol{i}_s^k)$ is not executed in the same way as in [23], where the corrected angle is included in the actual estimation, but rather it is added only to the output angle used in in the reference frame transformations for the current controller. Although both methods were attempted, the latter was more stable. Secondly it was found to be more

convenient to construct LUT for the saliency shift which was based on the dq-currents instead of $\boldsymbol{i}_{\mathrm{s}}^{s}$. The reference voltage, $\boldsymbol{u}_{\mathrm{s},ref}^{k}$ is also used as a substitute for the actual machine voltages in the same way as the compensation terms for the non-linear current controller. If the calculation of the saliency shift is done from FEM-based flux-linkage maps, then any difference between the FEM and measured results will result in deviations in the SSC curve and an offset error in $\hat{\phi}_{\mathrm{k}}$.

The final layout of the FS-PSC method is shown in fig. 3.14. In this instance the FS-method was found to perform better under transient and normal operating conditions when the SSC angle was not included in the internal FS-PSC feedback loop, but rather added to the output of the PLL $\hat{\phi}_{\mathrm{k}}$ to be used in all other park transformations. This allows the internals of the FS-method to track the uncorrected fundamental saliency (magnetic axis) of the rotor rather than the d-axis.

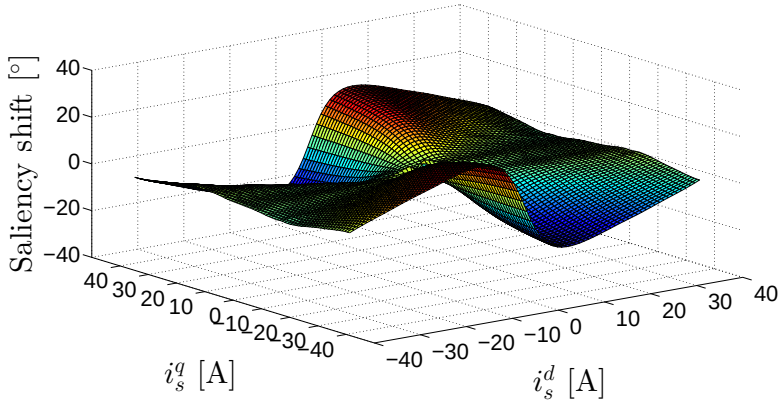

(a) FEM calculated.

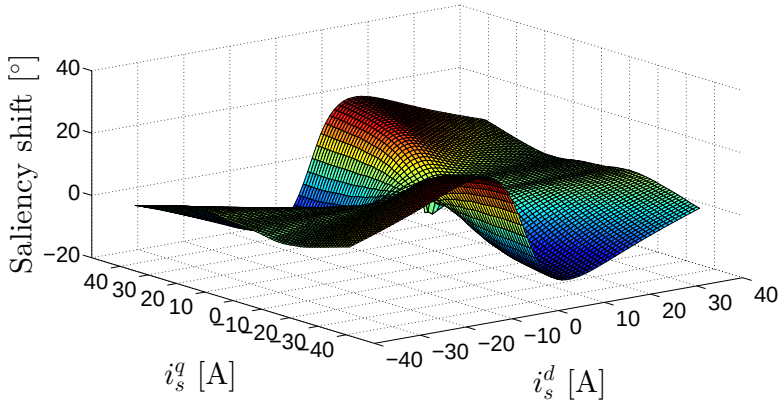

(b) Measured.

Figure 3.13: FEM-based and measured SSC maps for the 9 kW RSM.

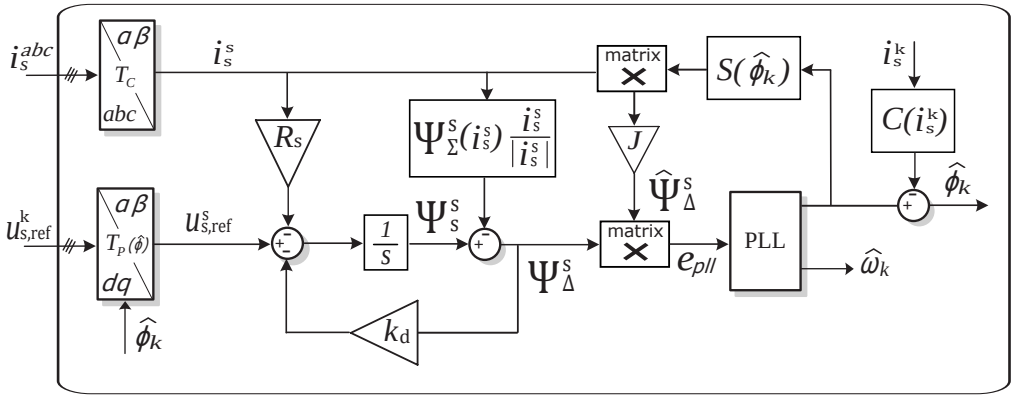

Figure 3.14: Continuous non-linear fundamental saliency control structure with saliency shift compensation.

3.2.2 Alternating High Frequency Injection

Saliency-based PSC (SB-PSC) methods have been extensively researched [87, 90, 91, 94, 97–99]. In SB-PSC methods external excitation voltage signals are applied to the machine terminals and the machine geometry is exploited to estimate the rotor position at standstill and low speeds. There are three categories: PWM excitation, transient signal injection and the focus of this section, continuous signal injection.

Two continuous signal injection methods exist, rotating and alternating high frequency injection (HFI). In both methods high frequency voltages are superimposed on the fundamental control voltages in the estimated rotating reference frame [79, 91]. Amplitude modulation is then used to track the inductance saliency along the axis orthogonal to the HF injection axis [91]. Since the anisotropy in the RSM has the same frequency as the rotor, the resultant HF currents can be demodulated to obtain the rotors position [79, 91].

Alternating HFI-PSC is reported to have less torque ripple than its counter part and is the least complex of all SB-PSC methods [91]. To date the progress made by [91] has reduced the complexity of alternating HFI by eliminating the band-pass filtering (BPF) in the PLL's and 4^{th}-order low-pass filters (LPF). This method can be optimised to operate at rated speed and rated torque, however in this project it is only required to provide an estimate of the rotor position/speed at standstill and very low speeds. No power generation is required while under the AHFI-PSC as it is only used as a transition to the FS-PSC. This greatly simplifies the control structure because no saliency shift compensation is required. It would be ideal to use as little q-axis saturation current and injection voltage as possible to minimise the standby losses of the WTS.

In this section the basic concepts of the AHFI-PSC method proposed by [91] such as carrier frequency injection, the modulation and the demodulation of the carrier signals are explained.

3.2.2.1 High Frequency Machine Model

In the rotor reference frame the RSM can be modelled by (3.39) as:

$$\boldsymbol{u}_{\mathrm{s}}^{k} = R_{\mathrm{s}}\boldsymbol{i}_{\mathrm{s}}^{k} + \boldsymbol{L}_{\mathrm{s}}^{k}\frac{d}{dt}\boldsymbol{i}_{\mathrm{s}}^{k} - \boldsymbol{M}_{\boldsymbol{s}}^{\boldsymbol{k}}\frac{d}{dt}\boldsymbol{i}_{\mathrm{s}}^{k} - \omega_{\mathrm{k}}\boldsymbol{J}\boldsymbol{L}_{\mathrm{s}}^{k}\boldsymbol{i}_{\mathrm{s}}^{k}. \tag{3.39}$$

where the mutual and tangential inductance matrices are defined as (3.40) and (3.41):

$$\boldsymbol{M}_{\boldsymbol{s}}^{\boldsymbol{k}} = \begin{bmatrix} 0 & L_{\mathrm{s}}^{dq} \\ L_{\mathrm{s}}^{qd} & 0 \end{bmatrix}, \tag{3.40}$$

$$\boldsymbol{L}_{\mathrm{s}}^{k} = \begin{bmatrix} L_{\mathrm{s}}^{d} & 0 \\ 0 & L_{\mathrm{s}}^{q} \end{bmatrix}, \tag{3.41}$$

$$u_{\mathrm{s},c}^{k} = \boldsymbol{L}_{\mathrm{s}}^{k}\frac{i_{\mathrm{s},c}^{k}}{dt}. \tag{3.42}$$

According to [79], when the RSM model is evaluated for HF signals within the boundaries of (3.43), the resistive, speed voltage and mutual inductance terms fall away due to their negligible signal magnitudes when compared to the flux linkage derivative term.

$$2\omega_{\mathrm{k}} < \omega_{\mathrm{c}} < \frac{2\pi f_{\mathrm{s}} - 2\omega_{\mathrm{k}}}{2}, \tag{3.43}$$

where ω_{k} is the rotor frequency, ω_{c} is the carrier injection frequency in radians and fc is the sample frequency in hertz.

3.2.2.2 Alternating Carrier Injection

The carrier signal $u_{\mathrm{s},c}^{\hat{k}}$ is represented by (3.44) with the superscript $\hat{k}$, denoting that the estimated rotating reference frame. In (3.44) the carrier signal is applied to the d-axis voltage, which is reported to produce less torque ripple than if it were applied to the q-axis. The injection voltage magnitude u_{c} will also vary depending on the saliency of the machine, typical voltages are between 50 V to 120 V.

$$u_{\mathrm{s},c}^{\hat{k}} = \begin{bmatrix} u_{\mathrm{c}}\cos(\omega_{\mathrm{c}}t) \\ 0 \end{bmatrix}. \tag{3.44}$$

In the rotating reference frame the inductance matrix can be defined as in section 3.2.1.1, (3.32). The HF voltage, demodulated in the estimate rotating reference frame, is misaligned by $\Delta\phi_{\mathrm{k}} = \phi_{\mathrm{k}} - \hat{\phi}_{\mathrm{k}}$. The estimate inductance matrix is then described by (3.45) where $\boldsymbol{L}_{\Sigma}$ and $\boldsymbol{L}_{\Delta}$ are the isotropic and rotating inductance terms, (see section 3.2.1.1).

$$\boldsymbol{L}_{\mathrm{s}}^{k} = \boldsymbol{L}_{\Sigma}\begin{bmatrix} 1 & 0 \\ 0 & 1 \end{bmatrix} + \boldsymbol{L}_{\Delta}\begin{bmatrix} \cos(2\Delta\phi_{\mathrm{k}}) & \sin(2\Delta\phi_{\mathrm{k}}) \\ \sin(2\Delta\phi_{\mathrm{k}}) & \cos(2\Delta\phi_{\mathrm{k}}) \end{bmatrix}. \tag{3.45}$$

The stator current $\boldsymbol{i}_s^s$ is converted from the measured stationary reference frame to the estimated reference frame $\hat{\phi}_k$ using ϕ_k and can be modelled by (3.49). The inverse inductance matrix (3.48) is derived as in [91].

$$i_s^{\hat{k}} = L_s^{\hat{k}-1} \int u_{s,c}^{\hat{k}} dt \tag{3.46}$$

$$= L_s^{\hat{k}-1} s \begin{bmatrix} \frac{u_c}{\omega_c} \sin(\omega_c t) \\ 0 \end{bmatrix}, \tag{3.47}$$

$$L_s^{\hat{k}} = \frac{1}{L_s^d L_s^q} \left(\boldsymbol{L}_\Sigma \begin{bmatrix} 1 & 0 \\ 0 & 1 \end{bmatrix} + \boldsymbol{L}_\Delta \begin{bmatrix} \cos(2\Delta\phi_k) & -\sin(2\Delta\phi_k) \\ -\sin(2\Delta\phi_k) & \cos(2\Delta\phi_k) \end{bmatrix} \right), \tag{3.48}$$

$$i_s^{\hat{k}-1} = \frac{u_c \sin(\omega_c t)}{L_s^d L_s^q \omega_c} \left(\boldsymbol{L}_\Sigma \begin{bmatrix} 1 \\ 0 \end{bmatrix} + \boldsymbol{L}_\Delta \begin{bmatrix} \cos(2\Delta\phi_k) \\ \sin(2\Delta\phi_k) \end{bmatrix} \right). \tag{3.49}$$

When the system is in steady state and provided that $\Delta\phi_k$ is small enough, it can be assumed that $\sin(\Delta\phi_k) \approx \Delta\phi_k$ and $\cos(\Delta\phi_k) \approx 1$ [22], which leads to the simplifications of Eq. (3.49) to Eq. (3.50).

$$i_s^{\hat{k}-1} = \frac{u_c \sin(\omega_c t)}{L_s^d L_s^q \omega_c} \left(\boldsymbol{L}_\Sigma \begin{bmatrix} 1 \\ 0 \end{bmatrix} + \boldsymbol{L}_\Delta \begin{bmatrix} 1 \\ 2\Delta\phi_k \end{bmatrix} \right). \tag{3.50}$$

We now have easy access to the estimation error using the second term on the right which is only scaled by the inductance saliency $\boldsymbol{L}_\Delta$.

3.2.2.3 Modulation and Demodulation of the Carrier Signal

Spectral separation of the carrier signal is achieved by low-pass-filtering (LPF) i_s^q in the demodulation scheme to extract only the frequencies around ω_c. The HF component of the filtered i_s^q contains the position estimation error, $\Delta\phi_k$. The spectrum of a signal is shifted to the carrier frequency if multiplied by $\cos(\omega_c t)$, shown by (3.51).

$$x(t)\cos(\omega_c t) = \frac{1}{2}[X(\omega+\omega_c) + X(\omega-\omega_c)]. \tag{3.51}$$

This is also done to the measured current where i_s^q in (3.50) is multiplied by $\sin(\omega t)$ which leads to the trigonometric identity Eq. (3.52).

$$x(t)\sin^2(\omega_c t) = \frac{1-\cos(2\omega_c t)}{2}. \tag{3.52}$$

In the frequency domain of (3.52) there are two HF components at twice the ω_c and one DC component. Both the DC and HF components contain information regarding $\Delta\phi_k$, but the DC part can be extracted easily if a LPF is used to separate the DC component from the HF signals [91]. After applying (3.52) and a LPF to the measured current, the filtered demodulated current can be written by (3.53).

$$i^{\hat{k}}_{s,lpf} = \frac{u_c}{L^d_s L^q_s \omega_c}\left(\boldsymbol{L}_\Sigma \begin{bmatrix}1\\0\end{bmatrix} + \boldsymbol{L}_\Delta \begin{bmatrix}1\\2\Delta\phi_k\end{bmatrix}\right), \tag{3.53}$$

$$i^{\hat{d}}_{s,lpf} = \frac{u_c}{L^d_s L^q_s \omega_c}\left[\boldsymbol{L}_\Sigma - \boldsymbol{L}_\Delta\right], \tag{3.54}$$

$$i^{\hat{q}}_{s,lpf} = \frac{u_c \boldsymbol{L}_\Delta (2\Delta\phi_k)}{L^d_s L^q_s \omega_c}. \tag{3.55}$$

Conveniently, only $i^{\hat{q}}_{s,lpf}$ is zero when $\Delta\phi_k$ is zero. A PLL structure can be used to drive $\Delta\phi_k$ to zero and thus align the two reference frames $\hat{k}$ to k. Note here that if the saliency $\boldsymbol{L}_\Delta$ is too small or if $L^d_s = L^q_s$ this method will not function correctly. The basic mathematical PLL structure is shown in (3.57) with input as $i^{\hat{q}}_{s,lpf}$, and k_{iPLL} and k_{pPLL} are respectively the integral and proportional gains.

$$\hat{\omega}_k = k_{i,PLL}\int i^{\hat{q}}_{s,lpf}\,dt, \tag{3.56}$$

$$\hat{\phi}_k = \int k_{p,PLL} i^{\hat{q}}_{s,lpf} + \hat{\omega}_k\,dt. \tag{3.57}$$

The saliency of the RSM is proportional to the stator current as indicated in fig. 3.10. The low saliency at a low operating current makes the AHFI-method unstable due to $L^d_s \approx L^q_s$. This problem is avoided by ensuring that there is always enough saliency in the machine by saturating the machine q-axis magnetic circuit. This is done by applying a minimum reference current even at zero load. The minimum current is machine specific but is typically around 0.2 p.u. When at the minimum saturation current, the RSM will not run at its highest possible MTPA efficiency until the current reference is above the saturation current. An example of how this is implemented is displayed graphically in fig. 3.15 along with the control structure of the AHFI-PSC in fig. 3.16.

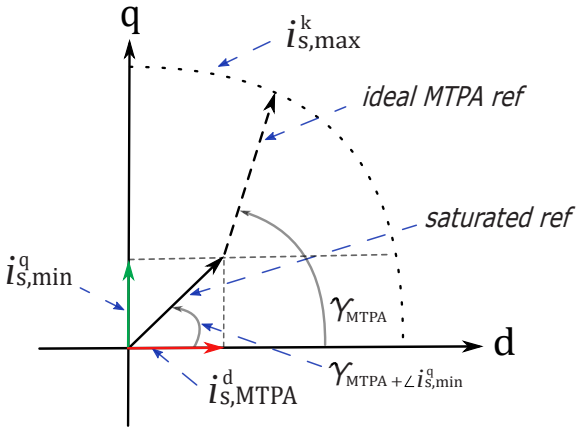

Figure 3.15: Current vector diagram comparison of MTPA and the minimum AHFI method current references.

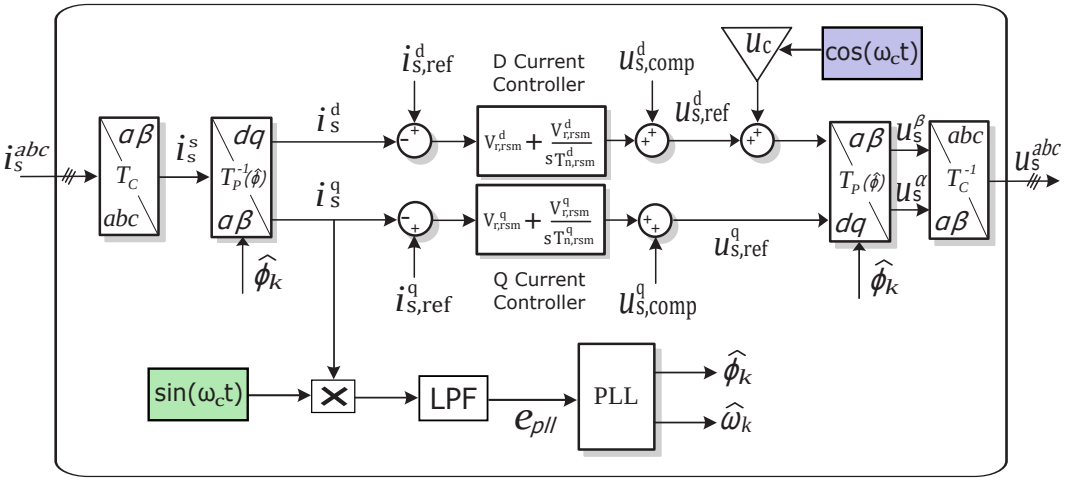

Figure 3.16: The alternating high frequency injection position sensorless control structure with current controller.

3.2.3 Hybrid PSC Methods with a Single Gain Scheduled PLL

Since FS-PSC cannot operate from standstill or very low rotor speeds and loads, HF-PSC must be incorporated in some way to allow the initial rotor angle to be estimated. [22, 88, 100] implemented a hysteresis method based on rotor speed where two separate PLL loops were utilised. This gives the advantage of optimising each PLL for its particular PSC method. However, since each method will track the rotor angle with its own unique steady state error, the sudden change from the estimated angle of one method to another causes current and torque ripple and overshoot. In fig. 3.17b the hybrid controller logic flow is illustrated and in fig. 3.18 the overall hybrid-PSC method structure is presented. As shown in fig. 3.17b, AHFI-PSC is active on initiation, and when $\hat{\omega}_k < \omega_{H1}$, can be active when $\hat{\omega}_k > \omega_{H1}$ and turned off when $\hat{\omega}_k > \omega_{H2}$. The FS-PSC method is on at all times, but for $\hat{\omega}_k < \omega_{H1}$ the angle and speed input to its FS-PLL is that of the AHFI-PSC. When inside the hysteresis band the FS-PSC method will observe by using its own FS-PLL and estimation outputs, but the FS-PLL $\hat{\omega}_k, \hat{\phi}_k$ will not be used for control purposes until $\hat{\omega}_k > \omega_{H2}$.

3.3 Current control with an LC Filter

Wind turbine investments can suffer greatly from down time due to component failures. Power electronic converter failures are the second most common next to pitch control failures [18]. It would therefore be beneficial to have power electronic devices at ground level for easy maintenance and repair access, however several complications arise from placing the VSC at a great distance from the generator.

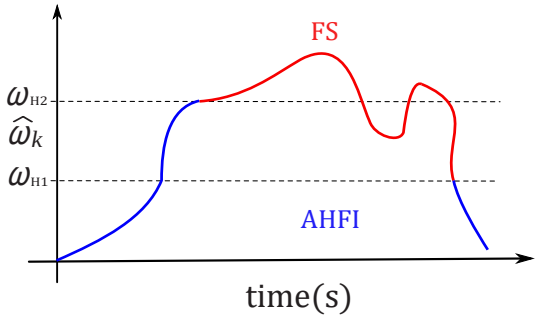

(a) Time series example.

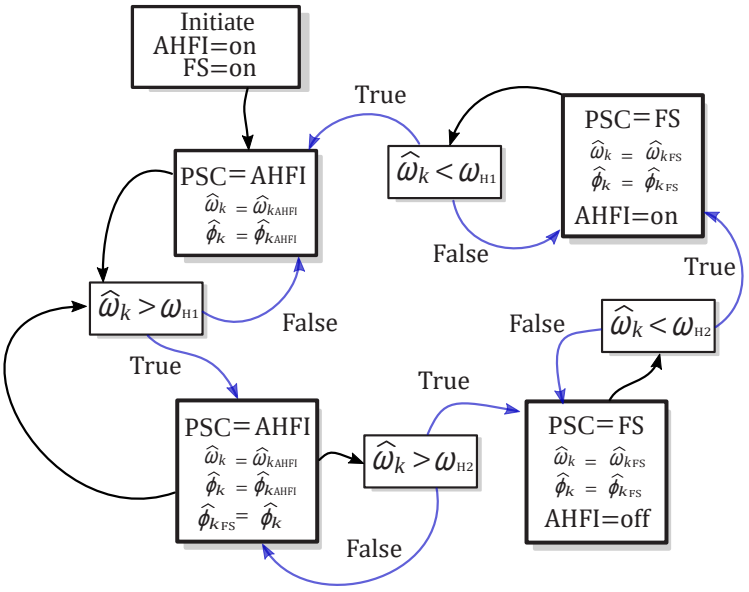

(b) Logic diagram.

Figure 3.17: Hybrid control method hysteresis logic example and diagram.

The main complication is the fast rise time of the PWM voltages (du/dt) propagated over the inductance of a long cable which causes over-voltage spikes, due to "ringing" at at the terminals of the machine[97, 101, 102]. This can cause damage to both cable and machine insulation. This phenomenon depends on the cable length and thickness and its effects are well documented, [97, 101–103], with most articles dealing with PM or IM machines. Only one article contains LC-filter tests on an RSG [18]. The critical cable length for $10\,000\,\mathrm{Vs}^{-1}$ is $\approx 5\,\mathrm{m}$, for $1000\,\mathrm{Vs}^{-1}$ is $\approx 50\,\mathrm{m}$ and for $500\,\mathrm{Vs}^{-1}$ is $\approx 100\,\mathrm{m}$ [101]. Essentially the higher the impedance of the cable, the larger the mismatch between the source and sink, which causes higher frequency voltage harmonics that cannot be absorbed fast enough by the generator and propagate back and forth over the cable. There are a several methods available to deal with this issue, which are detailed in [102], such as stator capacitors or RLC-filters, but perhaps the best choice and most commonly used method in industry is to add a du/dt LC-filter to the output of the inverter [97, 102]. The

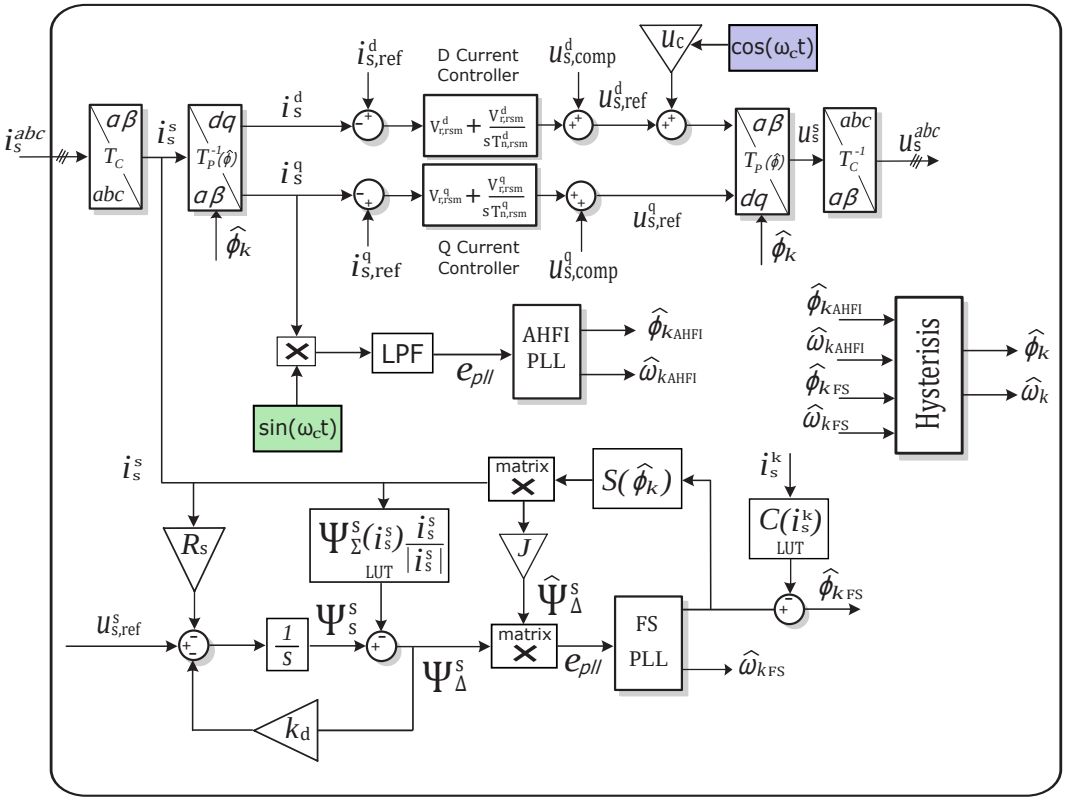

Figure 3.18: Hybrid control method structure.

LC-clamp variation of this filter is the most effective type [102], but its implementation is beyond the scope of this project, so a standard passively damped, LC-filter was chosen.

Placing an LC-filter on the output of the VSC complicates the RSM control structure because stator currents are not equal to inverter current ($\boldsymbol{i}_{\mathrm{s}}^{k}, \neq \boldsymbol{i}_{\mathrm{i}}^{k}$) and the stator voltages are not equal to inverter voltages ($\boldsymbol{u}_{\mathrm{s}}^{k} \neq \boldsymbol{u}_{\mathrm{i}}^{k}$). The difference in inverter and stator quantities are shown in fig. 3.19, where the LC-filter capacitor current is i_{cap} and the injected current angle and actual machine current angles are γ and γ_i respectively.

The discrepancy is also directly proportional to the machine's operating frequency and can cause either a stator current set-point offset, leading to incorrect torque, or total failure of the current controller. Under PSC the flux-linkage estimations used in the FS-method become significantly inaccurate because inverter quantities are used in the estimation instead of the stator quantities. At the very least a very large increase in the saliency shift will be visible, or at worst, fail to track the rotor angle entirely.

Either additional sensors placed at the stator terminals must be used to acquire the correct current and voltage measurements or if the LC-filter and machine parameters are well known, the system states can be estimated using the estimator proposed by [18].

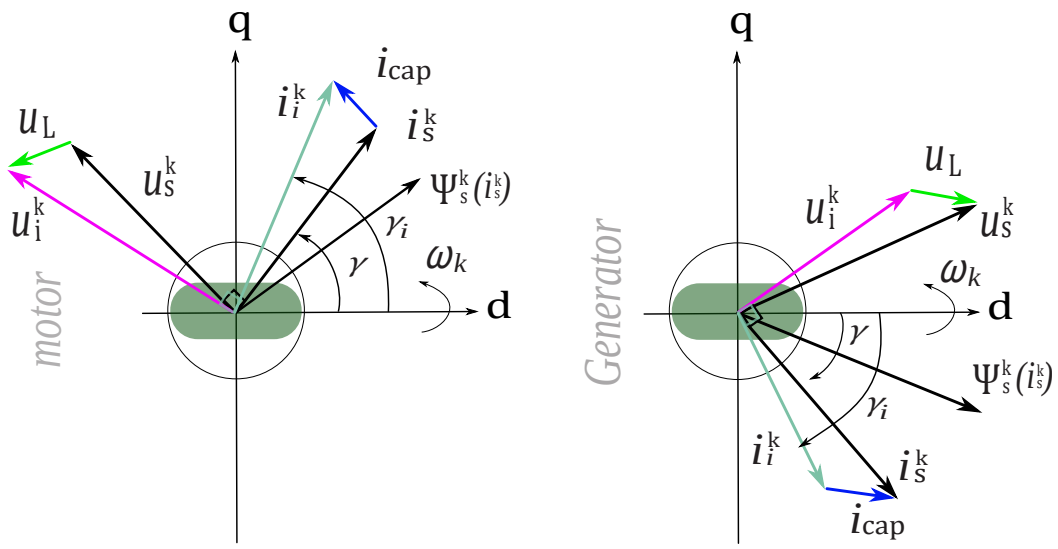

Figure 3.19: Diagram of the LC-filter capacitor currents and inductor voltages with respect to the RSG and RSM stator quantities in the dq-reference frame (not to scale).

3.3.1 LC Filter Design

There are various degrees of output LC-filter attenuation that are application specific. For example sin-wave filters are the most aggressive form, and have very low cut-off frequencies and produce a near sinusoidal output voltage. A du/dt filter has a moderate cut-off frequency, just enough to eliminate motor-cable ringing for which the output voltage does not need to be a pure sinwave [104]. The du/dt filter compared to a sine-wave filter has lower capacitance and inductance (higher cut-off frequencies), thus it is cheaper and smaller. A du/dt filter voltage wave form is still pulse shaped but the current is sinusoidal, as shown in fig. 3.20. According to [104] the use of du/dt filters is only recommended for applications with cable lengths up to 150 m, which is exactly what this project requires.

In medium voltage applications the motor voltage will contain visible harmonics resulting from PWM as the filter resonance will always be excited [101]. It is thus vital to damp the excitation. Simple resistors in series with the capacitors is the ideal passive damping method and was chosen for this project. Active damping using inverter control is the most ideal active method because it is lossless, but its implementation is beyond the scope of this project.

The individual values of L_f and C_f are the remaining degrees of freedom for which cost and weight must be factored in. With regard to inverter current, a large choke is advantageous in reducing (limiting) the reactive capacitor current of the filter and thus the losses in the damping circuit which the inverter has to provide. A smaller choke will either reduce the output power of the inverter or increase the semiconductor component costs. In a WT application weight is not a huge factor since the output filter will be at

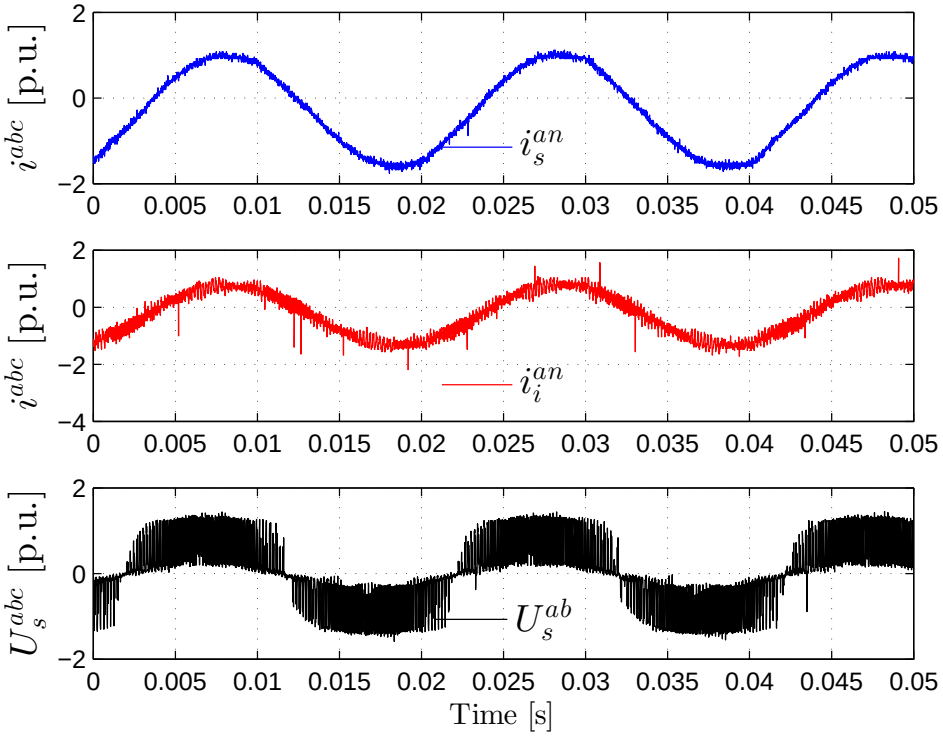

Figure 3.20: Measured stator voltages and currents of a du/dt LC-filter with a cut-off frequency at 918 Hz and resonant over-damping at 55 Ω.

ground level. Cost is thus of the highest importance. The inverter power rating must be kept as close to the generator power rating since the cost of the VSC scales rapidly with its power rating.

The three-phase circuit of the LC-filter and RSG configuration are shown in fig. 3.21. To design the LC-filter, stationary reference frame quantities are used. The frequency response of the LC-filter and RSG are evaluated in the dq-reference frame, Where L_f , C_f $R_{f,L}$, $R_{f,c}$ L_{cable} and R_{cable} are the filter inductance, capacitance, series inductor resistance, series capacitor damping resistance, the cable inductance and cable resistance respectively. The open loop frequency domain characteristics of the LC-filter can be modelled by the second order transfer function, (3.58) which is then used to formulate (3.60) the cut-off frequency, the resonant frequency (3.61) and the damping resistance (3.63).

When modelling the LC-filter it is important to consider the cable inductance. This model can be represented by a LCL-filter, which also makes the inclusion of the capacitor damping resistance easier. The inductance of the RSG also plays a role in shifting the resonant frequency of the LC-filter, however because the inductance of the machine is sinusoidal and load dependent it is difficult to design a static passive damping filter to perfectly damp the shifting resonant peak. It was decided that the standard LCL-filter

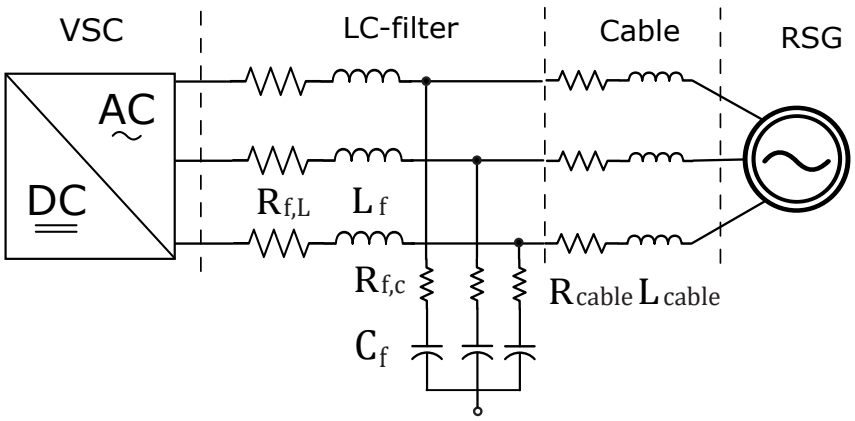

Figure 3.21: Three-phase RSG and cable connected LC-filter circuit with the capacitors connected in wye with a floating neutral point.

method of damping would be sufficient for application in this project. Eq. (3.62) is used to calculate the new and slightly lower, resonant damping resistance. It is mentioned in [102] that the damping resistance should over-damp the circuit. It was also found through practical implementation and simulation that the required damping resistance needed to be many times larger (≈ 10) times) than what is specified by (3.62).

$$\frac{\boldsymbol{u}_s^s(s)}{u_i^s(s)} = \frac{\dfrac{1}{L_f C_f}}{s^2 + s\dfrac{R_f}{L_f} + \dfrac{1}{L_f C_f}}, \tag{3.58}$$

$$\frac{\boldsymbol{u}_s^s(s)}{u_i^s(s)} = \frac{C_f R_{f,c} s + 1}{L_f L_{cable} C_f s^3 + C_f R_{f,c}(L_f + L_{cable}) s^2 + (L_f + L_g) s}, \tag{3.59}$$

$$f_{cut} = \frac{1}{2\pi\sqrt{L_f C_f}}, \tag{3.60}$$

$$f_{sw} >> f_o >> f_1,$$

$$\omega_{LC,res} = \sqrt{\frac{1}{C_f L_f}}, \tag{3.61}$$

$$\omega_{LCL,res} = \sqrt{\frac{L_f + L_{cable}}{L_f L_{cable} C_f}}, \tag{3.62}$$

$$R_{f,c} = \frac{1}{3\omega_{LCL,res} C_f}. \tag{3.63}$$

The cut-off frequency, F_{cut}, of the LC filter, (3.60) must be significantly below the switching frequency of the drive, but higher than the fundamental frequency of the ma-

chine to allow adequate decoupling. The resonant frequency in (3.62) as a rule of thumb, can be damped by using (3.63).

For this project a cut-off frequency of 918 Hz was chosen for the du/dt LC-filter with the guidance of [104]. A moderate capacitance of 15 µF and an inductance of 2 mH was chosen. Keeping L_f to a minimum is also ideal since building an inductor rated for 150 % power is costly and the inductor is bulky. Figure 3.22 illustrates the frequency response of the combined LC-filter and transmission cable as in fig. 3.21 with the parameters as in table 3.1.

Table 3.1: Undamped LC-, damped LC- and damped LCL-filter parameters.

LC-filter parameters	
F_{cut}	918 Hz
L_f	2 mH
L_{cable}	6.7 mH
R_{cable}	4.62 Ω
$C_{f,Y}$	15 µF
$\omega_{LC,res}$	5773.5 rad s^{-1}
$\omega_{LCL,res}$	6575.4 rad s^{-1}
$10 \times R_{damp,Y}$	33.79 Ω

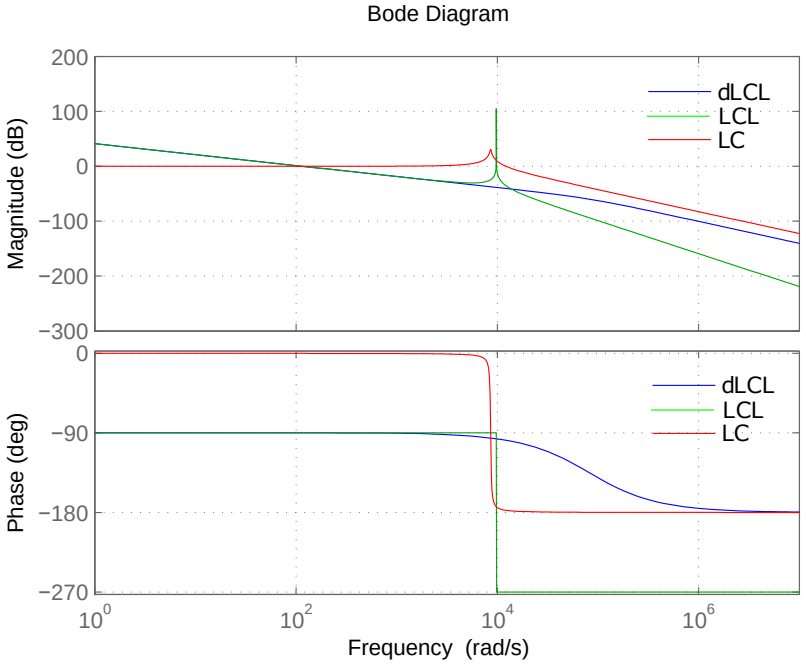

Figure 3.22: Undamped LC-filter, series damped and undamped LCL-filter bode plots.

3.3.2 LC-Filter Estimators and Observers

At the time of this research there was no available literature regarding LC-filter estimators/observers specifically for the RSG except in [18], where a model-based estimator for the stator voltages and currents without the use of feedback gain is used. PSC techniques then make use of the estimated quantities to acquire the rotor angle. In several publications an LC-filter full order observer for the PMSM is mentioned. Generally regarded as a linear machine, the PMSM has a constant flux-linkage and inductance which makes the observer easier to derive. The inverter current is used as feedback and the outputs are the stator voltage current and rotor angle. [97, 103] document the design of such speed-adaptive model-based full and reduced order observers for a PMSM. A linearisation technique is used to analyse the adaptive part of the observer. The adaptive speed estimator, implemented in the stator reference frame, is used for estimating the rotor angle as well as high frequency injection based methods. Using this research and the work of [105], a similar model-based full order observer (without adaptive-speed or linearisation) for the RSG was developed. This observer updates its flux-linkage, speed and inductance quantities on-line using flux-tables and measured quantities in a similar way to the non-linear current controllers discussed in section 3.1.2. Although the observer was able to estimate the stator currents and voltages when not being used in the control loop, the observer failed to stabilise when used for current control or PSC. A simpler method was then attempted, which is similar to the method used by [18], but this model-based estimator is derived differently and includes the capacitor damping resistance in the $\alpha\beta$ reference frame. The basic model is illustrated in fig. 3.23.

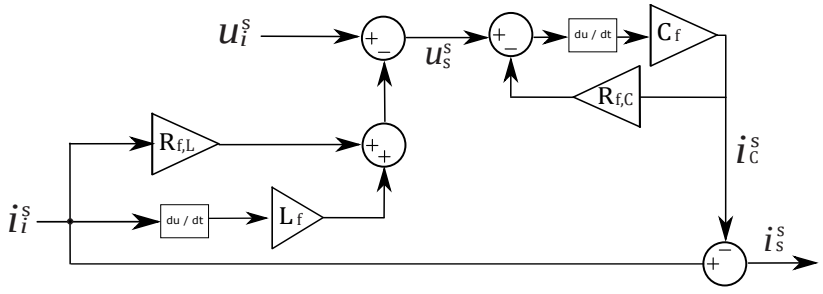

Figure 3.23: LC-filter estimator with capacitor damping resistance.

The combined RSG, VSC and LC-filter voltage transfer function, $\boldsymbol{u}_s^s(s)$, $\boldsymbol{u}_i^s(s)$, inductance L_f, and inductor resistance $R_{f,L}$ is shown in (3.64). The equations are set up so that power into the RSM (motor mode) is positive.

$$\boldsymbol{u}_s^s(s) = \boldsymbol{u}_i^s(s) - R_{f,L}\boldsymbol{i}_i^s(s) - sL_f\boldsymbol{i}_i^s(s). \tag{3.64}$$

With the stator voltage ($\boldsymbol{u}_s^s(s) = \boldsymbol{u}_c^s(s)$) known, the capacitor current $\boldsymbol{i}_c^s$ can be found using (3.65), the transfer function of a series resistor capacitor circuit.

$$\frac{\boldsymbol{i}_c^s(s)}{\boldsymbol{u}_s^s(s)} = \frac{sC_f}{sC_f R_{f,c} + 1}. \tag{3.65}$$

Finally the stator current can be estimated using (3.66).

$$\boldsymbol{i}_s^s(s) = \boldsymbol{i}_i^s(s) - \boldsymbol{i}_c^s(s). \tag{3.66}$$

This method of estimation correctly estimates the stator quantities in simulation with the modelled VSC and in practice and is further discussed in section 4.6.1.

3.3.3 Position Sensorless Control with an LC Filter

The addition of the LC-filter not only affects the classic control structure of the RSG, but also the PSC methods, as will be explained in this section. According to [18] the resonant frequency can be used to boost the injection voltage of the AHFI-PSC, however it was found in practice and simulation, that a system which was not over-damped caused instability and failure of the current controller and the PSC-method. Therefore a standard 80-120 V injection voltage should be used for over-damped systems and the injection frequency placed slightly below F_{cut}. The estimated stator voltages and currents are used directly in the PSC control loops and thus any deviations in the estimator quantities from the actual quantities will cause errors in the estimated angle.

3.4 Grid-Connected Current Control

The electrical grid is a complex dynamic system that consists of a wide variety of disturbances, eventualities, faults and resonances due to harmonic currents in the power lines. Therefore grid-connected power converters must hold an interactive relationship with the grid. The safety, stability and quality of the grid can be severely affected by the presence of power converters and it is for this reason that international grid codes have been developed and enforced to regulate and control the power flow from external power electronic sources such as renewable energy systems [24].

Power electronic converters must monitor the grid variables in order to utilise the power bus of the grid. Whether power is injected or extracted the power converter must be synchronised with the grid frequency and voltage. In fact grid synchronisation is nothing more than the instantaneous monitoring of the grid's state. Data gathered from this synchronisation is used at different levels in the control algorithm. As explained in this section the electrical angle of the grid phase voltages is fundamental to utilising the

Clark and Park transformations (synchronous to stationary reference frame) to represent the system's dynamic AC variables by DC quantities which are easily controlled.

Classical PI control with grid voltage feed-forward, as depicted in fig. 3.24, is frequently used in industry, however this controller exhibits two drawbacks: poor sinusoidal reference tracking with steady-state error and poor disturbance rejection capability. The main cause of this is the integral action of the PI loop which suffers if the disturbance is a periodic signal [24, 106].

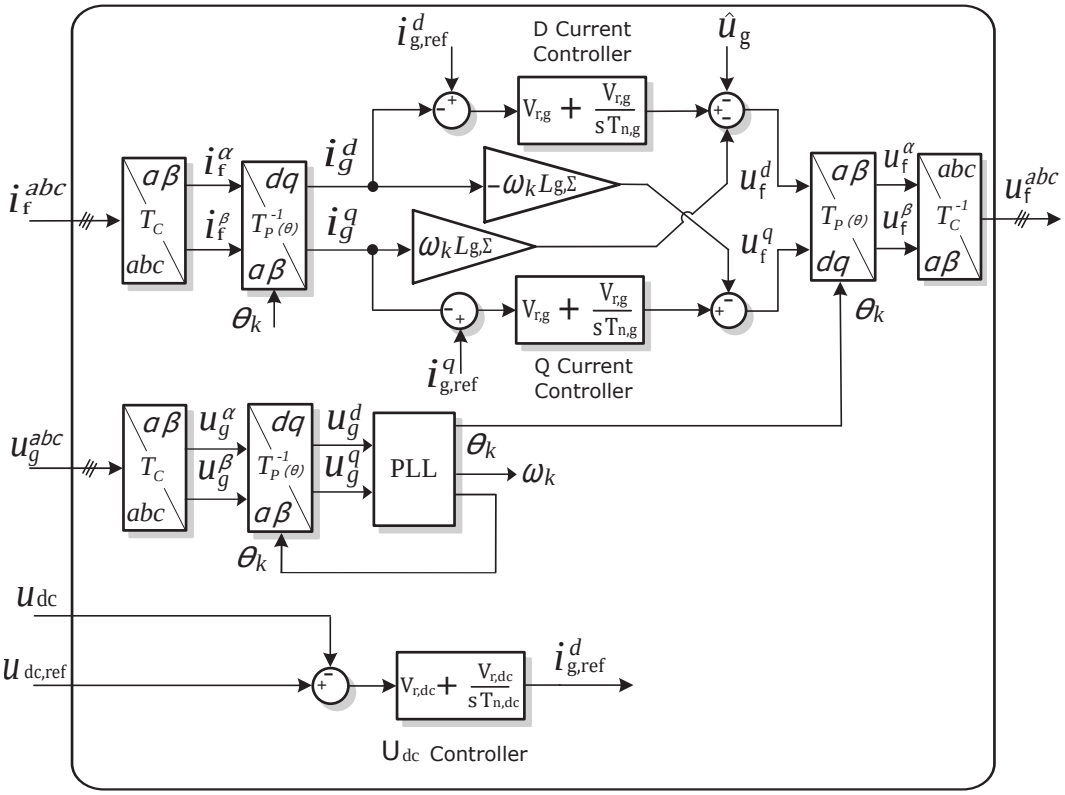

Figure 3.24: Cascaded open loop synchronous grid-tie current and DC bus voltage control structure.

In this section each component in fig. 3.24 will be explained and derived. The section begins with techniques for grid synchronisation, followed by the methods used for controlling power flow, power quality and DC bus voltage.

3.4.1 Phase Lock Loops for Utility Synchronisation

Phase Lock loops (PLL) are predominantly used in various applications such as motor control, telecommunications, radio and other power electronic applications [107]. The three main types of PLL system used in phase synchronisation are the zero crossing, stationary reference frame and synchronous reference frame. More elaborate methods have

been developed such as the double second order generalised integrator FLL (DOSOGI-FLL) or the decoupled double synchronous reference frame method which improves the synchronous PLL by using two rotating reference frames which independently track the positive and negative sequence frequencies and thus provide a more stable phase extraction under unbalanced conditions and in the case of grid faults [24, 107]. However, these intensive methods are not with the scope of this project.

Three-phase grid synchronisation is slightly more complex than single-phase methods because multiple phase voltages must work in a cohesive manner to keep certain parameters such as phase shift and phase sequencing correct. The phase voltages can be considered as a vector, $\boldsymbol{u}_{\mathrm{g}}^{abc}$, consisting of three components spaced 120°. The frequency of their rotation and magnitude is kept constant at the utility grid frequency and amplitude [24].

Under these ideal conditions the Clark and Park transforms can be used to transform the three vectors into the Alpha beta plane or dq-reference frame for easier manipulation. However, in practice there are many discrepancies which cause disturbances on the three-phase vectors and the connected electrical equipment such as resonance, unbalanced voltages, power loss and premature degradation of equipment. These disturbances can be classified by their harmonic composition, amplitude and period [24]. The advanced methods of dealing with grid disturbances is out of the scope of this project and will not be dealt with here.

The most versatile technique used for frequency-sensitive, non-ideal, distorted three-phase grid synchronisation applications is the synchronous reference frame PLL (SRF-PLL) shown in fig. 3.25, [24, 107]. The basic principle of the SRF-PLL is to control the angular position of the qd-reference frame by using a feedback loop which drives the q-component error to zero. Thus when steady state is reached ($q = 0$) the d-component represents the amplitude of the sinusoidal positive sequence vector and its phase angle is determined by the output of the PLL feedback loop[24]. A great benefit of the SRF-PLL is its ability to attenuate harmonic distortion of the grid voltage. [24] shows that a slight reduction in the bandwidth of the PLL controller improves its response such that high-order harmonics effects are almost completely rejected on the PLL output signals. In typical PI tuning for the PLL the symmetrical optimum criterion is used, which maximises the phase margin at a given crossover frequency, e.g. 50 Hz, [108]. The gain selection for SO is decribed by (3.67).

$$\left.\begin{aligned} a &= \frac{1}{\omega_c T s}, \\ T_{n,PLL} &= a^2 T_{\mathrm{s}}, \\ V_{r,PLL} &= \frac{1}{a u_0 T_{\mathrm{s}}}. \end{aligned}\right\} \tag{3.67}$$

where u_0 is the peak grid phase voltage ($\sqrt{2} \times 230\,\text{V}$) and ω_c is the crossover frequency which must be equal to the grid frequency ω_g.

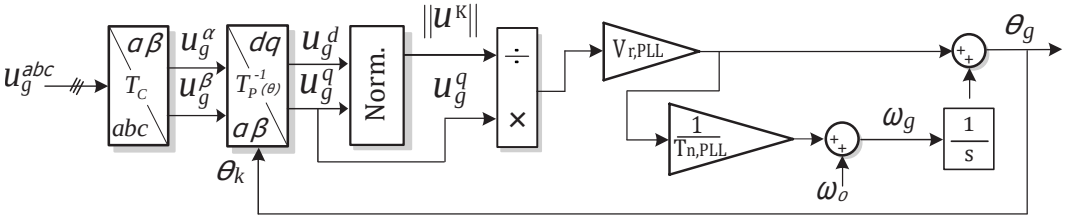

Figure 3.25: Basic Structure of a SRF-PLL.

3.4.2 Current Control

Current control of $\boldsymbol{i}_{\text{g}}^{abc} = (i_{\text{g}}^{a}, i_{\text{g}}^{b}, i^{bc})^{\top}$ is required to regulate the active and reactive power exchange with the grid [24, 74]. Filtering of the grid currents is also necessary to reduce THD, caused by the VSC modulation (PWM or SVM), so that it stays within interconnection standards. The LCL-filter has been shown in numerous works to have the best performance when compared to that of L- and LC-filters, and its design has been researched extensively [24, 109–111]. Dynamic current control with an LCL-filter can be achieved with a 1^{st} order transfer function of the simplified LCL-circuit because the LCL-filter behaves like an L-filter for frequencies lower than that of the LCL resonant frequency (or when a damping resistance R_{damp} is considered). The approximated filter and estimated grid inductances at the output of the VSC, L_{f} and L_{g} respectively, are combined into one total inductance $L_{\text{g},\Sigma} = L_{\text{f}} + L_{\text{g}}$ along with their parasitic resistances $R_{\text{g},\Sigma} = R_{\text{f}} + R_{\text{g}}$ [24, 111]. The influence of the LCL-filter capacitor can also be neglected, since it only interacts with high switching ripple frequencies [24], to allow the current measurement to be sampled at the inverter side, $\boldsymbol{i}_{\text{f}}^{abc} = \boldsymbol{i}_{\text{g}}^{abc}$ as shown in fig. 3.24. Once cascaded with the time delay transfer function of the VSC, the system model becomes a 2^{nd} order transfer function which can be easily controlled with PI regulators.

Synchronous reference frame voltage-oriented control, shown in the previous section fig. 3.24, is the most direct implementation of grid current control and can be achieved using PI regulators implemented in the d/q-reference frame [24, 74, 111]. The active and reactive power can be controlled by adjusting the d and q-axis current references, whereby a unity power factor is obtained by setting $i_{g,ref}^{q} = 0$. The d/q-reference frame requires the grid angular frequency ω_{g} to be tracked with a phase lock loop (PLL) so that the electrical angle $\theta_g = \int \omega_{\text{g}} \text{d}t$ for the Park transformation $\boldsymbol{T}_{\text{p}}(\theta_g)$ is known [24, 74]. The dynamic model for a grid-connected VSC, fig. 3.26, is derived from Kirchhoff's current and voltage laws in the (a, b, c)-reference frame, (3.68), whereby the application of the Clarke transformation, $\boldsymbol{T}_{\text{c}}$ yields the $\alpha\beta$-reference frame (3.69), and the inverse Park

transformation, $\boldsymbol{T}_{\mathrm{p}}$, the dq-reference frame (3.70).

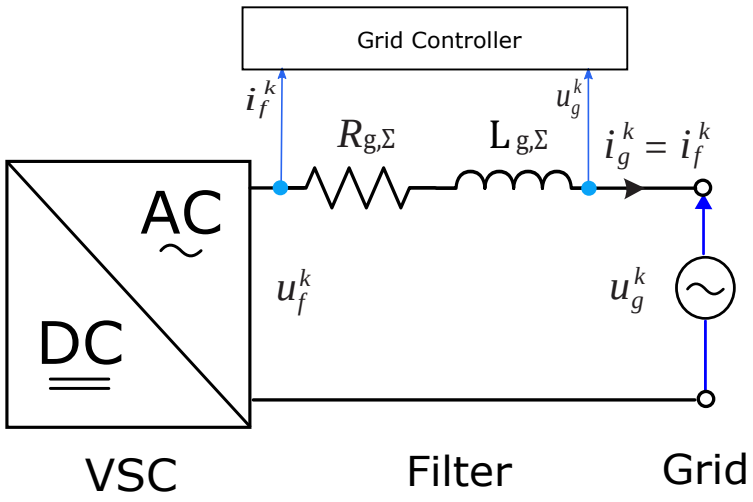

Figure 3.26: Simplified circuit layout for grid-connected VSC current controller.

$$\boldsymbol{u}_{\mathrm{f}}^{abc} = R_{\mathrm{g}}\boldsymbol{i}_{\mathrm{g}}^{abc} + L_{\mathrm{g},\Sigma}\frac{d}{dt}\boldsymbol{i}_{\mathrm{g}}^{abc} + \boldsymbol{u}_{\mathrm{g}}^{abc}, \tag{3.68}$$

$$\begin{aligned}\boldsymbol{u}_{\mathrm{f}}^{s} &= \boldsymbol{T}_{\mathrm{c}}\boldsymbol{u}_{\mathrm{f}}^{abc},\\ &= R_{\mathrm{g},\Sigma}\boldsymbol{i}_{\mathrm{g}}^{s} + L_{\mathrm{g},\Sigma}\frac{d}{dt}\boldsymbol{i}_{\mathrm{g}}^{s} + \boldsymbol{u}_{\mathrm{g}}^{s},\end{aligned} \tag{3.69}$$

$$\begin{aligned}\boldsymbol{u}_{\mathrm{f}}^{k} &= \boldsymbol{T}_{\mathrm{p}}^{-1}\boldsymbol{u}_{\mathrm{f}}^{s},\\ &= R_{\mathrm{g},\Sigma}\boldsymbol{i}_{\mathrm{g}}^{k} + L_{\mathrm{g},\Sigma}\tfrac{\mathrm{d}}{\mathrm{d}t}\boldsymbol{i}_{\mathrm{g}}^{k} - \omega_{\mathrm{g}}L_{\mathrm{g},\Sigma}\mathbf{J}\boldsymbol{i}_{\mathrm{g}}^{k} + \boldsymbol{u}_{\mathrm{g}}^{k},\end{aligned} \tag{3.70}$$

where $\boldsymbol{u}_{\mathrm{f}}^{k}, \boldsymbol{u}_{\mathrm{f}}^{s}$ are the dq and $\alpha\beta$ VSC voltage respectively, $\boldsymbol{u}_{\mathrm{g}}^{k}, \boldsymbol{u}_{\mathrm{g}}^{s}$ are the grid voltages and $\boldsymbol{i}_{\mathrm{g}}^{k}, \boldsymbol{i}_{\mathrm{g}}^{s}$ the grid currents which are assumed to be (almost) equal to the measured inverter current $\boldsymbol{i}_{\mathrm{f}}^{k}$. For the grid voltage amplitude $\hat{u}_{\mathrm{g}} := \|\boldsymbol{u}_{\mathrm{g}}^{k}\|$ and grid voltage orientation, the grid coupling disturbance terms can be defined as:

$$\left.\begin{aligned}u_{\mathrm{g},dist}^{d}(i_{\mathrm{g}}^{q}, \omega_{\mathrm{g}}, \hat{u}_{\mathrm{g}}) &= +\omega_{\mathrm{g}}L_{\mathrm{g},\Sigma}i_{\mathrm{g}}^{q} + \hat{u}_{\mathrm{g}},\\ u_{\mathrm{g},dist}^{q}(i_{\mathrm{g}}^{d}, \omega_{\mathrm{g}}) &= -\omega_{\mathrm{g}}L_{\mathrm{g},\Sigma}i_{\mathrm{g}}^{d}.\end{aligned}\right\} \tag{3.71}$$

For ideal compensation of these coupling terms, the model (3.70) can be rewritten as a general transfer function:

$$\frac{\boldsymbol{i}_{\mathrm{g}}^{k}(s)}{\boldsymbol{u}_{\mathrm{f}}^{k}(s)} = \frac{\frac{1}{R_{\mathrm{g},\Sigma}}}{(1 + sT_{\mathrm{g},\Sigma})(1 + sT_{\mathrm{vsc}})}, \tag{3.72}$$

where $T_{\mathrm{g},\Sigma} := \frac{L_{\mathrm{g},\Sigma}}{R_{\mathrm{g},\Sigma}}$ is the filter time constant and T_{vsc} the (averaged) time constant of the VSC. The parameters of the grid-side PI controllers under Modulus Optimum criterion

are defined in (3.73).

$$\left.\begin{aligned} \textbf{Gain: } V_{\mathrm{r,g}} &= \frac{T_{\mathrm{g},\Sigma} R_{\mathrm{g},\Sigma}}{2T_{vsc}} \\ \textbf{Time Constant: } T_{\mathrm{n,g}} &= 4T_{\mathrm{g},\Sigma}. \end{aligned}\right\} \tag{3.73}$$

Using (3.72) any gain calculation method can be used. The modulus optimum (MO) method was used in this case where the closed-loop current dynamics can be approximated by a first-order lag system with time constant $T_{eq} := 2T_{vsc}$ [74]. An over view of the grid-tie current controller is presented in the introduction to this section in fig. 3.24.

3.4.3 LCL-Filter

In order to preserve the power quality and safety of the grid network, various standards have been developed. Currently, the most influential distributed resource interconnection standard that applies to all technologies is the IEEE 1547-2003 Standard for Interconnecting Distributed Resources with Electric Power Systems [24, 112]. This standard details technical specifications for testing and the interconnection itself, general requirements, abnormal condition responses, power quality, islanding test specifications and various requirements for the design, production, installation evaluation, commissioning and periodic tests. Due to the difficulty in testing and implementing an anti-islanding setup, anti-islanding protection was omitted from the scope of this project. With regard to power quality, the IEC 61000 Electromagnetic Compatibility (EMC low frequency) [113] deals with grid-injected current harmonic limitations for the public grid supply. Harmonic content limits are specified for the input current as a THD quantity. This part of IEC 61000-3-2 applies to electrical and electronic equipment with an input current of ≤ 16 ampere per phase connected to the low voltage public grid supply. Regulations for power factor are not mentioned in the IEEE 1547, however in IEC 61727 it is stated that PV inverters for utility-interconnected systems must have an average lagging power factor greater than 0.9 when the output is greater than 50 %. In table 3.2 highlights the main standards that are considered in this project are highlighted. In order for power electronic devices such as VSC to achieve these standards, output filters are required.

Table 3.2: Various interconnection standard requirements considered in this project.

	Requirements	Standard
Voltage Regulation	≤ 5 %	ANSI C84
Current Regulation, THD (%)	≤ 5 %	IEEE 1547, IEC 61000-3-2
Power Factor	≥ 0.9	IEC 61727
Saftey		NFPA, NEC,IEEE, NESC

The two most common filter approaches to reduce PWM and harmonics are the LCL- and LC-filter [24]. The LCL-filter overcomes the effects of dynamic grid inductance,

which can cause resonance problems when using a LC-filter [24]. The added inductance on the grid side reduces the influence of stray grid inductance of the resonance of the filter. The LCL-filter has an attenuation of -20dB/decade for frequencies lower than the resonant frequency which is similar to an L-filter fig. 3.27. For frequencies greater than this there is a -60dB/decade. This allows the LCL-filter to meet more stringent grid requirements at a cheaper cost because smaller inductors can be used and at lower switching frequencies. If designed correctly the filter can provide lower current ripple across the grid inductor (which improves switching loss) and better decoupling between filter and grid impedance.

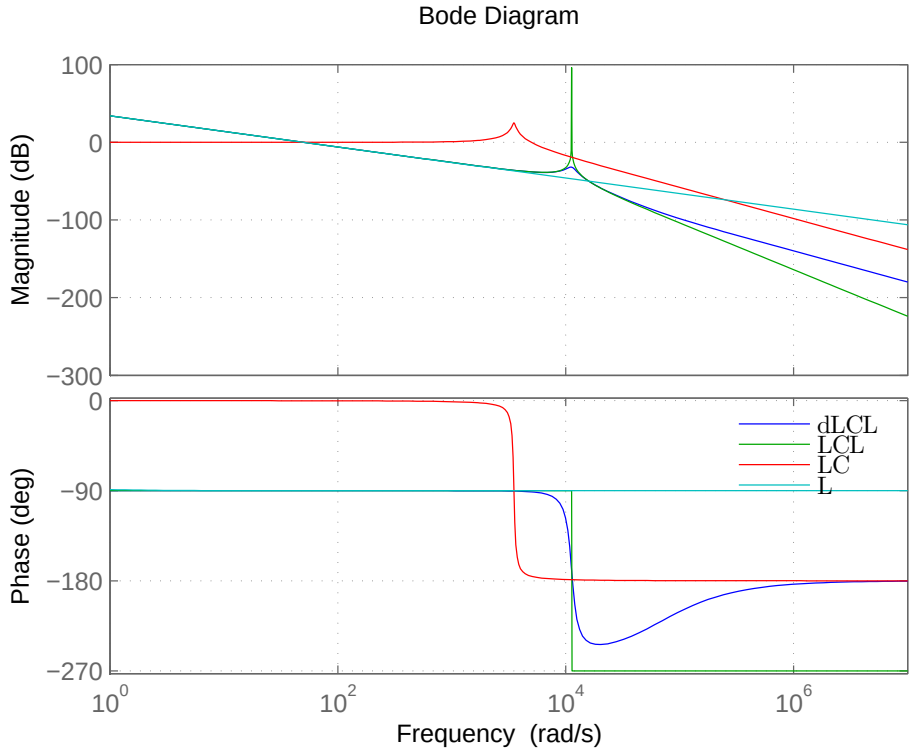

Figure 3.27: Magnitude and phase response plot for the damped and undamped LCL-filter, the damped LC-filer and the L-filter.

The resonant peak caused by the LCL-filter makes dynamic control more difficult than with a regular L-or LC-filter. Active or passive damping methods can be implemented to mitigate this issue [24, 114, 115]. The resonant peak can be seen in fig. 3.27 for the undamped case. This resonance must be damped appropriately to avoid instability. There are essentially two methods for damping, active and passive damping [24, 114, 115]. During active damping a control algorithm (no additional hardware) is used, which eliminates harmonics at the resonant frequency and passive damping in-

volves additional components such as resistors, inductors and/or capacitors placed in the LCL-filter circuit. Passive damping was chosen for simplicity and ease of implementation. Common passive damping methods are arranged with the capacitor and resistor in series or parallel, fig. 3.28. [110, 114] shows that series damping results in slightly increased THD with minimal losses and better stability, compared to parallel damping which has lower THD, but much higher losses and less stability due to the lower resistance path of the capacitor. To minimise power loss, series-connected damping resistors were chosen for this project.

3.4.3.1 LCL-Filter Analysis

The LCL-filter design and modelling in this project is based mainly on the research done by [110, 111, 114] which has shown promising results with relatively simple design equations. Very similar design procedures for the LCL-filter are shown throughout the literature with some deviations detailing more in-depth studies which involve the power loss of the filter and the inductor design in the optimisation algorithms [109, 116].

The LCL-filter per-phase model is shown in fig. 3.28 where L_f is the inverter-side inductor, L_g is the grid-side inductor, Rf and Rg are inductors resistances, R_d is the damping resistor, C_f is the capacitor of LCL-filter and $\imath_f, i_c, i_g$ are the inverter output current, capacitor current, and grid current, respectively.

A three-phase LCL-filter can be connected in delta or wye, fig. 3.29. The wye connection requires the availability of the neutral point and the DC bus voltage midpoint. Common practice is to ground the neutral and this is required by the U.S. National Electric Code (NFPA-70). By grounding a wye system the ground referenced voltages are stabilized and controlled, which makes the system less susceptible to faults and surges. Grounding a system correctly can be difficult especially if there are several VSCs and other machines present, thus to avoid any additional grounding issues, the delta connection can be chosen. A delta-connected system also requires less capacitance than a wye system, because of the cross-coupling between phases and the reduction of the phase current. For these reasons a delta connection was chosen for this project.

$$Z_{f,\Delta} = \frac{Z_{f,\gamma}}{3} \tag{3.74}$$

$$C_{f\Delta} = \frac{C_{f,\gamma}}{3} \tag{3.75}$$

$$R_{f\Delta} = 3R_{f\gamma} \tag{3.76}$$

Probably the most important characteristic for the LCL filter is the transfer function of the injected grid current and VSC voltage, $H_{LCL} = \frac{i_g}{v_i}$. This equation provides insight

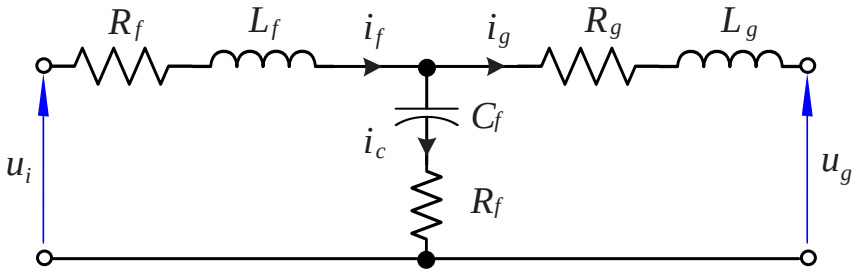

(a) Series damping.

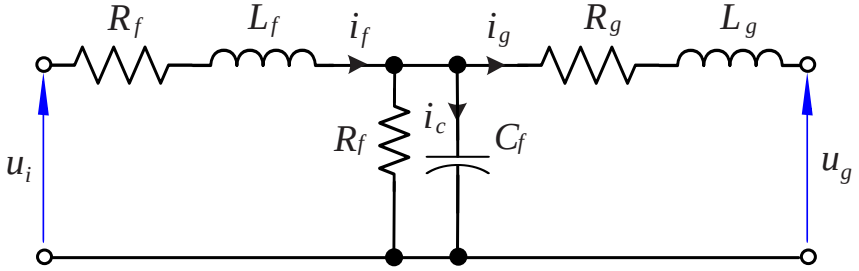

(b) Parallel damping.

Figure 3.28: Single-phase series and parallell damping LCL-filter configurations.

into the filter frequency response and thus the design of the filter parameters. The undamped (3.77), series damped (3.78) and parallel damped (3.79) transfer functions are shown below [110]. From (3.77) the resonant frequency can be extracted.

$$H_{LCL} = \frac{1}{L_f L_g C_f s^3 + (L_f + L_g)s}, \tag{3.77}$$

$$Hsd_{LCL} = \frac{C_f R_f s + 1}{L_f L_g C_f s^3 + C_f R_f (L1 + L2)s^2 + (L_f + L_g)s}, \tag{3.78}$$

$$Hpd_{LCL} = \frac{R_f}{L_f L_g C_f R_f s^3 + (L1 + L2)s^2 + R_f (L_f + L_g)s}, \tag{3.79}$$

$$\omega_{res} = \sqrt{\frac{L_f + L_g}{L_f L_g C_f}}. \tag{3.80}$$

It is important to minimise the power dissipated in the LCL filter. Power loss in an inductor is the result of complex eddy current, hysteresis, winding losses and skin effect phenomena [116]. Correctly optimising an LCL-filter for minimal losses is beyond the scope of this project. However, some literature regarding filter loss was reviewed.

There are two types of loss in an inductor, fundamental loss, predominantly caused by the resistance of the inductor, and switching losses which prevail in the core of the inductor. Core-losses, directly proportional to switching frequency, are composed of two types of losses, magnetic hysteresis loss and eddy current loss. Magnetic hysteresis loss is due to the flux density versus inductance (B-H) curve, which does not allow

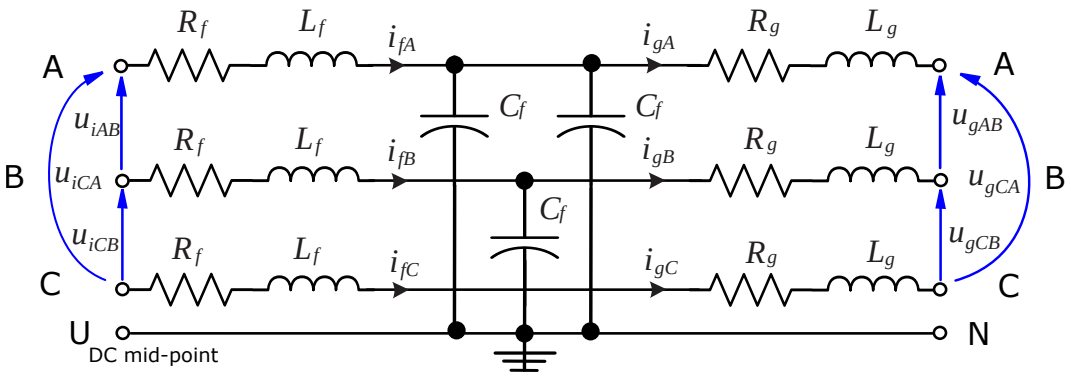

(a) Wye Connected 3-phase LCL-filter.

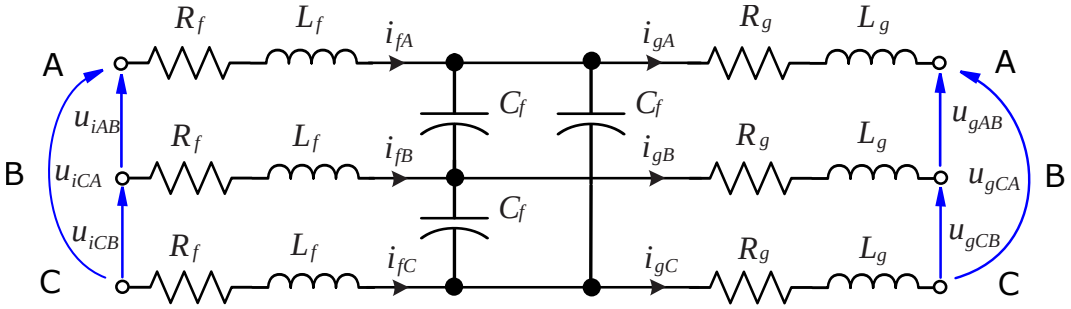

(b) Delta Connected 3-phase LCL-filter.

Figure 3.29: Three-phase Wye and Delta connected LCL-filter configurations.

all of the energy gained during the magnetisation of the core to be released back into a load during demagnetisation. Eddy-current loss is due to circuiting currents induced in the core material by the oscillating flux $\frac{d\phi}{dt}$ in accordance with Lenz's Law and causes further I^2R loss. Total inductor loss is directly proportional to switching frequency and inversely proportional to the inductance. Thus, making L_f larger than L_g reduces the switching frequency losses of the system and since L_g has almost no switching current ripple, the only loss present is fundamental losses, L_g should therefore be as small as possible within the design limitations.

3.4.3.2 LCL-Filter Design

Designing an LCL-filter is not a trivial task and a multitude of complex numerical algorithms exist for achieving a desired filter power, attenuation, loss and size. Research done by [116, 117] took into account several harmonics and core losses which affect the final dimensions of the inductors. Some prefer a more straight forward analytical approach where the ripple current, resonant frequency and attenuation factors are approximated using simple equations [24, 110, 111, 114, 115, 118]. This research was utilised greatly for the design approach detailed in this section. The theoretical results were then validated in Matlab Simlulink, and then further validated in practice in section 4.7.2.

The basic LCL-filter design parameters are the power rating of the converter, the grid frequency, the switching frequency and the desired attenuation factor. In any design optimisation problem it is important to set up constraints so that the design achieves a realistic values.

- **Constraint 1**
  It is important that the maximum voltage drop across the inductor is not too large. Typical values are less than 10 % of the output voltage [110, 114]. A large voltage drop requires an increase in the DC bus voltage and therefore the switching losses of the inverter. The voltage drop across the total inductance can be expressed by $V_{drop} = L_{g,\Sigma}\frac{di}{dt}$. In accordance with constraint 1 the maximum inductance $L_{max} = 0.1L_b$ [109].

- **Constraint 2**
  The resonant filter frequency should be less than half of the switching frequency and greater ten times the fundamental frequency.

- **Constraint 3**
  The total reactive power and power factor imposed by the filter should be limited to less than 5 % of the base capacitance [107].

- **Constraint 4**
  The overall switching loss and inductor core loss must be kept as low as possible. The base impedance, inductance and capacitance are defined by eqs. (3.81) to (3.83). In accordance with constraint 3 the maximum capacitance $C_{max} = 0.05C_b$, but can be larger if required to compensate for the inductance [111].

$$Z_b = \frac{U_{LL}^2}{P_n}, \tag{3.81}$$

$$C_b = \frac{1}{\omega_n Z_b}, \tag{3.82}$$

$$L_b = \frac{Z_b}{\omega_n}. \tag{3.83}$$

A rough approximation of the filter dynamics can be acquired with consideration of the capacitor short-circuited at the ripple current frequency [24, 110, 111]. This is described by (3.84). The maximum switching ripple current at the output of the inverter ΔI_{Lmax}, is based on the DC bus voltage u_{dc} modulation factor m, inverter inductance L_f and the switching period T_{sw} of the converter. The equation is simplified by assuming that the maximum peak to peak ripple occurs when $m = 0.5$. Attenuation is generally set below 10% of the rated current (3.85), [111], but can be much lower or higher depending on grid requirements [114].

$$\begin{aligned}\Delta I_{Lmax} &= \frac{2u_{\mathrm{dc}}}{3L_f}(1-m)mT_{sw}, \\ &= \frac{u_{\mathrm{dc}}}{6f_{\mathrm{sw}}L_f}, \qquad (3.84) \\ &= 0.1I_{max}, \qquad (3.85) \\ &= 0.1\frac{P_n\sqrt{2}}{3U_{ph}}.\end{aligned}$$

By solving (3.84) for the inverter side inductance (3.86), a rough estimation of L_f [111] is formulated. High DC bus voltages and low switching frequencies (3.86) can lead to very large L_f values which conflict with constraint 1. Large inductances are expensive to manufacture, bulky, reduce the response time of the current controllers and increase the switching losses of the VSC. It is therefore ideal to keep the total inductance as low as possible without incurring additional switching losses. As demonstrated by the contrast between [110, 111, 114], opinions on (3.86) vary greatly in literature, however [111] who proposed, (3.86), validates his calculations though practical experiments.

$$L_f = \frac{u_{\mathrm{dc}}}{6f_{\mathrm{sw}}\Delta I_{Lmax}}. \qquad (3.86)$$

The ratio $k_a = \dfrac{i_g(f_{\mathrm{sw}})}{i_f(f_{\mathrm{sw}})}$ in (3.87) sets the filter attenuation magnitude between the inverter and grid currents at the switching frequency where $a = L_f C_f \omega_{sw}^2$, $\omega_{sw} = 2\pi f_{\mathrm{sw}}$ and $Cf = xC_b$. Simulations of the filter in Matlab Simulink were required to check the current THD of the design so that the grid standards are met. It was found that k_a should be below 0.04 for the THD average to be below 5 %.

$$\frac{i_g(f_{\mathrm{sw}})}{i_f(f_{\mathrm{sw}})} = \frac{1}{|1+r(1-a)|} \qquad (3.87)$$

The constant r is defined as the relation between the grid and inverter side inductances.

$$r = \frac{L_g}{L_f} \qquad (3.88)$$

The choice of $L_{\mathrm{g},\Sigma}$ is made to minimise the total power loss in the VSC and the LCL-filter. Although this problem can be computational complex to solve, there are some guidelines that can be used to limit the scope of the filter design. Power loss in the VSC LCL circuit is composed primarily of losses at both the fundamental and the switching frequency, $P_{loss}(F_0), P_{loss}(f_{\mathrm{sw}})$. Power loss at F_0 is lowest when $L_{\mathrm{g},\Sigma} = L_{min}$ whereas the switching frequency ripple loss is smallest when $L_{\mathrm{g},\Sigma} = L_{max}$. There is a compromise between the two losses where $L_{\mathrm{g},\Sigma}$ reduces both. Finding the optimum point of these two

parameters is however, outside the scope of this project. Power quality was chosen as the overriding constraint and thus $L_{g,\Sigma} = L_{max}$ was chosen because of the greater attenuation characteristics.

L_g can be calculated using (3.89) which was found to provide a good approximate value for L_g. However, it was found that the attenuation of the filter could be improved by running Matlab current THD simulations for various L_g and L_f values while keeping to $L_{max} \leq L_{g,\Sigma} = L_f + L_g$. It was found that the system's THD decreased with a slightly higher value for L_g than what is calculated by 3.89.

$$L_g = \frac{\sqrt{\frac{1}{k_a^2}+1}}{C_f \omega_{sw}^2}. \tag{3.89}$$

Solving all these equations can be done step-by-step and then iterated until the desired values are obtained. However, a slightly different approach is adopted by calculating a large range of possible values for r, k_a and L_f and then selecting the desired values, within the range of the constraints, from this map using interpolation. Figure 3.30 maps the parameter space for filter parameters of r, k_a and L_f with the selected parameter values highlighted.

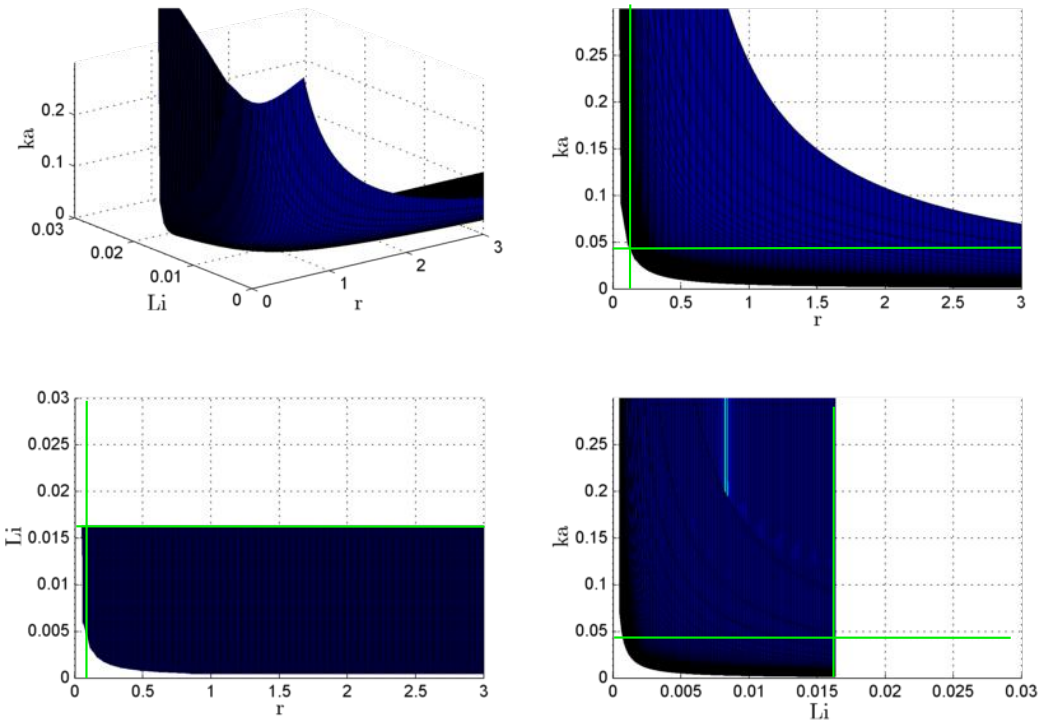

Figure 3.30: LCL-filter parameters for a range of L_f, r and k_a.

Table 3.3: Grid and LCL-filter design parameters and results.

Grid Parameters	
Rated power	3 kW
Phase voltage	230 V
f_g	50 Hz
Z_b	52.9 Ω
C_b	60.17 µF
L_b	16.84 mH
Inverter Parameters	
f_{sw}	10 kHz
f_s	10 kHz
u_{dc}	600 V

LCL Parameters	
L_f	16.8 mH
L_g	2.2 mH
r	0.1350
R_{Li}	0.166 Ω
R_{Lg}	0.064 Ω
$R_{g,\Sigma}$	1.2 Ω
C_f	3 µF
$R_{f,g}$	7.33 Ω
k_a	0.04
I_{max}	6.14 A
ΔI_{max}	0.6149 A
f_{res}	2.09 kHz

Once r, k_a, L_f and L_g are selected, the resonant frequency (3.90) (in rad/s) and damping resistance R_d can be calculated [111].

$$\omega_{res} = \sqrt{\frac{L_f + L_g}{L_f L_g C_f}}, \tag{3.90}$$

$$10 f_g < f_{res} < 0.5 f_{sw}, \tag{3.91}$$

$$R_{f,g} = \frac{1}{3\omega_{res} C_f}. \tag{3.92}$$

Below is table 3.3 which contains the final design values for the filter. The equations above were used as guide lines, but ultimately simulations of the filter performance are what dictated the final choice of parameters. See appendix D.0.6 for more details on the Matlab scripts used to obtain these values.

The rated power of the LCL-filter should be selected to match the electrical output power of the generator, since the filter design process minimises the THD at the intended rated current. At currents lower than the design current the THD will increase. At currents higher than the rated the THD will decrease. Saturation effects in the inductors also need to be avoided but this can be achieved by designing the inductors for 150 % rated power. Figure 3.31 is the bode plot of an LCL-filter with the parameters as in table 3.3.

In appendix E the design and manufacturing process of the LCL-filter inductors L_f and L_g is detailed. The most important design aspects of inductors are their dimension, material, air gap and the winding (no. of turns and conductor dimensions). Typical magnetic core material is ferrite, laminated steel and powered metal. A detailed inductor design Matlab script is available in appendix D.0.7.

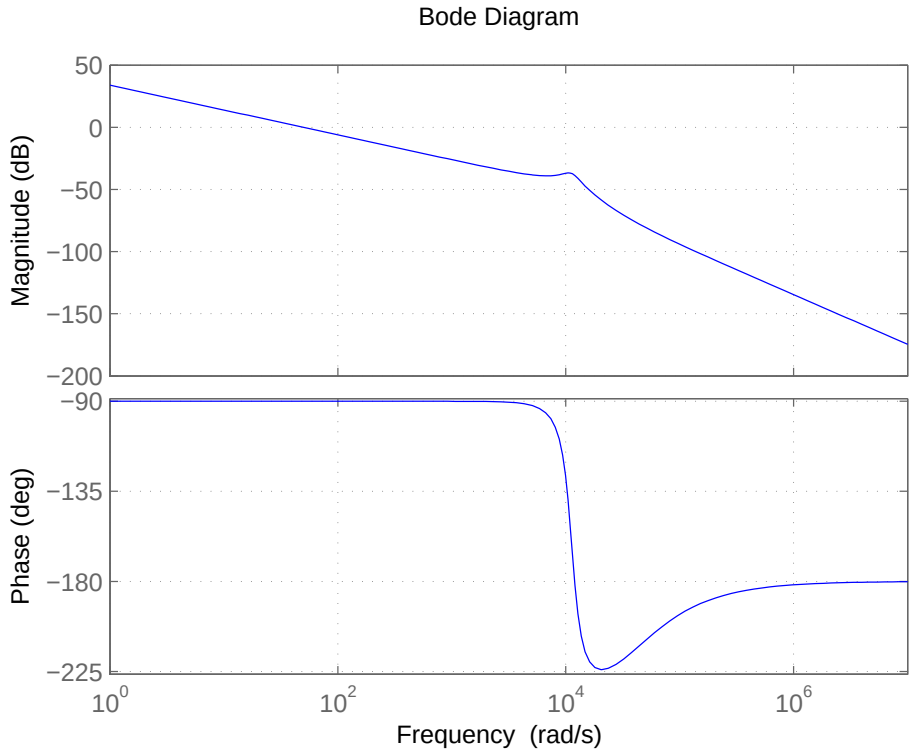

Figure 3.31: Magnitude and phase response plot for the designed LCL-filter.

3.4.4 DC Bus Voltage Control

DC bus power control is very well documented in many published papers [38]. However, the non-linear DC bus dynamics and non-minimum phase properties are mostly overlooked in the controller design. A number of methods have been developed to deal with this behaviour using VSCs (see [38] and references therein). Linearisation is the most common technique [24, 38], but there are more advanced methods such as state feedback [38] and model predictive strategies [39]. In [40], the non-linear DC bus dynamics and the control of bidirectional power flow for an airborne wind energy system are discussed in detail, which will serve as a basis for the later development of a stable bidirectional DC-link controller used for the back-to-back DC bus.

3.4.4.1 Dynamic Non-linear DC Bus Model

In a nutshell, DC bus voltage control can be achieved by controlling the injected and absorbed power (actively rectified) to and from the grid. The method used in this project is an indirect method whereby the grid connected VSC actively manages its power exchange with the grid using cascaded control, a structure to regulate the DC voltage. This method is motivated by the non-linear and unstable zero dynamics of the system [24].

Power changes from the generator side result in voltage fluctuations that must be compensated for by the controlled charging or discharging of the DC-link capacitor. There are two variations in DC voltage: The first is the AC type, caused by instantaneous power fluctuations due to unbalanced grid conditions. This type of DC bus disturbance is beyond the scope of this project and will not be discussed here. The second or DC type is caused by a change in the average power transmitted through the DC-link or a change in its set-point [24, 119].

In the case of the DC type fluctuations, deviations from the reference value $u_{\mathrm{dc},ref}$, require energy to be gained or discharged in order for the capacitor to reach the set-point. This energy fluctuation is described by (3.93) and the corresponding power exchange by (3.94).

$$\Delta E = C_{\mathrm{dc}} \frac{(u_{\mathrm{dc},ref})^2 - u_{\mathrm{dc}}^2}{2} \approx u_{\mathrm{dc}}^* \Delta u_{\mathrm{dc}} C_{\mathrm{dc}}, \tag{3.93}$$

$$\Delta P = C \frac{2\Delta E}{(3+n)T_{\mathrm{g},\Sigma}}, \tag{3.94}$$

The estimated DC link voltage error is defined by:

$$\Delta u_{\mathrm{dc}} = C \frac{\Delta P (3+n) T_g}{2 C_{\mathrm{dc}} u_{\mathrm{dc},ref} T_{\mathrm{g},\Sigma}}, \tag{3.95}$$

where C_{dc} is the DC-link capacitance, $\Delta E, \Delta P, \Delta u_{\mathrm{dc}}$ are the error in DC energy, power and voltage, T_g is the inner loop current control delay, $nT_{\mathrm{g},\Sigma}$ is the DC-link filter delay and $u_{\mathrm{dc}}, u_{\mathrm{dc},ref}$ are the DC bus voltage and reference voltage respectively. The above energy equations highlight the importance of the DC capacitance and the inner and outer loop time delay. Large capacitance is clearly favoured as well as a fast $T_{\mathrm{g},\Sigma}$. From these equations it can be deduced that the control of the DC voltage can be achieved through a controlled power exchange with the grid, either by controlling the current or voltage across C_{dc}.

The zero-loss dynamic model for the DC bus is suggested by [24, 40] and is derived by considering the instantaneous power balance for the grid connected VSC in the synchronous dq-reference frame, as shown by fig. 3.32 and (3.96). It is assumed that the grid phases are balanced and that the magnitude $\hat{u}_{\mathrm{g}}$ of the grid voltage is large compared to the voltage drop over the filter resistance, $2R_{\mathrm{g},\Sigma} i_{\mathrm{g}}^d(t) + \hat{u}_{\mathrm{g}} > 0$ for all $t > 0$.

$$\begin{aligned} P_{\mathrm{dc}} &= P_{\mathrm{g}} - P_{\mathrm{m}}, \\ u_{\mathrm{dc}} C_{\mathrm{dc}} \frac{d}{dt} u_{\mathrm{dc}} &= \frac{3}{2} \boldsymbol{u}_{\mathrm{g}}^k \boldsymbol{i}_{\mathrm{g}}^k - u_{\mathrm{dc}} i_o. \end{aligned} \tag{3.96}$$

where u_{dc} is the DC bus voltage, $\boldsymbol{u}_{\mathrm{g}}^k$, $\boldsymbol{i}_{\mathrm{g}}^k$ are the dq grid voltage and currents. P_{g} is the injected grid power (positive sign into the grid). P_{m} is the electrical power of the generator (negative sign in generator mode) and i_o is the DC bus injected current.

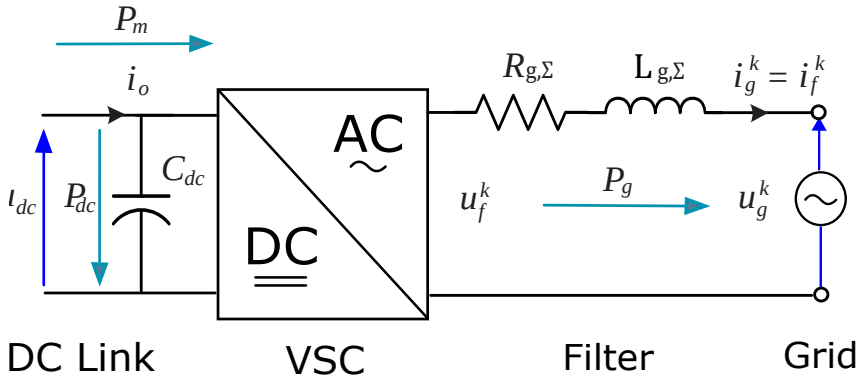

Figure 3.32: Dynamic DC bus link model with VSC and grid in the synchronous d axis reference frame.

Eq. (3.97) expands on (3.96) to obtain the non-linear voltage dynamics, $\frac{d}{dt}u_{\mathrm{dc}}$.

$$\begin{aligned}\frac{d}{dt}u_{\mathrm{dc}} &= \frac{1}{u_{\mathrm{dc}}C_{\mathrm{dc}}}\left[\frac{3}{2}\boldsymbol{u}_{\mathrm{g}}^k\boldsymbol{i}_{\mathrm{g}}^k - u_{\mathrm{dc}}i_o\right], \\ &= \frac{3}{2u_{\mathrm{dc}}C_{\mathrm{dc}}}\left[R_{\mathrm{g},\Sigma}||\boldsymbol{i}_{\mathrm{g}}^k||^2 + L_{\mathrm{g},\Sigma}(\boldsymbol{i}_{\mathrm{g}}^k)^\top\frac{d\boldsymbol{i}_{\mathrm{g}}^k}{dt} + \hat{u}_{\mathrm{g}}i_{\mathrm{g}}^d\right., \\ &\quad \left.\underbrace{+\omega_{\mathrm{g}}L_{\mathrm{g},\Sigma}(\boldsymbol{i}_{\mathrm{g}}^k)^\top\boldsymbol{J}^\top\boldsymbol{i}_{\mathrm{g}}^k}_{=0} - \frac{2}{3}P_{\mathrm{m}}\right].\end{aligned} \tag{3.97}$$

The above system can be linearised around an equilibrium point (denoted by $(.)^*$) at, $\frac{du_{\mathrm{dc}}}{dt} = 0$, to produce (3.98), the small signal system dynamics [40] or [38].

$$\begin{aligned}\frac{d}{dt}\tilde{u}_{\mathrm{dc}} &= \frac{3}{2u_{\mathrm{dc}}(t)C_{\mathrm{dc}}}\left[(\hat{u}_{\mathrm{g}} + 2R_{\mathrm{g},\Sigma}i_{\mathrm{g}}^{d,*})\tilde{i}_{\mathrm{f}}^d - L_{\mathrm{g},\Sigma}i_{\mathrm{g}}^{d,*}\frac{d}{dt}\tilde{i}_{\mathrm{f}}^d\right., \\ &\quad \left.+(2R_{\mathrm{g},\Sigma}i_{\mathrm{g}}^{q,*})\tilde{i}_{\mathrm{f}}^q + L_{\mathrm{g},\Sigma}i_{\mathrm{g}}^{q,*}\frac{d}{dt}\tilde{i}_{\mathrm{f}}^q - \frac{2}{3}P_{\mathrm{m}}^*\right].\end{aligned} \tag{3.98}$$

Removing the q-axis components from the system is achieved by the realisation that the reactive power at the point of common coupling (PCC), $q_{pcc} = \frac{3}{2}\hat{u}_{\mathrm{g}}i_{\mathrm{g}}^q$, is dependent on the users' reactive power reference $q_{\mathrm{pcc},ref}$. Hence the q component of the system for all $t \geq 0$ is represented by (3.99) as a time varying, but bounded disturbance to the system dynamics [24]. The injected power components of the system can be treated in a similar way.

$$|i_{\mathrm{g}}^q| = \frac{2||q_{\mathrm{pcc},ref}||}{3\hat{u}_{\mathrm{g}}}. \tag{3.99}$$

The transfer function of the linearised system, with consideration of the inner loop current dynamics T_{eq}, given by (3.101). The closed current loop dynamics can be approximated by a first-order lag system, $\frac{d\boldsymbol{i}_{\mathrm{g}}^{k}}{dt} = \frac{1}{T_{eq}}(-\boldsymbol{i}_{\mathrm{g}}^{k} + \boldsymbol{i}_{\mathrm{g,r}ef}^{k})$, with $T_{eq} := 2T_{\mathrm{v}sc}$.

$$\frac{d}{dt}u_{\mathrm{dc}} = \frac{3}{2u_{\mathrm{dc}}C_{\mathrm{dc}}}\left[(R_{\mathrm{g},\Sigma} + \frac{L_{\mathrm{g},\Sigma}}{T_{eq}})||\boldsymbol{i}_{\mathrm{g}}^{k}||^2 - \frac{L_{\mathrm{g},\Sigma}}{T_{eq}}(\boldsymbol{i}_{\mathrm{g}}^{k})^{\top}\boldsymbol{i}_{\mathrm{g},ref}^{k}\right., \\ \left. + \hat{u}_{\mathrm{g}}i_{\mathrm{g}}^{d} - \frac{2}{3}P_{\mathrm{m}}\right]. \tag{3.100}$$

$$F_{\mathrm{dc}}(s) = \frac{\tilde{u}_{\mathrm{dc}}(s)}{\tilde{i}_{\mathrm{f}}^{d}(s)} = \frac{-V_{\mathrm{s},dc}(1+sT_{\mathrm{s},dc})}{s(1+sT_{eq})}. \tag{3.101}$$

The parameters of the linearised system are given by:

$$\left.\begin{aligned} V_{\mathrm{s},dc}(i_{\mathrm{f}}^{d,\star}, u_{\mathrm{dc}}^{\star}) &= \frac{3(\hat{u}_{\mathrm{g}} + 2R_{\mathrm{g},\Sigma}i_{\mathrm{f}}^{d,\star})}{2C_{\mathrm{dc}}u_{\mathrm{dc}}^{\star}}, \\ T_{\mathrm{s,dc}}(i_{\mathrm{f}}^{d,\star}) &= \frac{L_{\mathrm{g},\Sigma}i_{\mathrm{f}}^{d,\star}}{\hat{u}_{\mathrm{g}} + 2R_{\mathrm{g},\Sigma}i_{\mathrm{f}}^{d,\star}}. \end{aligned}\right\} \tag{3.102}$$

where for generator operation, $i_{\mathrm{f}}^{d,\star} = -\frac{\hat{u}_{\mathrm{g}}}{2R_{\mathrm{g},\Sigma}}\left(1 - \sqrt{(1 - \frac{4R_{\mathrm{g},\Sigma}d^{\star}}{\hat{u}_{\mathrm{g}}^2}}\right)$, $d^{\star} = \frac{2}{3}P_{\mathrm{m}}^{*}$ and $u_{\mathrm{dc}}^{\star} = u_{\mathrm{dc},ref}$.

Note that, depending on the equilibrium, $i_{\mathrm{f}}^{d,\star}$ might be positive, negative or zero. Hence, the time constant $T_{\mathrm{s,dc}}$ might change sign and, for $i_{\mathrm{f}}^{d,\star} < 0$, is negative which gives a non-minimum phase transfer function (the zero is in the left complex half-plane!). The stability analysis for PI controller design is omitted for space reasons, but can be found in [38, 40]. Through the Hurwitz criterion the boundary conditions of the PI controller parameters $V_{\mathrm{r,dc}}$ (gain) and $T_{\mathrm{n,dc}}$ (time constant) which ensure system stability, can be derived and are given by [38, 40]

$$0 < V_{\mathrm{r,dc}} < \frac{1}{|T_{\mathrm{n,dc}}|V_{\mathrm{s},dc}}, \tag{3.103}$$

$$T_{\mathrm{n,dc}} > \frac{T_{eq}}{1 - |T_{\mathrm{s},dc}|V_{\mathrm{s},dc}V_{\mathrm{r,dc}}} + |T_{\mathrm{s},dc}| > 0. \tag{3.104}$$

The final controller parameters can now be easily tuned for stability and the desired response e.g (3.105). Depending on the availability of bus voltage, the DC bus controller bandwidth can be decreased to reduce the grid current THD from power injection pulses. This will cause larger DC bus voltage overshoot and decrease the harmonics on the DC bus. Higher controller bandwidth will lead to greater current distortion on the grid side, but tighter DC voltage tolerance, increased DC harmonics and faster response times.

$$\left.\begin{aligned} \textbf{Gain: } V_{\mathrm{r,dc}} &= \frac{0.1}{|T_{\mathrm{s},dc}|V_{\mathrm{s},dc}}, \\ \textbf{Time Constant: } T_{\mathrm{n,dc}} &= \frac{5T_{eq}}{1-|T_{\mathrm{s},dc}|V_{\mathrm{s},dc}} + |T_{\mathrm{s},dc}|. \end{aligned}\right\} \tag{3.105}$$

3.4.4.2 Cascaded DC Bus Power Control

Cascaded active and reactive power control of the DC link voltage is common practice in the literature [24, 120]. The basic control structure requires an outer DC voltage loop which is focused on regulation and stability and an inner grid current loop which is focused on response settling times. With the inner loop being sufficiently faster than the outer loop, they can be considered decoupled. It is mentioned in [24] that in specific scenarios such as under startup or unbalanced conditions the control loops become coupled and interact and the performance of the controller cannot be guaranteed.

With the assumption that the PLL has perfectly aligned the d-axis with the grid voltage, the q-axis voltage component becomes zero, $u_{\mathrm{g}}^{q} = 0$. The active and reactive power are thus reduced to (3.106), which is used to derive the reference currents, (3.107) for power control. In fig. 3.33 the cascaded control structure is illustrated. For most applications such as WTS, the active and reactive power references are set to zero. This results in active power being transferred only when perturbations of the DC bus voltage are caused from injected DC current from the generator.

$$\left.\begin{aligned} P_{PCC} &= \frac{3}{2}u_{\mathrm{g}}^{d}i_{\mathrm{g}}^{d}, \\ Q_{PCC} &= -\frac{3}{2}u_{\mathrm{g}}^{d}i_{\mathrm{g}}^{q}. \end{aligned}\right\} \tag{3.106}$$

$$\left.\begin{aligned} i_{\mathrm{g,ref}}^{d} &= \frac{2P_{ref}}{3\hat{u}_{\mathrm{g}}}, \\ i_{\mathrm{g,ref}}^{q} &= -\frac{2Q_{ref}}{3\hat{u}_{\mathrm{g}}}. \end{aligned}\right\} \tag{3.107}$$

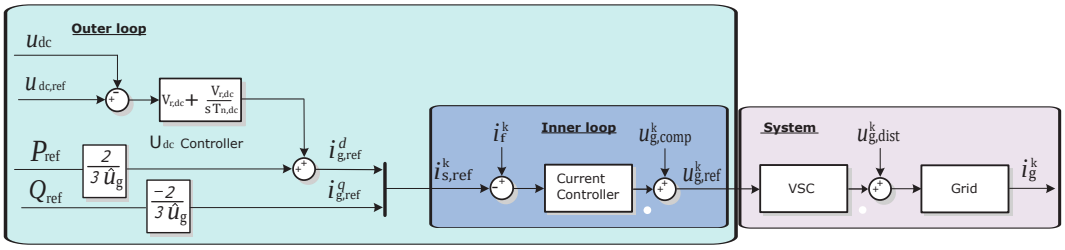

Figure 3.33: Cascaded DC bus active and reactive power control structure.

3.4.4.3 DC Bus Control Over a DC-Link Transmission Cable

In WTS systems it may benefit the layout to have the back-to-back VSC split in a similar fashion to that in a DC distributed power system. Placing the generator VSC in the nacelle and the grid connected VSC on the ground requires that the DC bus of each VSC be linked over considerable distance using a high voltage DC transmission cable, fig. 3.34. To analyse the behaviour of the DC-link cable the additional impedance dynamics are described by eqs. (3.108) to (3.110).

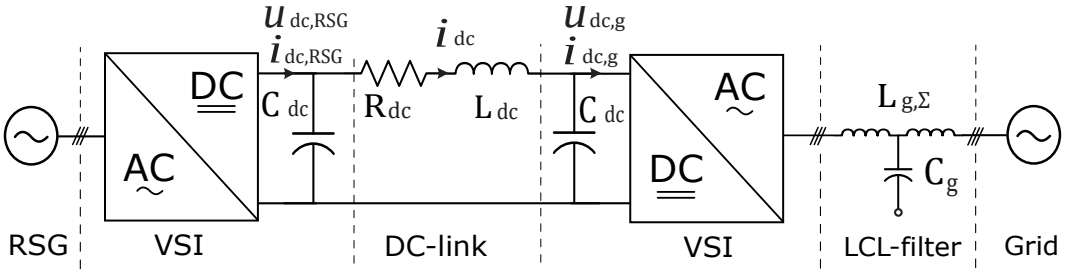

Figure 3.34: Back-to-to WTS system with a DC-link cable.

$$u_{dc,RSG} = u_{dc,g} + L_{dc}\frac{d}{dt}i_{dc} + R_{dc}i_{dc}, \tag{3.108}$$

$$\begin{aligned} i_{dc} &= i_{dc,RSG} - i_{c1}, \\ &= i_{dc,RSG} - \frac{d}{dt}u_{dc,RSG}, \end{aligned} \tag{3.109}$$

$$\begin{aligned} i_{dc,g} &= i_{dc} - i_{c2}, \\ &= i_{dc} - \frac{d}{dt}u_{dc,g}. \end{aligned} \tag{3.110}$$

In order to simplify the above equations, the voltage term, $u_{dc,RSG}$, is treated as an external disturbance and removed from the equation to acquire the transfer function (3.111). This process can also be followed for $u_{dc,g}$ which results in a similar but stable transfer function (3.112). Looking more closely at the DC-link circuit reveals that the cable dynamics can be viewed as a common LC-filter with transfer function (3.113), if the RSG side "de-coupling capacitor" capacitor is neglected. The large RSM side capacitor acts as a high frequency sink to reduce ripple from the VSC side and further stabilises and attenuates the systems dynamic response. Neglecting this capacitor is therefore a plausible assumption which is necessary to simplify the system so that the input output voltage dynamics can be analysed analytically. This can be applied to either side depending on the direction of the power flow.

$$\frac{i_{dc}(s)}{u_{dc,RSG}(s)} = \frac{1}{sL_{dc} + R_{dc}}, \tag{3.111}$$

$$\frac{i_{dc}(s)}{u_{dc,g}(s)} = \frac{-1}{sL_{dc} + R_{dc}}, \tag{3.112}$$

$$\frac{u_{dc,g}(s)}{u_{dc,RSG}(s)} = \frac{\frac{1}{L_{dc}C_{dc}}}{s^2 + s\frac{R_{dc}}{L_{dc}} + \frac{1}{L_{dc}C_{dc}}}. \tag{3.113}$$

From eqs. (3.111) to (3.113) it is apparent that the impedance of a cable is dominated by its large "damping resistance" which makes the dynamics very stable, as can be seen in the bode plots of fig. 3.35.

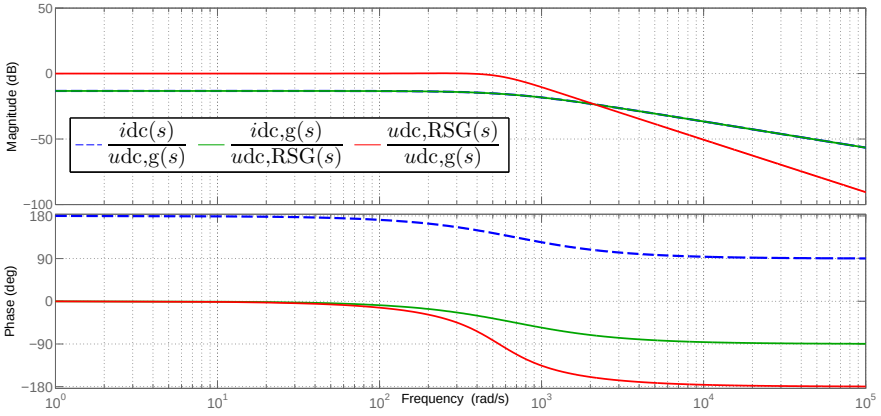

Figure 3.35: A bode plot of the various input-output transfer functions for a 150 m DC-link cable.

The cable's resistance imposes a limit on the power than can be transmitted through the DC cable because the voltage at the generator VSC DC bus is not controlled and will rise or fall in accordance with the power transferred through the cable due to the voltage drop over the cable resistance. This power limit is a function of the cable resistance, DC bus voltage reference and the maximum hardware DC bus voltage limit at the generator VSC, see (3.114). The power limit is further imposed by South African Electrical Standards, SANS 10142-1:2003, which require the voltage drop for single-phase circuits to not be below 5% of the cable terminal voltage (30 V 600 V DC). E.g A DC bus reference voltage and voltage limit of 600 V DC and 750 V DC respectively and a twin 150 m single core DC-link cable, which has an impedance of 4.62 Ω & 6.7 mH, can transfer a maximum of 8.11 A DC @ 600 V DC, according to (3.114), however according to SANS, a maximum

current of 6.51 A DC @ 600 V DC can be safely transferred.

$$u_{\mathrm{dc,drop,max}} = u_{\mathrm{dc,max}} - u_{\mathrm{dc},ref},$$
$$P_{\max}(u_{\mathrm{dc},ref}, u_{\mathrm{dc,max}}, R_{cable}) = \frac{(u_{\mathrm{dc,max}} - u_{\mathrm{dc},ref})^2}{R_{cable}}. \tag{3.114}$$

Chapter 4

Simulation and Measured Results

In this chapter the various results from practical and simulated experiments of the theory discussed in chapters 2 and 3 are presented. The chapter begins by presenting the measured results of the FEM designed 3 kW RSM followed by a comparison of its FEM model with measured results, with special focus on the flux-mapping, which is used for all current and torque controllers. These maps are compared to actual measured maps for two separate machines, a 3 kW and 9.6 kW RSMs. The RSM current controllers are then discussed and comparisons are made between simulation and measured results. Both RSMs are tested in this section and the results are discussed. Torque control using an MTPA algorithm is investigated by comparing measured results of torque responses for FEM based MTPA curves and measured flux-based MTPA curves. Simulations of the MTPA torque response are also presented and compared to measured results for both RSM's. Hybrid PSC and its various components are then presented, starting with the non-linear FS-PSC. LC-filter control is investigated and comparisons are made between simulated and measured results. Grid connection and power control using a back-to-back VSC is then analysed by comparing measured results for grid PLL tracking, current control, LCL-filter performance and DC bus control with and without the DC-link. Finally the measured and simulated results of the WTE and WTC are presented.

4.1 RSM Performance

The performance of the 3 kW RSM/RSG deviated from the original design quite substantially, as shown in fig. 4.1. The largest discrepancy was found in the maximum-torque-current-angle. In motor mode the performance was substantially lower with a peak torque at 16.55 N m, current angle 51°, an output power of 3 kW, efficiency of 87.2 % and power factor of 0.71. In generator mode the RSM could only reach an output power of 2.3 kW with an efficiency of 77 % and power factor of 0.65 at a peak torque of 19.1 N m at a current angle of 57°. Since it was not possible to remove the RSM from the gearbox, the

damping torque for the gearbox was measured to compensate and correctly calculate the input and output torque for this test. In fig. B.13b in section 4.9 the damping torque for the gearbox when cold and hot from two hours of operation is illustrated, from which it can be seen that there is $\approx 3\,\mathrm{N\,m}$ of damping torque on the low side. The Norma signal analyser was used to take all electrical measurements for this test.

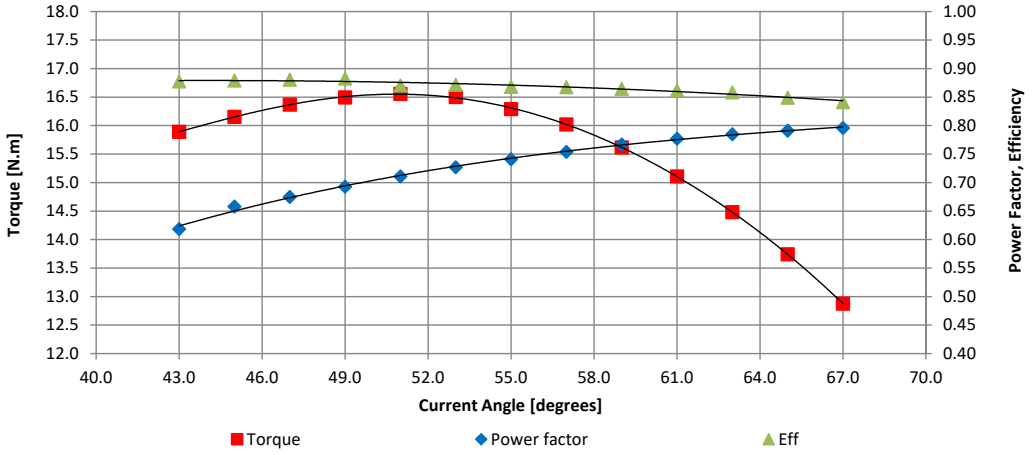

(a) 3 kW RSM performance in motor mode.

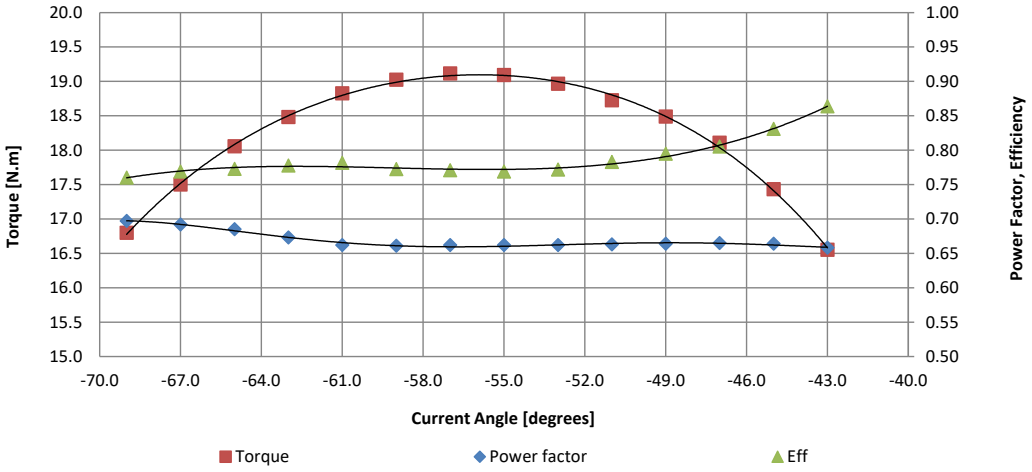

(b) 3 kW RSM performance in generator mode.

Figure 4.1: Performance of the 3 kW RSM in motor and generator mode. Power factor and efficiency.

4.2 Practical Validation of FEM Calculated Flux-linkage Mapping

For effective operation and control of an RSM using MTPA and adaptive gain techniques, the machine's dq flux-linkage maps are required. These maps can be generated using FEM packages such as the Stellenbosch SEMFEM package, Maxwell or JMAG. In this section the aim is to compare flux maps of a 9.6 kW RSM and a 3 kW RSM using SEMFEM and measured flux-linkage data. These two machines have very difference rotor and stator designs, which adds a robustness to these tests. Tests were also conducted on two separate test benches, the details of which can be found in appendix B.1 and appendix B.2.

A measured flux map is created by measuring the stator currents, voltages and the machine speed for a number of points in every quadrant. The flux-linkage at each discrete measurement point is calculated using (4.1). In this experiment the stator current was increased and decreased in steps lasting 5 seconds each. Since the flux-linkage of the RSM is highly non-linear at lower currents, in both ψ_s^d and ψ_s^q, higher resolution current steps were provided for the lower current regions. It is important that values are only sampled at steady state i.e not during the transients for each current step, the data is then manipulated to extract the steady state values of each 5 second interval. This leads to several hundred values per current set-point of which the mean is taken. The size of the resultant flux matrix is dependent on the peak operating parameters at which the machine was tested. For the 9.6 kW RSM a 40 x 40 matrix up to 200% rated load was produced. For the 3 kW RSM it was only possible, due to equipment limitations, to produce a 25 x 25 matrix up to 130% rated load. To avoid any potential stator and rotor operating temperature discrepancies, all measurements were conducted while the machine was at a stable temperature of 45° +- 5° degrees throughout the tests. Stator resistances were also measured, at this steady-state operating temperature, for the 9.6 kW and 3 kW RSM and found to be 4.9 Ω and 2.1 Ω respectively .

$$\left.\begin{aligned} \psi_s^d(\boldsymbol{i}_s^k(t)) &= \frac{R_s i_s^q}{\omega_k} - \frac{u_s^q}{\omega_k}, \\ \psi_s^q(\boldsymbol{i}_s^k(t)) &= -\frac{R_s i_s^d}{\omega_k} + \frac{u_s^d}{\omega_k}. \end{aligned}\right\} \tag{4.1}$$

The rate term, $\frac{d}{dt}\boldsymbol{\psi}_s^k$, seen in equation (2.22) can be removed because measurements are only taken in steady state. Several maps were taken at different speeds, with only a slight change in flux map amplitude and shape was observed.

From figs. 4.2 and 4.3 the error between FEM and measured maps can be seen, where comparisons are made by superposing the measured maps (solid/opaque) on the FEM maps (transparent). Figures 4.2a, 4.2c and 4.2e present an isometric view, an orthogonal view and the difference between the measured and FEM based d-axis flux (ψ_s^d – mea-

sured ψ_s^d). The same is repeated for the q-axis and both machines.

The error in the flux mapping is attributed to several assumptions that are made during the SEMFEM modelling. The static SEMFEM models did not accurately account for or include some stator and rotor phenomena such as heavy saturation effects, magnetic hysteresis, end-winding inductance and core losses. The stator and rotor steel also cannot be perfectly modelled. The B-H curve of the steel used in the rotor and stator is typically, as in this case, interpolated by SEMFEM and does not match the real material B-H curve perfectly. Often manufacturers will provide a conservative B-H curve for their materials and this leads to FEM estimation errors.

This is highlighted in fig. 4.3 where a larger error is present and can be attributed to the the lack of knowledge regarding the stator lamination material. It is also possible that the stator and rotor are constructed from different materials which can also influence the flux in its own unique way. A very conservative EN400 steel, which saturates at a much lower current magnitude, was used to model the stator. This grossly affects the current angle at which the machine will reach peak torque. It will be shown in subsequent sections that the deviations in flux also affect the MTPA angles and torque response, but do not affect the current controllers significantly. Measured flux maps were used throughout this project for the remainder of the practical tests unless otherwise stated.

The 3 kW RSM was designed to reach peak torque at 60°, however it is shown in section 4.4 that peak torque is reached at much lower current angles and this is due to the higher saturation properties of the actual rotor and stator. The optimisation of the rotor is also affected by this, leading to over compensated rotor air gaps. The performance of the machine can be further decreased if two separate materials are used for the rotor and the stator [121]. It will be shown in the following sections that despite the error shown between measured and SEMFEM calculated flux-linkage maps for the 9.6 kW, the current and torque controllers can operate the RSM effectively because the deviations are so small ($\leq$ 5% on the q-axis and $\leq$ 10% on the d-axis,fig. 4.2f). The error presented in figs. 4.2e, 4.2f, 4.3e and 4.3f could not be displayed as percentages due to scaling issues. However, as can be seen in fig. 4.3, the 3 kW RSM has much larger deviations and subsequently degrades the open loop torque control. The deviations are particularity noticeable on the q-axis (figs. 4.3a, 4.3c and 4.3e) due to the heavy saturation of the small lamination segments. The 9.6 kW RSM has much larger q-axis flux segments, which makes the modelling of saturation and flux-linkage within in these segments easier. Additionally the B-H magnetic saturation curves for 9.6 kW RSM designed by Prof. M. J. Kamper [122], were investigated very far into the saturation regions and thus could more accurately model heavier saturation. This is not the case with the 3 kW RSM, which has a limited B-H curve. Thus the 9.6 kW RSM displays lower error, $\approx$ 10%, at almost all loads (fig. 4.3f).

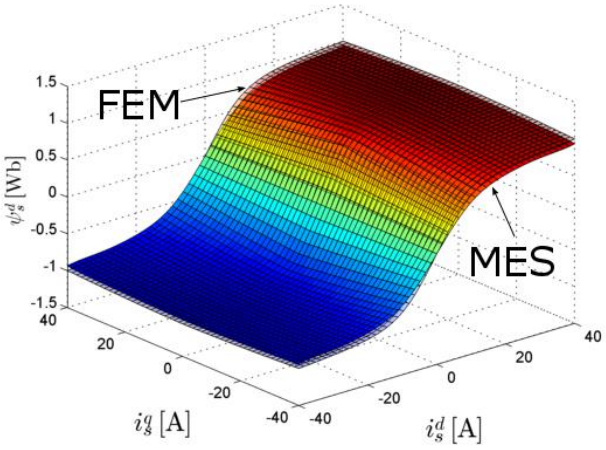

(a) FEM and measured d-axis flux maps

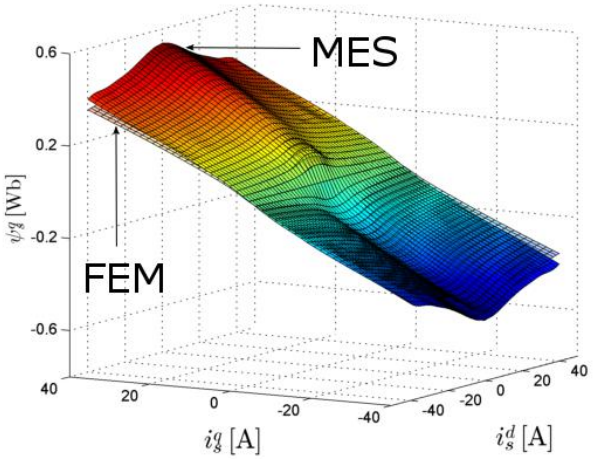

(b) FEM and measured q-axis flux maps

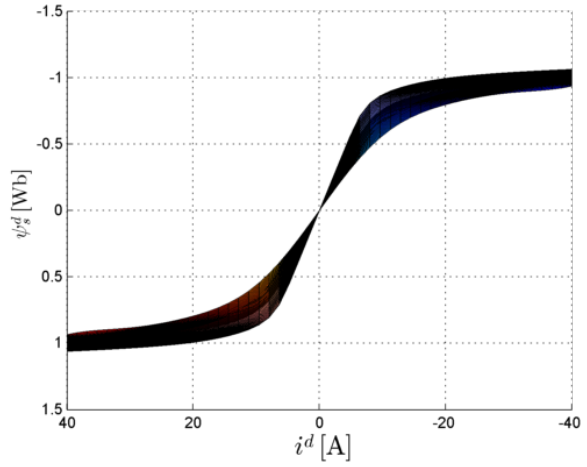

(c) d-axis view of ψ_s^d maps

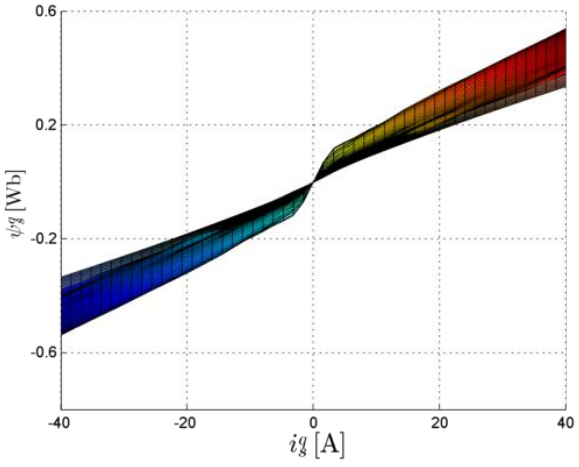

(d) q-axis view of ψ_s^q maps

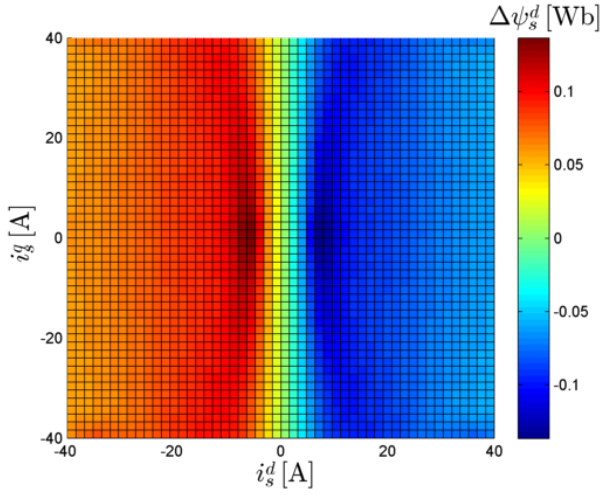

(e) $\Delta\psi_s^d$ = FEM - measured.

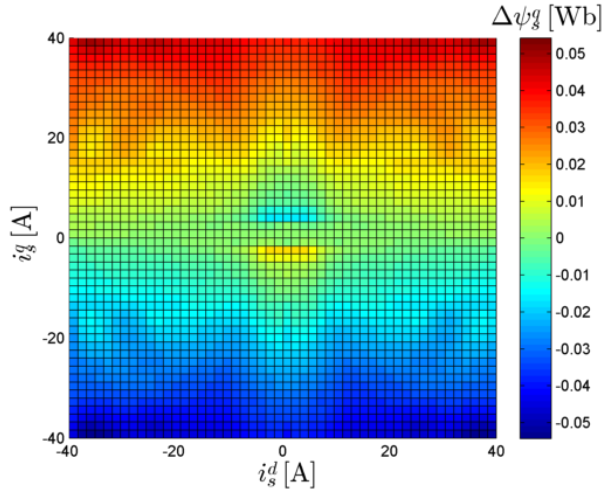

(f) $\Delta\psi_s^q$ = FEM - measured.

Figure 4.2: Comparison between FEM and measured $\boldsymbol{\psi}_s^k(\boldsymbol{i}_s^k(t))$ flux linkage maps for the 9.6 kW RSM. Transparent maps are FEM-based. Opaque maps are measured.

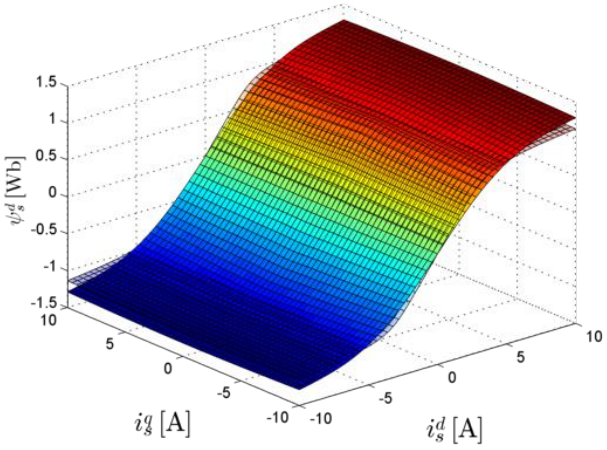

(a) FEM and measured d-axis flux maps

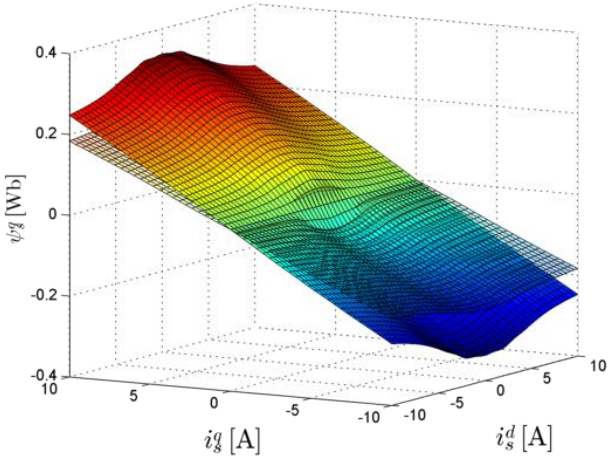

(b) FEM and measured q-axis flux maps

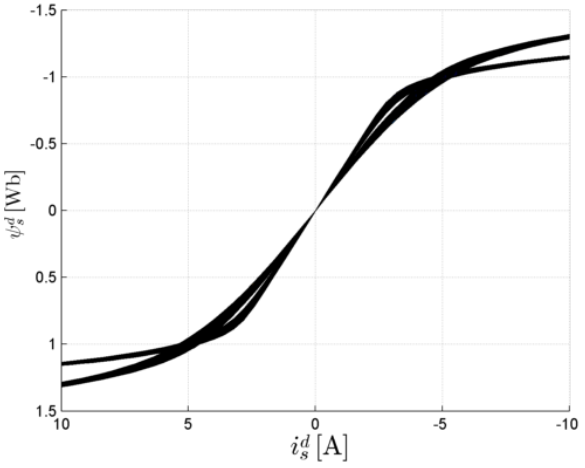

(c) d-axis view of ψ_s^d maps

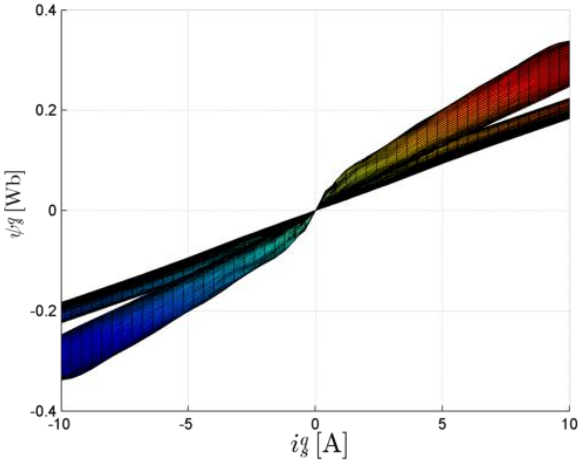

(d) q-axis view of ψ_s^q maps

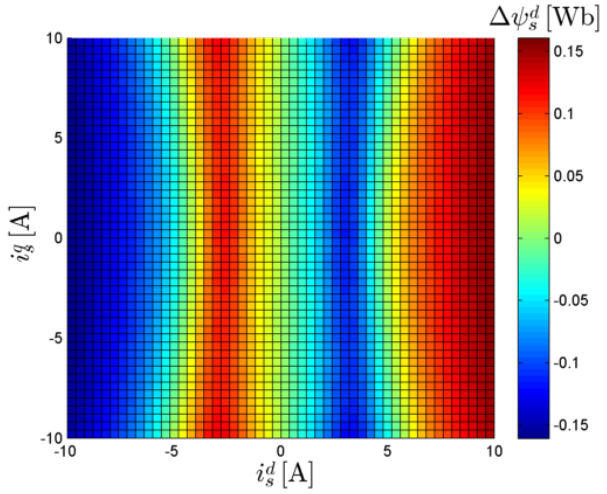

(e) $\Delta\psi_s^d$ = FEM - measured.

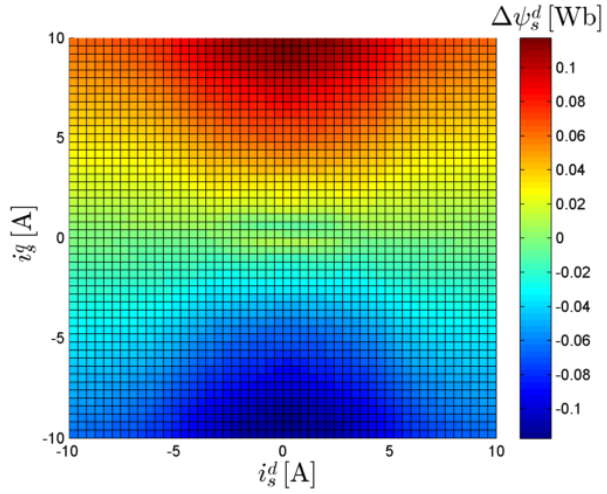

(f) $\Delta\psi_s^q$ = FEM - measured.

Figure 4.3: Comparison between FEM and measured $\boldsymbol{\psi}_s^k(\boldsymbol{i}_s^k(t))$ flux linkage maps for the 3 kW RSM. Transparent maps are FEM-based. Opaque maps are measured.

From these flux maps the various inductance maps can also be calculated, as shown in fig. 4.4. Deviations from the measured data will be present, but this does not significantly affect the adaptive gain current controller response.

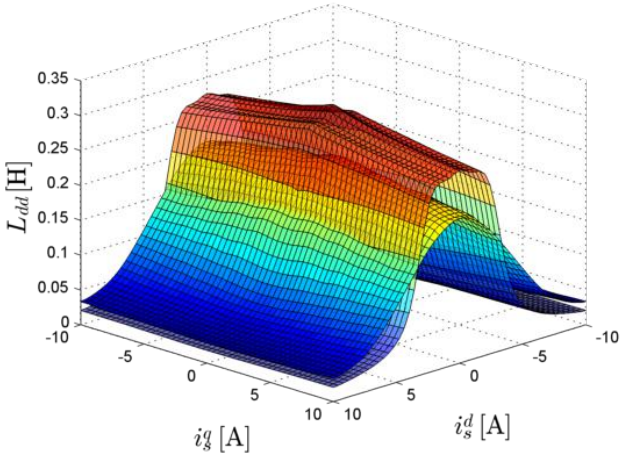

(a) 3 kW L_s^{dd} inductance.

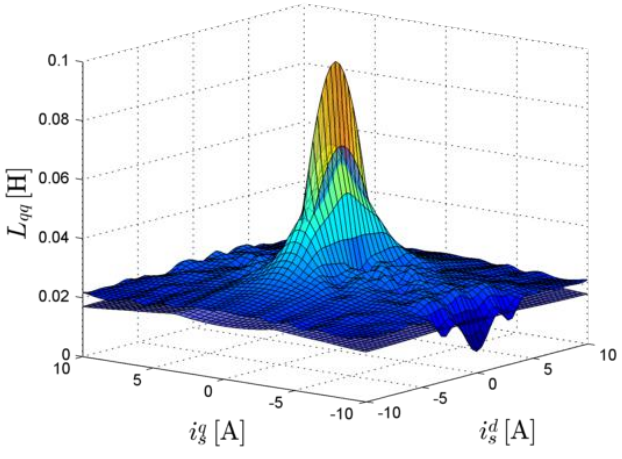

(b) 3 kW L_s^{qq} inductance.

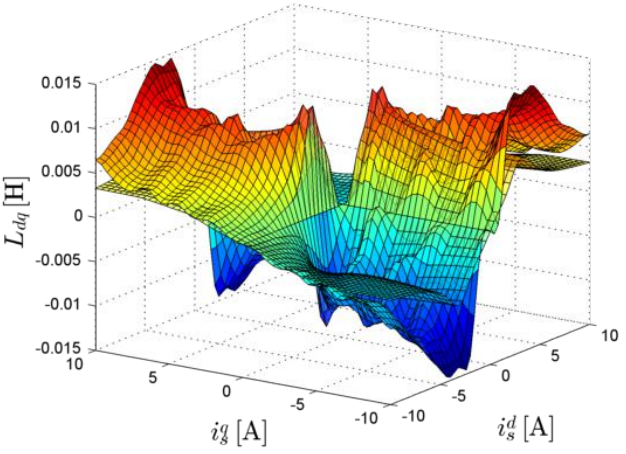

(c) 3 kW L_s^{dq} inductance.

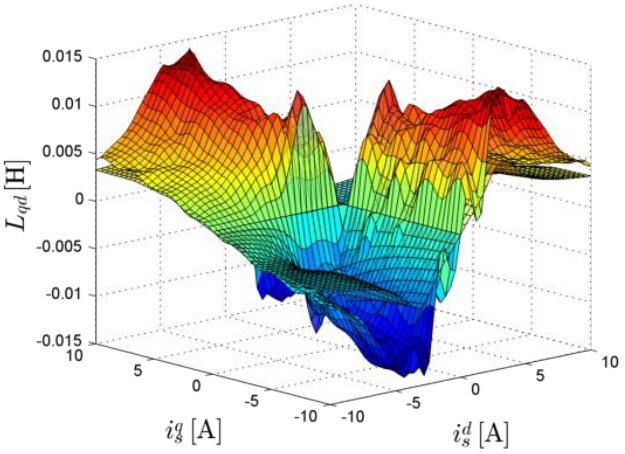

(d) 3 kW L_s^{qd} inductance.

Figure 4.4: Comparison between FEM and measured mutual and cross-coupling inductance maps for the 3 kW RSM. Transparent maps are FEM-based. Opaque maps are measured.

4.3 RSM Current Control

The performance of the on-line update Modulus Optimum current controller is demonstrated in this section. The controller was tested on a 9.6 kW RSM and a 3 kW RSM. The flux-linkage data generated by SEMFEM was used for calculating the controller gains in simulation and in practice. This was done to show the robustness of the current controller to deviations in the inductance and flux mapping. Testing equipment from appendix B.1 was used for the 9.6 kW RSM and equipment for the 3 kW RSM tests from appendix B.2. Only the simulated results for 9.6 kW RSM are shown here and are compared to the practical measurements. The 3 kW RSM practical results are shown at the end of this section. Table 4.1 contains all the parameters that were used for simulated and practical tests done on both machines.

The benefit of the simulated VSC detailed in appendix C.1.2 is that it introduces harmonics that are otherwise not present when using a PT_1 system. This is shown in fig. 4.5 below and indicates that the current controller is robust enough to deal with the additional harmonics.Figure 4.5 indicates a satisfactorily stable and sufficiently fast response at standstill. The current response at rated speed, in fig. 4.6, is shown to have a number of large, but rapidly decaying overshoots. These overshoots are common characteristics due to the high gains produced by the Modulus Optimum criterion and the feed-forward compensation voltages. They are more amplified in the $PT1$ system than in the simulated inverter (SI) system because there is no voltage limit, which would other wise be imposed by a DC bus or modulation index in the SI system. At higher speeds compensation terms $\boldsymbol{u}^k_{\mathrm{s},comp}$ have a greater influence over the controller outputs. With the SI the q-axis reference voltage, u^q_{s}, becomes noisy, due to the added switching harmonics. Coincidently u^q_{s} is also used to calculate $u^d_{\mathrm{s},comp}$ which leads to a noisy compensation voltage. The d-axis voltage is not as noisy and thus the q-axis compensation does not cause the same disturbance on the q-axis current. The offset in the d-axis current is actually only a transient and decays after 10 ms to the correct reference set-point. For improved response the transient offset can be solved by introducing a low-pass filter on the output of the d-axis compensation voltage. Figure 4.7 shows the response of the system with the compensation filter and various loads as in Figure 4.6 above. The overshoot can also be mitigated by using a less aggressive PI tuning technique.

Table 4.1: 3 kW & 9.6 kW RSM controller parameters.

3 kW RSG/RSM parameters	Simulation	Practical
Rated input/output power (electrical)	3 kW	2.4 kW
Rated torque @ rated speed	20 N m	19.6 N m
Rated speed	157 rad s^{-1}	"
R_s and n_p	2.1 Ω and 2	"
Phase voltage	230 V	"
9.6 kW RSG/RSM Parameters		
Rated input/output power (electrical)	9.6 kW	9.6 kW
Rated torque	60 N m	54 N m
Rated speed	157 rad s^{-1}	"
R_s and n_p	4.6 Ω and 2	"
Phase voltage	230 V	"
VSC parameters		
Switching frequency	10 kHz	"
Sampling frequency	continuous	10 kHz
DC Bus voltage	600 V	"
Controller gains and time constants		
Solver	Ode3 (Bogacki-Shampine)	N.A
Time step	50 µs	N.A
$V^k_{\mathrm{r,rsm}}(\boldsymbol{i}^k_s)$	$\frac{L^k_s(\boldsymbol{i}^k_s)}{T_{vsc}}$	$\frac{L^k_s(\boldsymbol{i}^k_s)}{T_{vsc}}$
$T^k_{\mathrm{n,rsm}}(\boldsymbol{i}^k_s)$	$T^k_s(\boldsymbol{i}^k_s)$	$T^k_s(\boldsymbol{i}^k_s)$

Practical measurements for the 9.6 kW RSM are shown in figs. 4.8 and 4.9 at standstill and rated respectively for half and rated load. From figs. 4.8 and 4.9 it is apparent that, although present, the offset in d-axis current is more pronounced in simulation than in reality. The lack of overshoot or reference offset means that adding the compensation voltage term does not provide much improvement to the controller's response and is thus not necessary in the control loop. As can be seen in fig. 4.8 the current response shows a satisfactory settling time of 5 ms at half and rated speed. This settling time is constant at all loads and rated or under-rated speed. Notice that in fig. 4.8b at rated speed the measured q-axis current response cannot achieve its rated set-point, due to the DC bus voltage limit (output voltage saturation of VSC). To achieve this fast response at rated speed the DC bus voltage needs to be above 600 V, which indicates a deviation from the rated operating point that was designed in FEM. In the case of generator mode or at low speed back EMF speed voltage is much smaller and therefore an RSG requires less DC bus voltage to operate. The generator mode current response is very similar to motor mode. The above data validates the current response and controllability of the on-

line update modulus optimum method using FEM calculated flux maps for the 9.6 kW.

Since the remaining tests for wind turbine control will be conducted on the 3 kW RSM, the current response of this machine is also demonstrated in fig. 4.10. During tests it was again established that the overshoot and offset error visible in simulations was not present in the 3 kW RSM current response and thus the addition of the LPF in the d-axis distortion compensation term was not necessary. A 600 V DC bus is used throughout these tests to allow the motor mode set-points to be reach at rated speed. There is minimal current ripple on both axes, minimal overshoot (more present on the q-axis) and very fast setting times of $\approx$ 10 ms, which is suitable to be used for the inner loop of the WTS. The 3 kW RSM also shows much less current ripple than the 9.6 kW RSM.

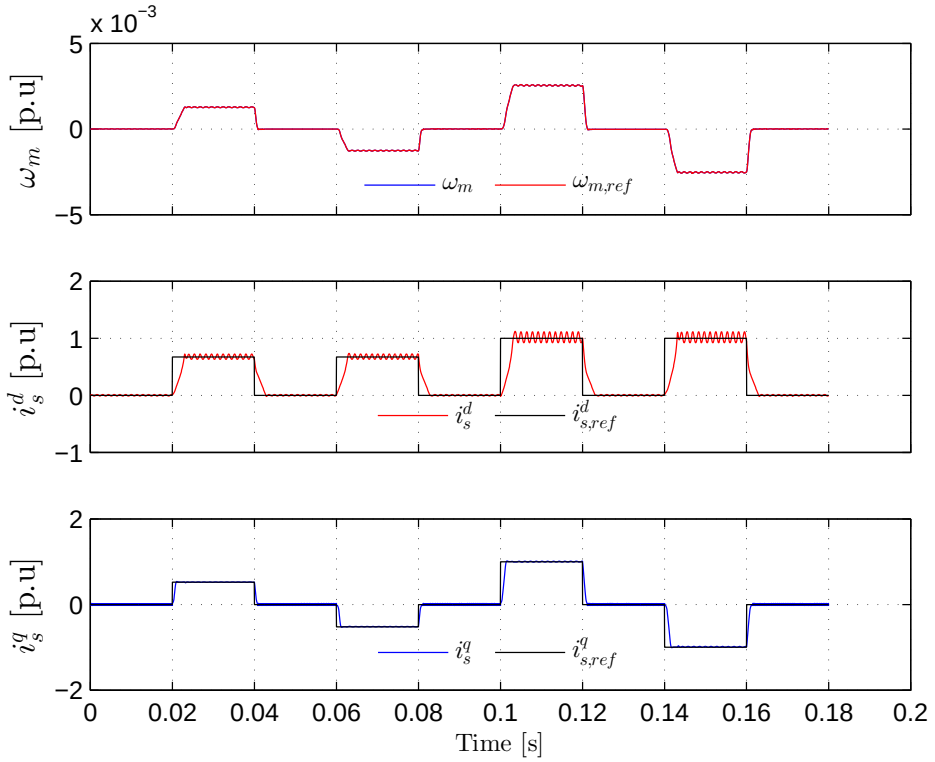

(a) PT_1 system

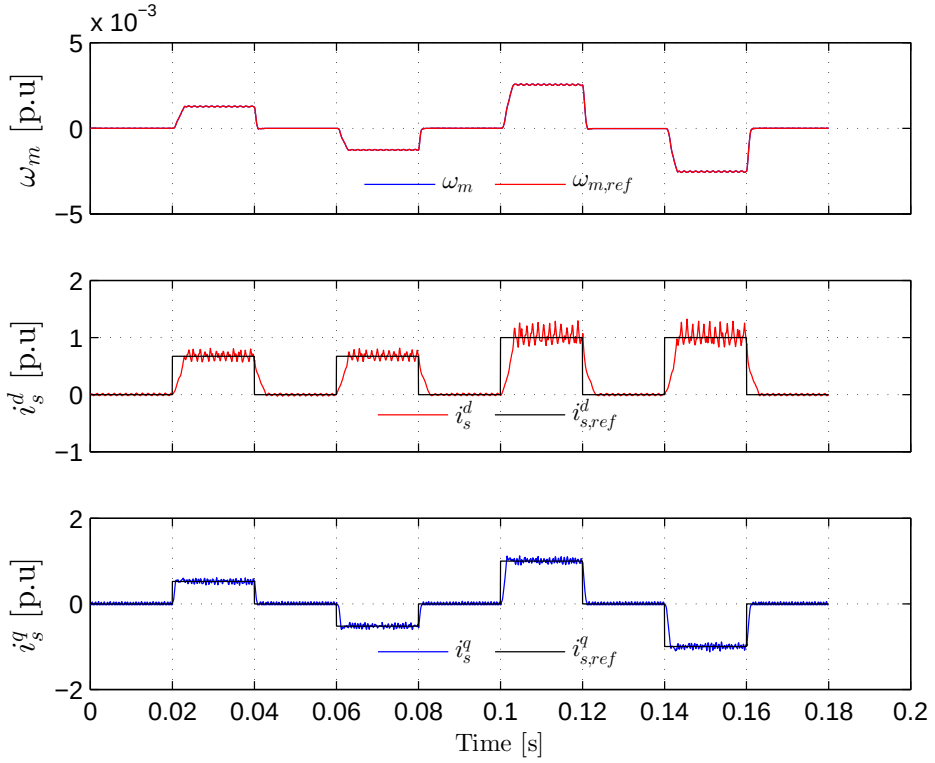

(b) Simulated VSC

Figure 4.5: Simulated response for the current controller using an SI with SVPWM and a PT_1 system at standstill.

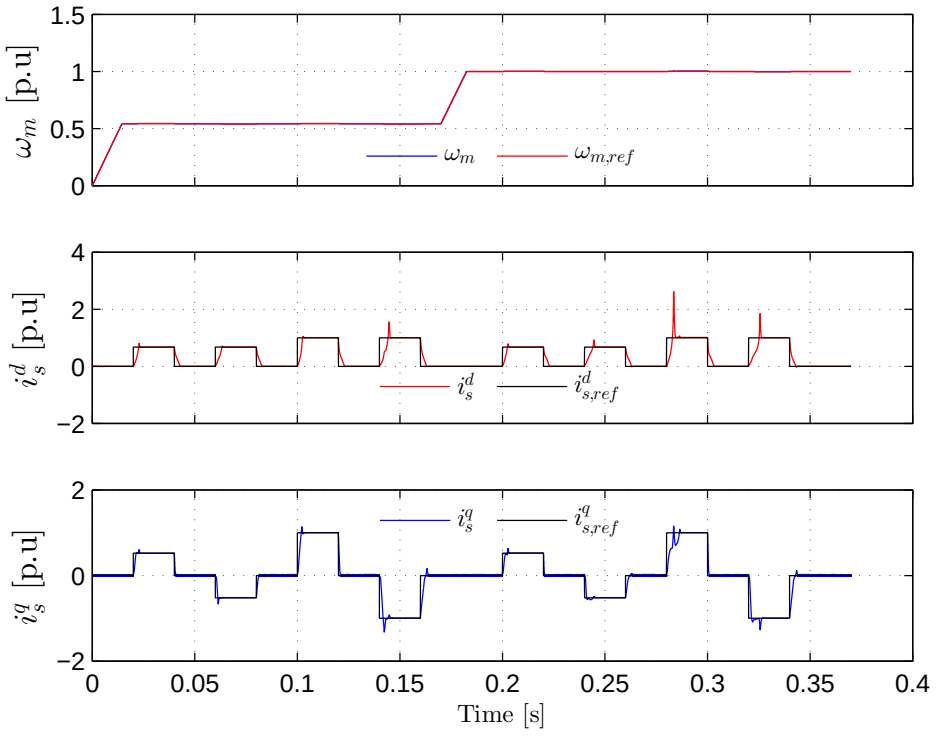

(a) PT_1 system

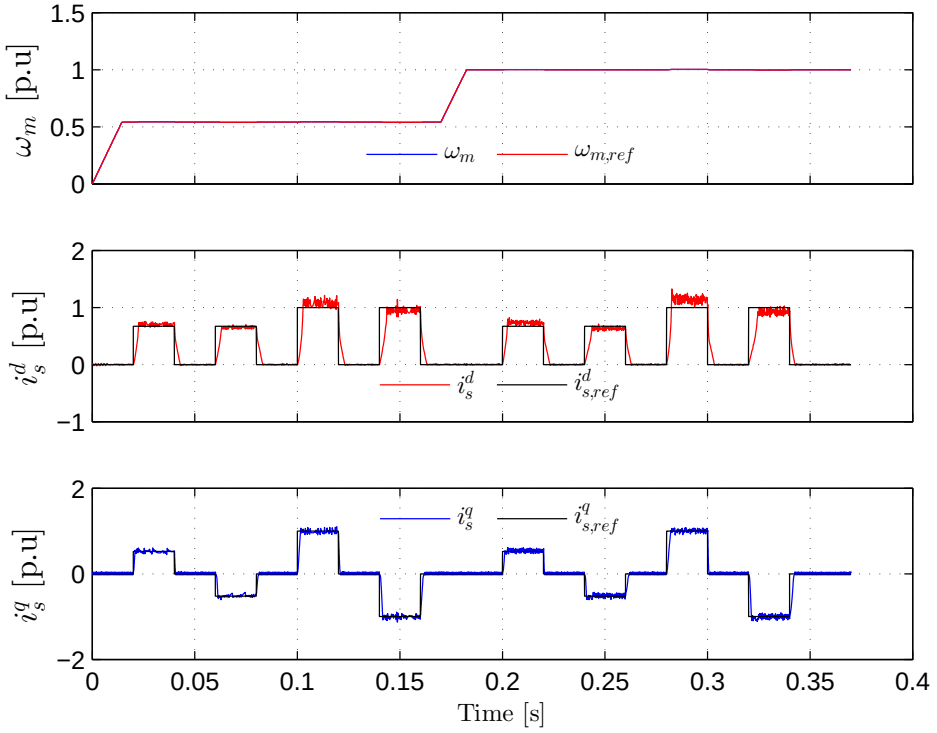

(b) Simulated VSI

Figure 4.6: Simulated response for the 9.6 kW RSM current controller using the SI with SVPWM and a the PT_1 system at rated speed and half rated speed.

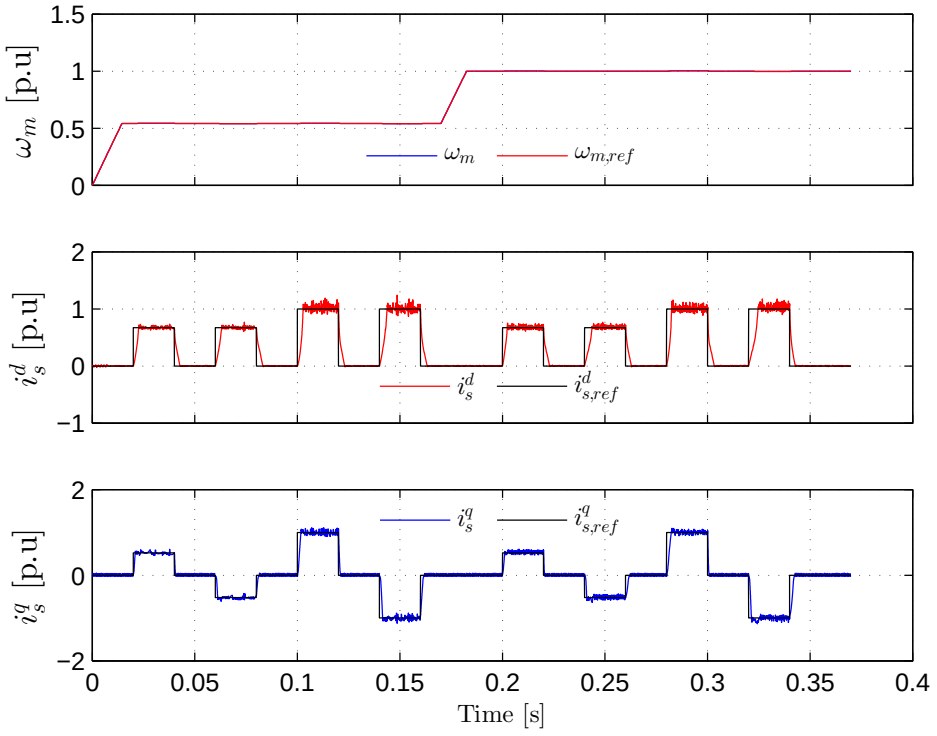

Figure 4.7: Simulated response for the 9.6kW RSM current controller with the compensation term $u_{s,comp}^d$ low-pass filtered, $F_{cutoff} = 500Hz$. The test is run at rated and half rated speed at various loads.

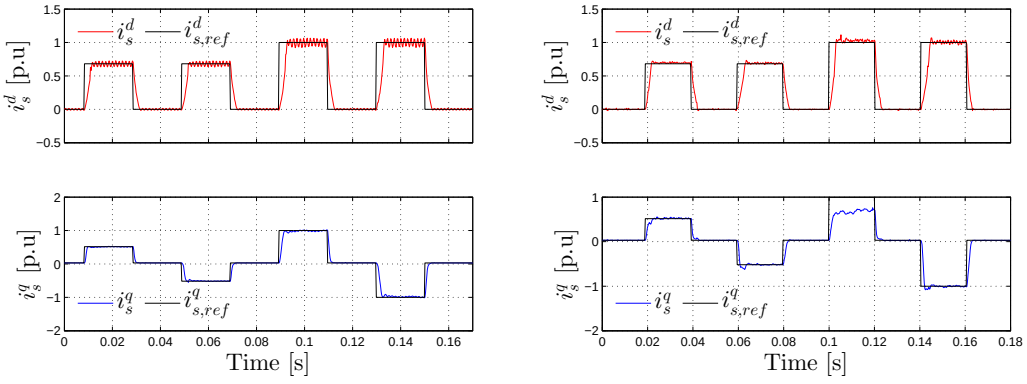

(a) $\omega_m = 0 rad/s$. (b) $\omega_m = 157 rad/s$.

Figure 4.8: Measured current response for the 9.6kW RSM without the compensation term $u_{s,comp}^d$ low-pass filtered. The test is run at rated and zero speed at various loads.

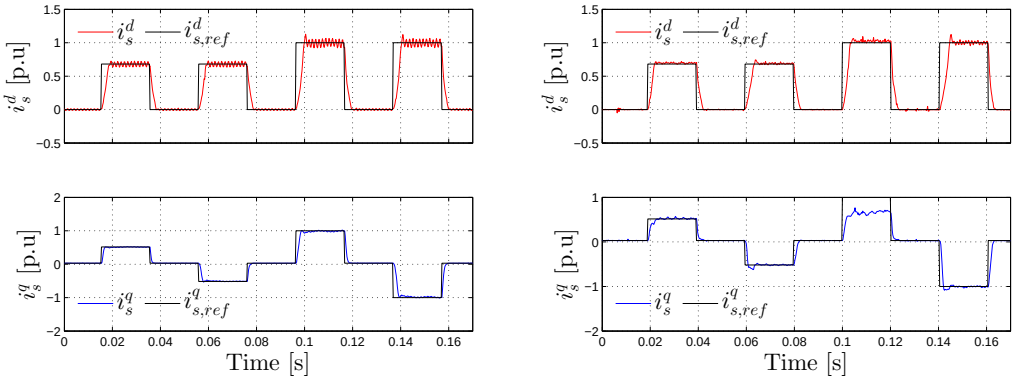

(a) $\omega_m = 0 rad/s$. (b) $\omega_m = 157 rad/s$.

Figure 4.9: Measured response for the 9.6 kW RSM current controller with the compensation term $u_{s,comp}^d$ low-pass filtered, $F_{cutoff} = 500 Hz$. The test is run at rated and zero speed at various loads.

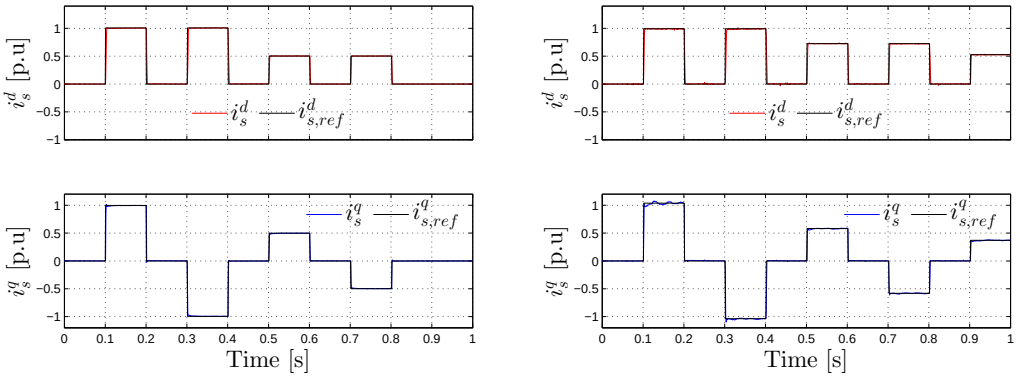

(a) $\omega_m = 0 rad/s$. (b) $\omega_m = 157 rad/s$.

Figure 4.10: Measured current response for the 3 kW RSM. The test is run at 0 % and 100 % rated speed at half and rated load in motor and generator mode

4.4 MTPA Validation and Torque Response

In this section the MTPA algorithm detailed in section 3.1.5 is validated through practical measurement. Using the equipment and testing apparatus in appendix B.1 and appendix B.2, the MTPA operating points calculated from the SEMFEM flux maps were compared to the MTPA operating points calculated from the measured torque and flux maps. The response of the measured and the SEMFEM MTPA data to torque set-points was also compared. Torque maps were taken at several speeds to identify core, winding and friction losses. In the case of both machines is was found that the torque maps are affected by core loss, which causes a slight reduction in torque but the 3 kW RSM was more affected. Therefore the flux and torque maps were measured at a machine speed of 105 rad/s, which was used as the standard for all further calculation and mapping.

In section 4.2 the deviation between measured and FEM calculated flux maps is demonstrated. It follows that the MTPA curves obtained using measured and FEM calculated flux maps also results in similar deviations, which then cause offsets in the steady state torque response. In fig. 4.11 the magnitude difference between actual measured torque, FEM calculated torque and torque calculated using measured flux data (TCMF) is compared, as well as the deviations in MTPA for the 9.6 kW RSM. The deviation between actual torque and FEM torque becomes larger with increased load. This is because static SEMFEM models do not accurately account for or include some stator/rotor properties and core loss, which are discussed in section 4.2. The same comparison for the 3 kW RSM is made in fig. 4.12. The 9.6 kW RSM demonstrated far less deviation between actual torque and TCMF due to the low error between the measured flux and FEM flux maps. The error is less than 5 % in the rated areas but increases at over rated loads. The VSC dead-time and deviations in the FEM material magnetic characteristics increases the measured flux, which causes a slightly higher torque to be calculated when compared to FEM. Damping friction is also a factor that reduces the actual motor torque and increases the deviation from TCMF in the motor region. TCMF map averaging could also play a role in this and is discussed at the end of this section.

Any error in flux data will manifest itself in an MTPA current angle error (figs. 4.11e, 4.11f, 4.12e and 4.12f), which further affects and causes a steady state offset in the torque response that increases with load. It can be seen from fig. 4.13a that the simulated MTPA torque controller response is satisfactory with very little ripple or steady-state offset. The MTPA algorithm performs very well with small offsets because the SEMFEM maps used to calculate the MTPA are the maps used to simulate the RSM without losses. Figures 4.13b, 4.13c, 4.14a and 4.14b show the steady state torque offset by plotting the torque response for two MTPA curves: one calculated from SEMFEM and the other measured flux-linkage data. This is done for both machines. Note that the results for the 3 kW RSM were affected by a faulty torque sensor in low positive (motor) torque regions,

fig. 4.12. The fault manifests as the large torque spikes seen in the measured torque map. This is not a representation of the actual torque in these small localised regions. The spikes can also not be filtered out. This was the only sensor available which could synchronise with the pentium system to obtain a torque map based on dq currents. The spikes therefore affect the MTPA algorithm and the "curv-fit" for motor mode (fig. 4.12e). However, generator operation of the torque sensor was satisfactory and thus a MTPA poly-curve could be fitted.

Figures 4.13 and 4.14 demonstrate that in reality both machines have a torque offset in motor mode due to core, end winding inductance and friction losses which are not taken into account in the SEMFEM mapping. Generator mode exhibits better performance with a set-point error within 5 %. This is because the losses are taken by the prime mover. The deviations increase with load because core losses increase with load. Motor mode and generator mode are improved with MTPA calculated from TCMF, but a small error still remains due to deviations in actual flux.

Larger discrepancies are more apparent in fig. 4.14 for the 3 kW RSM as expected, due to greater deviations present in the flux map and MTPA. Motor mode torque offsets in this case are compounded by the gear box efficiency which is not precisely known. According to manufacturers, the gearbox efficiency is approximately 95 % - 97 % at rated load when warm from operation. It was also observed that the damping factor and efficiency of the gearbox is considerable when cold and drops dramatically when warm (fig. B.13b). The 3 kW RSM was tested at a speed of 157 rad/s which corresponds to $\approx 0.4 Nm$ of frictional loss (seen at the high speed side) within in the gearbox when warm and $\approx 1 Nm$ Nm when cold. For motor mode the measured torque will be less than what is generated by the RSM by $\approx$ 3 %. In generator mode the measured torque will be greater than the torque produced by the RSG by $\approx$ 3 %. This is an almost insignificant error and thus the gearbox efficiency or damping torque was not included in the results.

Using MTPA curves generated from TCMF improved the 3 kW RSM performance in motor mode, but it decreased the performance in generator mode (fig. 4.14b) by causing overshoot, which is a similar result to that of fig. 4.13c for the 9.6 kW RSM. It is shown in figs. 4.11f and 4.12f that the actual MTPA curve in generator mode deviates significantly from that of motor mode for both FEM-based or TCMF-based MTPA. It would be rational to assume that measuring the actual flux-linkage of the machine would provide the correct torque and MTPA curves for both operating regions. However, because of the dead-time associated with the VSC, each point in the the flux map must be averaged over the four quadrants to correct for the dead-time flux-skewing effect. The averaging effectively smooths out the flux map so that the generator and the motor quadrants have the same flux-linkage data. This erases or attenuates the core losses, which would otherwise alter the generator mode flux-linkage and increase the torque, power factor and current

angle. The result is a map that represents the inner flux of the machine as is the case with FEM based flux-linkage. Since the aim during this project is only to provide a working torque control model for generator mode, an MTPA curve was generated from measured torque data to correct the offset, as shown in fig. 4.14c. This MTPA curve provided better open-loop generator torque response with an offset error of less than 6.5% at rated torque.

It is noted that the symmetrized data includes end-winding inductances, but core loss is cancelled out. Manipulating the FEM data account for end-winding inductances and core loss or measured data to account for core loss would probably correct the issue of the increased current angle in generator mode. The accuracy of the core loss and end-winding inductance models would then have to be tested and verified, which is beyond the scope of this project and was therefore not attempted.

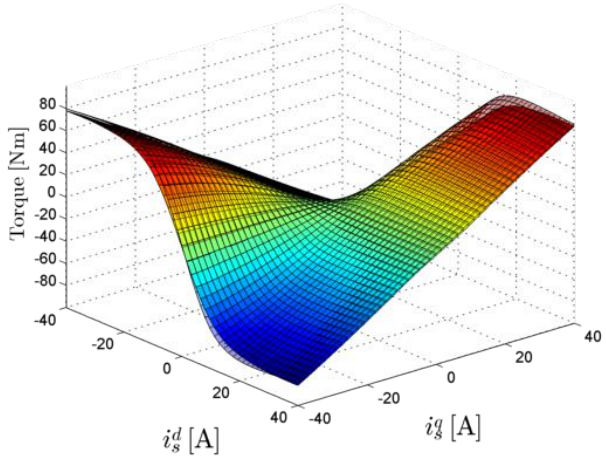

(a) T_{FEM} map (transparent) vs T_{mes} map (opaque).

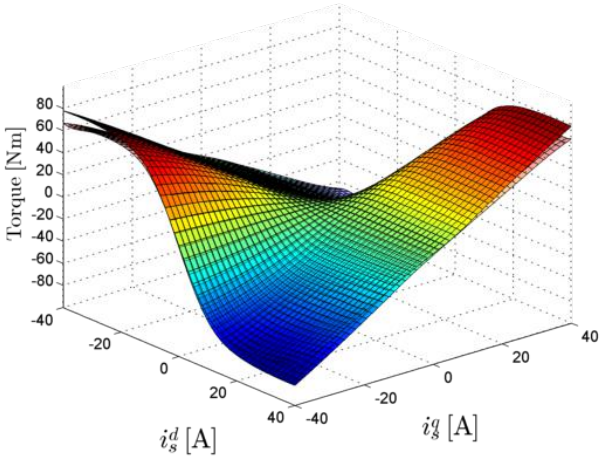

(b) T_{TCMF} map (transparent) vs T_{mes} map (opaque).

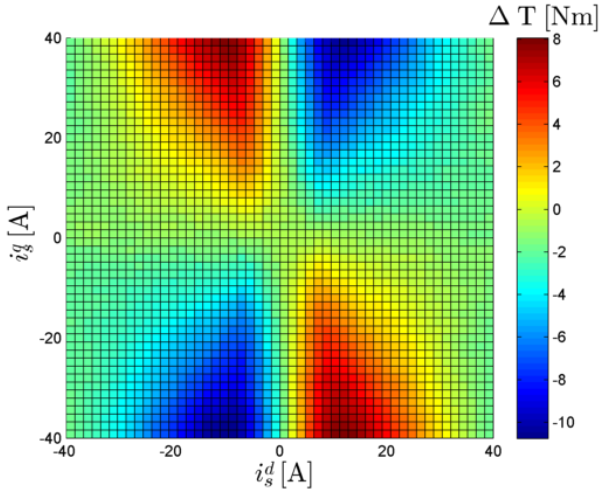

(c) $\Delta T = T_{mes}$ - T_{FEM}.

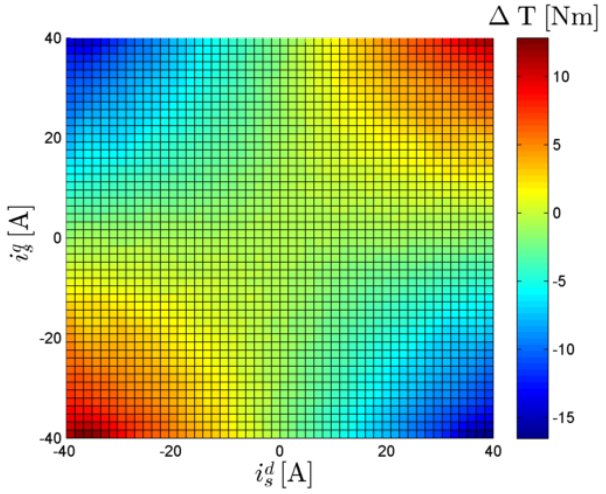

(d) $\Delta T = T_{mes}$ - T_{TCMF}.

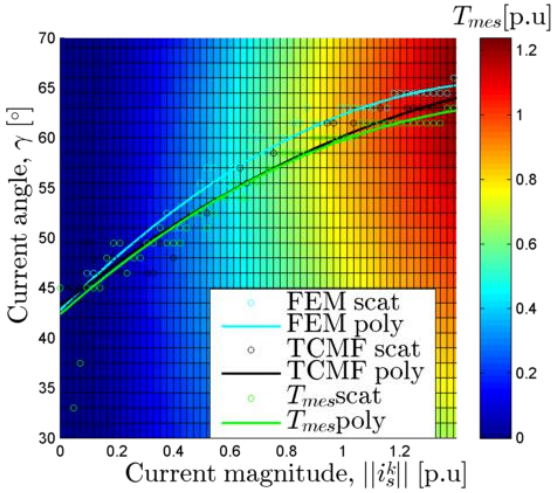

(e) Motor mode MTPA curve comparison.

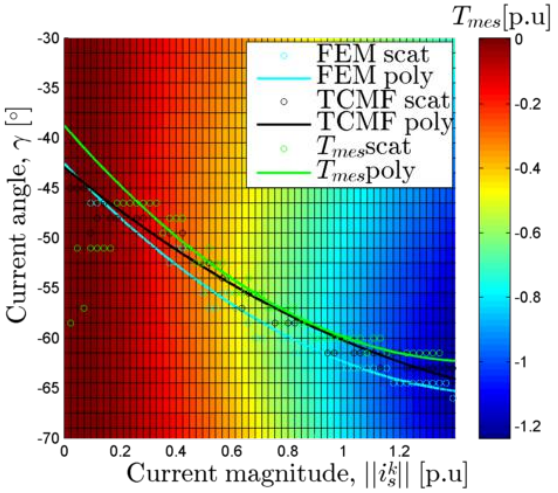

(f) Generator mode MTPA curve comparison.

Figure 4.11: Comparison of FEM-torque, TCMF-torque and measured torque. The respective MTPA curves are also provided. Tests were conducted on a 9.6 kWRSM.

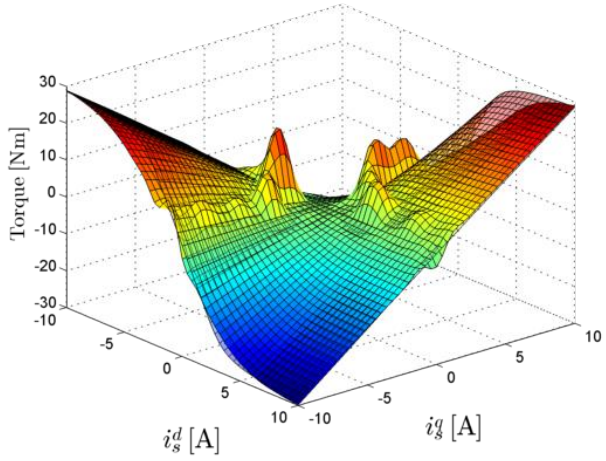

(a) T_{FEM} map (transparent) vs T_{mes} map (opaque).

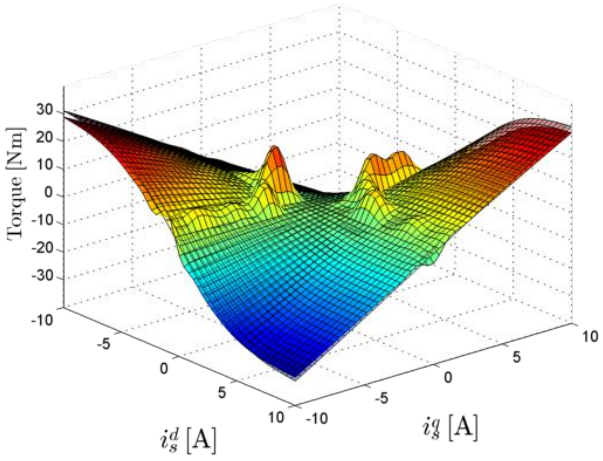

(b) T_{TCMF} map (transparent) vs T_{mes} map (opaque).

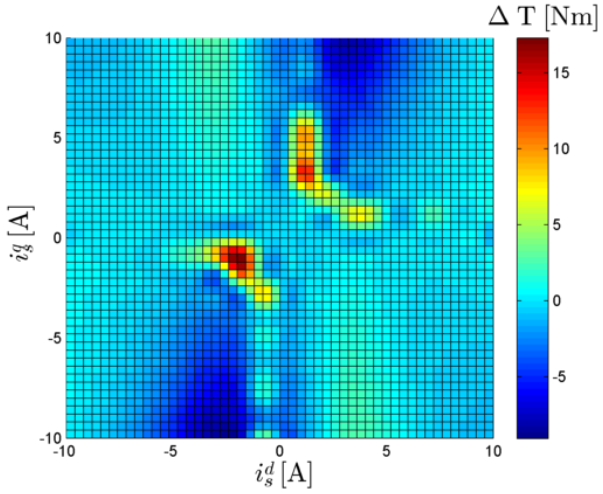

(c) $\Delta T = T_{mes}$ - T_{FEM}.

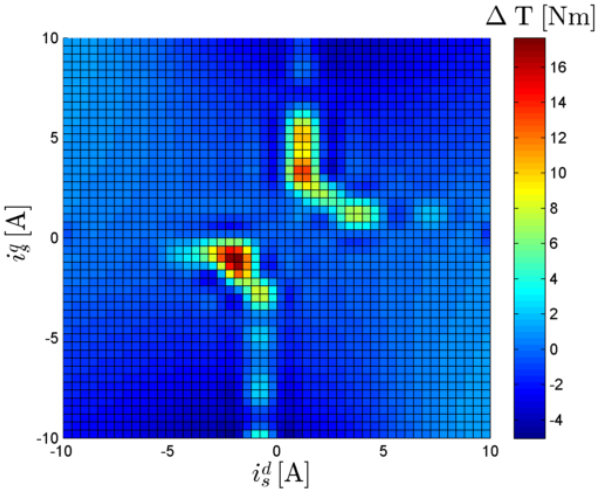

(d) $\Delta T = T_{mes}$ - T_{TCMF}.

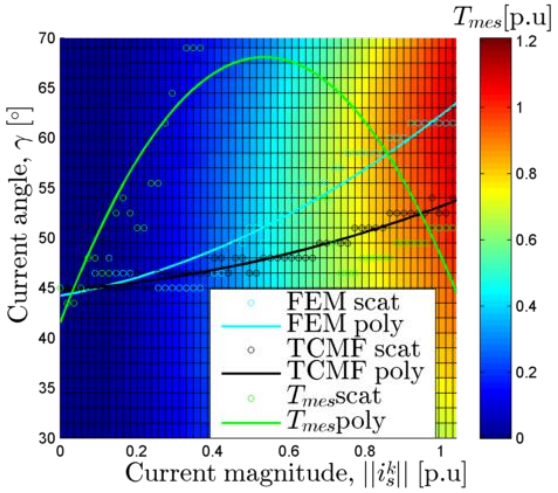

(e) Motor mode curve comparison.

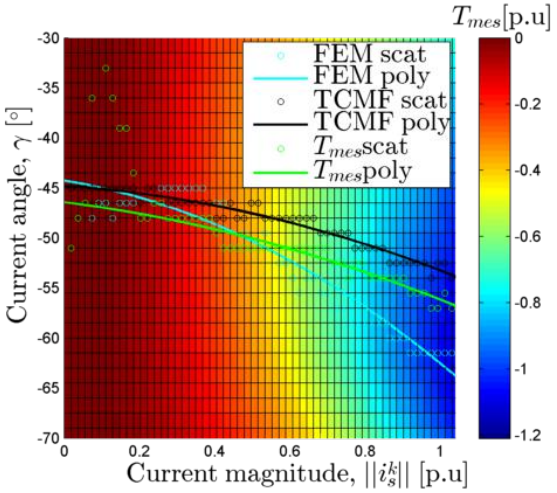

(f) Generator mode curve comparison.

Figure 4.12: Comparison of FEM-torque, TCMF-torque and measured torque. The respective MTPA curves are also provided. Tests were conducted on a 3 kW RSM.

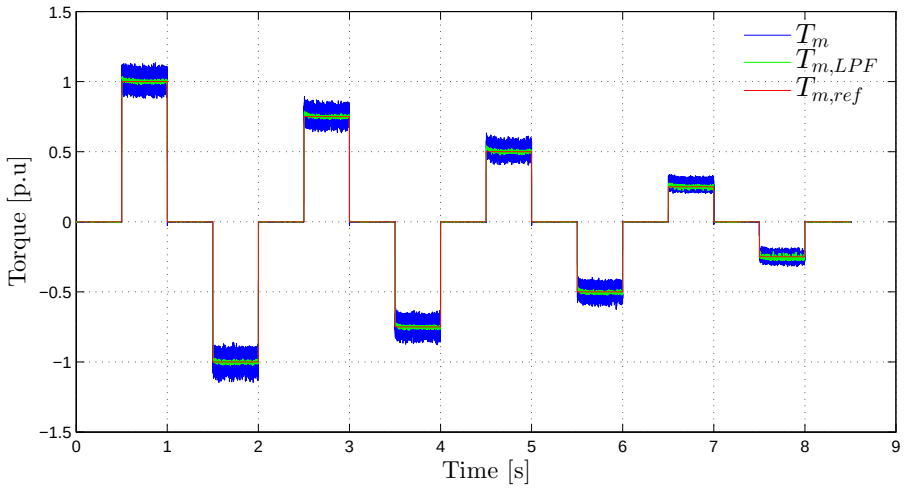

(a) Simulated torque response using FEM MTPA.

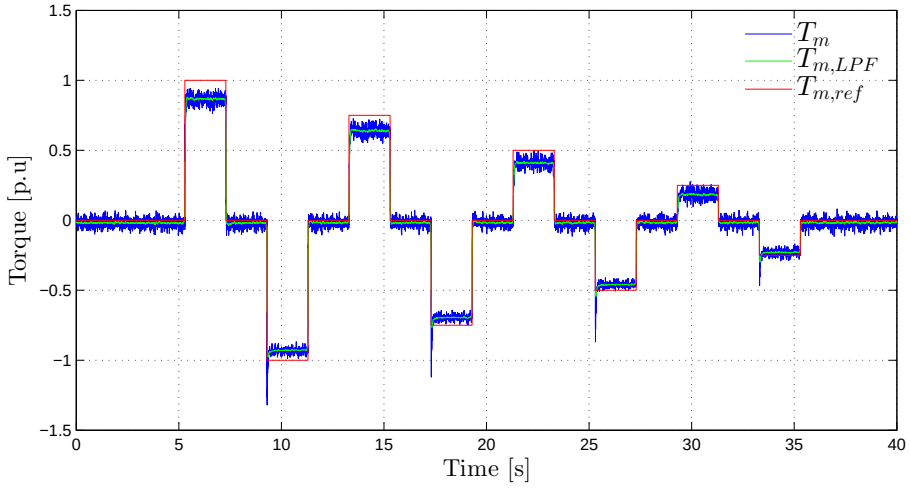

(b) Measured torque response using MTPA calculated from FEM flux data.

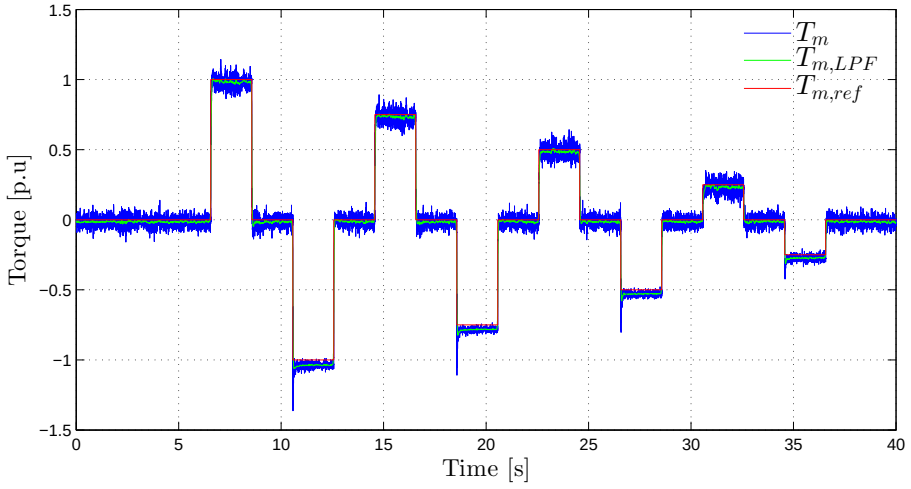

(c) Measured torque response using MTPA and TCMF data.

Figure 4.13: Measured torque response using MTPA curves calculated from FEM-torque and TCMF data. Tests conducted on a 9.6 kW RSM up to rated load. All values are in per unit.

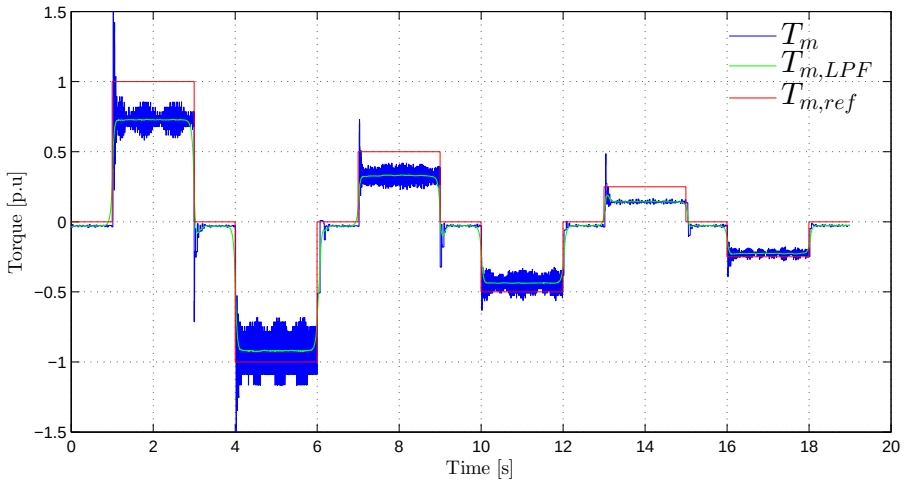

(a) Measured torque response for the 3 kW RSM MTPA calculated from FEM data.

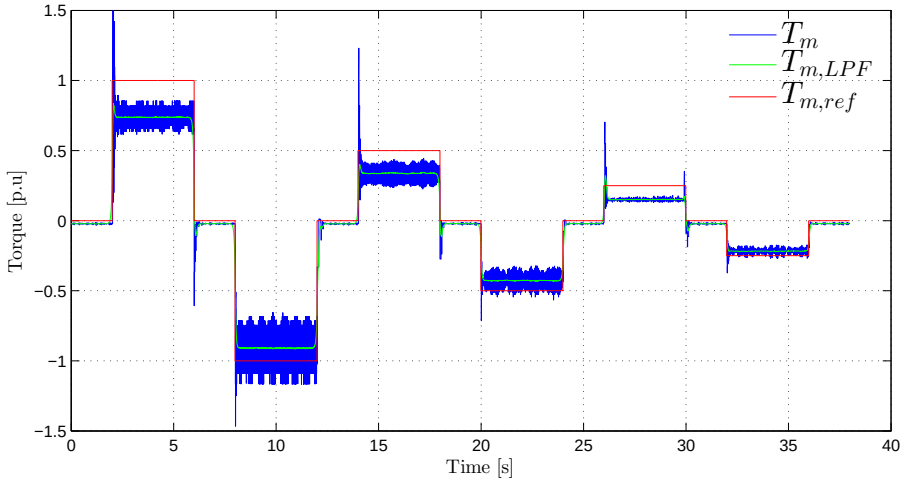

(b) Measured 3 kW RSM torque response using MTPA and TCMF data.

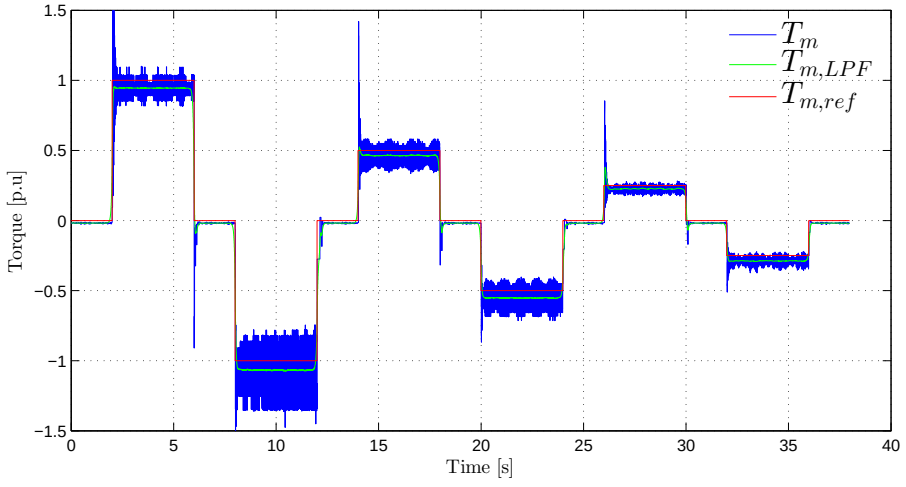

(c) Measured 3 kW RSM torque response using MTPA calculated from measured generator torque.

Figure 4.14: Measured torque response using MTPA curves calculated from FEM-torque, TCMF data and measured torque. Tests conducted on a 3 kW RSM up to rated load at rated speed.

4.5 Position Sensorless Control of the RSM

In the following section the practical and simulated results of the FS- and AHFI-PSC methods are presented. Simulations were conducted in Matlab and the practical tests were conducted on the set-up detailed in appendix B.2. Both practical and simulated tests are performed for motor and generator mode, but to limit scope and for space reasons only the relevant generator mode tests are presented here.

4.5.1 Fundamental Saliency

As discussed in section 3.2.1, the fundamental saliency method can only operate when the machine's saliency is visible. For the FS-PSC this requires a minimum rotor speed and saturation current. The saturation current appears as a small offset in torque for a zero torque reference in either the positive or negative direction (depending on mode). The FS method also suffers from a saliency shift under load where the magnetic axis will shift from the actual d-axis of the rotor. Table 4.2 contains the various parameters used in the simulated and measured tests.

Table 4.2: FS-PSC simulation and practical controller parameters.

RSM / RSG parameters	Simulation	Practical
Rated input / output power (electrical)	3 kW	2.4 kW
Rated torque @ rated speed	20 N m @ 157 rad s^{-1}	19.6 N m @ 157 rad s^{-1}
R_s and n_p	2.1 Ω and 2	"
VSC parameters		
Switching frequency	10 kHz	"
Sampling frequency	continuous	10 kHz
Saturation current	0.15 p.u @ 45°	0.19 p.u 45°
DC Bus voltage	700 V	600 V
Controller gains and time constants		
k_{drift}	15	30
$K_{p,FS,opt}$	107	125
$K_{i,FS,opt}$	1733	4621
Solver	Ode3 (Bogacki-Shampine)	N.A
Time step	50 µs	N.A

Simulated tests for the stability and performance of the FS-PSC method are presented in figs. 4.15 and 4.16. To test the dynamic response and steady state error for several operating conditions, ascending torque steps are applied to the RSG at three different speeds, the lowest possible rotor speed of 0.2 p.u, rated speed and twice rated speed. The current references are obtained using the measured torque MTPA curves generated

in section 4.4. A comparison between the torque response and estimation error for the FS method without saliency shift compensation (SSC) and with SSC is also investigated.

Without SSC the performance of the FS-method is still usable, but a visible offset in the torque response is present as shown in fig. 4.15a. The current references in the estimated dq-reference frame, $\widehat{k}$, will still be met, but if the deviation is large enough the steady state torque will be incorrect, because the current vector in $\widehat{k}$ is deviated by the saliency shift error, which misaligns the reference frame. The shift can be more clearly seen in the estimation error in fig. 4.15b under various operating conditions. At the lowest speed the FS-method can operate, a large estimation error is observed. This is the result of the deviation of the $\alpha\beta$ reference voltages from the actual $\alpha\beta$ voltages used to calculate $\boldsymbol{\psi}_{\mathrm{s}}^{s}$ and integration drift. At higher speeds the shift resembles the expected angle estimation error observed in simulation and literature.

The estimation error can be improved using SSC as shown in fig. 4.16. Even though the steady state torque response is not greatly changed by SSC, having the correct rotor angle allows the correct MTPA current references to be applied, which results in a small increase in efficiency and is also necessary for the correct application of other inner loop control subsystems such as dq-based LUTs and distortion voltage compensation. It must also be noted that at high speeds the FS-PSC with SSC causes saturation of the VSC output voltage as opposed to the tests with no SSC which does not cause the saturation. The reason for this is that the SSC increases the machine current angle by 5° to 20° depending on load, which requires more voltage.

To investigate the actual performance of FS-PSC on the 3 kW RSG, the same test procedures as in the simulated versions were conducted. The set-up detailed in appendix B.2 was used to collect the data. An encoder was used on the RSG to record the actual angle of the rotor, but was not used for any control purposes. To demonstrate the effects of the saliency shift a torque ramp is measured at rated speed with and without SSC, fig. 4.17. The correction of the shift is indeed solved, however at the saturation current reference (i.e no d-axis current) there remains a 6° offset even with SSC. This is an anomaly that is not present in the calculated FEM-based SSC map and indicates a reversal of the saliency shift angle and is likely due to core loss. The anomaly is easily corrected with an angle offset when $i_{\mathrm{s}}^{d} = 0$, as demonstrated in the following uncorrected and correct results, as shown in figs. 4.18 and 4.19 respectively.

Figure 4.18 shows the response of the real system to several torque steps without SSC upto 1.5 p.u speed. The estimation error is very similar to that in the simulated test with offsets present in the torque set-points due to the reference frame shift. Note that at 1.5 p.u speed voltage saturation becomes an issue because the DC bus voltage is set at 600 V, thus the maximum torque references was limited at this speed. This problem was avoided in simulation by raising the DC bus voltage to 900 V, which could not be done in

practice. The first 0.2 p.u speed reference is the lowest speed FS-PSC can handle before it becomes unstable, as discussed in the simulated case above, fig. 4.18b demonstrates the same increase in error due to the inaccurate $\boldsymbol{\psi}_{\mathrm{s}}^{s}$ calculation. At 1.5 p.u speed the system starts to become more unstable, which is likely due to PLL bandwidth.

The improvement to the estimation angle and torque response using SSC is shown in fig. 4.19. The torque response at rated load and estimation error improvement is significant, as shown in fig. 4.19b, which also has the SSC saturation current offset included. The SSC was implemented in the same way as in simulation, using a 2D LUT-generated off-line using the adjusted FEM flux map. Therefore any error in this map will propagate through to the output estimation angle.

During tests it was noted that the use of $\boldsymbol{u}_{\mathrm{s,r}ef}^{s}$ does not provide an ideal source for voltage estimation. Calibration at rated voltage was attempted to ensure that $\boldsymbol{u}_{\mathrm{s,r}ef}^{s}$ matched the fundamental $\boldsymbol{u}_{\mathrm{s}}^{s}$, however the estimation would increase in error as the modulation index of the VSC changed, i.e with voltage magnitude, due to an increase or decrease in PWM harmonics. Thus $\boldsymbol{u}_{\mathrm{s,r}ef}^{s}$ becomes highly speed and load dependent. The easiest way to identify if the voltage estimation is through error in estimation angle, which will be consistently positive at all loads for positive $\boldsymbol{u}_{\mathrm{s,r}ef}^{s} - \boldsymbol{u}_{\mathrm{s}}^{s}$ error and negative for negative $\boldsymbol{u}_{\mathrm{s,r}ef}^{s} - \boldsymbol{u}_{\mathrm{s}}^{s}$ error.

Overall, the practical results compare well with simulations. The simulations show lower steady state angle error with SSC and less oscillation than in practical measurements because there are several simplifications that are made in simulation, which are not present in the practical system such as; flux-map error, losses, other mechanical and electrical harmonics, variations in the stator and rotor dimensions, encoder angle harmonics, the encoder resolution, encoder error and many others.

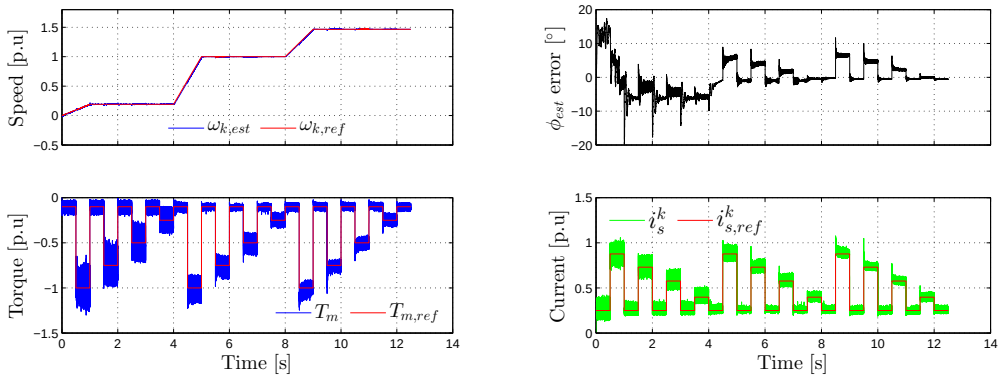

(a) (b)

Figure 4.15: Simulated response of an RSG using FS-PSC without saliency shift compensation, (a) Electrical speed, estimated electrical speed and torque response. (b) Position estimation error and current response.

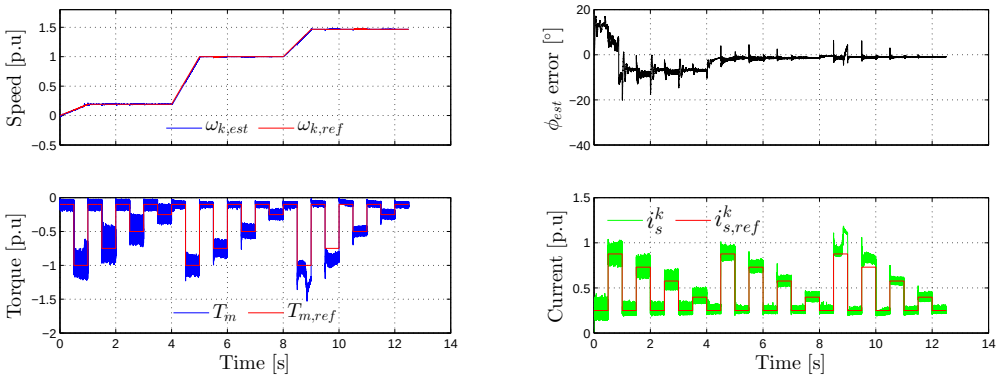

(a) (b)

Figure 4.16: Simulated response of an RSG using FS-PSC with saliency shift compensation.

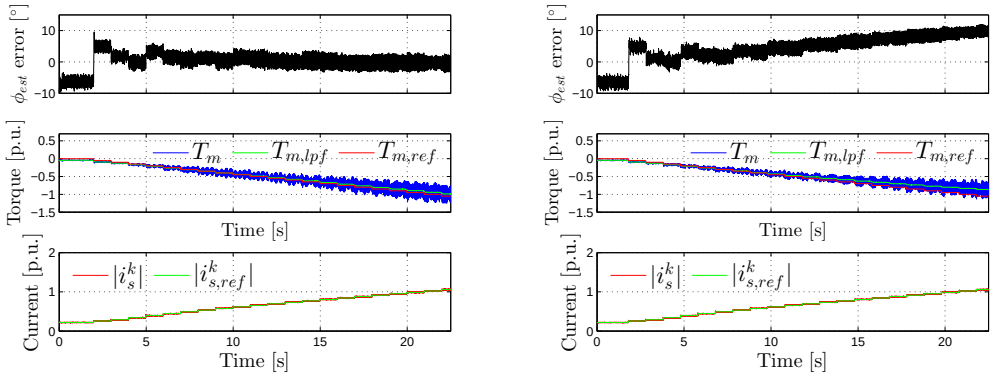

(a) FS-PSC torque ramp with SSC. (b) FS-PSC torque ramp without SSC.

Figure 4.17: Measured load ramp at 0.6 p.u speed for the RSG using FS-method with (a) and without SSC (b). Current vectors are selected using MTPA.

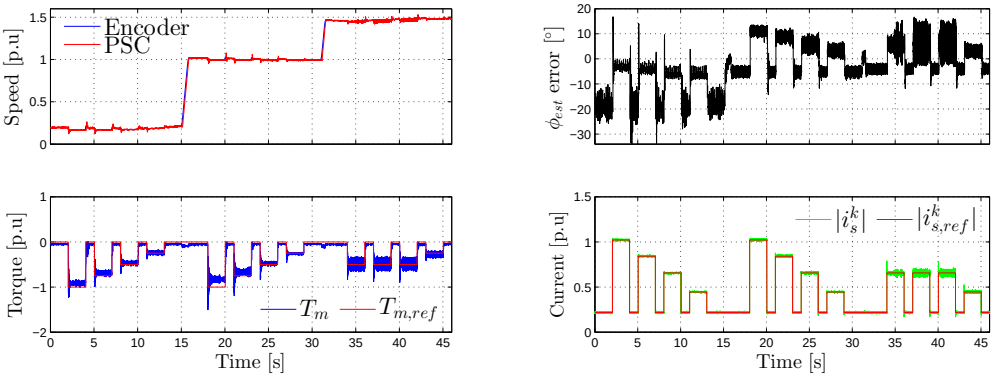

(a) (b)

Figure 4.18: Measured response of an RSG using FS PSC without SSC and without angle correction at the minimum $\boldsymbol{i}_{s,ref}^k$.

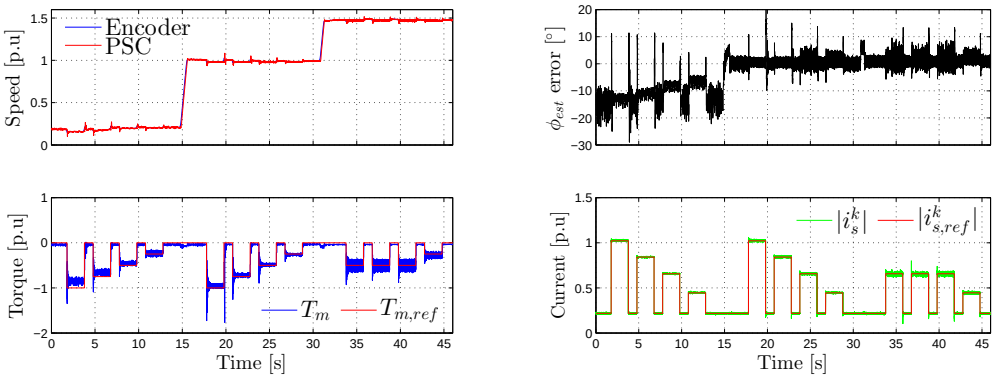

(a) (b)

Figure 4.19: Measured response of an RSG using FS-PSC with SSC and angle correction at the minimum $\boldsymbol{i}_{s,ref}^{k}$. (a) Electrical speed, estimated electrical speed and torque response. (b) Position estimation error and current response.

4.5.2 Alternating High Frequency Injection

AHFI-PSC is used primarily to estimate the initial state of the RSM rotor, more specifically, the stationary rotor angle and angle up to low speeds (0.2 p.u.). In this case, torque response accuracy is not necessary because the wind turbine controller is not executed at these low speeds and power extraction is not required. Although this method is reported to be capable of starting at twice rated torque, it is not required in this project. The AHFI-PSC will simply act as a stepping stone for the FS-PSC. The scope of the investigation was also limited to generator mode with only sufficient saturation current to remain stable and track the rotor position ($\boldsymbol{i}_s^k = 0.15\ [p.u]$), although tests at rated and half p.u. load are presented to indicate robustness. Table 4.3 contains the various parameters used for the simulated and measured tests.

In fig. 4.20 the simulated estimated angle error, torque and current response for a ramp to 1 p.u speed are illustrated. Although there is considerable offset in the estimate angle, the method continues to function and track the rotor angle. In fig. 4.20 the estimation error is shown to be dependent on the direction of acceleration, which brings into question the accuracy of a current-dependent SSC curve during transients. This is another reason why the scope AHFI-PSC was limited to not include a SSC curve in this method. In practice the modulation scheme and sampling of the system is discretised at the sampling frequency. This can affect the performance of the AHFI-method and was not considered in these basic continuous time domain simulations. The simulated inverter model does, however substantially influence the performance of this method as can be seen by comparing the results of figs. 4.20 and 4.21.

Measured tests were conducted with a range of different values, but only tested values relating to the above simulations are presented in fig. 4.22. In simulations and practice the performance of the AHFI-method was found to be extremely parameter sensitive in almost every aspect, e.g type of simulated RSM, PLL gains, LP filter bandwidth, saturation current vector, injection axis and the injection voltage and frequency. Tuning this method is highly time consuming. It was observed that higher injection voltages allowed the AHFI-PLL to operate at lower bandwidths, but increased the operating acoustic noise. Higher injection voltages also slightly reduced the minimum current required to observe the saliency, although they did not eliminate it entirely. High bandwidths allowed the PLL to lock on faster and respond to fast changes in rotor angle, but too much bandwidth made the system unstable as it became more susceptible to signal noise and disturbances. The phase current and high frequency current ripple caused by the injection voltage is presented in fig. 4.23, as well as the measured line voltage with the injection voltage, the encoder rotor angle and estimated rotor angle.

Table 4.3: AHFI-PSC simulation and practical controller parameters.

RSM / RSG parameters		
Rated input / output power (electrical)	3 kW	2.4 kW
Rated torque @ rated speed	20 N m @ 157 rad s^{-1}	19.6 N m @ 157 rad s^{-1}
R_s and n_p	2.1 Ω and 2	"
VSC parameters		
Switching frequency	10 kHz	"
Sampling frequency	continuous	10 kHz
Saturation current	0.15 p.u @ 45°	0.22 @ 45°
DC Bus voltage	700 V	600 V
Controller gains and time constants		
Injection frequency	750 Hz	"
Injection voltage	120 V	"
Axis of injection	U_s^d	"
LP-filter type	1^{st} order Butter-worth	"
$F_{LP,cut}$	100 Hz	"
$K_{p,AHFI,opt}$	620.54	"
$K_{i,AHFI,opt}$	23105	"
Solver	Ode3 (Bogacki-Shampine)	N.A
Time step	50 µs	N.A

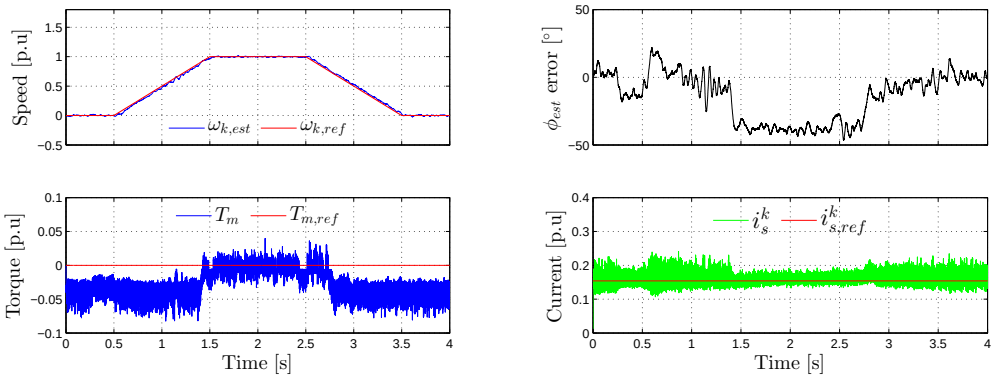

(a) (b)

Figure 4.20: A simulated speed ramp using AHFI-PSC at 0.15 p.u load with the VSC model. (a) Electrical speed, estimated electrical speed and torque response. (b) Position estimation error and current response.

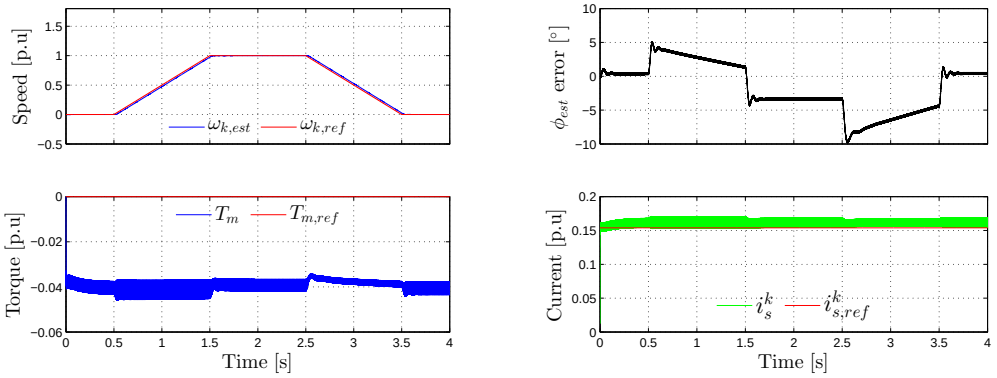

(a) (b)

Figure 4.21: A simulated speed ramp using AHFI-PSC at 0.15 p.u load without the VSC model.

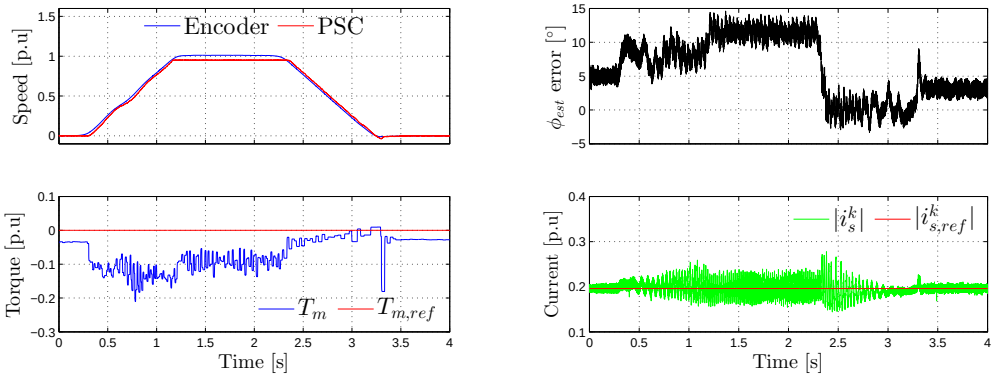

(a) (b)

Figure 4.22: A measured speed ramp using AHFI-PSC at 0.22 p.u load (saturation).

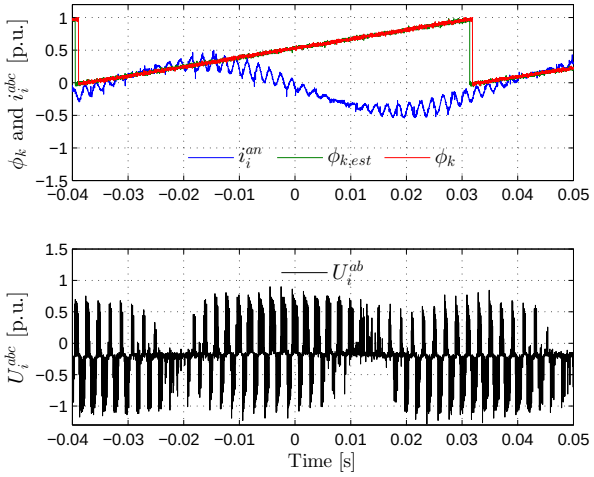

Figure 4.23: Measured encoder angle, estimated rotor angle, injected ripple on phase current i^s_{An} and injection voltage on line to line voltage u^s_{AB} for the AHFI-method.

4.5.3 Hybrid Position Sensorless Control

In this section the transient dynamics of the transition between the AHFI- and FS-methods using two PLL's and hysteresis switching is investigated. The impact of the PLL bandwidth on the torque response and acceleration of the rotor is significant. However, a full analysis of the whole range of permissible bandwidths and their effects cannot be undertaken in this project. Rather an application specific PLL bandwidth is chosen and tested for an acceleration rate within the bandwidth of the PLL. Since this WTS application does not require the transition to take place at any load above saturation load, the investigation was also limited to the minimal saturation load 0.23 p.u. Table 4.4 presents the various system parameters that were used in simulation and in practice.

The simulated results of the hybrid method under saturation load with the AHFI-PSC operating from stand still up to 0.2 p.u speed are presented in fig. 4.24. Above 0.2 p.u speed FS-PSC takes over as is indicated by the black hysteresis transition line in fig. 4.24a, where 1 = AHFI-PSC and 0 = FS-PSC. As expected there is larger estimation error at standstill due to the AHFI-PSC which has no SSC. A load 0.5 p.u is also demonstrated in fig. 4.25 to show that the effects of the AHFI-method become more significant due to the saliency shift and can cause the system to "skip poles" and cause a significant torque reference offset. However, it does not present any limitations to the transition into the FS-method, that once active stabilises and corrects the output.

The measured results from practical tests that mimic the simulated tests are presented in figs. 4.26 and 4.27. The performance of the hybrid-method compares well to that of simulations, with approximately similar torque and estimation angle offset using

AHFI-PSC. The FS-method still has the 5° estimation angle offset due to the discrepancy in the flux map but the torque dynamics are satisfactory.

Normally a hybrid-method is initiated when the rotor is at rest. However, this may happen in practice when the wind turbine is already rotating at an arbitrary speed. The hybrid-method must be able to lock on and track the rotor in both of these cases. Figure 4.28 shows AHFI-method tracking the rotor at rated speed. When the hybrid-PSC system is off-line the estimation error oscillates from 90° to −90° during which time $\hat{\omega}_k = 0$ and $\hat{\phi}_k = 0$. When initiated the system begins to track the rotor angle, at which point regular "pole skipping" is observed until the correct $\hat{\omega}_k$ is obtained. A saturation load current of 0.22 p.u load is required for this type of test.

Table 4.4: Hybrid-PSC simulation and practical controller parameters.

RSM / RSG parameters		
Rated input / output power (electrical)	3 kW	2.4 kW
Rated torque @ rated speed	20 N m @ 157 rad s^{-1}	19.6 N m @ 157 rad s^{-1}
R_s and n_p	2.1 Ω and 2	"
VSC parameters		
Switching frequency	10 kHz	"
Sampling frequency	continuous	10 kHz
Saturation current	0.15 p.u @ 45°	0.19 p.u @ 45°
DC Bus voltage	700 V	600 V
Controller gains and time constants		
Injection frequency	750 Hz	"
Injection voltage	120 V	80 V
Axis of injection	U_s^d	"
LP-filter type	1^{st} order Butter-worth 100 Hz	" LC, 60 Hz
Switch over speed	25.25 rad/s (mech)	"
Switch back speed	15 rad/s (mech)	"
Injection off/on speed	40 rad (mech)	"
k_{drift}	15	30
$K_{p,AHFI,opt}$	620.54	"
$K_{i,AHFI,opt}$	23105	"
$K_{p,FS,opt}$	250	"
$K_{i,FS,opt}$	4621	"
Solver	Ode3 (Bogacki-Shampine)	N.A
Time step	50 µs	N.A

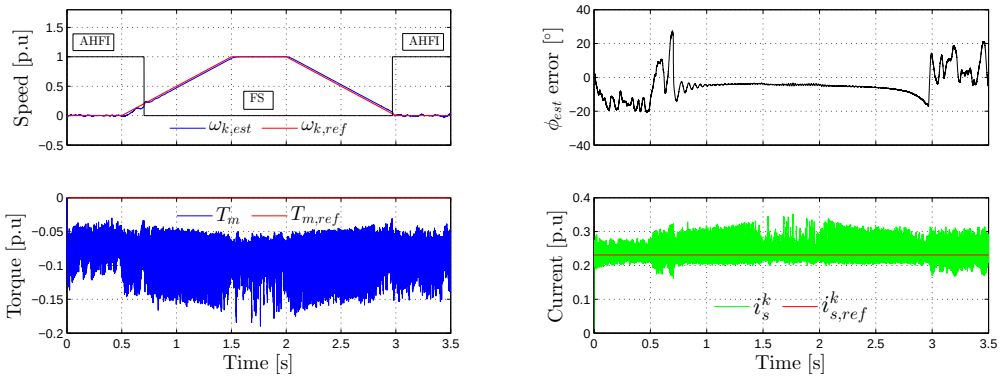

(a) (b)

Figure 4.24: A simulated speed ramp using hybrid-PSC at 0.23 p.u load. (a) Electrical speed, estimated electrical speed and torque response. (b) Position estimation error and current response.

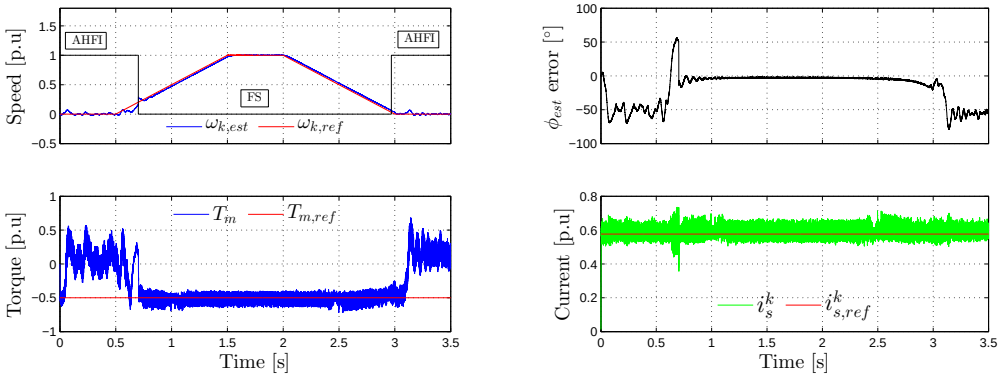

(a) (b)

Figure 4.25: A simulated speed ramp using hybrid-PSC at 0.85 p.u load.

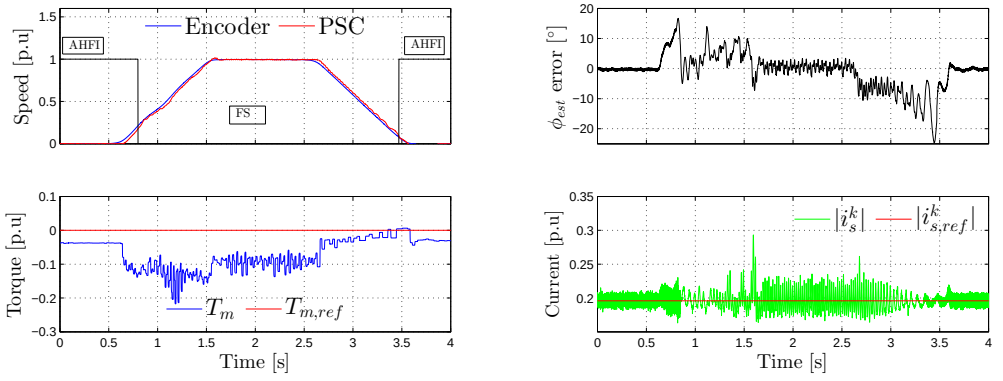

(a) (b)

Figure 4.26: A measured speed ramp using hybrid-PSC at 0.19 p.u load (saturation).

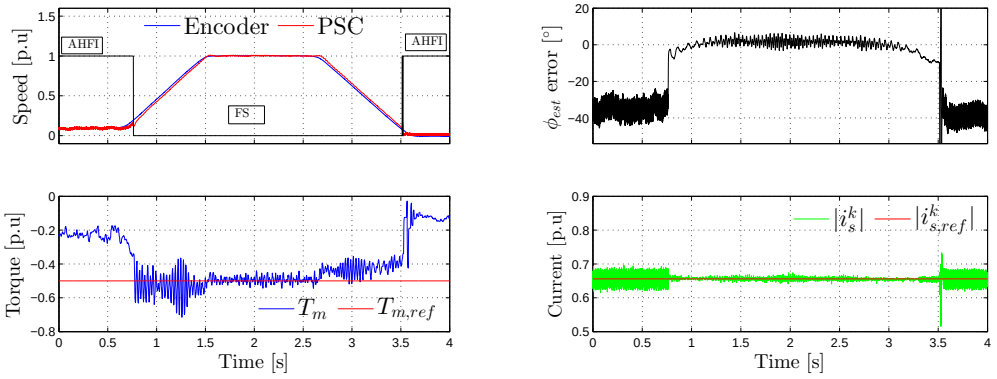

(a) (b)

Figure 4.27: A measured speed ramp using hybrid PSC at 0.5 p.u load. (a) Electrical speed, estimated electrical speed and torque response. (b) Position estimation error and current response.

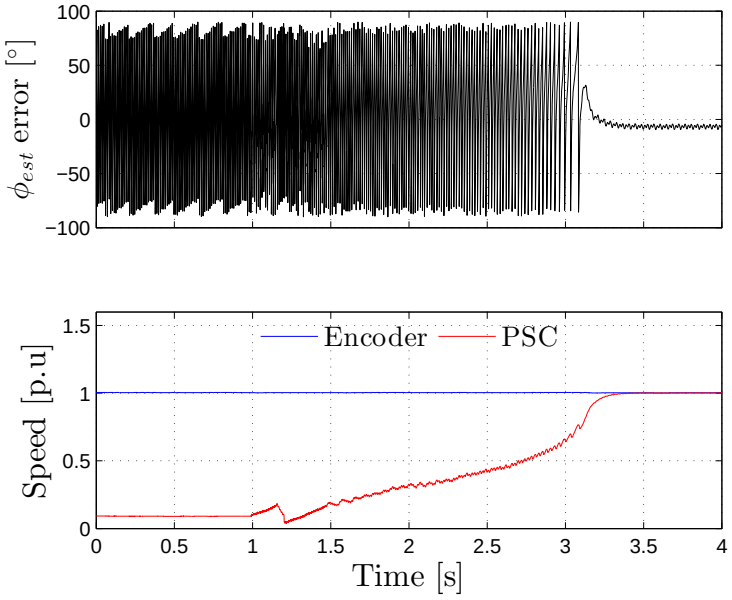

Figure 4.28: Measured position tracking error, encoder and PSC electrical speed. PSC is initiated when the RSG is at rated speed and 0.2 p.u load.

4.6 Control of the RSG with an LC-Filter and AC-link

In this chapter simulations and practical measurements of the LC-filter without PSC techniques are presented to initially verify the performance and control of the RSG using various current feedback methods. PSC tests using the hybrid-PSC method, LC-filter and the inclusion of the AC-link (RSG transmission cable) are then introduced.

4.6.1 Direct FOC of the RSG with an LC-Filter

Table 4.5 contains the parameters which were used for the simulations and practical measurements of the LC-filter system using and encoder. Figure 4.29 shows the simulated (A) and measured (B) VSC quantities, $\boldsymbol{i}_i^s, \boldsymbol{u}_i^s$ versus the output LC-filter RSG stator quantities, $\boldsymbol{i}_s^s, \boldsymbol{u}_s^s$ using $\boldsymbol{i}_s^s$ as feedback. In fig. 4.29 the current and voltage attenuation of the VSC output is clearly visible with the simulated results showing better filtering than in practice. This is likely due the fact that the simulation is an ideal case and in reality greater harmonic content is generated by the VSC and the RSG. The discrepancy between $\boldsymbol{i}_i^s$ and $\boldsymbol{i}_s^s$ also becomes apparent as $\boldsymbol{i}_s^s \approx 1.3 \times \boldsymbol{i}_i^s$ in generator mode. The current vector $\boldsymbol{i}_i^s$ also leads $\boldsymbol{i}_s^s$ due to the reactive component of the LC-filter, this is less visible in the practical results because of the greater harmonic content on $\boldsymbol{i}_i^s$.

Fast Fourier Transforms (FFT) of the simulated quantities are presented in fig. 4.30 to further verify the THD and fundamental content at rated load. The FFTs show that the LC-filter reduces the voltage and current THD by 86.51 % and 4,24 % respectively.

In reality the VSC takes ADC samples of $\boldsymbol{i}_i^s$ in the middle of each switching interval. This automatically creates an effective filter due to an aliasing effect whereby the average of the ripple current is measured. It was not possible implement this in a continuous time based simulation model and with limit project time, therefore the VSC current was filtered using a second order Butter-worth LP-filter at $F_{cut} = 1900\,\text{Hz}$ as an approximation and this is necessary for the current controller to operate correctly.

To test the torque response of the RSG, simulations were conducted for three different feedback scenarios: stator current $\boldsymbol{i}_s^s$ as feedback, VSC current $\boldsymbol{i}_i^s$ and feedback and an estimated stator current $\boldsymbol{i}_{s,est}^s$ as feedback. Each feedback method is shown in fig. 4.31. The torque and current response using $\boldsymbol{i}_s^s$ as feedback is satisfactory and performs as if the LC-filter is not present. In contrast, if $\boldsymbol{i}_i^s$ is used, a clear torque and current offset is visible that becomes worse with increase in speed (electrical frequency). This is due to the increase in voltage magnitude and frequency applied to the LC-filter, which increases the harmonic content in the current and causes greater capacitor currents to circulate. This increases the difference in phase and magnitude between $\boldsymbol{i}_i^s$ and $\boldsymbol{i}_s^s$. The torque offset is due not only to the "filter loss", but also a slight phase shifting due to the filters reactive component (decrease in power factor), which causes early

voltage saturation of the output VSC. In simulation and practice the VSC requires significantly higher DC bus voltage to operate at rated load. As a side note, the torque and current offsets are positive ($T_{\mathrm{m},ref} - T_{\mathrm{m}}$) because $\boldsymbol{i}_i^s < \boldsymbol{i}_{\mathrm{s}}^s$ in generator mode, thus $\boldsymbol{i}_{\mathrm{i}}^k = \boldsymbol{i}_{\mathrm{s,r}ef}^k \therefore \boldsymbol{i}_{\mathrm{s}}^k > \boldsymbol{i}_{\mathrm{s,r}ef}^k \therefore T_{\mathrm{m}} > T_{\mathrm{m},ref}$.

Table 4.5: LC-filter parameters for simulations and practical measurements.

RSM / RSG parameters		
Rated input / output power (electrical)	3 kW	2.4 kW
Rated torque @ rated speed	20 N m @ 157 rad s^{-1}	
R_{s} and n_{p}	2.1 Ω and 2	
VSC parameters		
Switching frequency	10 kHz	"
Sampling frequency	continuous	10 kHz
DC Bus voltage	800 V	600 V
LC-filter parameters		
F_{cut}	918 Hz	918 Hz
L_f	2 mH	2.1 mH
$C_{f,Y}$	15 µF	15 µF
$R_{damp,Y}$	33.7960 Ω	45.6 Ω
k_{LC}	N.A	0.5
Controller gains and time constants		
Solver	ode8 (Dormand-Prince)	N.A
Time step	25 µs	N.A
$V_{\mathrm{r,r}sm}^k(\boldsymbol{i}_{\mathrm{s}}^k)$ @	$\frac{L_{\mathrm{s}}^k(\boldsymbol{i}_{\mathrm{s}}^k)}{6T_{\mathrm{vsc}}}$	$\frac{L_{\mathrm{s}}^k(\boldsymbol{i}_{\mathrm{s}}^k)}{20T_{\mathrm{vsc}}}$
$T_{\mathrm{n,r}sm}^k(\boldsymbol{i}_{\mathrm{s}}^k)$ @	$T_{\mathrm{s}}^k(\boldsymbol{i}_{\mathrm{s}}^k)$	$T_{\mathrm{s}}^k(\boldsymbol{i}_{\mathrm{s}}^k)$

The set-up detailed in appendix B.2.2 was used to record the following practical results. In practice connecting the capacitors in Y is essential, as Δ connected caps cause higher distortion, phase shifting and the immediate failure of the current controllers. Over-damping of the capacitors is also essential to ensure that the inverter current has sufficiently reduced ripple so that it can be used as a feedback current source. It must also be reiterated that the Pentium system includes built-in synchronised ADC sampling whereby the analogue phase currents from the SEW are sampled between switching pulses. This effectively filters the measured VSC current. Three unique scenarios in which the RSG is directly controlled using $\boldsymbol{i}_{\mathrm{s}}^s$, $\boldsymbol{i}_i^s$ and $\boldsymbol{i}_{\mathrm{s},est}^s$ under a rated load ramp from standstill to rated speed are illustrated in fig. 4.33 .

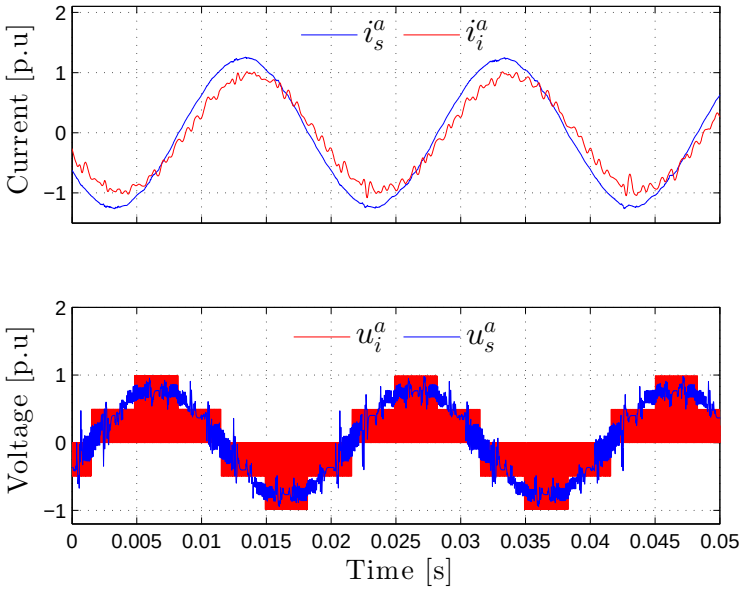

(a) Simulated LC-filter RSG quantities.

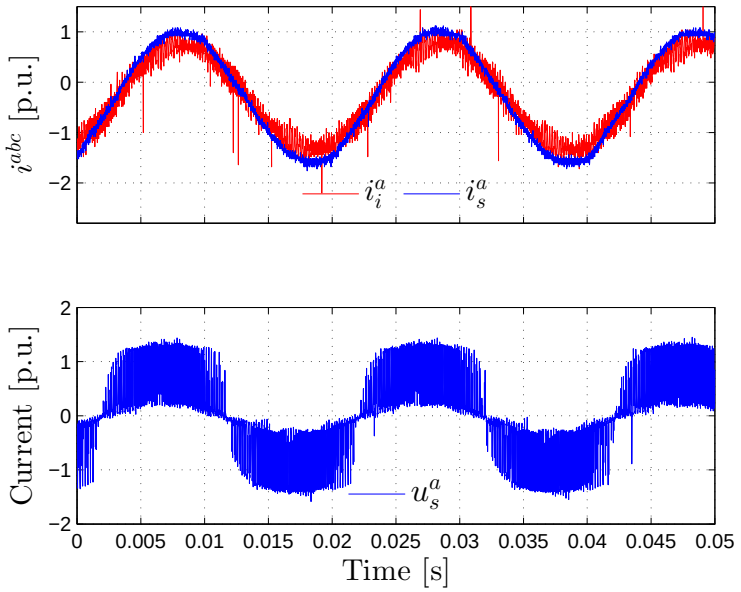

(b) Measured LC-filter RSG quantities not including $\boldsymbol{u}_i^s$.

Figure 4.29: Simulated and measured quantities of the RSG with an LC-filter at rated load and rated speed.

It can be seen in fig. 4.33b that the system was controlled using the stator current $\boldsymbol{i}_s^s$ which required additional current sensors placed at the output of the LC-filter. Using $\boldsymbol{i}_s^s$ as feedback the system performs as normal with no abnormal offset in torque. The slight offset at sub rated speeds is due to MTPA error (core loss is minimal at low speeds)

and not the LC-filter. A positive torque offset can clearly be seen in fig. 4.33c when using $\boldsymbol{i}_i^s$ as feedback, due to the capacitor currents which reduce the measured current so that $\boldsymbol{i}_{\mathrm{i}}^k = \boldsymbol{i}_{\mathrm{s},ref}^k \therefore \boldsymbol{i}_{\mathrm{s}}^k > \boldsymbol{i}_{\mathrm{s},ref}^k \therefore T_{\mathrm{m}} > T_{\mathrm{m},ref}$.

$$i_c^s(n) = C_f \frac{u_c^s(n) - u_c^s(n-1)}{T_{\mathrm{s}}} \tag{4.2}$$

$$i_c^s(n) = k_{LC} C_f \frac{u_c^s(n) - u_c^s(n-1)}{T_{\mathrm{s}}} \tag{4.3}$$

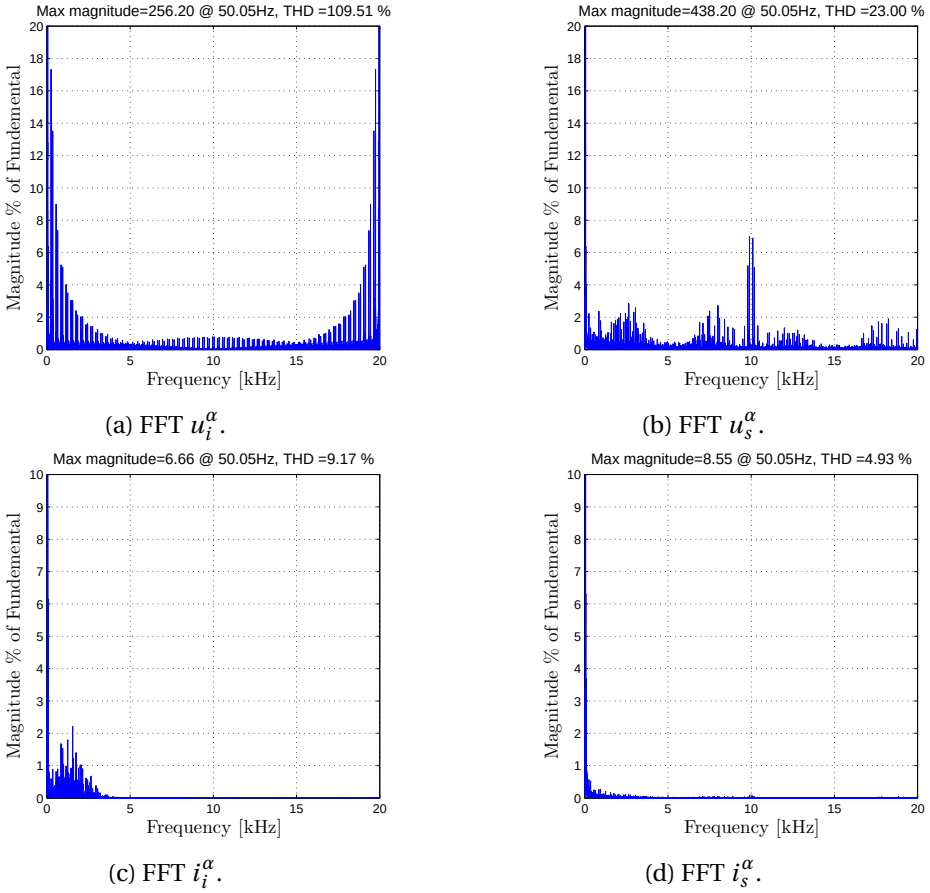

(a) FFT u_i^α.

(b) FFT u_s^α.

(c) FFT i_i^α.

(d) FFT i_s^α.

Figure 4.30: FFT of simulated α voltage and currents of the VSC model and LC-filter output. $F_{cut} = 918\,\mathrm{Hz}$, $R_{cf} = 45.6\,\Omega$, $L_f = 2\,\mathrm{mH}$, $C_f = 15\,\mu\mathrm{F}$, $\omega_{\mathrm{m}} = 157\,\mathrm{rad\,s^{-1}}$, $T_{m,ref} = 20\,\mathrm{N\,m}$.

Figure 4.33d demonstrates the performance of the LC-filter estimator. Although the estimator's performance is satisfactory and corrects the offset in torque and current, and reduces torque ripple as in accordance with simulations, its implementation is not as straight forward as in simulation. The main reason for this is the difficulty in estimating the capacitor current in a discrete manner. The backward Euler method is typically used,

(4.2), but due to the division of the very small sampling time the calculation often results in excessively large floating point numbers calculated from noise spikes, which can cause the controller to destabilise. To solve this without adjusting the capacitor and sampling time constants two methods are introduced. Firstly an additional gain term k_{LC} is added to the system, as shown in (4.3) and the resultant capacitor current i^c is low-pass filtered at 150 Hz, to extract only the fundamental and attenuate the high frequency ripple measured by $\boldsymbol{i}_i^s$, and then added to $\boldsymbol{i}_i^s$ to calculate $\boldsymbol{i}_{\mathrm{s},est}^s$. Without this adjustment the filter estimator fails. The variations between these three currents and more specifically the harmonics present on the measured VSC current are illustrated in fig. 4.32.

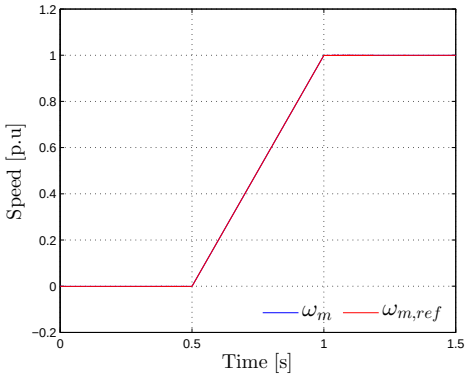

(a) Speed ramp for the simulated LC-filter response test.

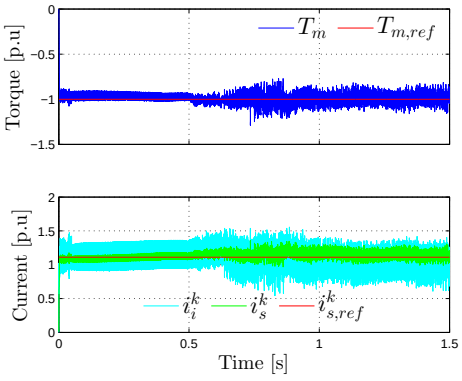

(b) Current feedback with $\boldsymbol{i}_{\mathrm{s}}^s$.

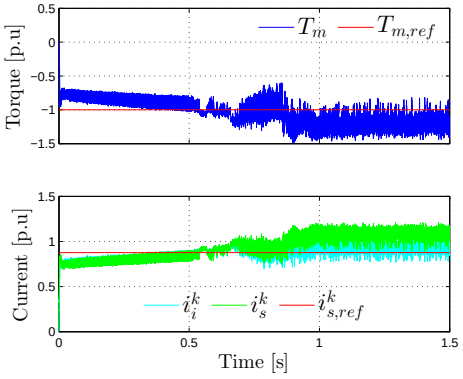

(c) Current feedback with $\boldsymbol{i}_i^s$.

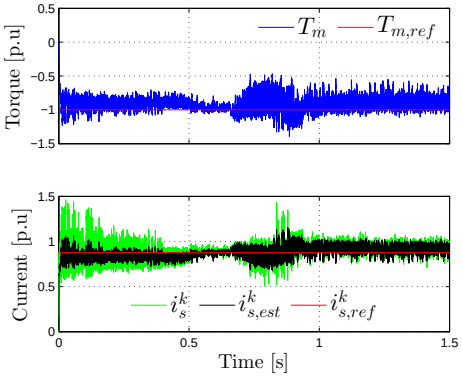

(d) Current feedback with $\boldsymbol{i}_{\mathrm{s},est}^s$.

Figure 4.31: Direct FOC simulated response of the LC-filter system with various current quantities as feedback. (a)ω_m (b) $\boldsymbol{i}_{\mathrm{s}}^s$, (c) $\boldsymbol{i}_i^s$ and (d) the estimate current $\boldsymbol{i}_{\mathrm{s},est}^s$.

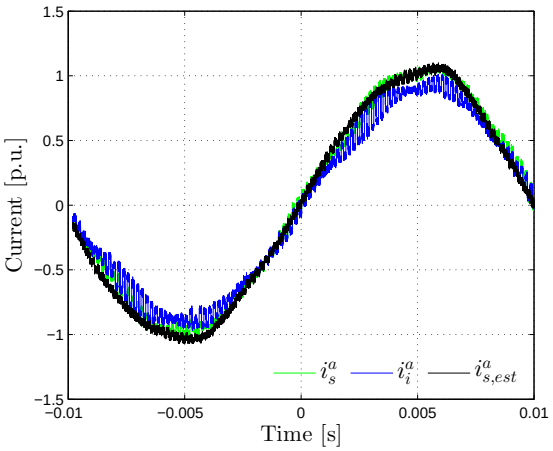

Figure 4.32: Measured $\boldsymbol{i}_{\mathrm{s}}^{s}$, $\boldsymbol{i}_{i}^{s}$ and $\boldsymbol{i}_{\mathrm{s},est}^{s}$ at rated load and speed with an output LC-filter. $\boldsymbol{i}_{i}^{s}$ is measured and used to calculate $\boldsymbol{i}_{\mathrm{s},est}^{s}$, which is then used for control purposes. For this measurement, signals are sampled at 10 kHz and transmitted at 5 kHz to an oscilloscope with the Pentium DAC.

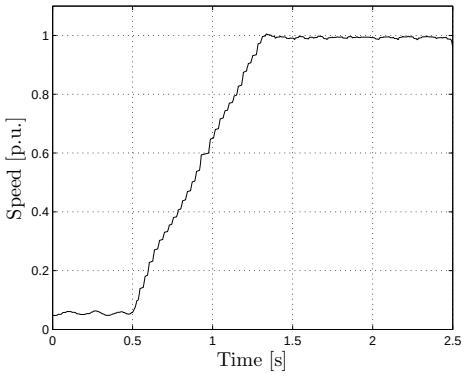

(a) Speed ramp for the measured LC-filter response test.

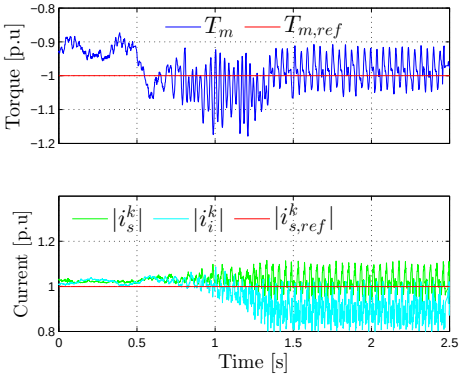

(b) Current feedback with $\boldsymbol{i}_{\mathrm{s}}^{s}$.

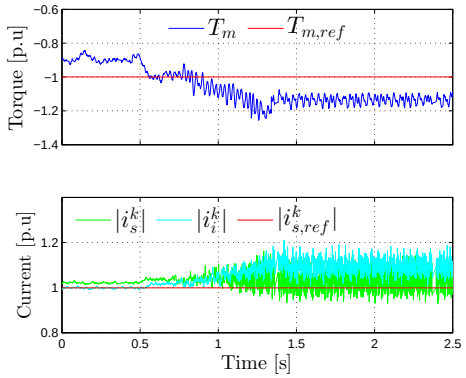

(c) Current feedback with $\boldsymbol{i}_{i}^{s}$.

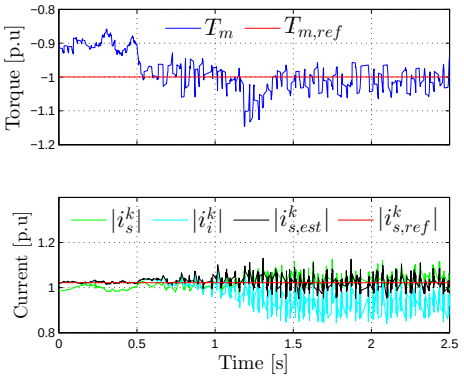

(d) Current feedback with $\boldsymbol{i}_{\mathrm{s},est}^{s}$.

Figure 4.33: Direct FOC measured response of the LC-filter system with various current quantities as feedback. (a)ω_m, (b) $\boldsymbol{i}_{\mathrm{s}}^{s}$, (c) $\boldsymbol{i}_{i}^{s}$ and (d) the estimated current $\boldsymbol{i}_{\mathrm{s},est}^{s}$.

4.6.2 Indirect FOC of the RSG with an LC-Filter

The investigation into LC-filter control using a hybrid PSC technique was implemented using the same Simulink model and practical apparatus as in section 4.6.1. Table 4.6 details the PSC parameters for simulation and practical experiments. It is important to note that the AHFI-PSC was found to function with better accuracy and stability if the injection axis was shifted to the $u^q_{\mathrm{s},ref}$, thus i^d_{s} is used in the demodulation scheme to extract the rotor angle.

Table 4.6: PSC LC-filter parameters for simulations and practical measurements.

RSM / RSG parameters		
Rated input / output power (electrical)	3 kW	2.4 kW
Rated torque @ rated speed	20 N m @ 157 rad s^{-1}	
R_{s} and n_{p}	2.1 Ω and 2	
VSC parameters		
Switching frequency	10 kHz	"
Sampling frequency	continuous	10 kHz
DC Bus voltage	800 V	600 V
LC-filter parameters		
F_{cut}	918 Hz	918 Hz
L_f	2 mH	2.1 mH
$C_{f,Y}$	15 µF	15 µF
$R_{damp,Y}$	83 Ω	83 Ω
k_{LC}	N.A	0.5
PSC parameters		
Injection frequency	918 Hz	"
Injection voltage	120 V	80 V
Axis of Injection	U^q_s	"
LP-filter type	1^{st} order Butter-worth	"
$F_{LP,cut}$	100 Hz	"
$K_{p,AHFI,opt}$	186	620
$K_{i,AHFI,opt}$	4610	23100
$K_{p,FS,opt}$	250	"
$K_{i,FS,opt}$	4621	"
Controller gains and time constants		
Solver	ode8 (Dormand-Prince)	N.A
Time step	25 µs	N.A
$V^k_{\mathrm{r,r}sm}(\boldsymbol{i}^k_{\mathrm{s}})$ @	$\frac{L^k_{\mathrm{s}}(\boldsymbol{i}^k_{\mathrm{s}})}{6T_{vsc}}$	$\frac{L^k_{\mathrm{s}}(\boldsymbol{i}^k_{\mathrm{s}})}{20T_{vsc}}$
$T^k_{\mathrm{n,r}sm}(\boldsymbol{i}^k_{\mathrm{s}})$ @	$T^k_{\mathrm{s}}(\boldsymbol{i}^k_{\mathrm{s}})$	$T^k_{\mathrm{s}}(\boldsymbol{i}^k_{\mathrm{s}})$

Figures 4.34 and 4.35 show the RSG operating at rated torque during a ramp to rated speed. The estimation error of the hybrid FS- and AHFI- PSC method is shown as well as the current magnitude. In fig. 4.34 the current and hybrid-PSC controller has access to $\boldsymbol{i}_{\mathrm{s}}^{s}$ and $\boldsymbol{u}_{\mathrm{s,r}ef}^{s}$ and uses this for control purposes. The PLL gain for the FS-PSC techniques is the same as without the LC-filter, however the current controller and AFHI-PSC PLL gain is reduced to decrease noise and instability. It is critical that the filter be over-damped for the PSC techniques to work. This is in contrast to the LC-filter working with moderate or optimal damping when using an encoder. Although less damping allows for better attenuation of the higher harmonics in the VSC voltage and current, it is a possible reason for the AHFI method to fail since this method is highly sensitive to the LC-filter resonance frequency. Figure 4.35 shows the same test, but the controller instead uses $\boldsymbol{i}_{i}^{s}$ and $\boldsymbol{u}_{\mathrm{s,r}ef}^{s}$ for current and hybrid-PSC control. An increase in error in $\hat{\phi}_{\mathrm{k}}$ is visible as well as the torque offset due to i_c discussed in section 4.6.1. Performance under $\boldsymbol{i}_{\mathrm{s}}^{s}$ or $\boldsymbol{i}_{i}^{s}$ feedback produces similar results compared to direct FOC with $\boldsymbol{i}_{\mathrm{s}}^{s}$ or $\boldsymbol{i}_{i}^{s}$ as feedback respectively, however there is a clear difference in the tracking error between the two feedback methods. Under $\boldsymbol{i}_{\mathrm{s}}^{s}$ feedback, T_{m} is affected predominantly by the error in $\hat{\phi}_{\mathrm{k}}$, whereas with $\boldsymbol{i}_{i}^{s}$ feedback, the torque offset is due to both the capacitor current offset and the larger estimation error present in $\hat{\phi}_{\mathrm{k}}$. The current angle using $\boldsymbol{i}_{\mathrm{i}}^{k}$ as feedback is also effected negatively by the LC-filter, which leads to a current magnitude and phase error of $\boldsymbol{i}_{\mathrm{i}}^{k}$ that causes the increase in estimation error.

Using the simulated LC-filter estimator with the AHFI-PSC did not produce consistent results at rated load and often failed to track the rotor angle. Simulated speed ramp tests at a maximum rated current load of 0.4 p.u are presented in fig. 4.36. Instability at rated start-up loads is due to larger discrepancies in the LC-filter estimator, which further destabilise the AHFI-method. The FS-PSC functions as normal, but with increased noise in the estimation angle, which is likely due to the filter noise caused by the time derivative in the estimator.

Measured tests using $\boldsymbol{i}_{\mathrm{s}}^{s}$ or $\boldsymbol{i}_{i}^{s}$ as feedback variables are not required because the performance of the controller using $\boldsymbol{i}_{\mathrm{s}}^{s}$ as feedback was already established in section 4.6.1 and in simulations. Thus only the measured response of the LC-filter RSG system under hybrid-PSC is presented in Figures 4.37 and 4.38. The transition between AHFI and the FS-PSC is tested with a rated speed ramp at 0.2 p.u. load and presented in fig. 4.37 and the dynamic torque response of the system under FS-PSC is tested at three different speeds as presented in fig. 4.38.

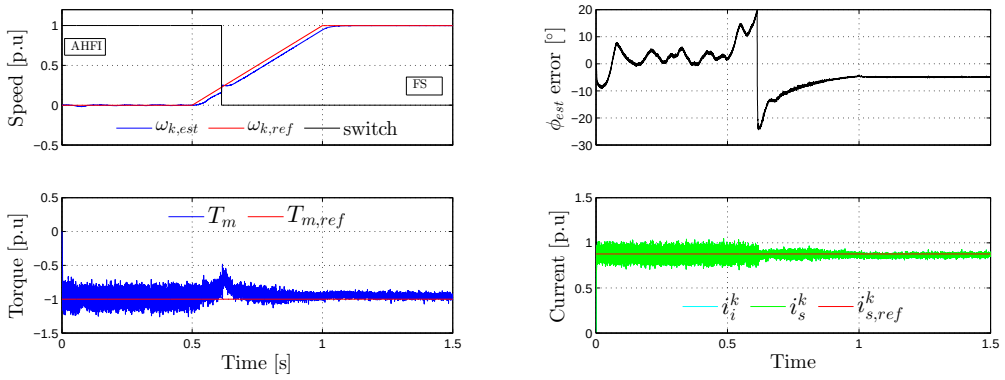

(a) (b)

Figure 4.34: Simulated response and control of an RSG using hybrid PSC with an LC-filter and using $\boldsymbol{i}_s^s$ as feedback. (a) Electrical speed, estimated electrical speed and torque response. (b) Position estimation error and current response.

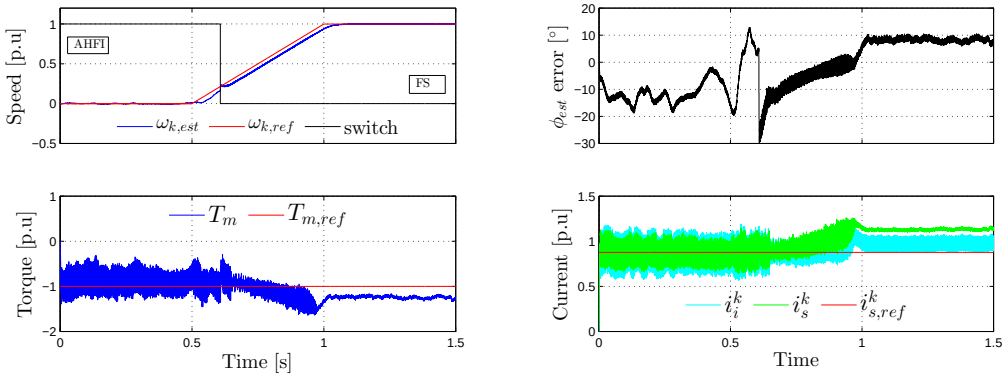

(a) (b)

Figure 4.35: Simulated response and control of an RSG using hybrid-PSC with an LC-filter and using $\boldsymbol{i}_i^s$ as feedback.

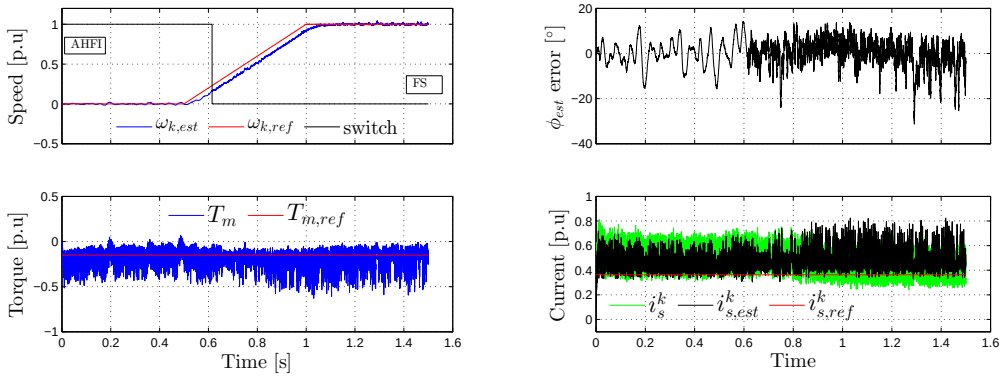

(a) (b)

Figure 4.36: Simulated response and control of an RSG using hybrid-PSC with an LC-filter and using $\boldsymbol{i}_{s,est}^s$ as feedback.

The AHFI-PSC is quite stable with the LC-filter and almost no difference in performance was noticed compared to that of direct FOC. The damping resistance of the filter is however, fairly critical to the stability of this PSC method and requires some tuning. The cut-off frequency of the filter should also not be below the injection frequency. Utilising the resonant peak of the filter to reduce the injection voltage was not possible, since the LC-filter is required to be over damped in order to allow the current controllers to function correctly. From fig. 4.38 it is apparent that although the FS-PSC is stable, the saliency angle of the RSG appears to have changed because the original saliency shift compensation curve no longer compensates correctly. This is the result of discrepancies between the estimated quantities and the real machine quantities (voltage and current). The larger "saliency error" at high speed is also due to saturation of the inverter output voltage. During saturation both $u^d_{\mathrm{s},ref}$ and $u^q_{\mathrm{s},ref}$ become highly oscillatory, which affects the estimated voltage and thus increases the estimated angle error. The performance of FS-PSC at rated speed is satisfactory, but due to the LC-filter voltage drop and losses, additional VSC output voltage is required for a given $T_{\mathrm{m},ref}$, which limits the maximum over-speed and power of the RSG.

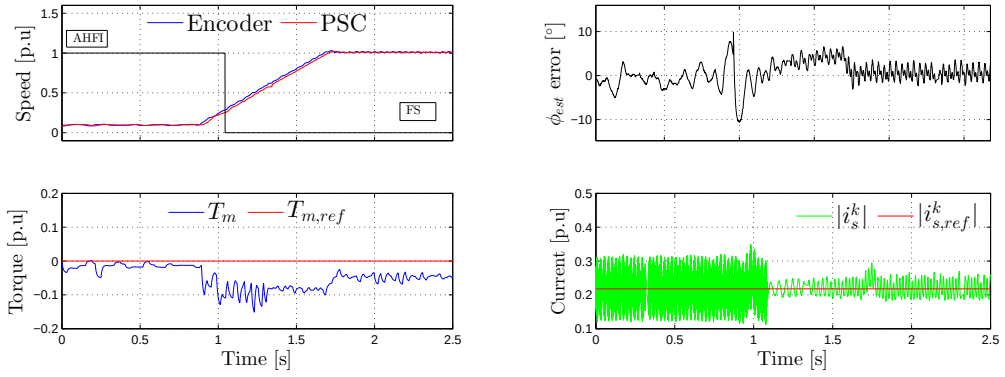

(a) (b)

Figure 4.37: Measured response and control with an VSC output LC-filter. Hybrid-PSC is used with $\boldsymbol{i}^s_{\mathrm{s},est}$ and $\boldsymbol{u}^s_{\mathrm{s},est}$ as feedback. (a) Electrical speed, estimated electrical speed and torque response. (b) Position estimation error and current response.

The stator voltage is also improved by the estimation, as shown in fig. 4.39. The estimator calculates an attenuated voltage signal, which is beneficial for FS-PSC. Measurements of the stator voltage and estimated voltage where not recorded due to time and space constraints. However, observations during measurements showed that the FS-method performed better with estimator voltage. This was expected because the FS-method evaluates the relation between stator voltage and current quantities (even if estimated) and not the inverter quantities, although some tuning of the estimator was required.

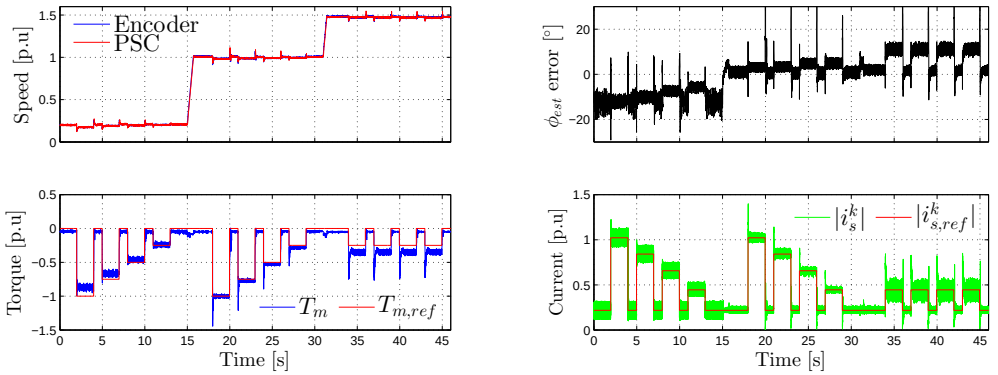

(a) (b)

Figure 4.38: Measured response and control of an RSG with an LC-filter. Hybrid-PSC is used (primarily FS-PSC in this case) with $\boldsymbol{i}^s_{s,est}$ and $\boldsymbol{u}^s_{s,est}$ as feedback. (a) Electrical speed, estimated electrical speed and torque response. (b) Position estimation error and current response.

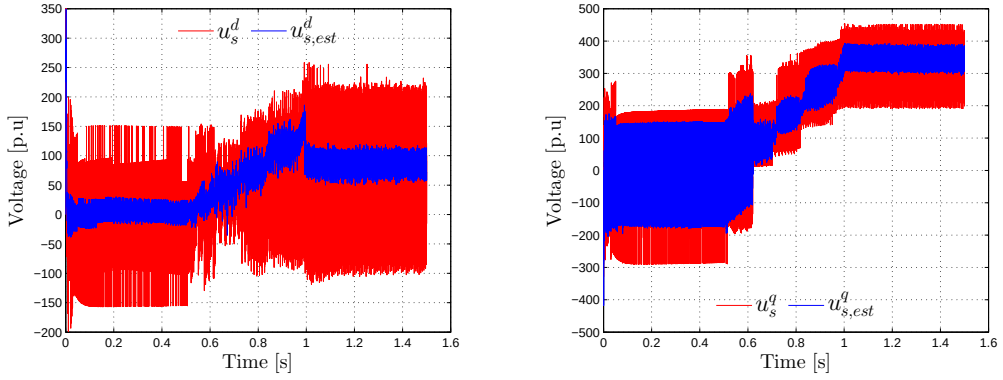

(a) (b)

Figure 4.39: Simulated stator voltage response during a rated load speed ramp to rated speed with an LC-filter. $\boldsymbol{i}^s_{s,est}$ and $\boldsymbol{u}^s_{s,est}$ are used as feedback. (a) d-axis stator and estimated stator voltage. (b) q-axis stator and estimated stator voltage.

4.6.3 Indirect FOC of the RSG with an LC-Filter and AC-link

Although the direct FOC current control system functions with both the AC-link and LC-filter, practical tests demonstrate that under a hybrid-PSC the control system fails. The main issue is the inability of the AHFI-PSC to stabilise when rotating or during the hysteresis transition, as shown in fig. 4.41. Various PLL gains, injection magnitudes, injection axes, filter cut-off frequencies and LC-filter parameters were investigated, but the results produced consistent failures. This is likely due to the additional filtering properties caused by the AC-link, which further distorts and attenuates the injection voltage and visible saliency. Perhaps there is a balance of system parameters such as a maximum cable resistance or inductance that would enable the AHFI-PSC to function, however this

project's limited time scale did not allow for a more extensive investigation.

The FS-PSC method does still function although there is a larger change in the saliency shift as shown in fig. 4.40, due to the additional loss in the cable and the estimated stator voltage that must be adjusted to allow this PSC method to function. The VSC output voltage required to operate at load is significantly increased to overcome the voltage drop on the AC-link. This prevented any loaded tests at 1.5 p.u speed. The minimum operating speed of the FS-PSC is also increased due to a larger discrepancy between $\boldsymbol{u}^s_{s,est}$ and $\boldsymbol{u}^s_s$ at low speed. A noticeable reduction in torque ripple was also observed. This is due to the lower current controller gain and the filtering characteristics of the AC-link, which further improves the applied voltage signal and thus reduces stator current harmonics.

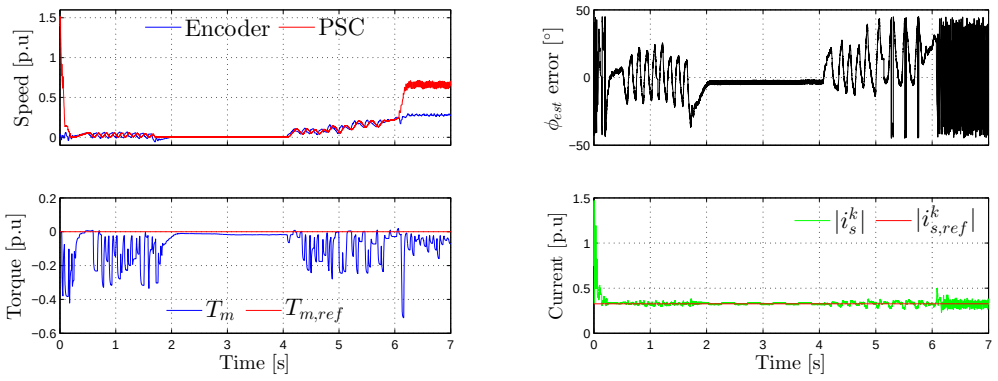

(a) (b)

Figure 4.40: Measured response of the RSG under AHFI-PSC with an AC-link and LC-filter. (a) Electrical speed, estimated electrical speed and torque response. (b) Position estimation error and current response.

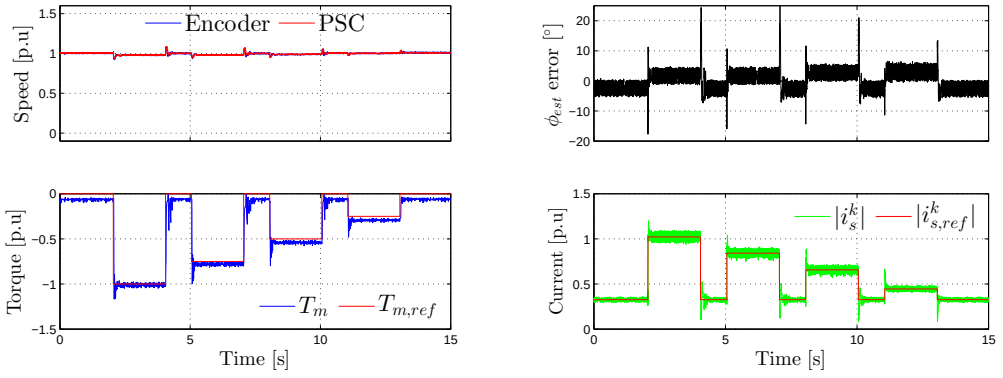

(a) (b)

Figure 4.41: Measured response of the RSG under FS-PSC with an AC-link and LC-filter at rated speed.

4.7 Grid-tie Connection

To verify simulations, a three-phase grid controller and LCL-filter were built and implemented in practice at Stellenbosch University on the test set-up detailed in appendix B.2.1. The results obtained from these practical tests are presented and compared to the results obtained through simulation. Figure 4.42 below shows the simulated phase voltage $u_{\mathrm{f}}^{\alpha} = u_{\mathrm{g}}^{\alpha}$ of the grid matching with the inverter output voltage. Figure 4.43 below shows the measured line-to-line voltage $u_{\mathrm{g}}^{ab} = u_{\mathrm{g}}^{\alpha}$ of the grid matching with the controller output reference voltage $u_{\mathrm{f}}^{ab} = u_{\mathrm{f}}^{\alpha}$. Grid line to line voltages were used in practice rather than the phase voltages to avoid unwanted unbalanced neutral currents and earthing issues.

In fig. 4.43 the measured phase current $i_{\mathrm{g}}^{a} = i_{\mathrm{g}}^{\alpha}$ lags the line voltages u_{g}^{ab} and u_{f}^{ab} by 30°. This is because the system is connected in delta, i.e if the PLL angle tracks u_{f}^{ab} and is used directly in the Park transformations, $\boldsymbol{T}_{\mathrm{p}}^{-1}, \boldsymbol{T}_{\mathrm{p}}$, the inverter will inject current which is 30° leading the grid phase voltage, resulting in a power factor less than 1 if power is transferred. To correct this, 30° must be subtracted from the PLL angle and used in either $\boldsymbol{T}_{\mathrm{p}}^{-1}$ or $\boldsymbol{T}_{\mathrm{p}}$.

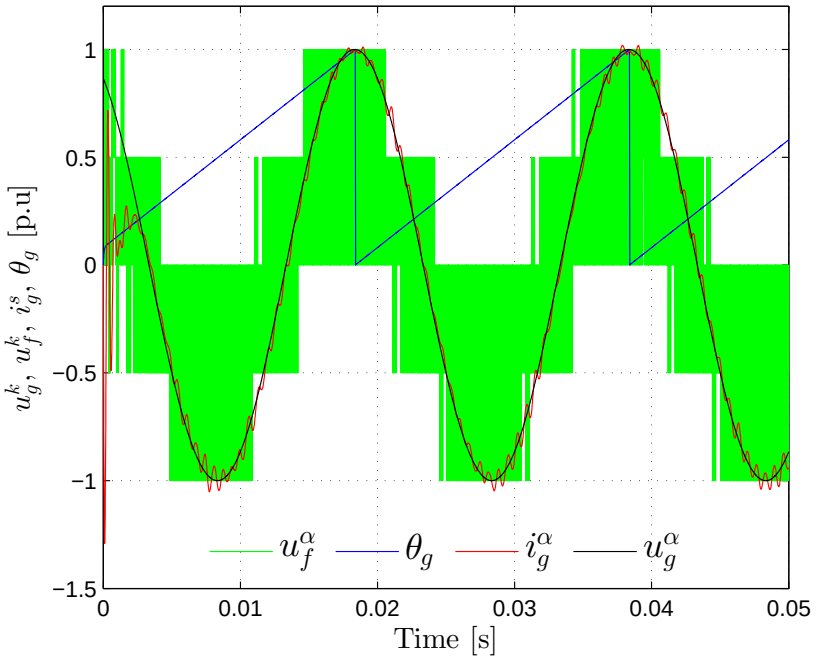

Figure 4.42: Simulated synchronised α voltages of the grid and VSC as well as the grid current and the tracked PLL electrical angle θ_g. All values are in p.u.

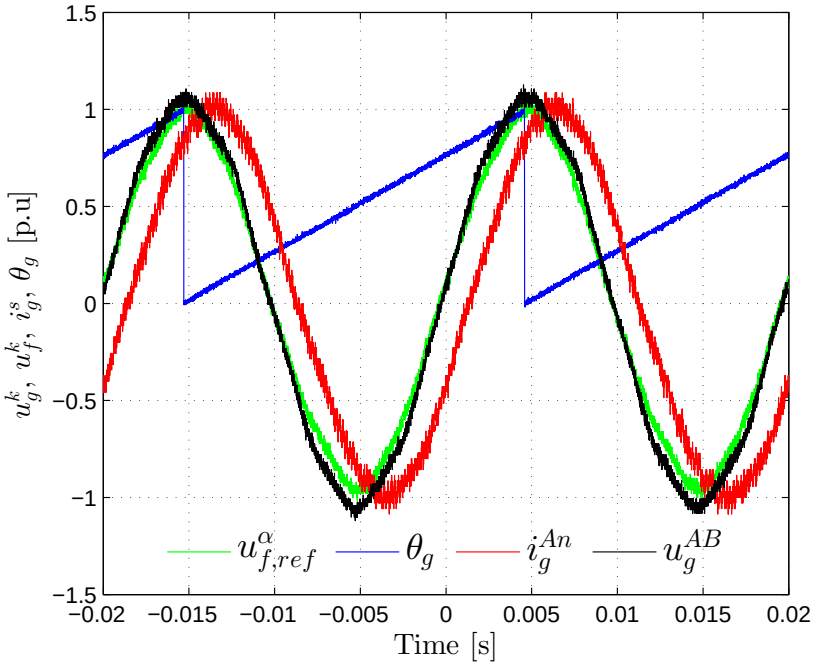

Figure 4.43: Measured and synchronised grid line voltage u_g^{α} as well as the grid phase current $i_g^a = i_g^{\alpha}$ and the tracked PLL electrical angle θ_g. All values are in p.u. Rated grid rms line voltage is 400 V, rated current is 4.2 A rms.

4.7.1 Grid-tie Current Control

Simulated and measured active and reactive power injection is demonstrated in fig. 4.44. In fig. 4.44a both reactive and active current injection in simulation, where current is injected into the grid at leading and lagging power factors are demonstrated. Similar steps are performed in measurement but with limitations due to equipment i.e. to absorb and inject active power, the RSG and IM prime mover are used as the back-to-back converter power source (generator mode) as shown by the set-up detailed in appendix B.2.

Reactive power can be absorbed and injected without the DC bus gaining net energy if DC bus voltage control is used. However, instability for absorbed reactive and active power was observed as predicted in section 3.4.4, which limited this test to only reactive and active power injection. This is discussed further in section 4.8. Note that because the DC bus controller controls the $i_{g,ref}^d$ command, a dynamic d-axis current reference is observed rather than a fixed set-point as in simulation. The active and reactive current responses are in practice satisfactory and compare well with the simulated results, thus validating the grid current controller. The LCL-filter was designed to operate at a power level of 3 to 4.5 kW but the RSG has a rated power output of 2.3 kW, which results in a slightly lower than rated measured power step, as shown in fig. 4.44b.

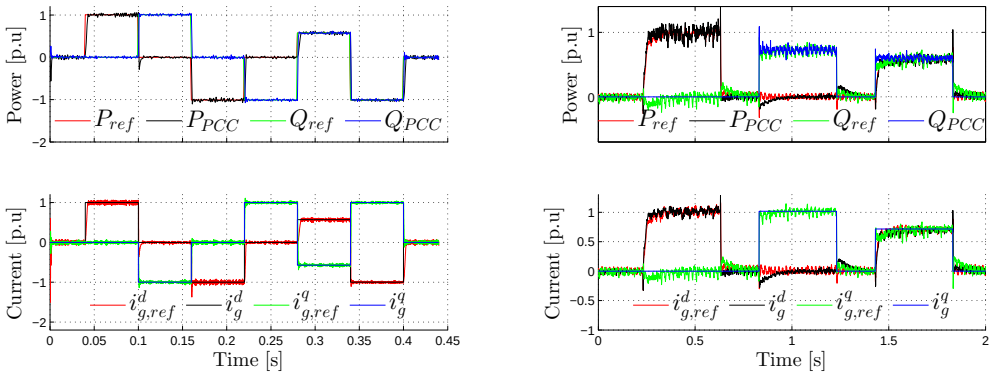

(a) Simulated power control, $P_{rated} = 3\,\text{kW}$. (b) Measured power control, $P_{rated} = 2.3\,\text{kW}$.

Figure 4.44: Measured and simulated grid current and power control at various power input levels in the dq reference frame.

4.7.2 LCL-Filter Validation

According to [110], it is necessary to limit the voltage drop across L_f to 5 - 10 % of the base inductance L_b. This is a requirement to prevent excessive inductor and IGBT switching loss and was initially used in the design of the filter. However, during the initial testing phase it was found that inductance values $< 22mH$ consistently failed the 5 % THD test ($u_{dc} = 600\,\text{V}$), regardless of filter capacitance size or grid inductor size. In order to achieve the necessary THD, these constraints had to be adjusted to 15 % of the base inductance L_b, which brings the inverter ripple current from 10 % to 5.5 %. This is in accordance with [111] who suggests a much larger primary inductance.

After increasing the inductance in practice, the simulations were redone using the new filter parameters displayed in table 4.7. The simulated results of the grid and VSC side, current ripple and THD are presented in fig. 4.45a and an FFT of the injected grid current is presented in fig. 4.45b. These simulations indicate that the simulation model can represent the harmonic quantities such as current ripple and that the LCL-filter is effective at attenuating them. When using these parameters the simulation compares very well with the actual results however, It is not yet clear why the simulations or the filter design process allow such low THD values to be generated for L_f at rated load. One possible reason could be that in reality the ripple current from the three-phase rectifier in the practical test bench detailed in fig. B.5 and appendix B.2.1 is at twice the fundamental frequency 100 Hz, which is not effectively attenuated by smaller inverter side inductances and therefore increases the THD. The simulation models do not have this issue. The simulated VSC switches are also ideal, which further reduces the resultant current THD. The measured current harmonics on the grid and VSC side, presented in fig. 4.46, are considerably nosier than in simulation. These measurements were taken using an oscilloscope and the NormaX FFT function.

Table 4.7: Grid VSC and LCL-filter simulation and practical controller parameters.

Parameters	Simulation	Practical
Rated power	3 kW	"
Phase voltage	230 V rms	"
$I_{rms,rated}$	4.2 A	"
ω_{grid}	314 rad/s	"
Switching frequency	10 kHz	"
Sampling frequency	continuous	10 kHz
DC Bus voltage	600 V	600 V
Grid / LCL-filter parameters		
$\hat{u}_g$ @ f_g	$\sqrt{2} \cdot 230$ V @ 50 Hz	
L_i	25.4 mH	"
L_g	1.8 mH	"
$C_{f,Y}$	3.0 μF	"
$C_{f,\Delta}$	1.0 μF	"
$R_{f,Y}$	7.3 Ω	"
$R_{f,\Delta}$	23.55 Ω	"
ω_{res}	14152 rad/s	"
Current THD @ I_{rated}	2.5%	4.44 %
Controller gains and time constants		
$T_{n,PLL}$	0.101	"
$V_{r,PLL}$	0.965	"
$K_{p,grid,MO}$	140	"
$K_{i,grid,MO}$	6000	"
$K_{p,grid,tuned}$	75	"
$K_{i,grid,tuned}$	1470	"
Solver	Ode3 (Bogacki-Shampine)	N.A
Time step	50 µs	N.A

The measured and simulated current THD are greatly influenced by the current controller gain, which affects the current ripple and additional distortion harmonics, as shown in fig. 4.47. The high gain produced by the modulus optimum criterion (MO) current controller detailed in section 3.4.2, increases the current THD by ≈ 3 - 5%, as shown in figs. 4.48 and 4.49. High gain values cause oscillation around the reference set-point, which adds harmonic content to the output current. The THD could be significantly reduced without drastically affecting the response time of the current controllers by reducing the bandwidth of the current controller. The PI controllers were tuned during testing to $K_{p,grid,tuned} = 75$ and $K_{i,grid,tuned} = 0.0561$, which brought the THD from ≈ 6.3% to ≈ 3.5% and the settling time from 50 ms to 100 ms. Simulations compare well to the actual measurements. The THD of the grid current throughout this test performs as

expected. At above rated power of (3 kW, 4.3 A) the measured THD in fig. 4.49 maintains a value of 4.4 %, which is in agreement with simulation.

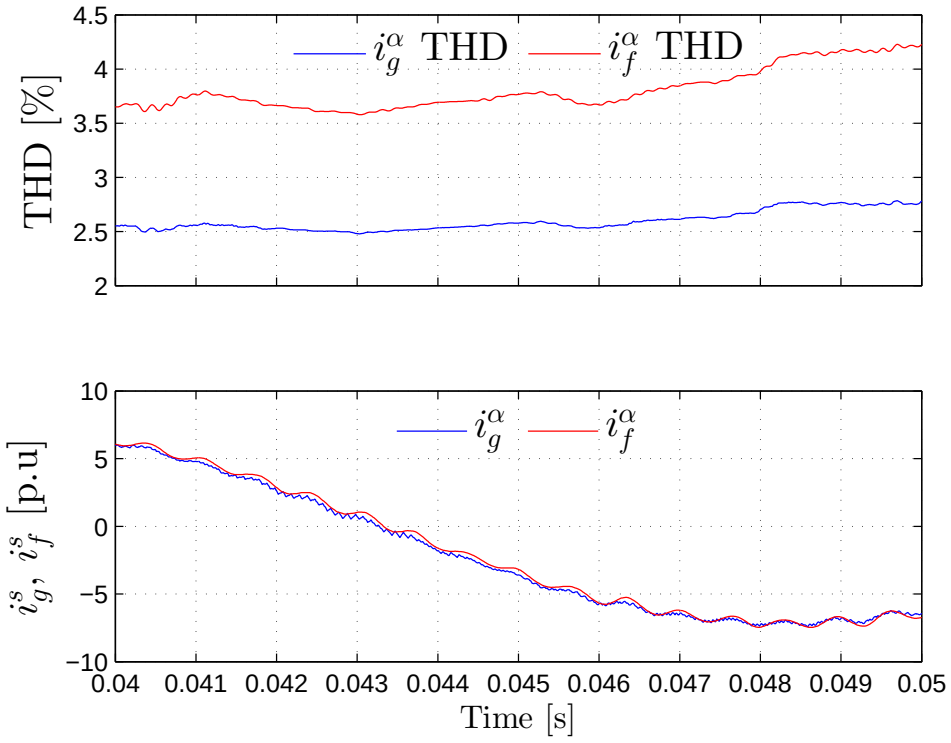

(a) Simulated VSC current i_f^α and injected grid current i_g^α with corresponding THD at 5A rms.

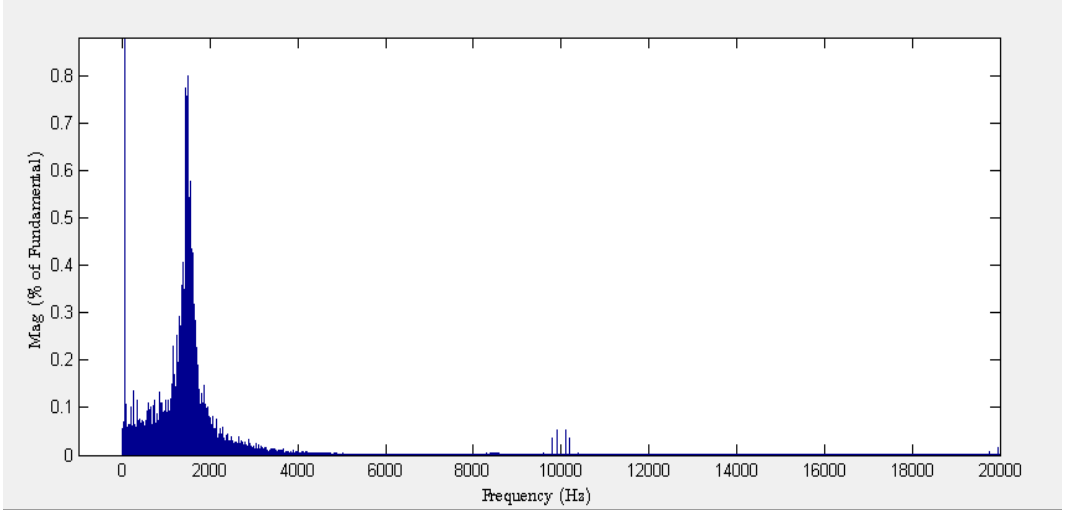

(b) FFT of the injected grid phase current i_g^α at 5A rms.

Figure 4.45: Simulated VSC current i_f^α and injected grid current i_g^α with corresponding THD. Notice the high frequency ripple on i_f^α in fig. 4.45a which is filtered out in i_g^α .

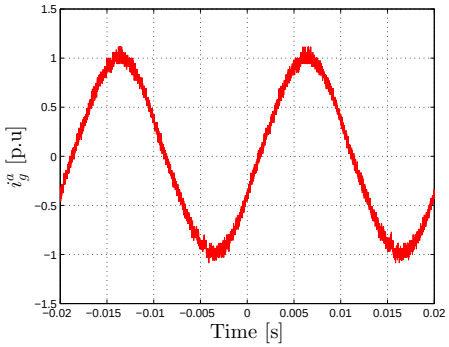

(a) Measured injected grid current i_{g}^{a}.

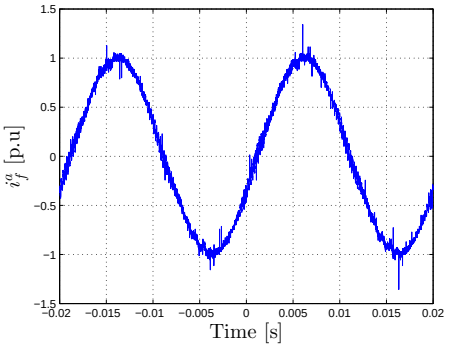

(b) Measured VSC phase current i_{f}^{a}.

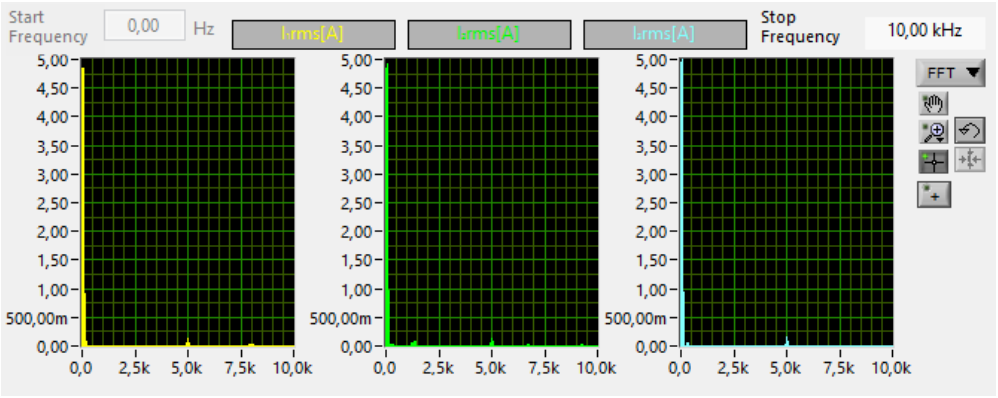

(c) FFT of the injected grid current i_{g}^{α}.

Figure 4.46: Measured rated VSC and injected grid current i_{f}^{α} and i_{g}^{α} with corresponding THD.

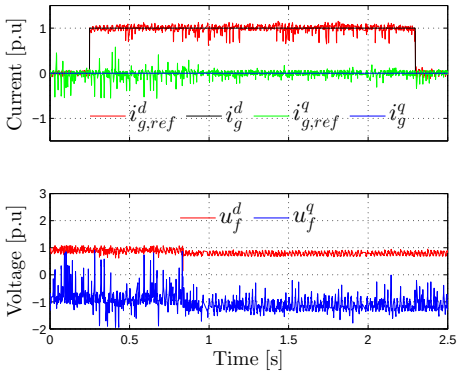

(a) Modulus optimum gain.

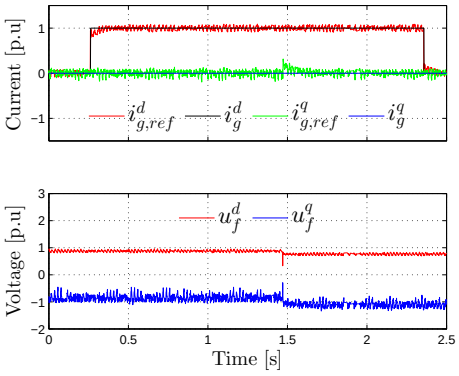

(b) Reduced gain.

Figure 4.47: Measured current response in the dq reference frame for, (a) high gain modulus optimum tuned PI controllers and (b) lower tuned gain PI controllers, sampled at 1.25 kHz. Step response $i_{\mathrm{s},ref}^{d} = 7A$.

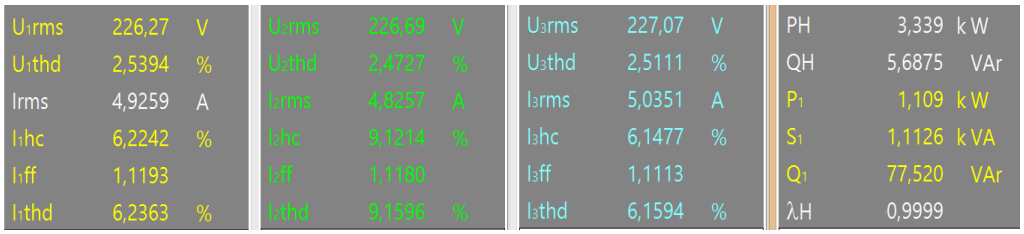

(a) LCL rated load of 5 A rms, $i_g^d = 7$ A, $i_g^q = 0$ A. ≈ rated load of 3.1 kW.

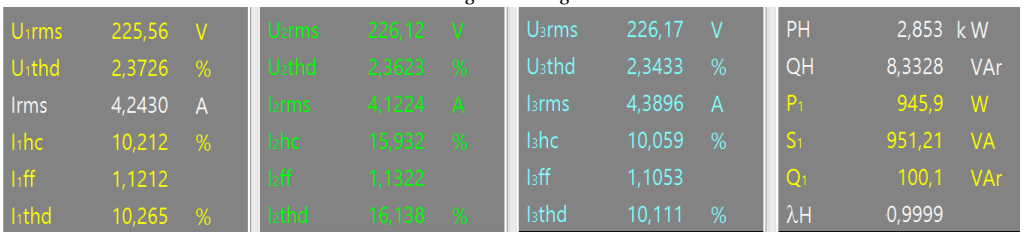

(b) THD at 4.2 A rms, $i_g^d = 6$ A, $i_g^q = 0$ A.

Figure 4.48: Three-phase grid injected rms current, rms voltage, harmonic THD, power factor, real power, apparent power, reactive power measured with the NormaX power analyser. The high gain current controller was used for this measurement.

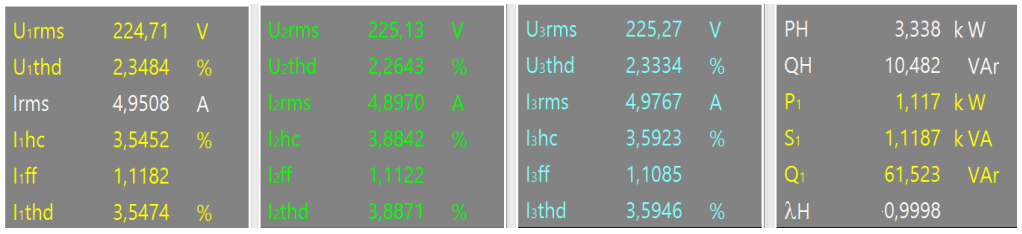

(a) LCL rated load of 5 A rms, $i_g^d = 7$ A, $i_g^q = 0$ A. ≈ rated load of 3.1 kW.

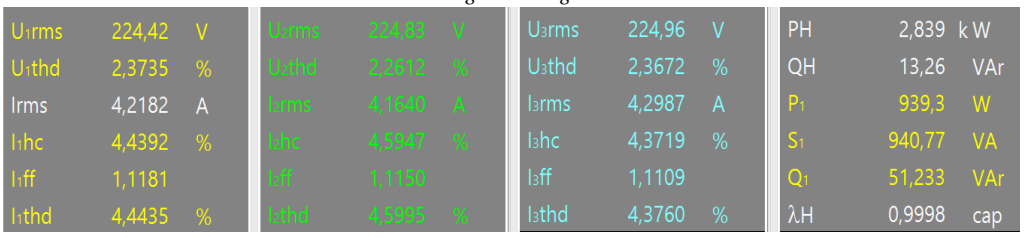

(b) THD at 4.2 A rms, $i_g^d = 6$ A, $i_g^q = 0$ A.

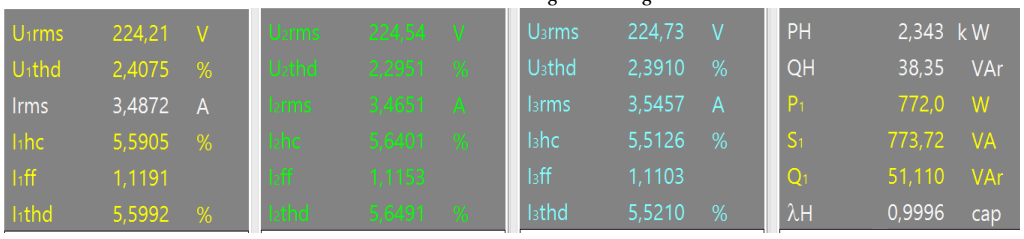

(c) THD at 3.5 A rms, $i_g^d = 5$ A, $i_g^q = 0$ A.

Figure 4.49: Three-phase grid injected rms current, rms voltage, harmonic THD, power factor, real power, apparent power, reactive power measured with the NormaX power analyser. The lower gain current controller was used for this measurement.

The input power quality of the DC bus has a significant effect on the current output THD and should be considered when designing a grid-tie VSC and filter. However, the literature reviewed in this project did not account for DC bus power quality and assumed a static DC voltage to calculate the parameters for output filter. Thus, to accurately measure the THD of the injected grid current in the scope of this project, it is essential to maintain a static DC bus voltage. In simulation the DC bus voltage is ideal, remaining fixed at 600 V, thus accurately estimating the current THD produced only by the output of the VSC and LCL-filter. In practice a DC bus with no ripple current or voltage is difficult to achieve with a three-phase rectifier (only available equipment), thus an additional capacitor bank of 5000 mF was added to the DC bus to help alleviate the ripple. The capacitor bank was effective and reduced the overall measured THD by 3%.

4.8 DC Bus Voltage Control

In this section the simulated and measured dynamic response for directly connected back-to-back and separated DC linked back-to-back DC bus voltage control, are presented in section 4.8.1 and section 4.8.2 respectively. Tests are conducted using the apparatus detailed in appendix B.2 whereby two back-to-back VSCs are directly connected with two standard high voltage $16^2\ mm$ cables. To emulate a cable at any length and cross sectional area, a variable power resistor and an additional inductance are added to the original high voltage DC cable. This allows the impedance of the cable to be adjusted for the 150 m and 450 m cable tests. In reality large wind gusts cause dynamic spikes in DC bus voltage from momentary bursts of input power from the turbine. To evaluate an exaggerated case of this several ascending power steps, up to rated power, are applied to the system. No emulated turbine is considered in this part of the experiment, instead torque steps are applied directly to the RSG controller and the prime mover holds the RSG at rated speed (1500 rpm).

4.8.1 Directly-Connected DC Bus Voltage Control

To test the response of the directly connected DC bus voltage controller, rated positive and negative grid current steps were applied over 2-second intervals. In simulation the bidirectional power flow is very stable and the controller bandwidth can be increased substantially without instability, as shown in fig. 4.50a. However, practice measurements, presented in fig. 4.50b, show that the controller gains must adhere to reduced gain, (3.105), to maintain static stability ($\boldsymbol{i}_{\mathrm{s}}^{k}(t) = 3.8\,\mathrm{A}$, $u_{\mathrm{dc}}(t) = 600\,\mathrm{V}$). Instability increases as power absorption increases, resulting in large oscillations in DC bus voltage. In this project only a low power input from the grid is required to initially charge and maintain the DC bus at 600 V when the generator is not operational, thus the complica-

tions of achieving stable bidirectional power flow can be avoided. The response of the controller is thus satisfactory with settling times below 10 ms.

The response of DC bus controller has a significant effect on current THD and it is therefore preferable to use a lower bandwidth in this application. Obviously it must remain stable and not allow for too much overshoot. Preventing voltage drift and keeping the DC voltage at 600 V is also important for the performance of the LCL-filter. Higher DC voltage produces a larger PWM pulse over L_f thus increasing the inverter current ripple, which increases the THD on the grid side and the IGBT stress. The balance between these two aspects is complicated and requires significant investigation and is unfortunately outside the scope of this research.

Table 4.8: DC controller gains and their linearisation points.

Back-to-back VSC Parameters	Simulation	Practical
Rated power	3 kW	2.3 kW
$I_{dc,rated}$	5 A	3.8 A
Switching frequency	10 kHz	"
Sampling frequency	continuous	10 kHz
u_{dc} and C_{dc}	600 V and 2 × 500 µF	"
C_{dc}	2 × 500 µF	"
Grid / LCL-filter parameters		
$\hat{u}_{\mathrm{g}}$	$\sqrt{2}\cdot 230$ V	"
f_{g}	50 Hz	"
$R_{\mathrm{g},\Sigma}$	1.2 Ω	"
$L_{\mathrm{g},\Sigma}$	25.3 mH	"
Controller gains and time constants		
$V_S(i_g^{d,*}, u_{dc}^*)$	$1.5615e^3$	$1.5785e^3$
$T_V(i_g^{d,*})$	$-4.8444e^{-4}$	$-3.5367e^{-4}$
$i_g^{d,*}$	-5.4024	-3.9870
$V_{n,dc}$	0.5288	0.7165
$T_{n,dc}$	0.0163	0.0130
Solver	Ode3 (Bogacki-Shampine)	N.A
Time step	50 µs	N.A

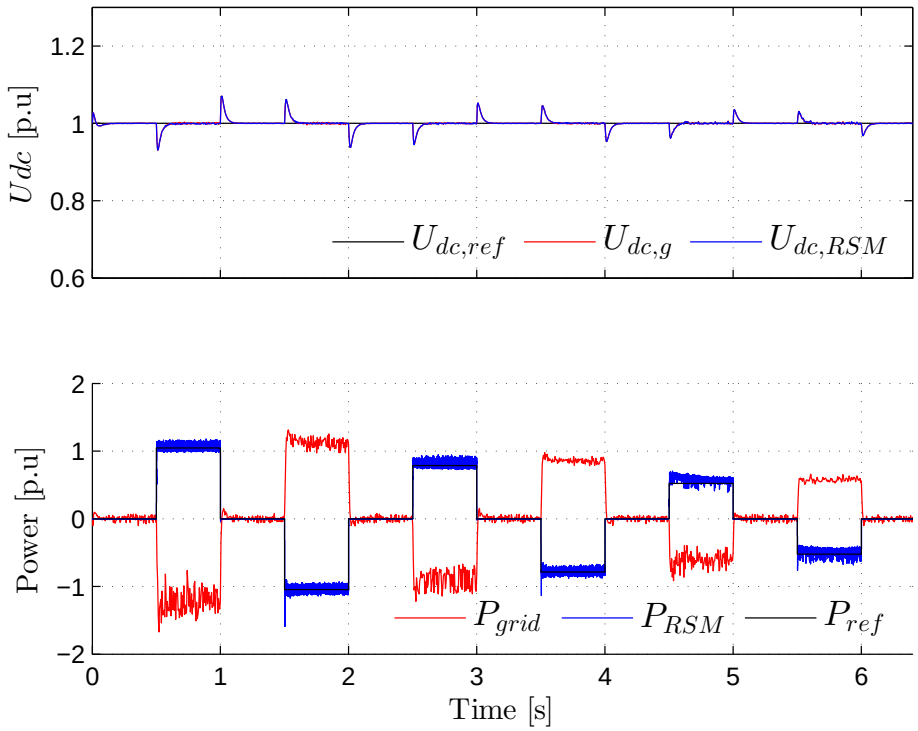

(a) Simulated DC bus voltage response to bidirectional power flow.

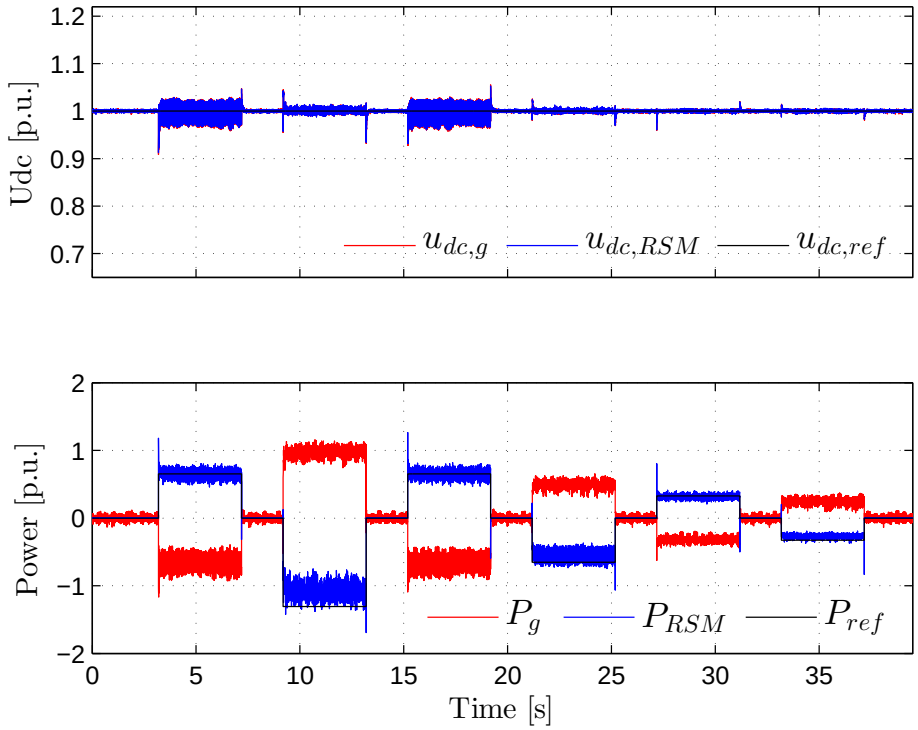

(b) Measured DC bus voltage response to bidirectional power flow.

Figure 4.50: Simulated and measured DC bus voltage response to bidirectional power flow through a directly connected back-to-back VSC with a DC bus voltage regulated to $U_{dc,rated}$ = 600 V. Rated power is 3 kW and 2.3 kW respectively.

4.8.2 Separated DC Link Cable DC Bus Voltage Control

The dynamic response of the DC bus controller with a long DC link cable was tested by emulating the transmission cables' resistance and impedance using various inductors and a high power potentiometer. It will be shown that the DC bus control of the grid side VSC functions as if the cable impedance is not present and maintains the DC bus reference of 600 V. The implications of this are that for grid power injection to occur, the RSG side DC bus voltage must rise above the nominal 600 V to overcome the cable impedance. According to the South African Electrical Standards, SANS 10142-1:2003, the voltage drop for single-phase circuits should not exceed 5% of the cable terminal voltage (30 V @ 600 V DC). Therefore, the correct cable diameter and impedance for a single core, twin 150 m cable carrying rated current (4 A DC @ 600 V) is 1.5 mm^2 with an impedance of $4.62 + 0.0423\,j\Omega$. The current carrying capacity of this cable is 21 A. To consider the effects of a cable which is not properly rated, a cable length of a 450 m ($13.86 + 0.1269\,j\Omega$) is also tested.

The simulated and measured dynamic responses for the 150 m and 450 m DC-link are presented in figs. 4.51 and 4.52 respectively. Measurements show that despite a relatively large cable inductance (22.0 mH at 450 m), the response dynamics remain very similar to those of a directly coupled back to back VSC with the exception of the resistance voltage drop. The inductance of the cable has no significant effect on the transient response of the bus voltage because the harmonics in the transient decay rapidly due to the capacitance of the DC bus. However, the DC bus does become sightly more unstable and requires a further reduction in bandwidth to maintain static stability. A possible explanation for this non-minimum phase behaviour is that the time constant of LCL-filter and the change in its magnetic energy constrains the time derivative of the DC-link when the system transfers power to the RSM (motor mode). The addition of inductance to the DC-link only exacerbates this behaviour, because the energy from the grid has to be stored in the DC-link before it can be transferred into the VSC.

Synchronous rectification (power absorption) at rated current was not tested due to the instability witnessed in simulation and during initial practical tests. It was observed that the DC-link resistance voltage drop causes the DC bus voltage on the RSM side to drop below the allowable limit for the VSC to function without voltage saturation. This saturation is visible in fig. 4.52a in the first power step which cannot reach rated power because there is not enough voltage to drive the RSM.

Table 4.9: DC-link parameters, controller gains and linearisation points.

Back-to-back VSC Parameters	Simulation	Practical
u_{dc} and C_{dc}	600 V and 2 × 500 µF	"
C_{dc}	2 × 500 µF	"
$R_{\mathrm{dc},150}$	4.64 Ω	"
$R_{\mathrm{dc},450}$	13.86 Ω	"
$L_{\mathrm{dc},150}$	6.7 mH	"
$L_{\mathrm{dc},450}$	22.0 mH	"
Grid / LCL-filter parameters		
$\hat{u}_{\mathrm{g}}$	$\sqrt{2}\cdot 230$ V	"
f_{g}	50 Hz	"
$R_{\mathrm{g},\Sigma}$	1.2 Ω	"
$L_{\mathrm{g},\Sigma}$	25.3 mH	"
Controller gains and time constants		
$V_S(i_g^{d,*}, u_{\mathrm{dc}}^*)$	$1.5615e^3$	$1.5785e^3$
$T_V(i_g^{d,*})$	$-4.8444e^{-4}$	$-3.5367e^{-4}$
$i_g^{d,*}$	-5.4024	-3.9870
$V_{n,dc}$	0.1322	0.1791
$T_{n,dc}$	0.0298	0.0232
Solver	Ode3 (Bogacki-Shampine)	N.A
Time step	50 µs	N.A

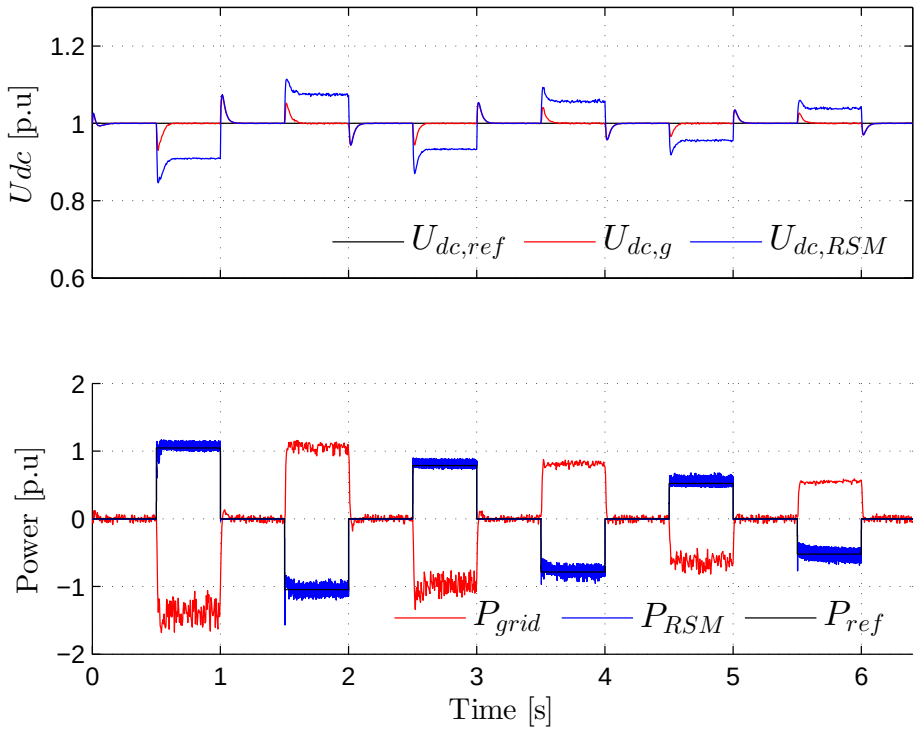

(a) Simulated 450 m DC link bus voltage response to bidirectional power flow.

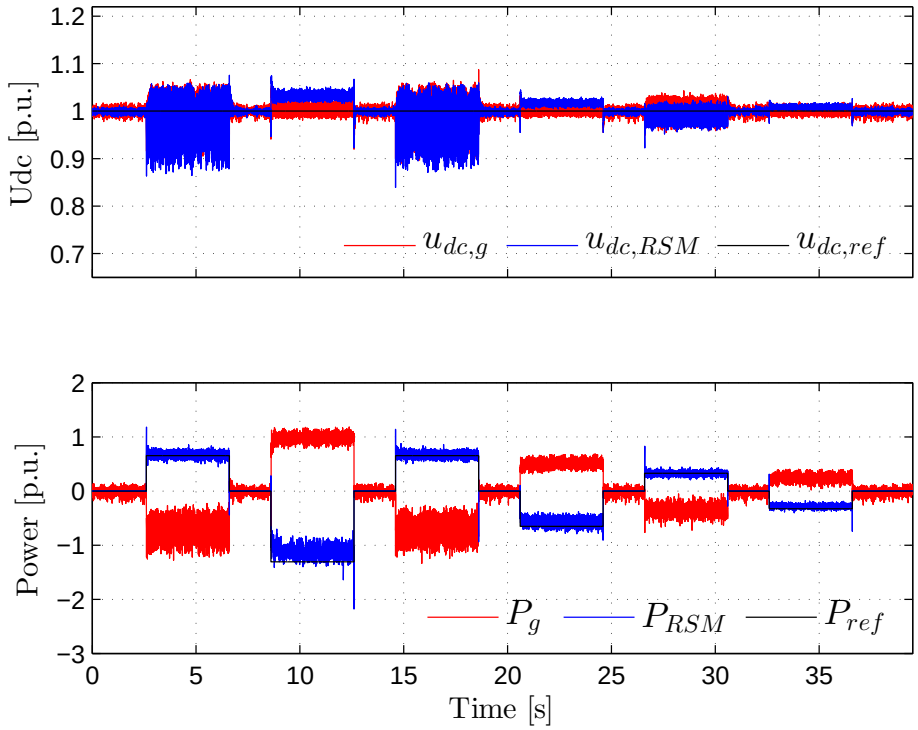

(b) Measured 450 m DC link bus voltage response to bidirectional power flow.

Figure 4.51: Simulated and measured DC bus voltage response to bidirectional power flow through a back-to-back VSC separated using a 150 m cable. The grid side DC bus voltage is regulated to $U_{dc,rated}$ = 600 V. The rated power is 2.3 kW.

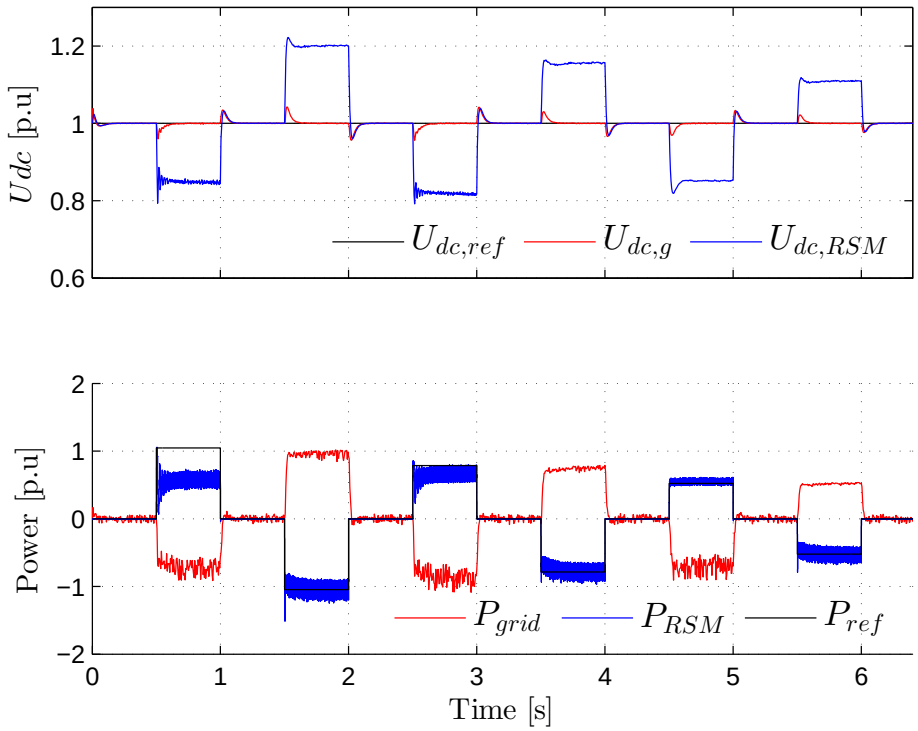

(a) Simulated450 m DC-link bus voltage response to bidirectional power flow.

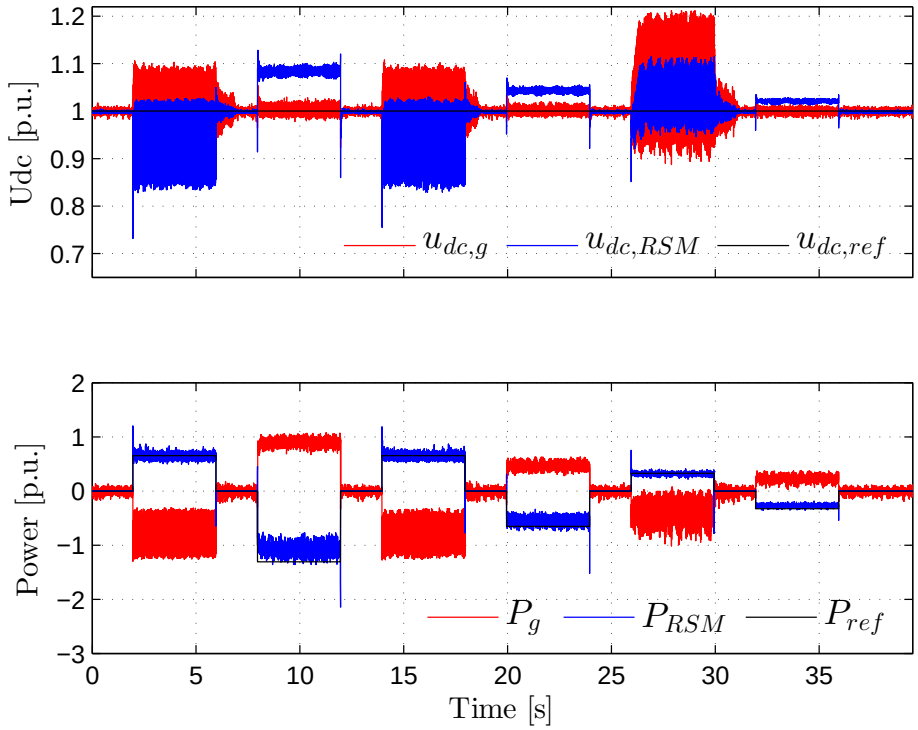

(b) Measured 450 m DC-link bus voltage response to bidirectional power flow.

Figure 4.52: Simulated and measured DC bus voltage response to bidirectional power flow through a back-to-back VSC separated using a 450 m cable. The grid side DC bus voltage is regulated to 600 V.

4.9 Wind Turbine System Control and Emulation

The practical and simulated results for the non-linear wind turbine controller in above and below rated wind speeds are described in this section. The section begins with a detailed analysis of the results obtained from simulation and practical tests on an emulated ∅ 3.8 m rotor wind turbine, which is detailed in appendix B.2.5.

4.9.1 Non-linear Wind Turbine Control

In fig. 4.53 the simulated performance of the WTS throughout regions II and III is illustrated. The turbine speed is precisely controlled to regulate the c_p and electrical output power. For the first set of results the turbine DC-link voltage was set to 600 V, but this proved to be too low to provide enough voltage to operate the RSG at high speeds due to saturation of the VSC output voltage. This is indicated in sections 4.9.1 and 4.9.1 by the deviations in the RSG torque and current references $\boldsymbol{i}^k_{s,ref}$, $T_{m,ref}$, which occur only in the high-speed regions. The DC bus voltage was subsequently raised to 700 V, so that higher rotor speeds could be achieved, to further demonstrate the power limiting capability. A higher rotor speed allows better power limiting (higher stall speeds) at greater over-rated winds speeds, as shown in fig. 4.54. In both cases the DC-bus voltage, RSG torque and grid injected power, remain controlled.

Practical measurements were taken using the WTS emulator, discussed in appendix B.2.5, under both direct and indirect FOC. The tests of the WTC under PSC are omitted here to reduce the length of this document and because the performance of open-loop torque control under FS-PSC was already verified in section 4.5.1. However, it was observed that there was almost no difference in the WTS results between encoder and PSC in both simulation and in practice. The start-up of the WTS using the AHFI-PSC is also verified in section 4.5.3 and is not dealt with here. Investigations of the WTC using PSC Direct FOC LC-filter tests was not conducted on the WTS emulator for the same reasons.

The results presented were achieved using an encoder and a 150 m DC-link cable at a fixed DC bus voltage of 600 V in accordance with the LCL-filter design in section 3.4.3. The DC voltage at the terminals of the DC input of the RSG VSC could not be recorded due to a lack of ADC ports on the Pentium system. Therefore the DC bus voltage on the RSG VSC side was calculated using the output power and the known DC-link resistance to give a voltage estimate. Figure 4.55 shows that the practical measurements agree very well with simulations. Spikes in output power in region III are also observed and are purely due to saturation of the VSC output voltage as in the simulated results, which causes an incorrect torque output. A brief confirmation of this is shown in fig. 4.56 where the same test was conducted with a 700 V DC bus and no saturation of the VSC output voltage occurs.

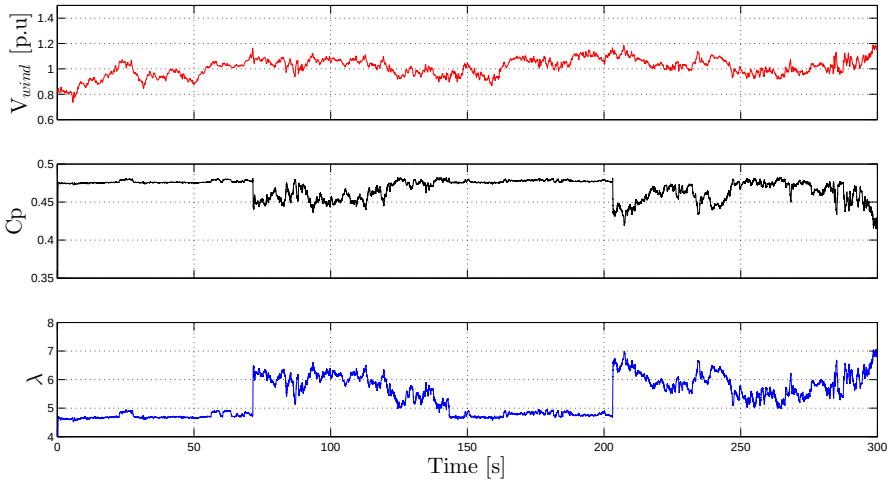

(a) Wind speed, turbine c_p and TSR.

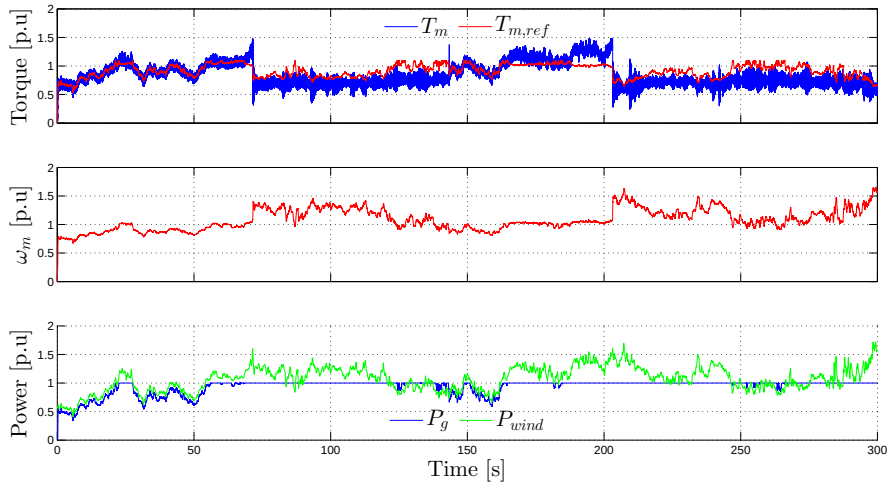

(b) RSG torque, speed, available wind turbine power and grid injected power.

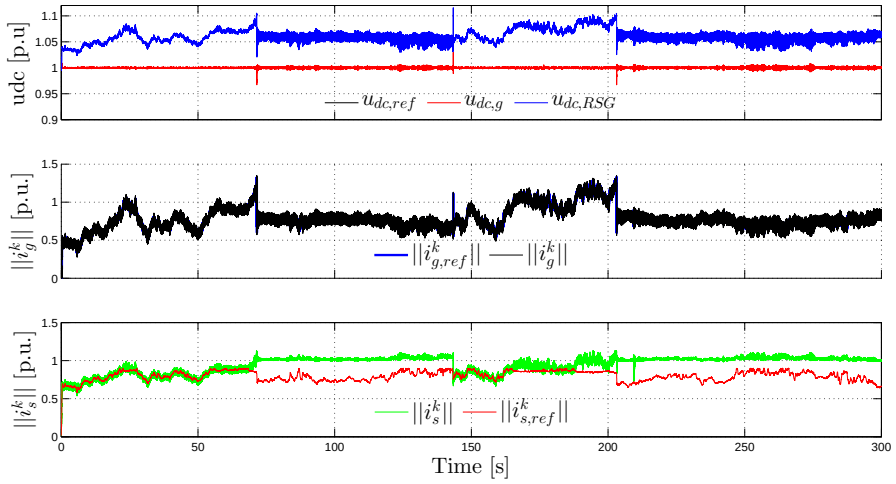

(c) DC bus voltage at both the terminals for a 150 m DC-link, RSG and injected grid current.

Figure 4.53: Simulated results for 300 s of the WTS controller over regions II and III.DC-link at 600 V DC.

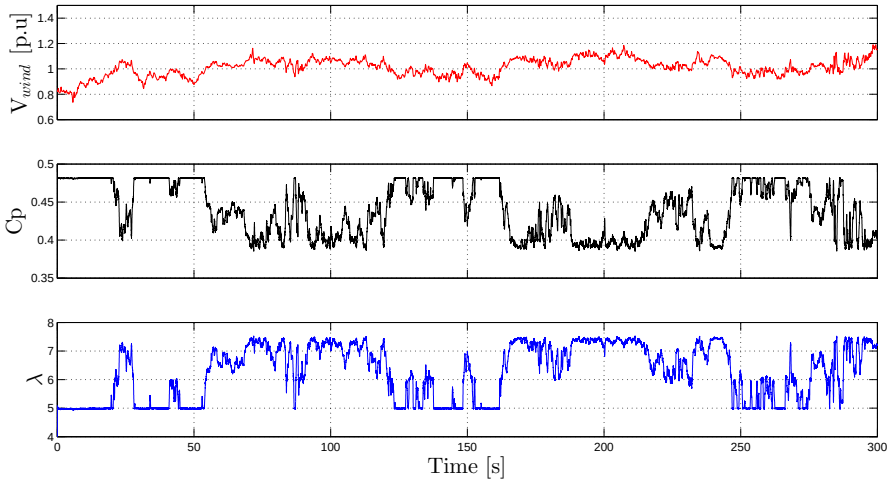

(a) Wind speed, turbine TSR and c_p.

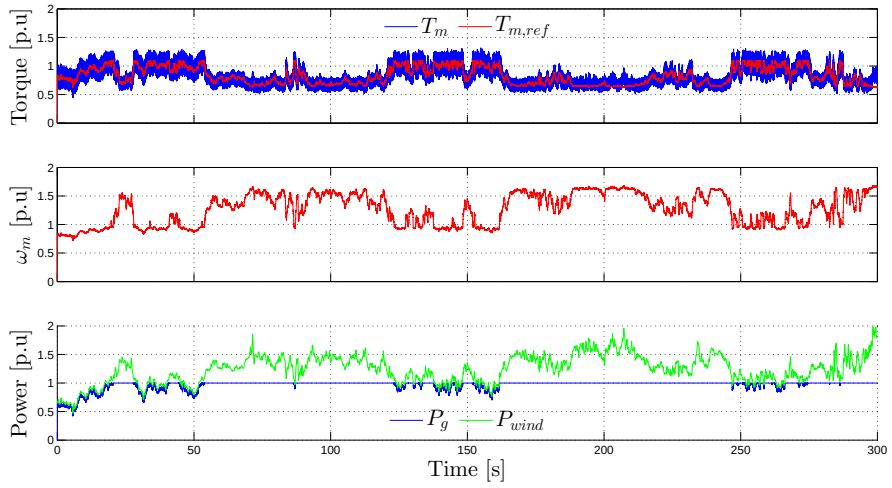

(b) RSG torque, speed, available wind turbine power and grid injected power.

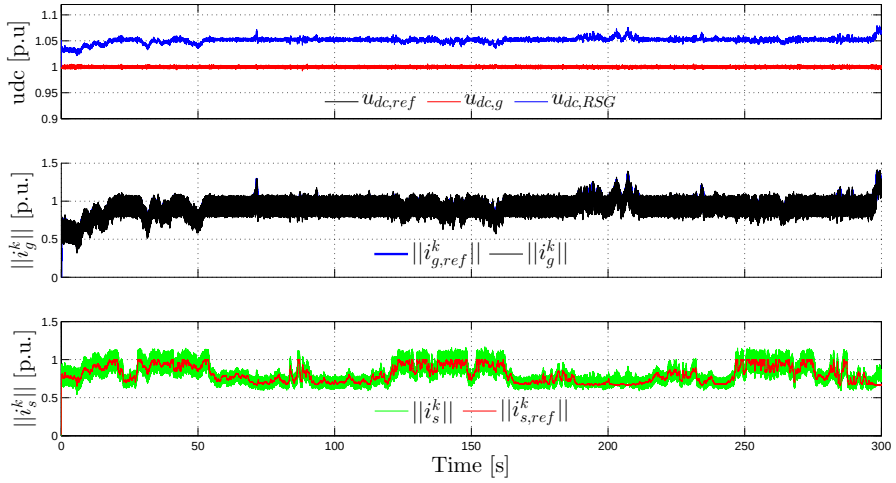

(c) DC bus voltage at both the terminals for a 150 m DC-link, RSG and injected grid current.

Figure 4.54: Simulated results for 300 s of the WTS controller over regions II and III.DC-link at 700 V DC.

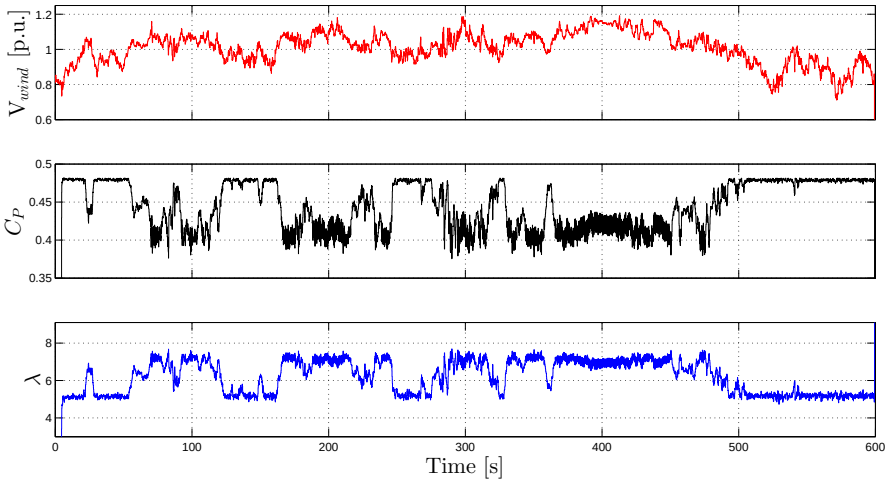

(a) Wind speed, turbine TSR and c_p.

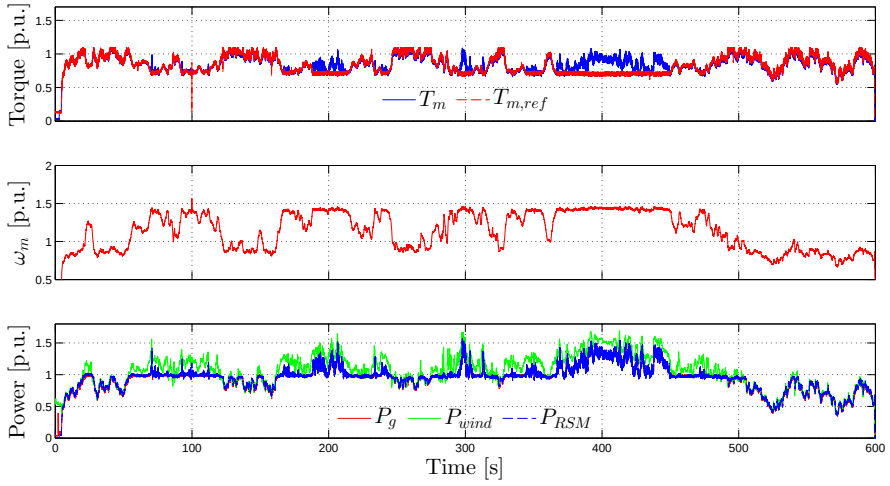

(b) RSG torque, speed, available wind turbine power and grid and RSG power.

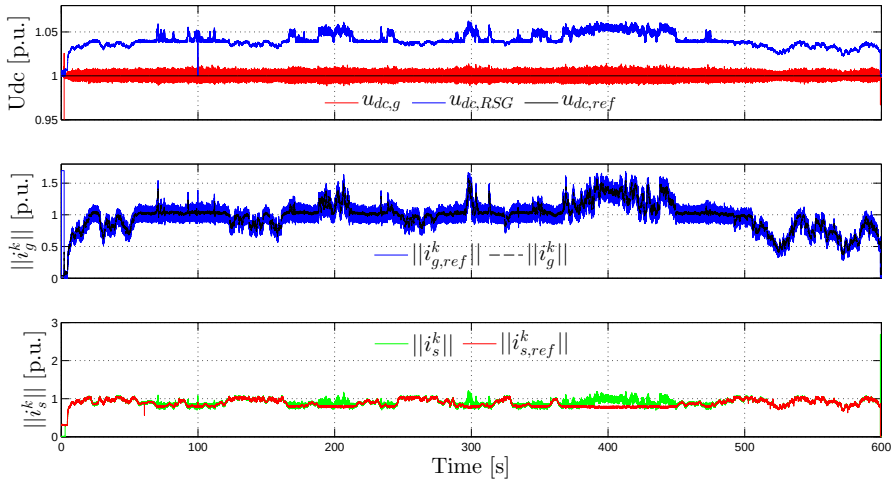

(c) DC bus voltage at both the terminals for a 150 m DC-link, RSG and injected grid current.

Figure 4.55: Measured results for 600 s of the WT emulator and WT controller over regions II and III using an encoder. DC-link at 600 V DC.

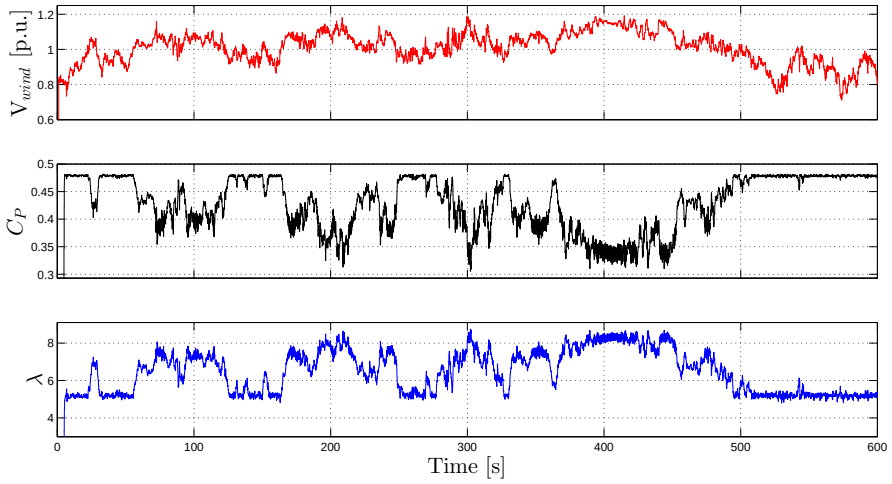

(a) Wind speed, turbine TSR and c_p.

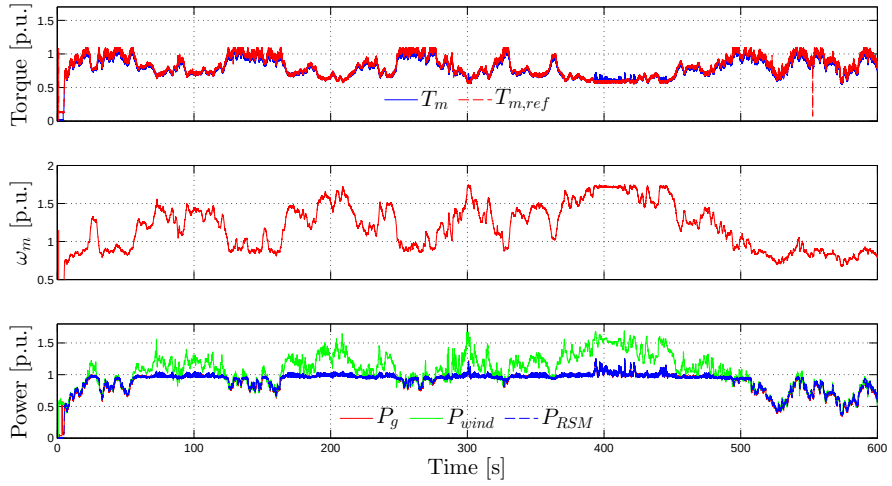

(b) RSG torque, speed, available wind turbine power and grid and RSG power.

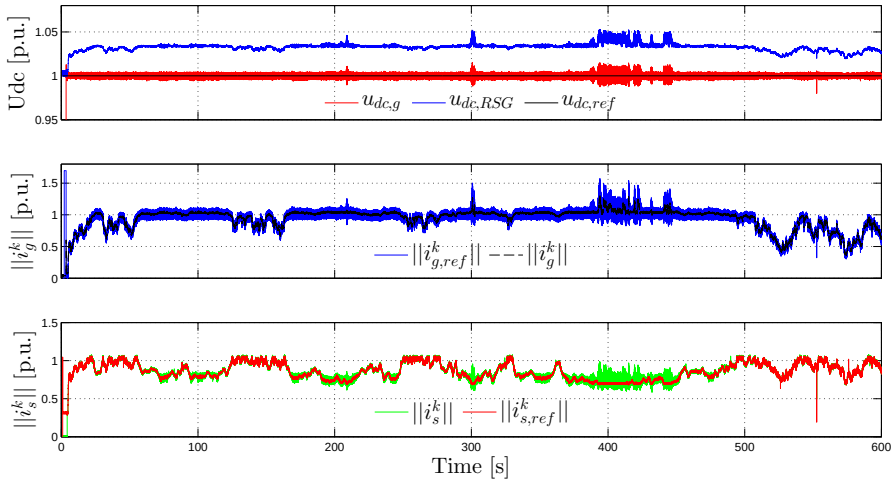

(c) DC bus voltage at both the terminals for a 150 m DC-link, RSG and injected grid current.

Figure 4.56: Measured results for 600 s of the WT emulator and WT controller over regions II and III using an encoder. DC-link at 700 V DC.

Chapter 5

Conclusions and Recommendations

In this chapter conclusions are drawn from the various sections of this thesis, the progress made is outligned and recommendations for future work are made.

5.1 Conclusions

There is still much progress to be made with regard to small-scale wind turbine systems (SSWTSs) by reducing costs and improving efficiency. Low-cost SSWTSs are particularly attractive to rural areas, which due to socio-economic or infrastructure factors, have no access to the national grid. With this objective in mind, an alternate variable-speed, downwind, fixed-pitch HAWT system was proposed. The modification of certain features of standard SSWTSs such as the elimination of the furling system, hydraulic pitching mechanisms and the inclusion of a gearbox and a reluctance synchronous generator (RSG), reduces cost and increases reliability, but also introduces several electrical and control challenges, which are the main focus of this thesis. Splitting the VSCs with a DC-link brings several benefits and overall increases the reliability and efficiency of the system. The RSG (on small-scale) also brings significant cost and efficiency benefits, and can be accurately torque controlled using FOC and PSC. Model- and saliency-based PSC techniques can easily be applied to the RSG (due to its salient properties). PSC adds significant value to the system and is necessary to ensure the feasibility of a SSWTS with the RSG.

Matlab was used extensively to analyse and synthesise collected data. Matlab Simulink was used for simulation of the control theory and various systems. Practical testing of the the systems and their control techniques was achieved using a rapid prototyping Pentium system developed by previous students. This system operates on Linux and allows control algorithms to be implemented easily in C-code and the data from tests to be viewed on-line as well as recorded for later analysis. The Pentium system integrates with customised SEW inverters which are used to actuate and measure various electrical

machines.

5.1.1 Conclusions: Small-Scale Wind Turbine System Layout

Although the use of power electronics for variable speed WTS, in the form of rated voltage source converters (VSCs), is known to decrease reliability and increase cost, there are several distinct benefits in using them, such as the efficient operation of a WTS over a large wind speed range, while remaining grid-connected, and power quality improvement when augmented with output filters (as opposed to fixed-speed systems). A key aspect of this project is the identification of the optimal layout for the back-to-back VSC in the SSWTS through practical experiments. The focus during this project is on three core system layouts. In layout one, a directly-connected back-to-back converter located in the nacelle and power transmission is achieved with a three-phase cable at the grid voltage, down the turbine tower. In layout two, the back-to-back converter is split by a DC-link transmission cable which links the grid VSC, at ground level, to the generator drive in the nacelle. In layout three, placement of the back-to-back converter is at ground level with the transmission of power achieved through an LC-filter and three phase AC-link cable through the turbine tower to the generator. The ideal layout was found to be layout two, for three main reasons, namely:

- It has the lowest power transmission losses.
- It reduces the cost of the system by eliminating one cable and one slip-ring.
- It reduces the weight and size of the nacelle.
- It provides greater facilitation of PSC or encoder control because the VSC is close to the generator.
- It allows the full rated power of the RSG to be used because an LC-filter is not required.

5.1.2 Conclusions: Small Scale Wind Turbine Control

The wind turbine section of this research focused on the control of small scale variable-speed systems without pitch control. A variable-speed fixed-pitch non-linear wind speed controller that operates seamlessly between above- and below-rated wind speed regions was developed, implemented and tested. The following conclusions are drawn:

- The controller brings the added benefit of limiting the generator current to only rated conditions when stalling the turbine in above rated conditions by increasing

the generator operating TSR. This reduces cost because the turbine can be equivalently matched to its generator size, but limitations to the maximum generator and turbine speed must be considered.

- Maximum power point tracking of the WTS is achieved with lowest cost since the anemometer is avoided. Instead the RSG speed, optimal turbine-specific c_p and λ values are used to calculate an optimal output torque reference.
- The non-linear wind turbine controller performs very well in simulation and in practice.
- The new power reference MPPT allows seamless transition between the MPPT in region II and stall regulation power-limiting in region III.
- Power-limiting is restricted by the maximum speed of the RSG and the DC bus voltage. A higher DC bus voltage and RSG speed would allow the turbine to operate at greater above-rated wind speeds without the need to shut down. The initial 600 V was not enough to allow sufficient stall and operation at above-rated rated wind speeds and was subsequently increased to 700 V.
- There is a trade-off between higher DC bus voltages, which increase switching losses, and the grid-tie VSC output filter size, and the added benefit of operating in over-speed regions, however this was not investigated.
- The PSC methods do not visibly affect the performance of the WTS and achieve similar, if not better, performance to that of an encoder based system. However, if the MTPA and PSC saliency compensation methods are not accurate enough, the torque response of the RSG will suffer. This will lead to a decreases in the c_p of the turbine and offset errors in the power limiting.

5.1.3 Conclusions: RSG Design

The transverse-laminated rotor (RSM) is a relatively new contender to the field of drives and has been shown to be more efficient than the more widely used squirrel cage induction machine. The RSM has significant cost benefits and is not only highly robust, but easy to manufacture. However, there are some draw backs to using the machine, such as the use of an encoder which limits the flexibility, increases cost and reduces reliability. The encoder can be overcome with the use of position sensorless control (PSC) techniques, which were also instigated in this project. A novel reluctance synchronous generator (RSG) designed by Eduan Howard, a doctoral candidate at the electrical machine laboratory at Stellenbosch University, was built specifically for this project. To save time and reduce costs, the rotor of the RSG was optimised to an existing standard SEW

squirrel cage induction motor stator. This is not the ideal stator for an RSG and significant improvements to the RSG performance can be made if the stator is optimised. The rotor was also skewed by 7.5° to improve the torque ripple. The main conclusions with regard to this section are as follows:

- Practical measurements of the RSG did not compare well with simulation due to higher levels of magnetic saturation in the actual machine, which indicates that there is a discrepancy between the actual B-H curves and the ones used in SEM-FEM.
- This decreased the optimum current angle, which was ≈ 10° lower than in simulation and increased the measured flux-linkage maps by ≈ 10%. This occurred for both motor and generator mode.
- The generator mode of the RSG had a significantly reduced power factor and efficiency, 0.66 and 77 % respectively, compared to its operation in motor mode where a power factor of 0.72 and an efficiency of 84% were achieved. This is in contrast to the simulated case which predicted much higher efficiency in generator mode and slightly higher efficiency in motor mode.

5.1.4 Conclusions: RSG Current Control

Non-linear current control of the RSM was investigated and in collaboration with the University of Munich, Kulick and Hackel, a new on-line update current controller for the RSM was developed. This method requires either FEM-based or measured flux-linkage maps in order to calculate the "adaptive" gains and feed-forward compensation voltages. The conclusions are as follows:

- The gain tuning method used for the PI controller, is not limited to the high gain Modulus Optimum (MO) method and can easily be adapted to suit less aggressive schemes. Fast dynamic response is achieved with MO, but additional noise on the stator current can be caused.
- The controller performs exceptionally at all speeds and loads in all operating quadrants, provided that there is enough DC bus voltage to prevent output saturation of the VSC. This is a limitation of the integration anti-wind up.
- The controller is highly robust and can still function adequately with large discrepancies in machine flux map data.

5.1.5 Conclusions: MTPA and Torque Control

To achieve the maximum possible efficiency of the RSM at all loads, a maximum torque per ampere method (MTPA) was investigated and implemented for both generator mode and motor mode. The MTPA operating current vectors are implemented using LUTs, which are calculated off-line using either FEM-based, measured flux-linkage maps or a measured torque map. The following conclusions for this section are drawn:

- If FEM-based flux-linkage maps are used, the torque response will be more inaccurate in generator mode than in motor mode, because the FEM-based models in this project only represented motor mode operation, which typically has a much lower current angle due to end-winding inductance, copper- and core-loss.
- Measured flux-linkage maps correct any error in the motor mode torque response and include the end-winding inductance, copper- and core-loss at the machine speed at which the maps were measured.
- It was found that the best results were achieved from physically measuring the torque at all loads in all quadrants (measured torque map) and using this as the basis for the MTPA off-line algorithm. Set-point deviations of less than 5 % at all generator loads were achieved using this method.
- If the torque map is measured at rated speed the current angles will include components of core loss at that speed. Thus a torque map measured at standstill will incur torque offsets at high speed and vice versa.

5.1.6 Conclusions: RSG Sensorless Position Control

Over the years various PSC methods have been investigated to over come the issue of rotor position sensors. PSC techniques typically utilise a machine's saliency properties or a machine model in order to estimate the rotor angle which is ideally suited to machines such as the RSM. SB-PSC methods such as the alternating high frequency injection (AHFI) have been shown to run at almost all loads and speeds provided there is no heavy saturation, but due to the excitation voltage there is increased torque ripple, and additional DC bus voltage margins are required which limit the maximum operating speed. Typically, SB-PSC methods are used at standstill and upto low speed. This method suffers from a large saliency shift which, if used for any accurate torque control, should be compensated for. However, in this project the AHFI-PSC was used as an auxiliary PSC technique, which operates only at lower speed and standstill and does not operate under any load. For medium to high speed regions the fundamental saliency and model-based methods are preferred. In this project a non-linear fundamental saliency method with saliency compensation was used. This method is independent of current angle, which

allows the use of MTPA, but does require a minimum quadrature saturation current to keep the rotor saliency visible to the estimator. The saturation current is very small, and in this case was 0.19 p.u current which is not enough to have any detrimental effects on the MTPA and motor efficiency in a WTS. Since the FS-PSC cannot be used at low speeds, the development of a hybrid controller that allows both the AHFI- and FS-PSC PSC methods to work seamlessly, was implemented. This hybrid system is based on a hysteresis effect where a speed dependent changeover is used to switch between the separate PLL's of each PSC method. The following conclusions for RSG PSC are drawn:

- Implementation of the FS-PSC is straight forward and requires little tuning compared to the highly sensitive AFHI-PSC.
- Both methods were shown to work in motor and generator mode and exhibit similar saliency shifts in each mode respectively. However, since the AHFI-PSC utilises inductance saliency and the FS-PSC utilises fundamental saliency, the saliency shift error is fundamentally different at various loads.
- Without machine specific saliency shift compensation (SSC), the FS-method cannot be used for accurate open-loop torque control or MTPA of the RSG.
- The SSC curves calculated using FEM-based flux-linkage maps compared well to measured saliency shifts, except for a single anomaly, which is only present with the minimum saturation quadrature axis current. This anomaly caused a shift in the opposite direction to what was indicated by the FEM SSC curve, but did not effect the performance of the PSC technique or torque response.
- Saliency-shift corrected FS-PSC performed well at tested loads and speeds and upto 2 p.u. and 1.5 p.u. respectively. The FS-PSC did not decease or prevent fast dynamic torque response and is shown to be an ideal PSC candidate for the open-loop torque-based WTS.
- The hysteresis approach of switching between the PSC methods does not perform well under high loads and suffers from occasional torque pulses and "pole skipping" during transitions, which are difficult to tune out.
- In WTS applications the transition from AHFI to FS-PSC does not need to be performed under any load provided that the transition speed is low and thus the hysteresis approach is adequate.

5.1.7 Conclusions: Grid-Tie Control

Grid connection of the back-to-back VSC was implemented using a basic open-loop synchronous rotating reference frame current controller. The grid voltage is tracked using

a dq Symmetrical Optimum tuned PLL and the power factor is controlled by manipulations of the dq currents. An LCL-filter was also developed and tested with this control system. The conclusions drawn from this section are as follows:

- Although the LCL-filter design methods adopted from literature produced congruent simulation results, the measured results did not. The main discrepancy found was the larger primary inductor size of, 25 mH, which was required to reduce the THD to less than 5%. This can be further investigated, but is likely due to higher harmonics produced by the VSC and perhaps larger core loss in the filter inductors due to the ferrite core material.
- Similar cases in literature obtained current THD values with primary inductances lower than 10 mH.
- The gain of the current controllers, tuned with the gain aggressive modulus optimum criterion (MO), were also found to negatively affect the THD by increasing noise response. Reducing the controller bandwidth decreased the overall THD by $\approx 3\%$.

5.1.8 Conclusions: RSG Current Control with an LC-filter

Although an output du/dt LC-filter is effective at reducing voltage travelling wave phenomena induced by the impedance of long cables, it has many disadvantages. The additional power factor caused by significant capacitor currents and the filter loss which decreases the performance of the RSG, are its main drawbacks. Torque response and PSC performance when using an LC-filter are significantly affected by the filter due to the discrepancy between stator and VSC quantities and subsequently require adjustment with a LC-filter estimator. The estimator performs adequately in simulation and in practice under both PSC and encoder control, but requires some modifications to be implemented discretely (sample-based system). The conclusions drawn from this section are as follows:

- To obtain accurate open loop torque response, either the stator or the estimated stator currents must be used in the feedback loop. Feedback with the VSC current causes torque offsets.
- Torque ripple is greatly reduced due to the improved stator voltage harmonics.
- A reduction in current controller gain is essential to allow the function of the VSC with the LC-filter. High current controller bandwidth causes instability due to excessive oscillation of the output voltage because the LC-filter slows the response of the applied stator voltage.

- Operating the RSG under AHFI-PSC with an LC-filter, requires that the filter be over-damped in order to prevent instability, which means that the resonant frequency of the filter cannot be used to boost the injection voltage. The start-up torque for the AHFI-PSC is also significantly reduced due to instability.
- FS-PSC functions as normal with the LC-filter estimator, but with an apparent increase in saliency shift angle caused by the estimator.
- Torque set-point offsets are not only caused by the magnitude of i_c, but also by a rotation of the estimated reference frame when under hybrid-PSC, due to an increase in the apparent saliency shift angle.
- Implementing the LC-filter with an emulated AC-link cable destabilises the AHFI-PSC, but does not dramatically affect the FS-PSC, which can function as normal.
- Overall, direct and indirect control with an LC-filter or/and AC-link is difficult to implement, increases the losses of the system and imposes more restrictions of the operating limits of the RSG. It is therefore not an ideal method for operating a generator especially with regard to cost- and efficiency-sensitive systems such as wind turbines.

5.1.9 Conclusions: Direct and DC-linked DC-bus Voltage Control

DC bus voltage control is a widely researched topic with a wide variety of control techniques. Further collaboration on this subject with the University of Munich facilitated the implementation of a non-linear bi-directional DC-bus voltage controller. Although bi-directional power-flow is not strictly needed for this application, special attention was paid during the derivation of the method to the non-minimum phase properties of the DC-bus and distinct boundary conditions for the PI controller bandwidth were provided. The boundaries are derived through the manipulation of linearised DC voltage equations around an operating point and Ruth Horwitz criterion. The dynamic response of this controller with the addition of the DC-link cable inductance and resistance was also investigated, but the DC-link quantities were not included in the derivation of the controller-gain-boundaries in an effort to simplify the derivation and reduce the project scope. The conclusions drawn form the results of this section are as follows:

- The transient dynamics of the the DC-link resemble that of an over-damped LC-filter, due to the large decoupling capacitance of the VSC and cable resistance.
- Although simulated and practical tests correlate well with direct- or separately-connected (DC-link) back-to-back-converters, practical tests show some instabil-

ity when the VSC absorbs power form the grid, which is not present in simulation, but identified in the literature.

- This instability is proportional to the DC-link impedance. Power-flow from the grid destabilises the controller due to the voltage drop over the DC-link resistance, and saturation effects on the grid VSC.

5.2 Recommendations

From the results and practical experience gained in this thesis, the following recommendations are proposed:

- Implementing this SSWTS technology in the field is a corner stone to its development. Customised, small-scale and programmable back-to-back VSCs need be developed so that the power electronic system can be implemented. The turbine blades, gearbox, RSG and braking systems have all be tested in this and previous projects and are ready for deployment. Generic remote monitoring systems can be installed to acquire the relevant data.

- There is a clear trade-off between operating at high DC-bus voltages and the additional loss and cost incurred from the higher voltage stress on the power electronics. This optimisation problem is complex because the basis of the problem is rooted in the duration of operation in the over-speed region, which is highly dependant on wind speed. Thus the duration in which the system operates in the over-speed region could be numerically formulated from locational wind-data to identify what the ideal DC-bus voltage is with regard to cost and power loss.

- One method for dealing with VSC voltage saturation is to dynamically change the DC-bus voltage. This method is attractive because it does not permanently increase the switching losses or output filter inductor size. The output voltage vector can be easily linked to the available DC-bus voltage and if a vector larger than the maximum is selected, the additional DC-bus voltage required is selected. The implications of a dynamically changing DC-bus may have a negative effect on the output THD on the grid side because the filter is designed and optimised around static DC bus voltage.

- Another method for dealing with VSC voltage saturation is to limit the voltage vector to the maximum available DC-bus voltage without changing the output torque. Since the MTPA vector cannot be reached, a less efficient current, but more efficient voltage vector is chosen, typically a vector with more d-axis current than q-axis current. A method which selects the minimum increase in d-axis current

and the minimum decrease in q-axis current to reach the required torque vector would help greatly in any saturation condition.

- It would be more computationally efficient to compile the MTPA LUTs in dq coordinates rather than polar coordinates. This would eliminate the trigonometric operations required to convert polar coordinates back to Cartesian dq co-ordinates on-line.
- An optimised stator should be developed for the RSG and another induction motor rotor purchased from SEW. These two machines can then be extensively tested so that the data can be published.

Appendices

Appendix A

Space Vector Transformations and Modulation

A.1 Space Vector Transformations of Three-Phase Systems

Three-phase electrical systems consist of three voltages and three currents which are spaced 120° out of phase from each other. The currents, placed in a separate reference frame, can shift in phase space independently to the voltages, but remain spaced at 120°. Space vector transformations provide a beautifully elegant and meaningful representation of this system so that all three-phases can be controlled entirely by simple PI-controllers [24]. In this appendix the space vector transformations more commonly used in the control of rotating electrical machines and grid connected power converters applications are reviewed.

A.1.1 Clark and Park transforms

In this section a practical understanding of the Clark and Park transforms in the contexts of grid connected systems and electrical machines is provided. Controlling three-phase sinusoidal signals is a difficult task and is much easier to control DC signals where by simple PI controllers can be used with minimal tracking error. Imagine that three-phase signals can be converted into a representation where there are only two DC quantises, but still represent all the information of the three original signals. This is where the Clark and Park transform are used. The three-phases signals have to be the same voltage and equally spaced in phase by 120° degrees. If the signals deviate from this, errors will be found in the dq quantities.

A.1.2 Clarke Transformation

The simplified Clarke transformation, denoted as $\boldsymbol{T}_{\mathrm{c}}$ and described by (A.1), reduces the order of a three-phase system of tri-dimensional, balanced and symmetric vectors $\boldsymbol{x}_s^{abc}(t) = (x_s^a(t), x_s^b(t), x_s^c(t))^\top \in \mathbb{R}^3$, into a two dimensional system, $\boldsymbol{x}_s^s(t) = (x_s^\alpha(t), x_s^\beta(t))^\top \in \mathbb{R}^3$. It is useful to the imagine the $\alpha\beta$ as vectors rotating at w and of constant magnitudes equal to the peak values of the $\boldsymbol{x}^{abc}$ reference frame vectors and the fundamental frequency w. In actual fact the $\alpha\beta$-reference frame has three vectors α, β, γ where γ can be described as the common mode vector component, which is the arithmetic mean of $\boldsymbol{x}^{abc}$.γ is zero for a balanced three-phase system and is projected into the $\alpha\beta$-reference frame on the z axis (into the page). The rotational matrix $\boldsymbol{T}_{\mathrm{c}}$ is orthonormal (vectors are orthogonal and have a unity norm) which implies that the transformation is invertible (inverse Clarke Transform, (A.2)) and the calculation of electrical power is not altered by the transformation [73]. $\boldsymbol{T}_{\mathrm{c}}$ an be power-invariant, $k = \sqrt{\frac{2}{3}}$, or amplitude-invariant, $k = \frac{2}{3}$. The calculations in this project utilise the amplitude-invariant case. The inverse Clarke transform, $\boldsymbol{T}_{\mathrm{c}}^{-1}$, also exists and allows a transformation back to the three-phase space, as shown in (A.2).

$$\boldsymbol{T}_{\mathrm{c}} = \underbrace{\frac{2}{3}}_{k} \begin{bmatrix} 1 & -\frac{1}{2} & -\frac{1}{2} \\ 0 & \frac{\sqrt{3}}{2} & -\frac{\sqrt{3}}{2} \end{bmatrix}, \tag{A.1}$$

$$\boldsymbol{x}_s^s(t) = \boldsymbol{T}_{\mathrm{c}} \boldsymbol{x}_s^{abc}(t),$$

$$\boldsymbol{T}_{\mathrm{c}}^{-1} = \underbrace{\frac{2}{3}}_{k} \begin{bmatrix} \frac{2}{3} & 0 \\ -\frac{1}{3} & \frac{\sqrt{3}}{3} \\ -\frac{1}{3} & -\frac{\sqrt{3}}{3} \end{bmatrix}, \tag{A.2}$$

$$\boldsymbol{x}_s^{abc}(t) = \boldsymbol{T}_{\mathrm{c}}^{-1} \boldsymbol{x}_s^s(t).$$

A.1.3 Park Transformation

The Park and inverse Park transformation, denoted as $\boldsymbol{T}_{\mathrm{p}}$ and $\boldsymbol{T}_{\mathrm{p}}(\phi)^{-1}$ and described by eqs. (A.3) and (A.4) respectively, enables the transformation of the static $\alpha\beta$-reference frame to a synchronous rotating one, $\boldsymbol{x}_s^k(t) = (x_x^d(t), x_s^q(t))^\top \in \mathbb{R}^2$ and visa verse. In the $\alpha\beta$ reference frame, $\boldsymbol{x}_s^s$, the vectors oscillate at the fundamental frequency ω, but can be reduced to DC vectors, $(x_x^d(t), x_s^q(t))$, if the reference frame rotates with the fundamental/intended frequency, hence the term rotating synchronous reference frame. The synchronous part refers to the intended quantity or angle that is tracked. For electrical machines, such as the RSM, the rotor angle, ϕ_{k} is tracked and is used as the basis for the alignment of the rotating reference frame. For grid connected systems the grid voltage angle,ϕ_{g} is tracked. Essentially, the dq-vectors represent the magnitude and phase of the output signal (e.g. VSC current) with respect to the signal that is tracked (rotor or grid

voltage). In the context of grid connected systems, a synchronised reference frame with only d-axis current as the output vector ,$\boldsymbol{x}_s^k(t) = (1,0)$, will produce a current vector in-phase with the grid voltage vector, i.e. unity power factor. A current vector, $\boldsymbol{x}_s^k(t) = (0,1)$ will produce a current vector 90° out of phase with the grid voltage. Direction of power flow can also be controlled by positioning the vector in one of the four quadrants. In the case of the RSM a vector $\boldsymbol{x}_s^k(t) = (1,0)$ will produce no torque, since the energy in the system is at its lowest, i.e. the rotating reference frame current vector is aligned with the least reluctance d-axis path. In fig. A.1the alignment of the Clark and Park reference frames with respect to eh RSM and the stationary reference frame three-phase stator phases is illustrated.

$$\boldsymbol{T}_{\mathrm{p}}(\phi_{\mathrm{k}}) = \begin{bmatrix} \cos\phi & -\sin\phi \\ \sin\phi & \cos\phi \end{bmatrix}, \tag{A.3}$$

$$\boldsymbol{x}_s^s(t) = \boldsymbol{T}_{\mathrm{p}}(\phi_{\mathrm{k}})\boldsymbol{x}_s^k(t),$$

$$\boldsymbol{T}_{\mathrm{p}}(\phi_{\mathrm{k}})^{-1} = \begin{bmatrix} \cos\phi & \sin\phi \\ -\sin\phi & \cos\phi \end{bmatrix}, \tag{A.4}$$

$$\boldsymbol{x}_s^k(t) = \boldsymbol{T}_{\mathrm{c}}(\phi_{\mathrm{k}})^{-1}\boldsymbol{x}_s^s(t).$$

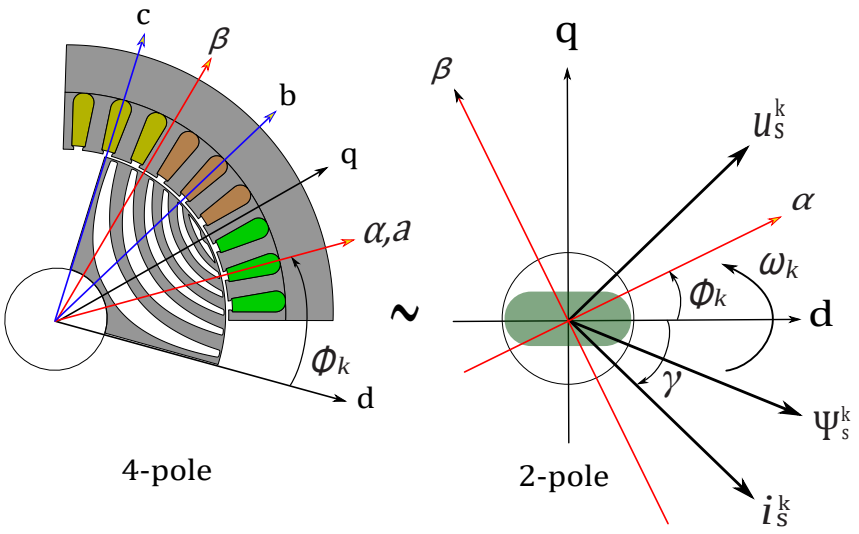

Figure A.1: Current flux and voltage vectors in the dq-reference frame.

A.2 Space Vector Modulation

As mentioned in section 2.3.1, space vector pulse width modulation SVPWM is a widely used PWM modulation scheme used for FOC motor control and more efficiently utilises the DC bus voltage than conventional sinusoidal PWM (SPWM) [1, 24, 75, 76]. As will be shown in this section, SVPWM is also easier to implement in digitally.

The VSC output voltage vector, $\boldsymbol{u}^s_{\mathrm{s},ref}$, in the $\alpha\beta$-reference frame is used as a reference to a sector based switching scheme as shown in fig. A.2. Respectively, the magnitude and angle of this vector are:

$$|\boldsymbol{u}^s_{\mathrm{s},ref}| = \sqrt{u_\alpha^2 + u_\beta^2}, \tag{A.5}$$

$$\theta = atan(\frac{u_\beta}{u_\alpha}). \tag{A.6}$$

In fig. A.2 each sector represents the state of the upper switches in a three-phase bridge, where the lower switches are always opposite to the upper switches and a 1 denotes that the switch is closed as shown in fig. A.3. It is obvious that each switching vector can either be zero or equal to the DC bus voltage and that the inverter can only produce one of the eight switching vectors at any given instant. With this in mind, the principle of SVPWM is straight forward. The desired output voltage vector $\boldsymbol{u}^s_{\mathrm{s},ref}$ is achieved by the superposition of three of the closest of the eight switching vectors so that on average over the modulation period the output voltage vector $\boldsymbol{u}^s_{\mathrm{s}}$ is equal to $\boldsymbol{u}^s_{\mathrm{s},ref}$. The three vectors consist of two active vectors and a third vector, the zero switching vector, V_0, which is either (111) or (000) depending on the modulation scheme and sector.The time period or duty times that each of the three switching vectors will occupy the output voltage is defined by (A.7) and illustrated in fig. A.2, [1, 75]. Where m is the modulation index defined as $m = \dfrac{\sqrt{3}\boldsymbol{u}^s_{\mathrm{s},ref}(t)}{u_{\mathrm{dc}}(t)}$.

$$\begin{aligned}
\int_0^{T_{sw}} \boldsymbol{u}^s_{\mathrm{s},ref}(t)dt &= \int_0^{T_1} u_1(t)dt + \int_0^{T_1+T_2} u_2(t)dt + \int_{T_1+T_2}^{T_{sw}} V_0(t)dt, \\
T_{sw}\boldsymbol{u}^s_{\mathrm{s},ref}(t)dt &= \frac{T_1 u_1(t)}{T_{sw}} + \frac{T_2 u_2(t)}{T_{sw}} + \frac{T_0 V_0(t)}{T_{sw}},
\end{aligned} \tag{A.7}$$

where the total switching cycle is $T_{sw} = T_1 + T_2 + T_0$. The position of u_1, u_2 and V_0 can be defined by the angle and magnitude of $\boldsymbol{u}^s_{\mathrm{s},ref}$ as demonstrated for sector 1 in (A.8). By analysing these vectors in all quadrants we find a general equation, (A.9), that calculates each of the duty times, T_1, T_2, T_0, for each of the sectors ($n = [1:6]$) [1].

$$T_{sw}\boldsymbol{u}^s_{\mathrm{s},ref}(t)\begin{bmatrix} cos(\theta) \\ sin(\theta) \end{bmatrix} = T_1\tfrac{2}{3}u_{\mathrm{dc}}(t)\begin{bmatrix} 1 \\ 0 \end{bmatrix} + T_2\frac{2}{3}u_{\mathrm{dc}}(t)\begin{bmatrix} cos(\frac{\pi}{3}) \\ sin(\frac{\pi}{3}) \end{bmatrix}, \tag{A.8}$$

$$T1 = mT_{sw}.sin(\frac{\pi}{3} - \theta + \frac{n-1}{3}pi),$$
$$T2 = mT_{sw}.sin(\theta - \frac{n-1}{3}\pi),$$
$$T0 = T_{sw} - T1 - T2. \tag{A.9}$$

Now that the three duty times have been calculated the last step is to assign the cor-

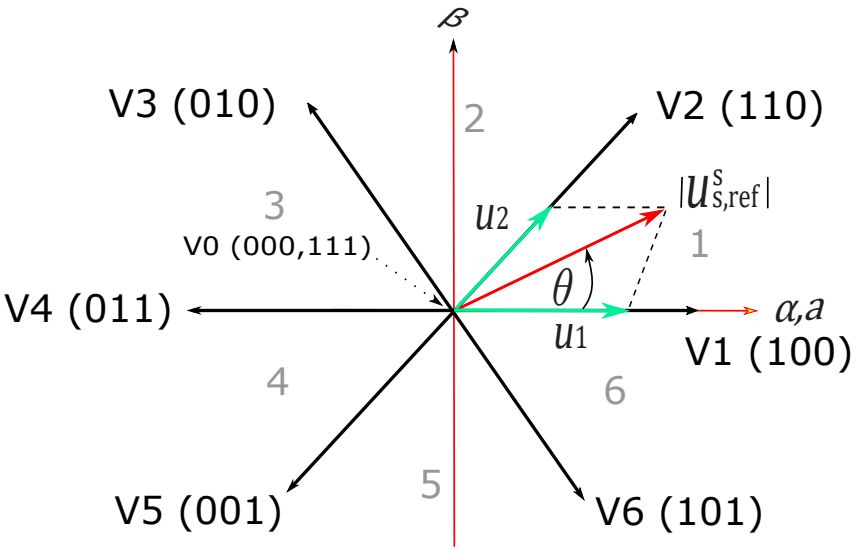

Figure A.2: Switching vectors for each sector in the $\alpha\beta$ reference frame.

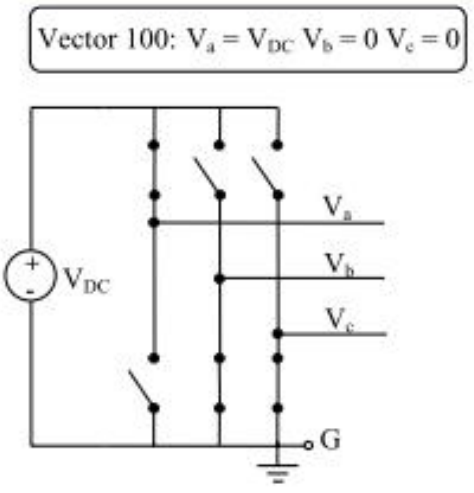

Figure A.3: Switching vector V1 (100) represented on a three-phase bridge [1].

rect time periods to each of the upper and lower switches. There are several ways to assign duty times (edge aligned, center aligned), but in this case a simple symmetrical

center aligned method is demonstrated. As $\boldsymbol{u}^{s}_{\mathrm{s,r}ef}$ rotates through each sector T_{sw} must be divided among seven switching states. e.g for sector 1 the symmetrical sequence is (000,100,110,111,110,100,000) which equates to (A.10). Each sector has its own assortment of duty times for each phase as demonstrated for sector 1 in fig. A.4. The other sectors are recorded in the SVPWM Matlab script in appendix D.0.2 and [1]. To determine the actual ON/OFF time period each switch is on, a saw tooth timer is used and the output duty cycle of each phase, $S1-S6$ are compared to this carrier wave form to produce either a 1 or 0, which then operates the switch.

$$T_{sw} = \frac{T_0}{4} + \frac{T_1}{2} + \frac{T_0}{2} + \frac{T_2}{2} + \frac{T1}{2} + \frac{T_0}{4}, \tag{A.10}$$

Sector	*Duty Time Upper Switches*		*Duty Time Lower Switches*	
1	S1	$T_1+T_2+\frac{T_0}{2}$	S2	$\frac{T_0}{2}$
	S3	$T_2+\frac{T_0}{2}$	S4	$T_1+\frac{T_0}{2}$
	S5	$\frac{T_0}{2}$	S6	$T_1+T_2+\frac{T_0}{2}$

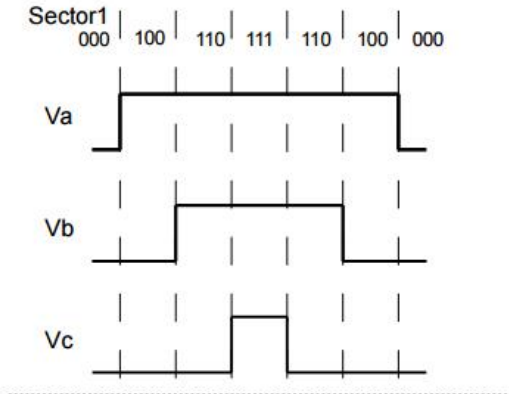

Figure A.4: Duty time and $\boldsymbol{u}^{abc}$ voltage wave form for sector 1 [1].

Appendix B

Practical Setup and Equipment

Practical investigations were carried out on several machines and test-benches during the course of this research. In this appendix the various equipment and electrical layouts used are detailed.

B.1 University of Munich Testing Apparatus

While on exchange in Germany, practical investigations were conducted on a D-space system in the drives laboratory at the University of Munich, depicted in appendix B.1. The D-space system interfaces directly with Matlab and Simulink which makes the implementation of simulations easier. A 20 kW PMSM was used as the prime mover for all test conduced on the 9.6 kW RSM. The two machines are coupled together with torque sensor.

B.2 Stellenbosch Testing Apparatus

The RTAI Pentium Based System developed by the University of Munich is a Linux based real time processor capable of sampling at the high frequencies (>=10kHz) necessary for the control of a PWM VSI. The hardware is comprised of an FPGA which samples measurements and sends PWM singles to and from the drives. The real time operating system runs on a 1.5 GHz pentium processor in Linux and transmits the control signals and data to and from the FPGA at a desired sampling frequency. All control algorithms in Linux are written in C. External sensors can also be connected to the Pentium system through the ADC ports. This was done for a TORQUE SENSOR NAME torque sensor.

The VSI hardware was developed by SEW an international company specialising in drives, machines and drive trains. The SEW VSIs provide the current protection on a hardware level and ensure the correct dead-time switching for an IGBT full bridge. These drives are connected directly to the Pentium system which receives current and voltage

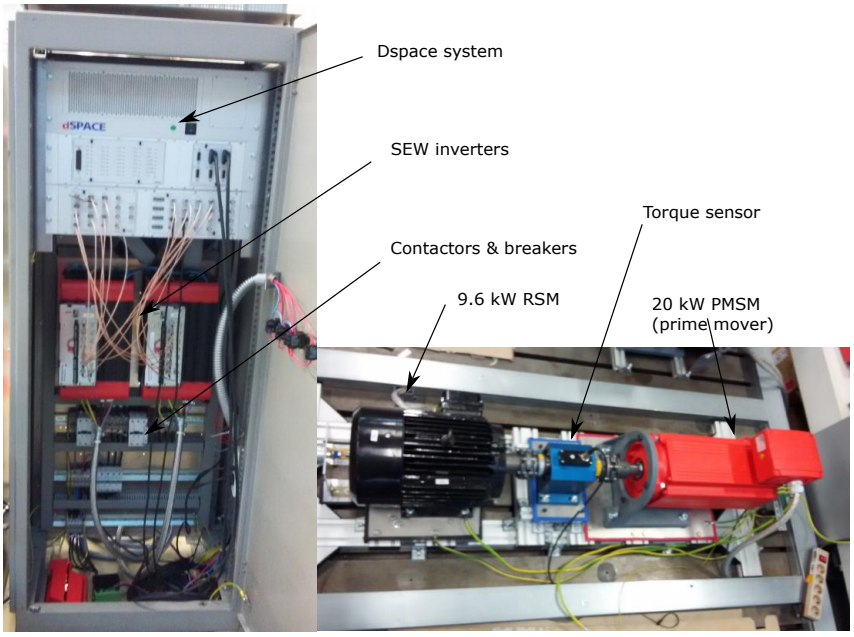

Figure B.1: D-space system at the University of Munich, Germany.

measurements for all three phases and the DC bus. The Pentium system transmits PWM signals via fibre optic cables to the SEW drives. Figure B.3 below illustrates the diagram and photos of the basic layout.

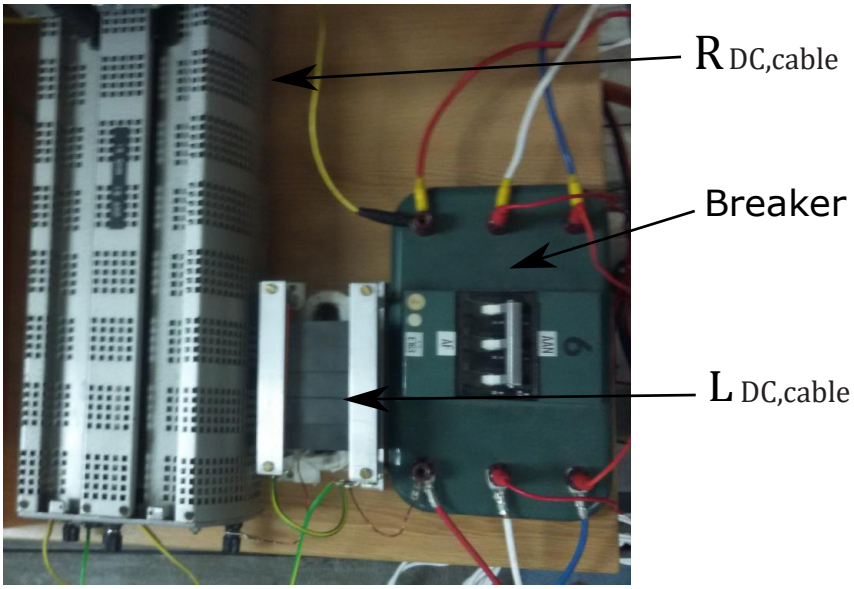

Figure B.2: Emulated DC-link with custom inductor and power resistor.

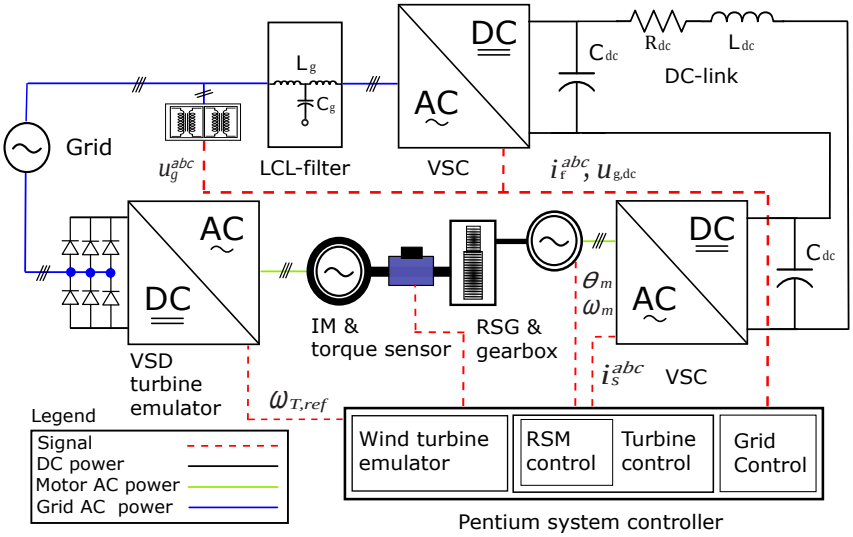

(a) Diagram of the grid tie set-up, IM, and RSG set-up.

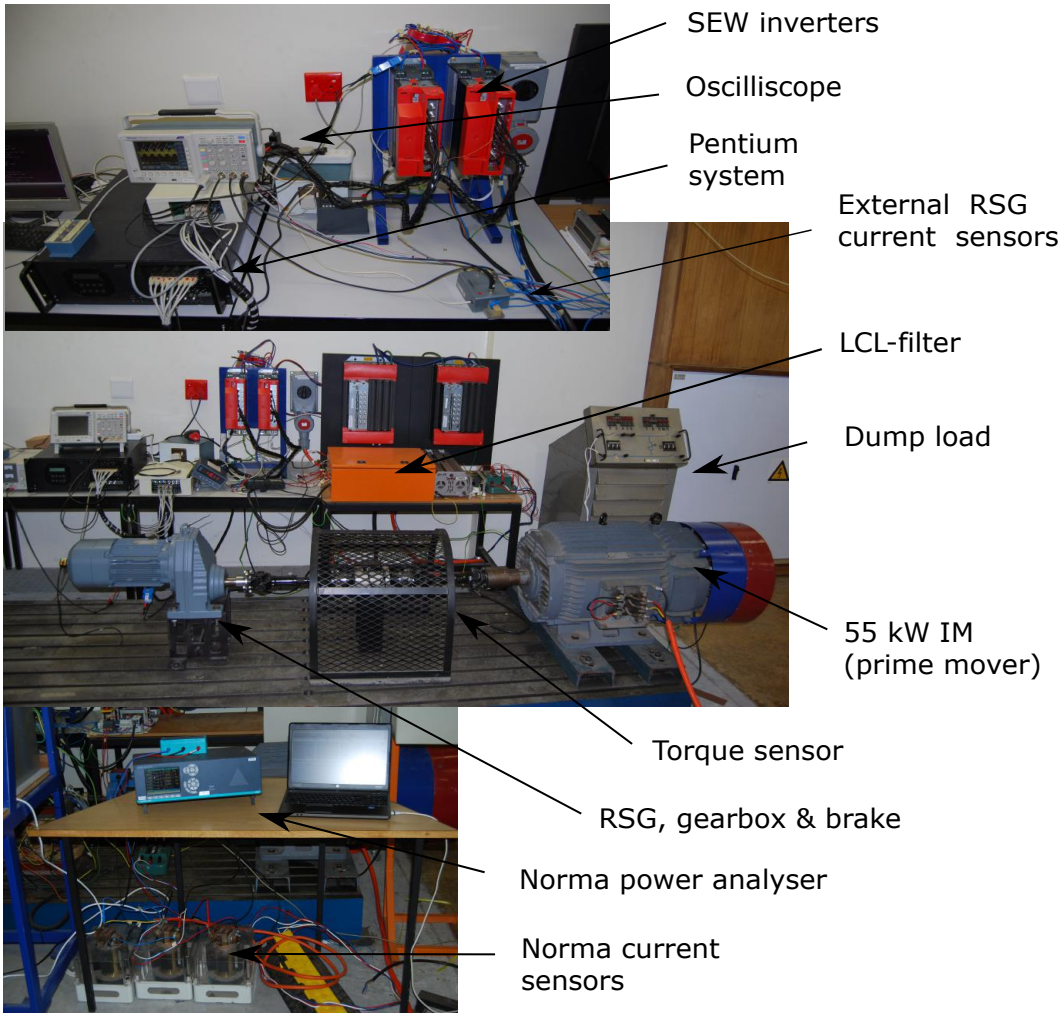

(b) RSG, grid-tie system, Norma power analyser, Pentium system and other measurement instruments.

Figure B.3: Diagram and photo of the grid tie set-up, LCL-filter, IM, various VSCs and Pentium system.

B.2.1 Grid Connection and LCL-filter Testing Apparatus

The grid tie system comprises of the LCL-filter a contractor/breaker, grid voltage measurement isolation transformers and an SEW drive. Figure B.4 shows the LCL-filter that was designed, built and used for testing. The inductors are large and bulky because ferrite cores were used as opposed to laminated steel cores. Ferrite is not the ideal material to used because it is typically used for high frequency applications and subsequently has a poor flux-saturation to size ratio. However, the ferrite cores where abundantly available and free to use, which saved manufacturing and design time.

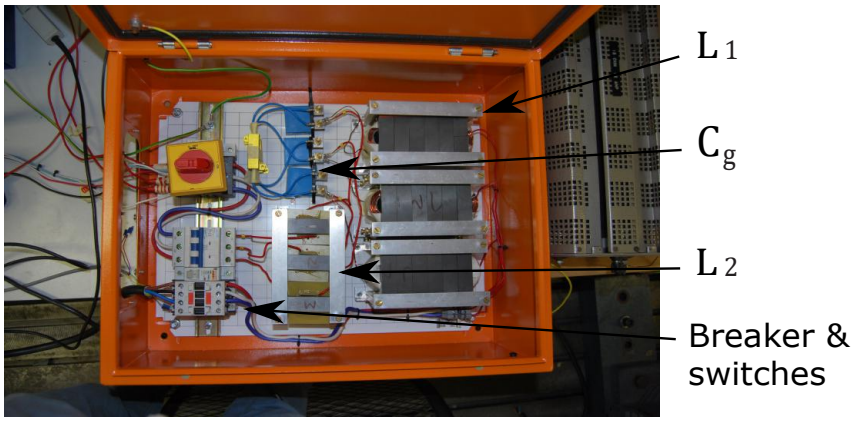

Figure B.4: LCL-filter with breakers in enclosure.

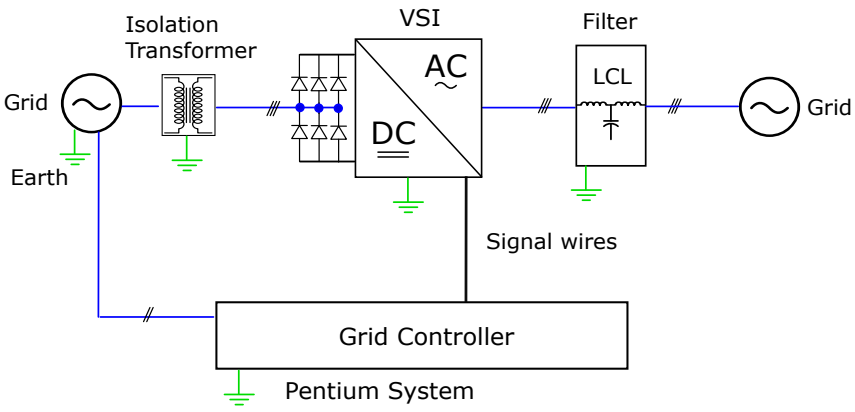

Figure B.5: LCL-filter test set-up.

B.2.2 LC-filter Testing Apparatus

Figure B.6 illustrates the set-up for testing the LC-filter and AC-link.

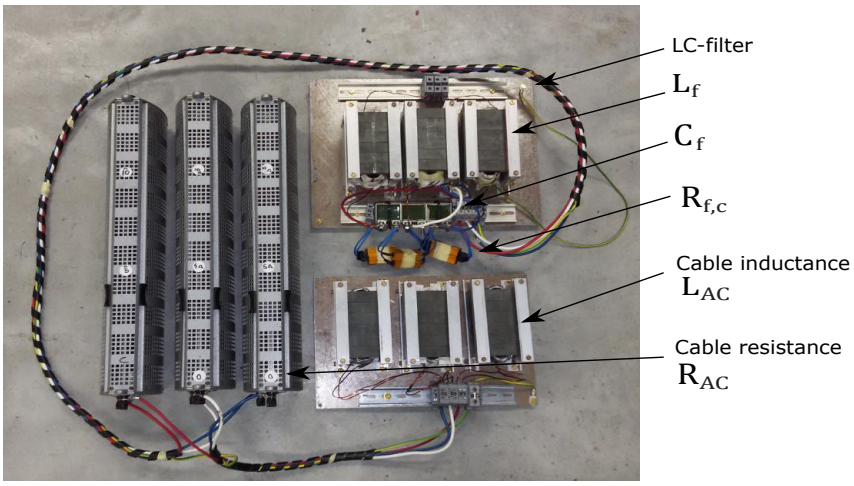

(a)

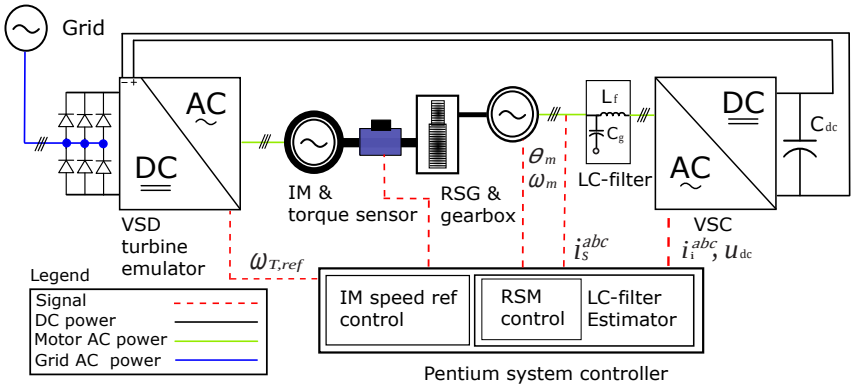

(b)

Figure B.6: (a) Emulated LC-filter with AC-link inductance and resistance. (b) Practical LC-filter testing set-up in the Electrical machines laboratory at the University of Stellenbosch.

B.2.3 Calibration of Various Sensors

The torque sensor was calibrated using the Pentium system and scale measured weights which were placed at different lengths to provide specific torque values up to 129 N.m. Figure B.7a shows the results after calibration. This specific sensor was used because it could be integrated into the pentium system. This allowed torque measurements to be synchronised with all other measurements, i.e. current and speed.

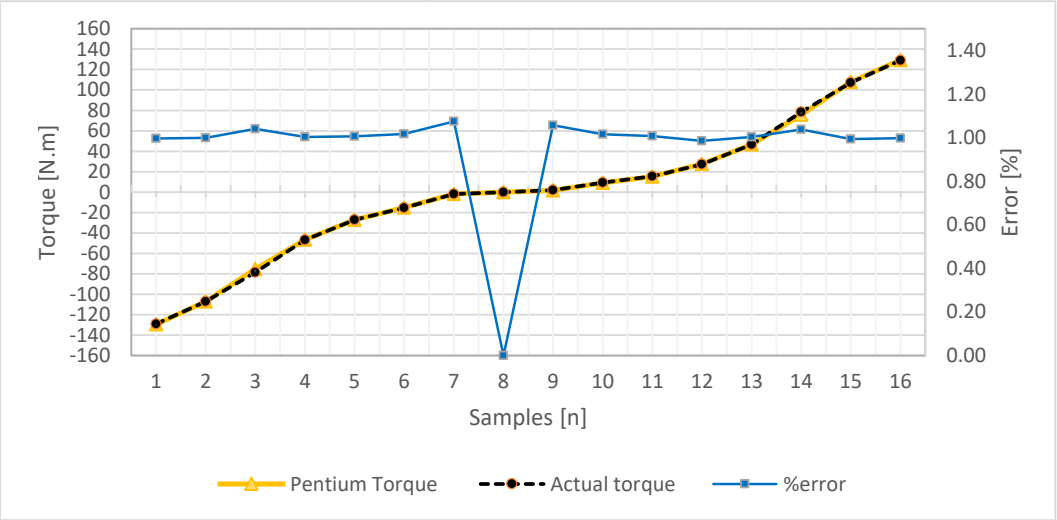

(a) Tokashima torque sensor calibration.

(b) Torque sensor from STKC Technology, Beijing.

Figure B.7: Torque sensor calibration and the torque sensor.

B.2.4 Photos and Diagrams of Laboratory Equipement

The images and diagrams below are the results of the work completed by primarily the author as well as and the machines laboratory at the University of Stellenbosch.

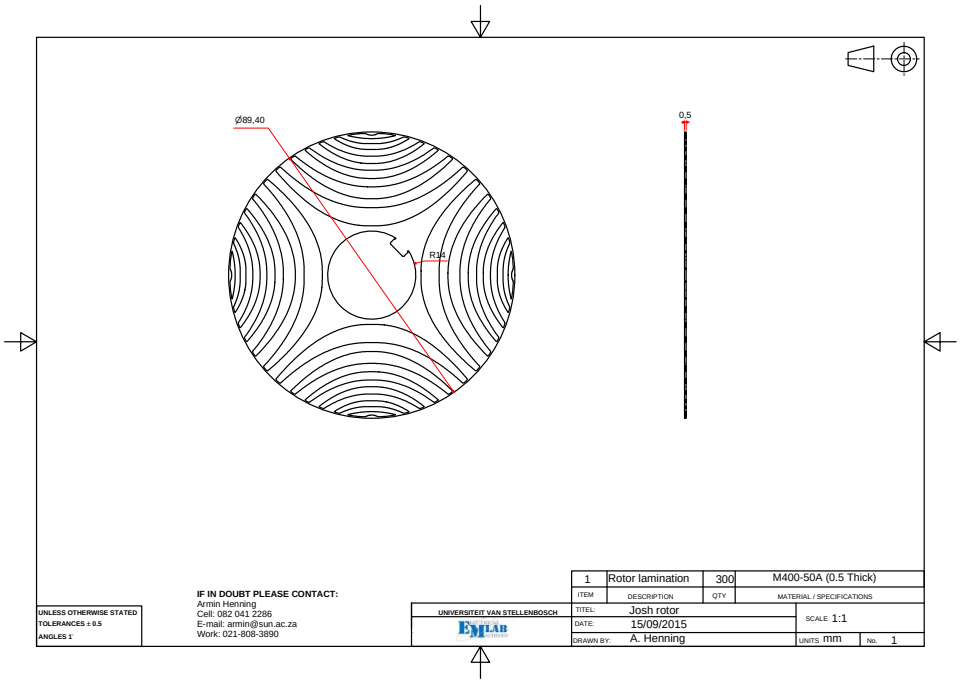

Figure B.8: RSM rotor shaft with skewed key way.

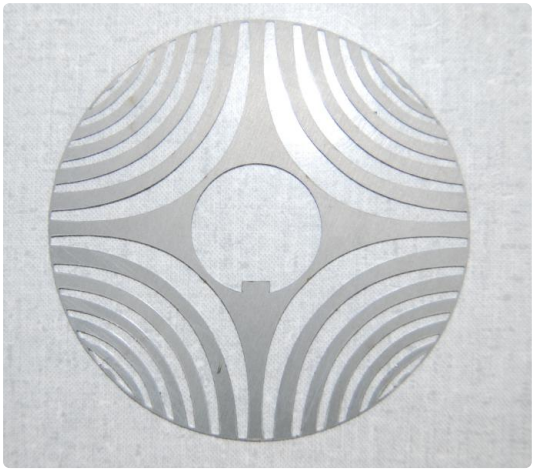

Figure B.9: RSM rotor lamination.

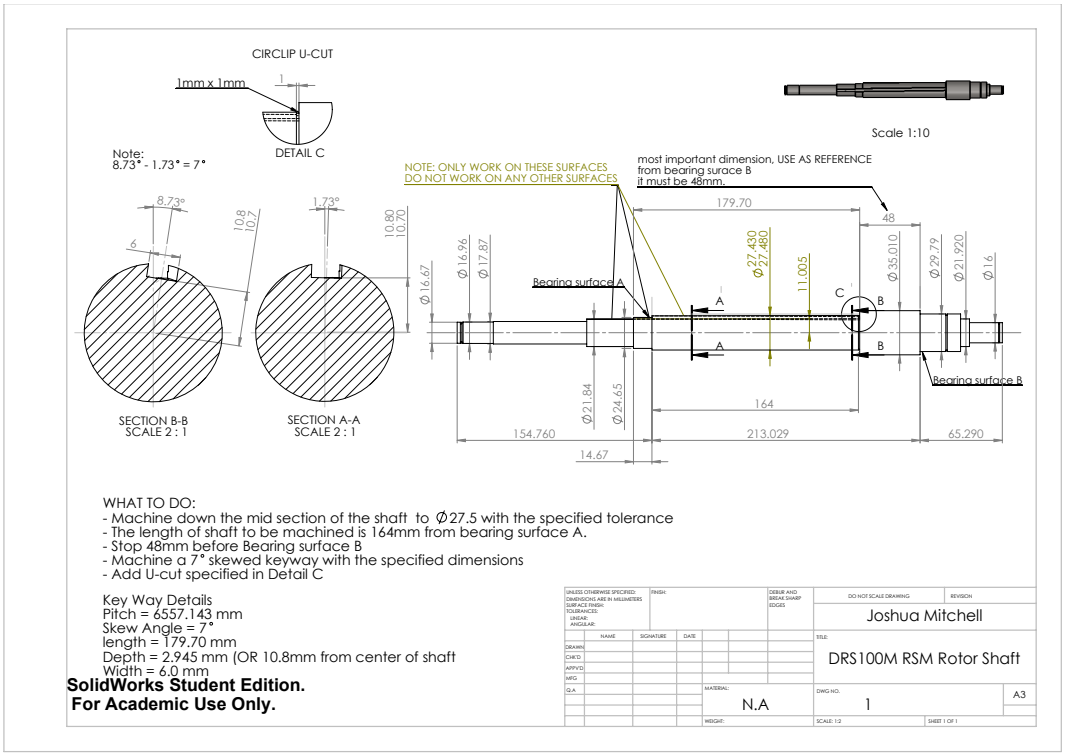

Figure B.10: DRS100M RSM rotor shaft with skewed key way..

Figure B.11: RSM rotor shaft with skewed key way and assembled shaft with RSM laminations.

B.2.5 Wind Turbine Emulator

For this measurement a wind turbine emulator was implemented using a 2000 N m, 55 kW induction machine. An Allen Bradley Power Flex 755 VSD, a STKC Technology 1000 N m torque sensor, a 12-bit encoder and the RTAI Pentium system were used. The torque sensor was calibrated using the Pentium system with scale-measured weights placed at different lengths to provide specific torque values up to 129 N m, see appendix B.2.3, fig. B.7a. Initially the preferred emulation control structure was to utilise the IM under the torque control methods from section 2.1.6, but the Allen Bradley VSD's flux-vector torque control could not be calibrated to produce consistent torque set points at all speeds and loads. This is likely due to the fact that the torque control performance is greatly reduced when operating at a fraction of the IM rated torque. It was thus decided to use the speed control methods detailed in section 2.1.6.

The Allen Bradley reads a [-10 ,10] V analogue signal transmitted from the Pentium system's DAC, which represents the desired the speed set point. In fig. B.12 the basic mechanical and electrical system layout is illustrated. The frequency-based signal from the torque sensor is first sampled and then calibrated using the Pentium system to get T_{mes}. Using T_{mes} and the emulated turbine torque T_w, (2.14), the turbines acceleration can be calculated with (2.17). ω_{m} is the shaft speed of the generator and is recorded using the RSG encoder and converted to turbine rotor speed using the gear ratio gr.

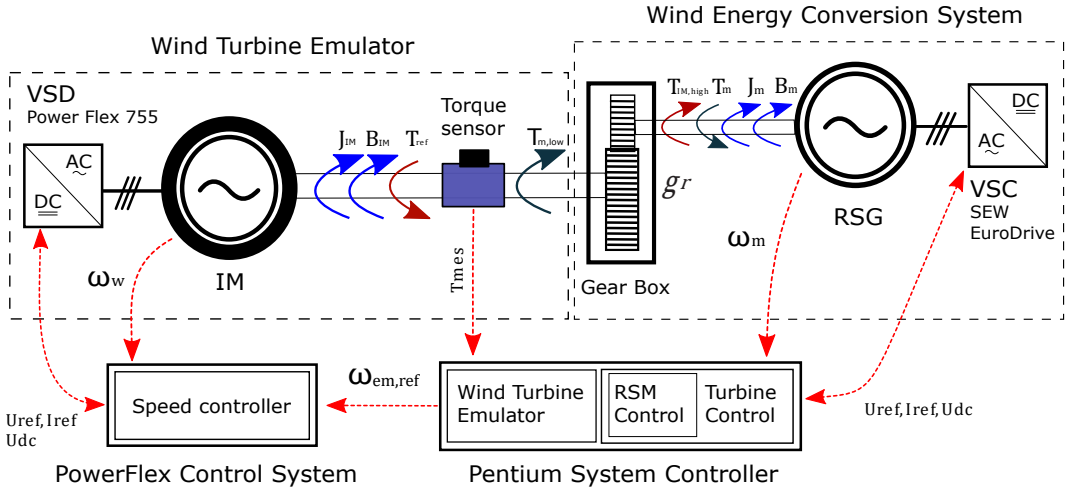

Figure B.12: A wind turbine emulator using a speed controlled 55 kW I.M and a energy conversion system using the RX-87 gear box and integrated 3 kW RSG. Signal wires are dotted in red. Power lines are black. Mechanical linkages are shaded.

To determine the various dynamic factors of the drive train, the inertia and damping factors of all the components were measured directly and indirectly. Due to set-up limitations only the high side RSG speed could be measured. This limited the ability

Table B.1: WTE aerodynamic and physical mechanical parameters as observed from the generator side of the gear box.

Wind Turbine Parameters	
Rated input power	3 kW
Rated wind speed	$10\,\mathrm{m\,s^{-1}}$
radius, r	1.9 m
ρ	$1.212\,\mathrm{kg\,m^{-3}}$
$c_{\mathrm{p}}^{\star}$	0.4814
λ^{*}	5
Rated torque	110 N m
Rated speed ω_T	275 RPM

Mechanical parameters (from the low speed side)	
J_{sys}	$1.312\,\mathrm{kg\,m^2}$
J_{im}	$0.741\,\mathrm{kg\,m^2}$
J_{RSG}	$0.071\,\mathrm{kg\,m^2}$
J_w	$0.139\,\mathrm{kg\,m^2}$
β_{sys}	$0.707\,\mathrm{N\,s\,m^{-1}}$
β_{im}	$0.587\,\mathrm{N\,s\,m^{-1}}$
β_w	$0.05\,\mathrm{N\,s\,m^{-1}}$
β_{RSG}	$0.12\,\mathrm{N\,s\,m^{-1}}$

to directly measure the induction motors inertia independently by calculating inertia from a speed decay transient. However, the response times of the whole coupled system and the RSG (incl. gear box) could be measured independently and thus the IM inertia and the damping factor could be inferred. The transient decay values of the system and the RSG (including the gear box), area shown in fig. B.13a. Theoretically the decay of a system with damping is exponential, however it was found that although the system behaves exponentially at higher speeds, the real system response deviates from an exponential function at lower speeds. This is due to a non-linear friction effect in the bearings and drive shafts which increases the friction at low RPM. However, for the calculation of J_{RSG}, J_{sys}, J_{IM} the upper most regions where the decay rate matches the curvature of the exponential function are used. The position of the torque sensor allows for the independent measurement of the damping coefficient for the IM, RSG and gearbox. Figure B.13b shows the measured reaction damping torque for the RSG (incl. gear box) and the IM. This test was only completed for the wind emulators clock-wise direction of rotation. Speeds above rated operation were also not tested as the damping coefficient can be assumed to remain constant. As illustrated by fig. B.13b and table B.1, the IM inertia and damping factor are significant and almost twice that of the emulated turbine rotor. It is thus necessary to program the Allen Bradley to reach any set-point in less than the time constant of the WTS $T_{wts} = 278\,\mathrm{ms}$ so that the emulated WTS inertia is visible. This is necessary so that the IM dynamics remain decoupled from the emulated turbine dynamics. There is a lower limit to the emulated WTS inertia as a consequence of this coupling. The desired WTS inertia of $T_{wts} = 27.8\,\mathrm{ms}$ is below this limit and thus had to be increased by a factor of 10. The Allen Bradley was programmed to reach to any speed-set-point in 100 ms.

Using the wind speed data in fig. 2.10b simulations in Matlab Simulink were conducted for an encoder controlled WTS with the parameters specified in table B.1. A comparison of the simulated and measured WTC response is shown in fig. B.14, where a rated

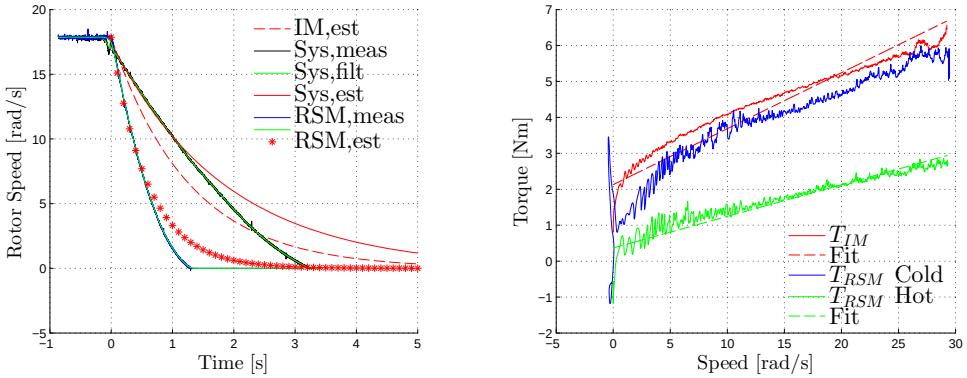

(a) System, RSG gear box and IM transient decay. (b) Combined RSG gear box and IM damping torque.

Figure B.13: (A) System speed decay transient response from a high side rotor speed of 100 rad/s (low side rotor speed of 17 rad/s, 160 RPM). The RSG decay curve includes the gear box. (B) Measured damping of the RSG, gearbox and IM. Coulomb friction is present in the system, but dissipates as speed and driving torque increase.

wind speed step is applied and the controller reacts accordingly to reach the optimum system c_p and TSR. Despite the large inertia difference (10×) between the simulated system and the emulated system, the controller response is almost identical, which is indicative of the emulators accuracy and the effectiveness of the practical outer and inner control loops of the WTC. The Simulated system reaches its set point in 0.3 s and the emulated system reaches its set point in 1.2 s.

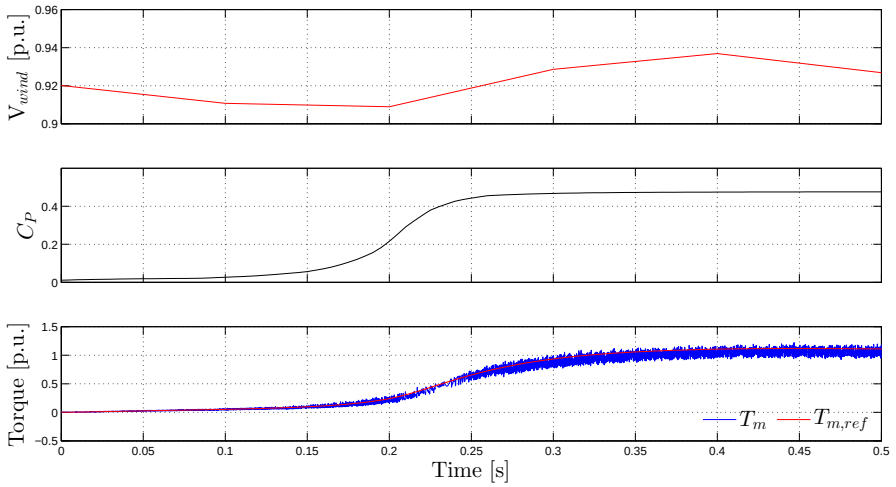

(a) Simulated.

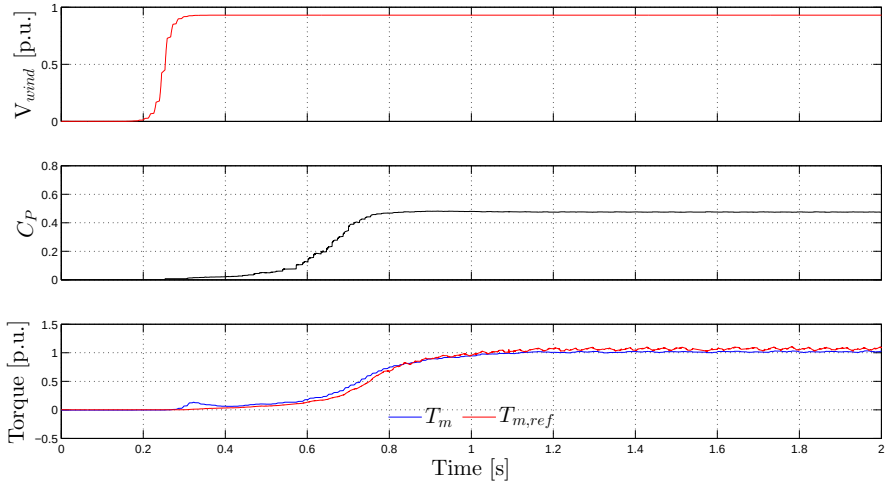

(b) Measured.

Figure B.14: Step response of the simulated and emulated WTS to a rated step in wind speed with RSG torque control. The emulated system has 10 times the inertia of the simulated system as indicated by its slow response.

Appendix C

Matlab Simulink Models

In this appendix the various simulation models used in this thesis such as the RSG, inverter, PSC-methods, LC-filter, grid, DC bus, DC-link and aero-dynamic and mechanical wind turbine models are presented. Simulation results are not presented here and are reserved for chapter 4 where comparisons are made to practical results.

C.1 Simulation Models

Initially the Simplorer simulation package was used for the full bridge inverters and grid control, but due to the added complication of including the non-linear RSM it was decided that Matlab Simulink would be easier and less time consuming to use.

Most of the simulation models used here have been developed by multiple students over the years in similar research fields. Some of the models were previously used in different applications and in different versions of Simulink. In this project the older simulations were used as guides to recreate new versions. The newer models were integrated together. Adjustments and

C.1.1 RSM Model

The Simulink RSM model shown in fig. C.1 has been developed over the years by various researchers. The main contribution has been from Dr. Landsmann who wrote the algorithms for the inverse bilinear interpolation (see appendix D.0.1 for details). The RSM model uses current dependant non-linear flux linkage maps (section 2.2.4) which uniquely characterise the machines behaviour. Continuous inverse mappings are required where the flux linkage vector (calculated using $\frac{\boldsymbol{\psi}_s^s}{dt} = \boldsymbol{u}_s^s - R_s \boldsymbol{i}_s^s$) is used as the input and the current vector as the output. This is mapped by $(i_s^d, i_s^q)^\top : \Re^2 \mapsto \Re^2, (\psi_s^d, \psi_s^q)^\top \mapsto (i_s^d(\psi_s^d, \psi_s^q), i_s^q(\psi_s^d, \psi_s^q))^\top$ and can be derived from the finite element method generated flux maps by means of inverse bilinear interpolation.

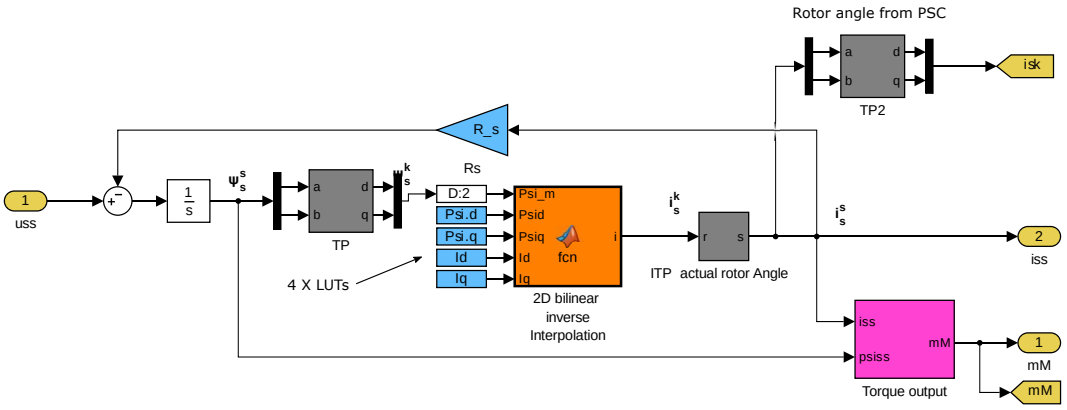

Figure C.1: RSM Simulink Model.

C.1.2 VSC Model

A three-phase bridge VSC with SVPWM and ideal switches was modelled to increase the accuracy of the simulation, fig. C.3. SVPWM was chosen over triangle pulse-width modulation because of the additional 3^{rd} harmonic SVPWM injects to obtain a more efficient utilisation of the DC bus voltage. The VSC model adds harmonic distortion to the system models, which is otherwise not present. The VSC model is beneficial because it generates the actual discrete space vector PWM signals, which are a better representation of reality rather than just injecting the continuous alpha beta control voltages into the RSM directly form the PI controllers. Both the discrete and filtered PWM signals are shown in fig. C.4 for a constant output current.

The basic inverter model was adapted from the PWM models created by Julian

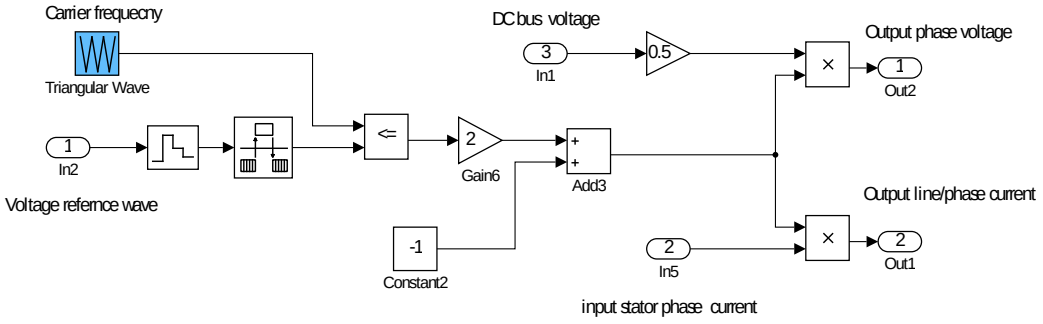

Figure C.2: A single digital voltage switch with voltage reference, DC bus voltage and the carrier frequency.

The VSC model uses basic digital blocks to simulate the pulsed voltage, as shown in fig. C.3. In fig. C.2 a single switch is shown for clarity. The digital switch output can only be 1 or -1 multiplied by half the dc bus voltage. The duration and frequency of a switches state is governed by a triangle wave with a period equal to that of the switching

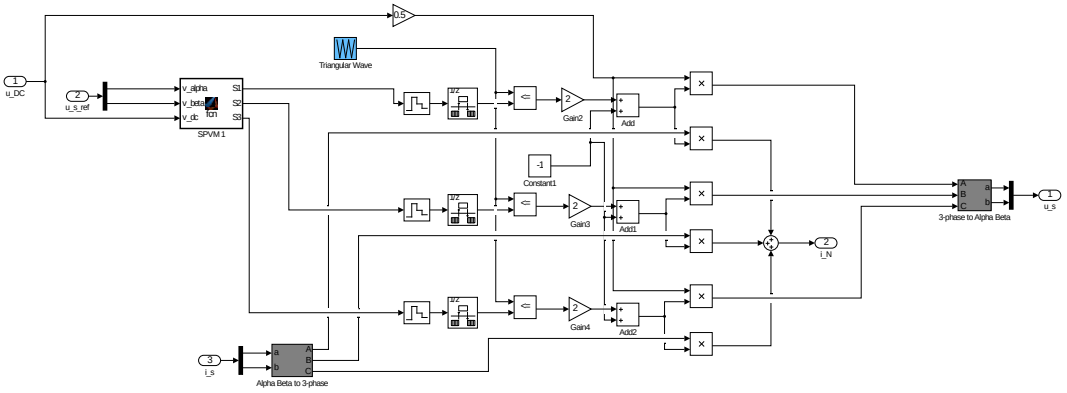

Figure C.3: Three-phase VSC model with space vector modulation.

frequency and the the fundamental voltage reference which is generated by the SVPWM algorithm. The SVPWM Matlab script is available in the appendix D.0.2. To simulate the inverter DC bus current, the continuous stator current is fed into the digital switches so that current will only flow for the duration and in the direction of a switch state, the outputs off all the switches are then summed together to get the net current in or out of the DC bus. The transformations from three-phase systems to two-phase $\alpha\beta$ and visa versa, are extensively used in the inverter models, but detail in section 2.3.

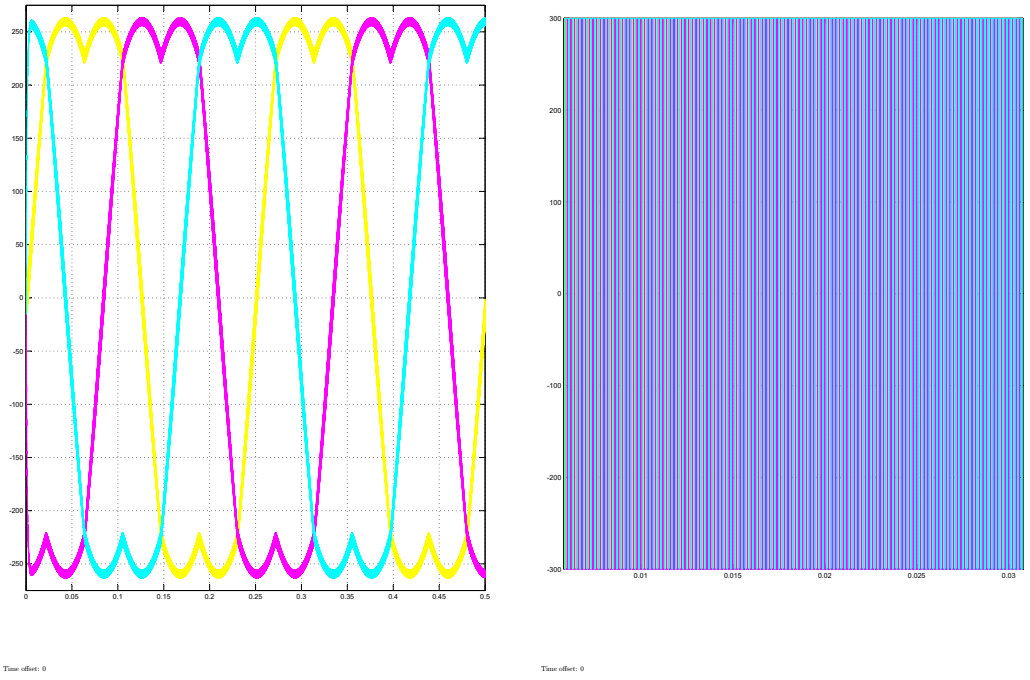

(a) Filtered. (b) Unfiltered.

Figure C.4: Filtered and unfiltered three-phase VSC PWM voltages.

C.1.3 Back-to-Back and DC linked Inverter Model

From section appendix C.1.2 the basic building blocks for the VSC model were shown. The DC link dynamic model is discussed here. The most basic model for the DC link is one with out resistance. Only two capacitance terms exist at the DC inputs to both inverters as is followed by the governing dynamic equations detailed in section 3.4.4.

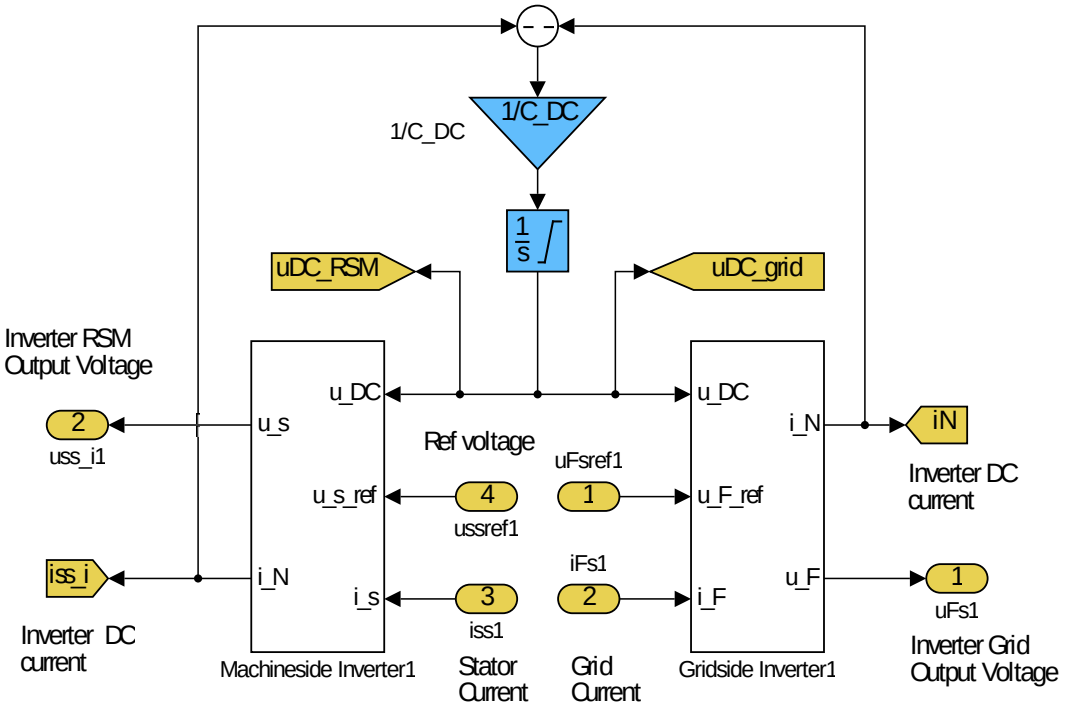

Figure C.5: DC-link Simulink model without cable impedance.

C.1.4 Current Control Models

Current control of the RSM is performed using the model blocks in fig. C.7a . Here the dq current control references and stator currents are fed into the non-linear Modulous Optimum gain updated PI-controllers. The internal PI-controller gain update model is shown in fig. C.7b. This model also as an anti-wind up feature to prevent the integrator from over saturation. The output of fig. C.7a is the stator reference voltages which are the inputs to the inverter model in fig. C.6a. This control model was developed by Julian.

It is noted here that the stator currents in this model can be obtained using either the estimated or the actual rotor angle.

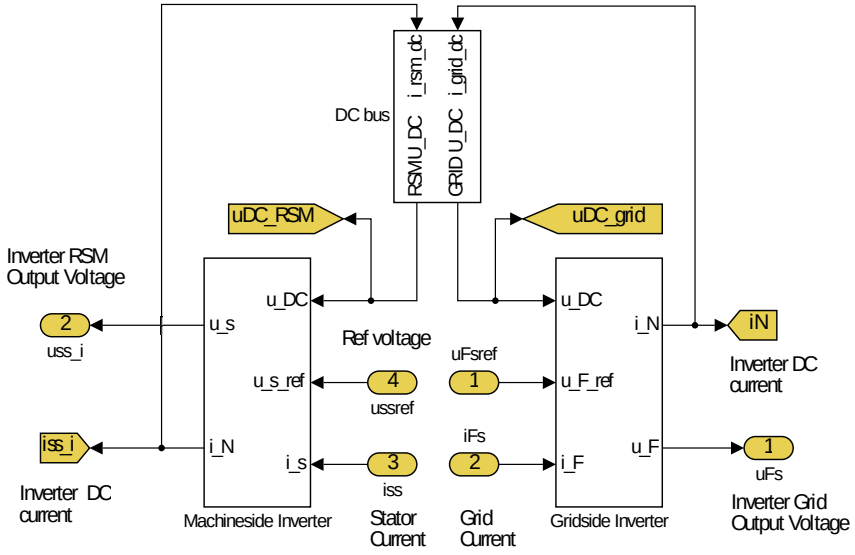

(a) Back-to-back inverter model with DC-link.

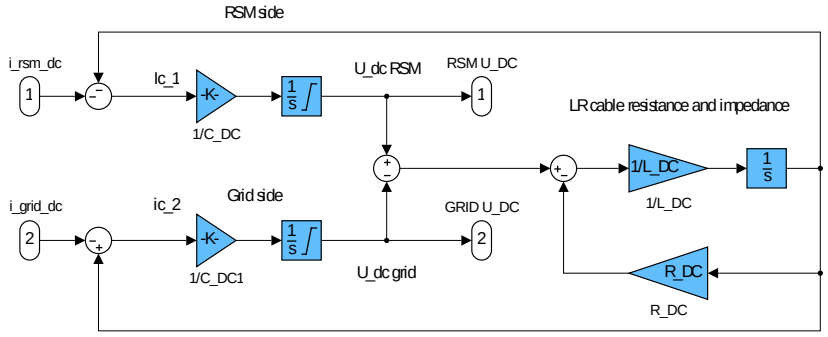

(b) DC bus link model with cable impedance.

Figure C.6: Simulink model of back-to-back converters with a DC-link transmission cable.

C.1.5 MTPA and Torque Control Models

The MTPA Simulink model is shown in fig. C.8 illustrates how the torque based MTPA LUTs for the current angle and magnitude are utilised to obtain the dq-current references.

C.1.6 AHFI-PSC Model

The AHFI-PSC presented in fig. C.9 might be simple and composed of only few element blocks; the LP filter, carrier wave, PLL and the signal injection, but it is quiet difficult to tune.

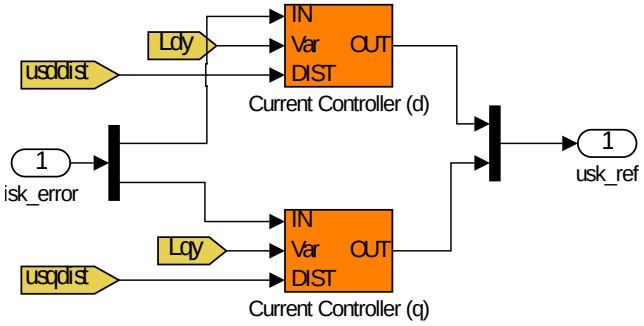

(a) dq PI-controller model.

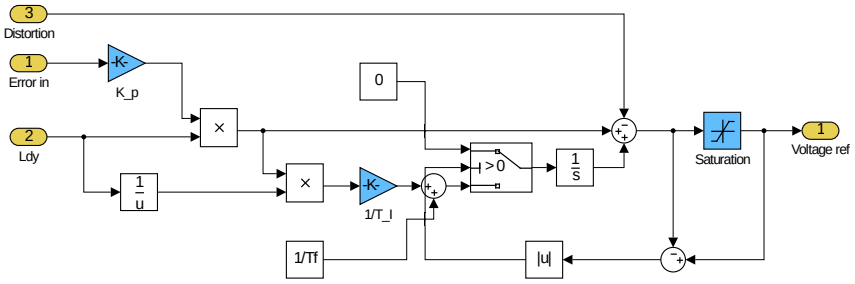

(b) Internal view of the d-axis PI-controller with anti-wind-up.

Figure C.7: DQ Non-linear Modulous Optimum gain updated PI-controller models.

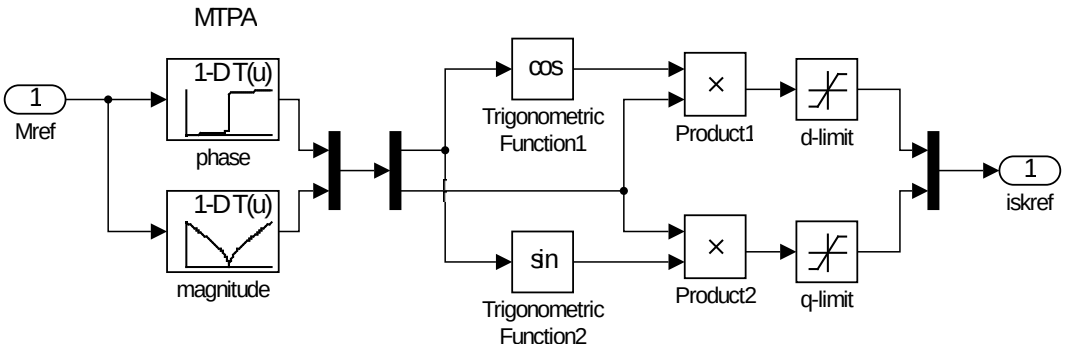

Figure C.8: MTPA and open loop torque control Simulnk model.

C.1.7 FS-PSC Model

The FS-PSC models were adapted from old Simulink versions created by Wikus Villet. The main change made was the replacement of the isometric-flux vector, ψ_Σ LUT by a version where the salient vector is calculated using the flux maps LUT.

C.1.8 Hybrid-PSC Model

The hybrid-PSC implemented in Simulink is presented in fig. C.11, note that there are two hysteresis actuators so that the injection voltage is always on before the switch to AHFI-PSC. In this case the saliency shit compensation (SSC) is turned off when AHFI-

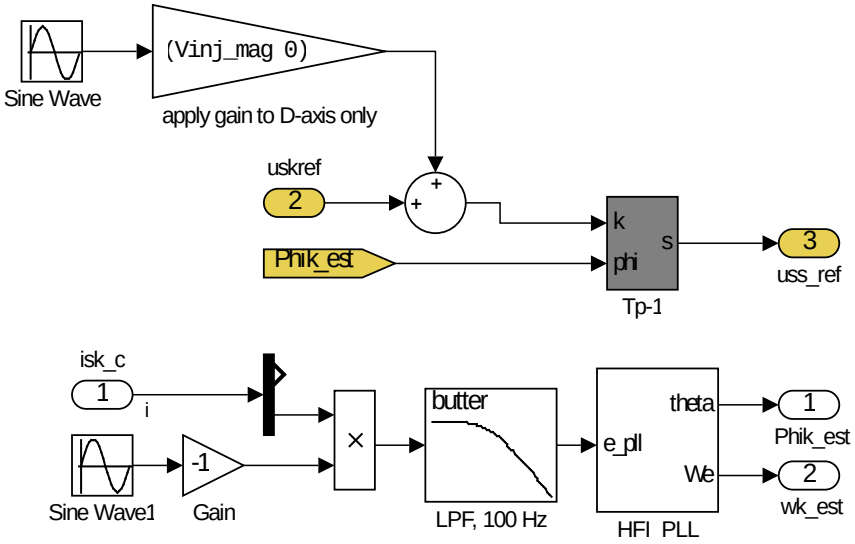

Figure C.9: AHFI-PSC Simulnk model.

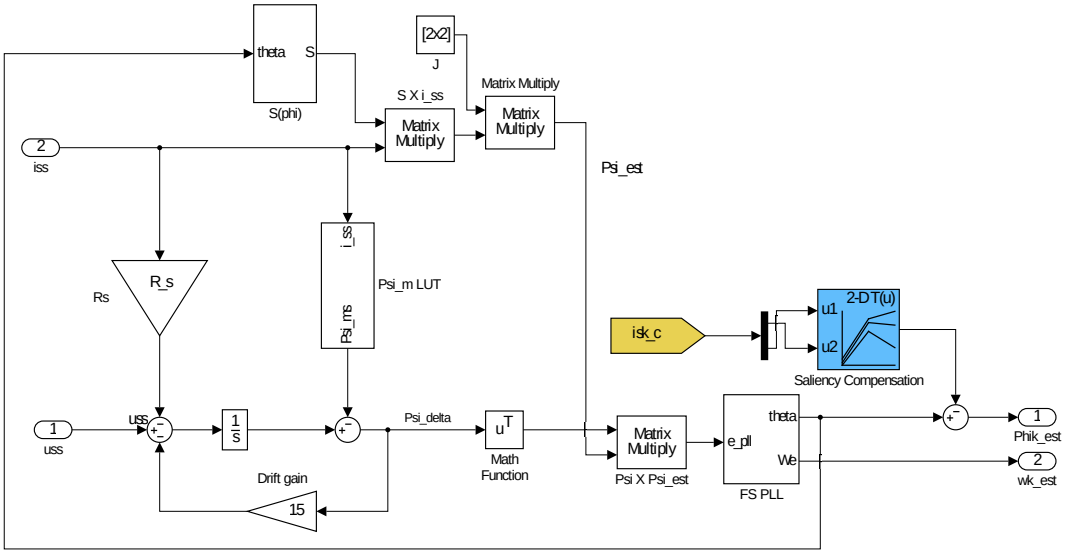

Figure C.10: FS-PSC Simulnk model.

PSC is active.

C.1.9 Wind Turbine Model

Matching the RSM mechanical side directly to the wind-turbine side required the wind turbine aerodynamic model, fig. C.12, to operate based on the input wind speed and the reaction torque from the RSM. The c_p and λ curves were also implemented as a modification to J. Kulick's original model [86], which operated without them. The wind speed reference is taken from actual measured data from (wind site) with two minutes of emulated wind speed data provided by J.P Du Plooy. The two-mass turbine and RSG mechan-

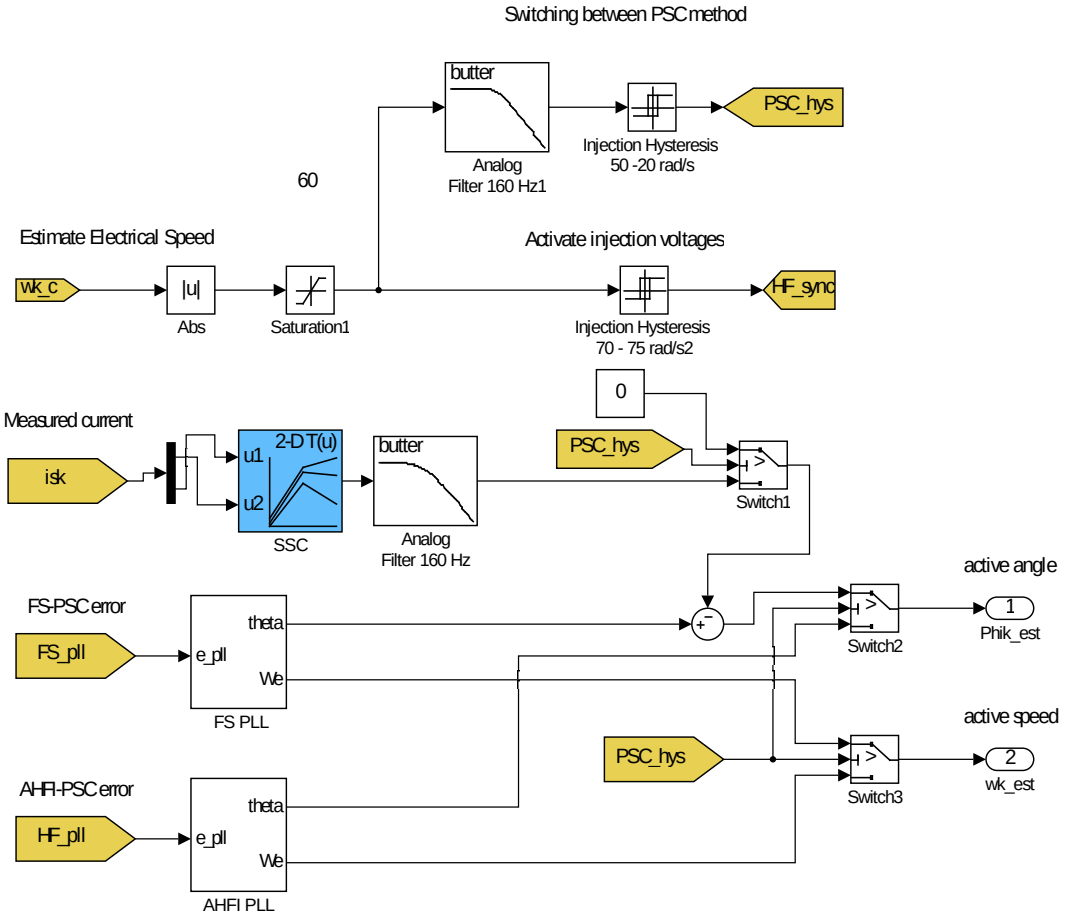

Figure C.11: Hybrid-PSC Simulnk model.

ical model is presented in fig. C.13 followed by the wind turbine controller in fig. C.14, which operates seamlessly between region II and III. Not that the damping compensation must be disabled for region III. This can be done with hysteresis and a switch.

C.1.10 Load Motor Model

To dynamically test the control methods over the entire load and speed range dealt with in this paper the speed on the machine must be kept constant and the load varied. A simple load motor which controls speed was implemented using a PI controller which regulates the target reference speed. The output of this PI is a torque command which replaces the turbine torque input to fig. C.13. Since this fictitious motor has no power restrictions it is the ideal load and will always hold the speed close to the desired reference and provide the necessary resistive torque for the RSM load. PI gains were chosen arbitrarily to give the system a faster response time than the RSM system. The load machine is directly coupled to the RSM in this case and no gear box is present.

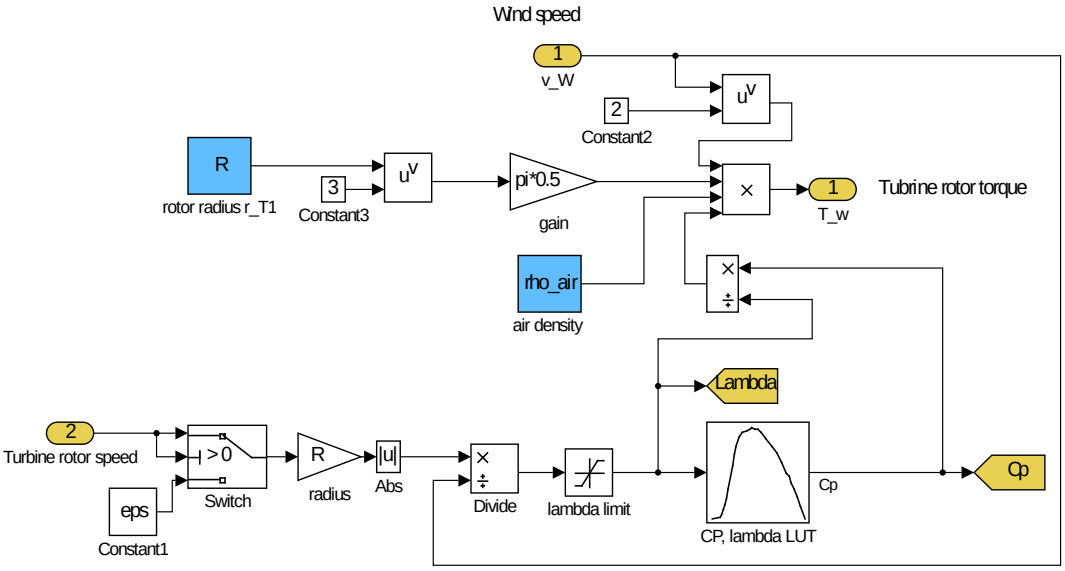

Figure C.12: Wind turbine aerodynamic Simulink model.

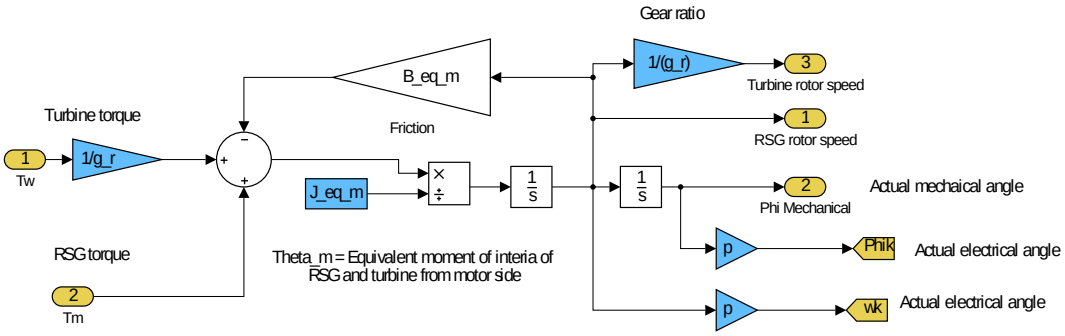

Figure C.13: Wind turbine and RSG mechanical Simulink model.

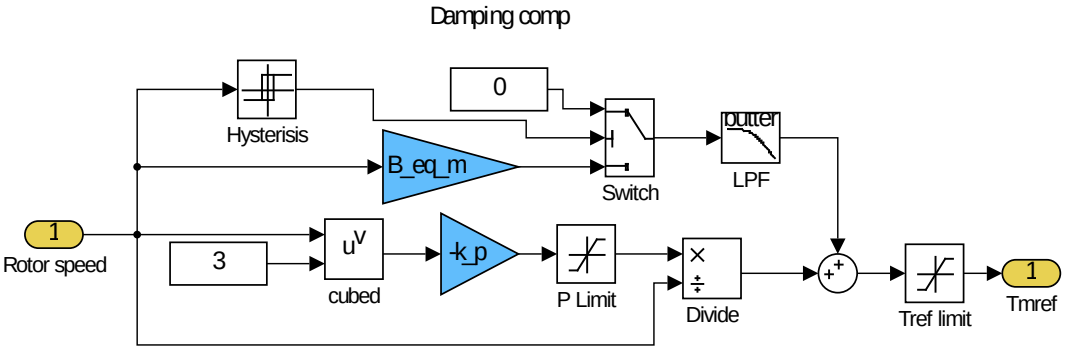

Figure C.14: Wind turbine controller Simulink model.

C.1.11 LC and LCL Filter Models

A Simulink implementation of the LC- and LCL-filter transfer functions in the stator reference frame is presented in figs. C.15 and C.16 respectively. Note that the outputs of

the LC and LCL-filter are different due to the manner in which the RSM and grid model operate, i.e one requires a voltage output and the other a current output. The LC-filter estimator with damping resistance and tuning gain k_f also presented in fig. C.17.

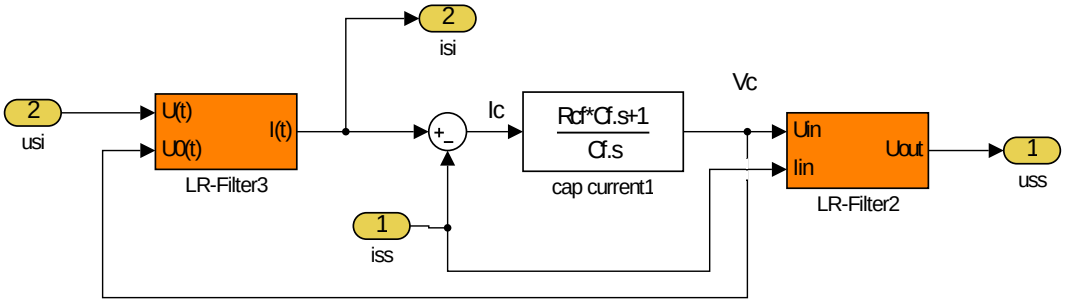

Figure C.15: LC-filter for output du/dt of the RSG VSC Simulink model.

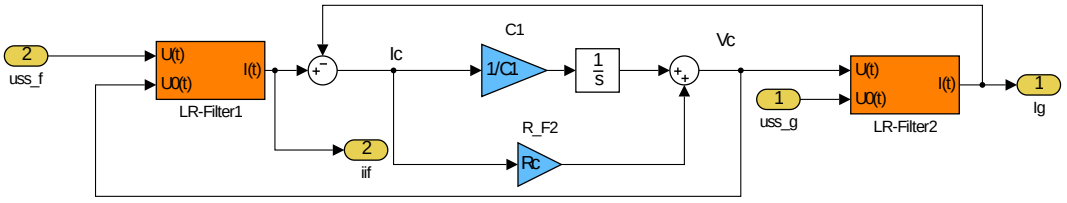

Figure C.16: Grid VSC LCL filter Simulink model.

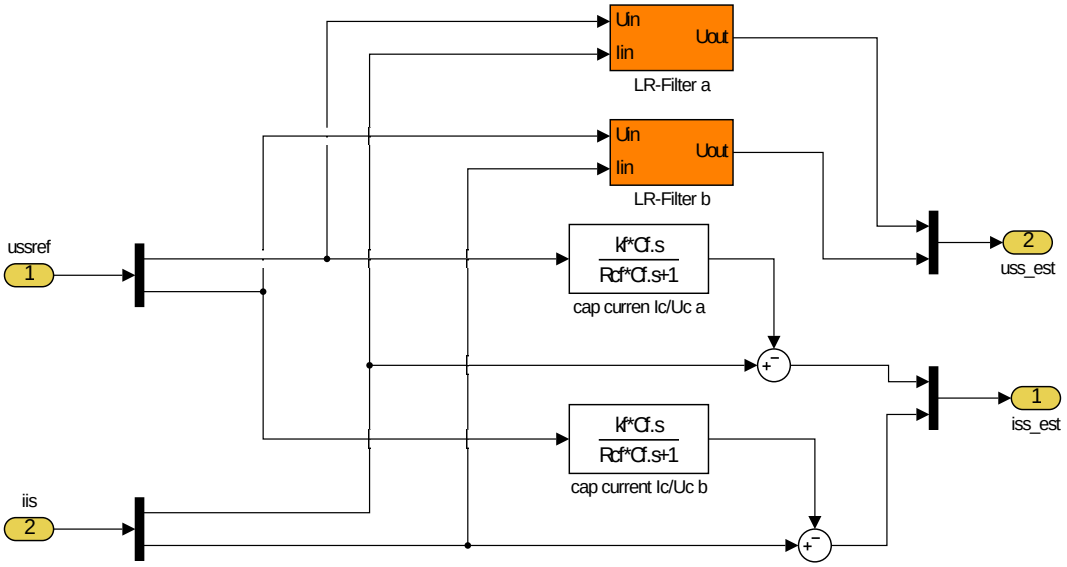

Figure C.17: LC-filter estimator Simulink model.

C.1.12 Grid Source and Grid Current Controller

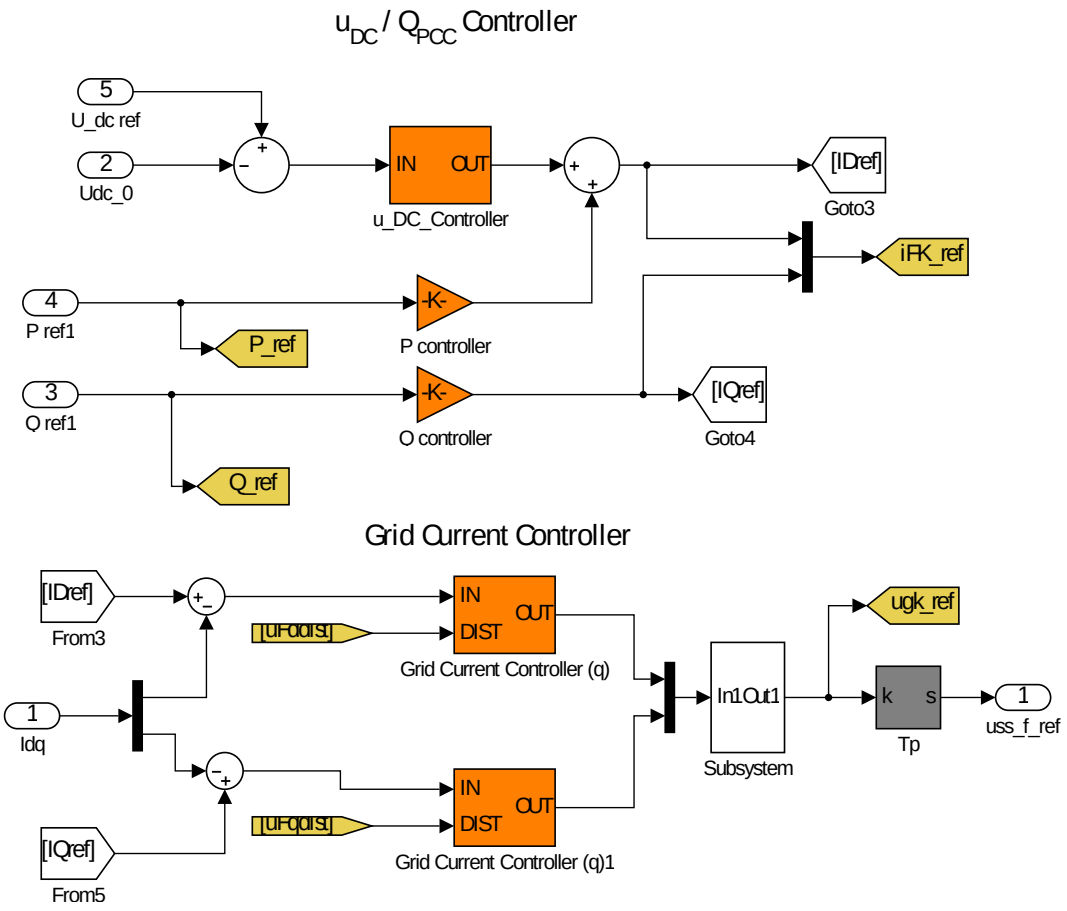

Figure C.18: Grid and DC bus controller Simulink model.

C.1.13 Flux-linkage and Inductance Look-up Tables

Look up tables are managed by Simulink's LUT functions, which automatically interpolates the data. There are various options for how this is done but simple linear and bilinear interpolation is selected. One property that is very important for the data to be interpolated correctly is that all matrices or vectors are monotonically increasing, which is why the flux-linkage data must be organised and compiled correctly before usage, (for details seeappendix D.0.4).

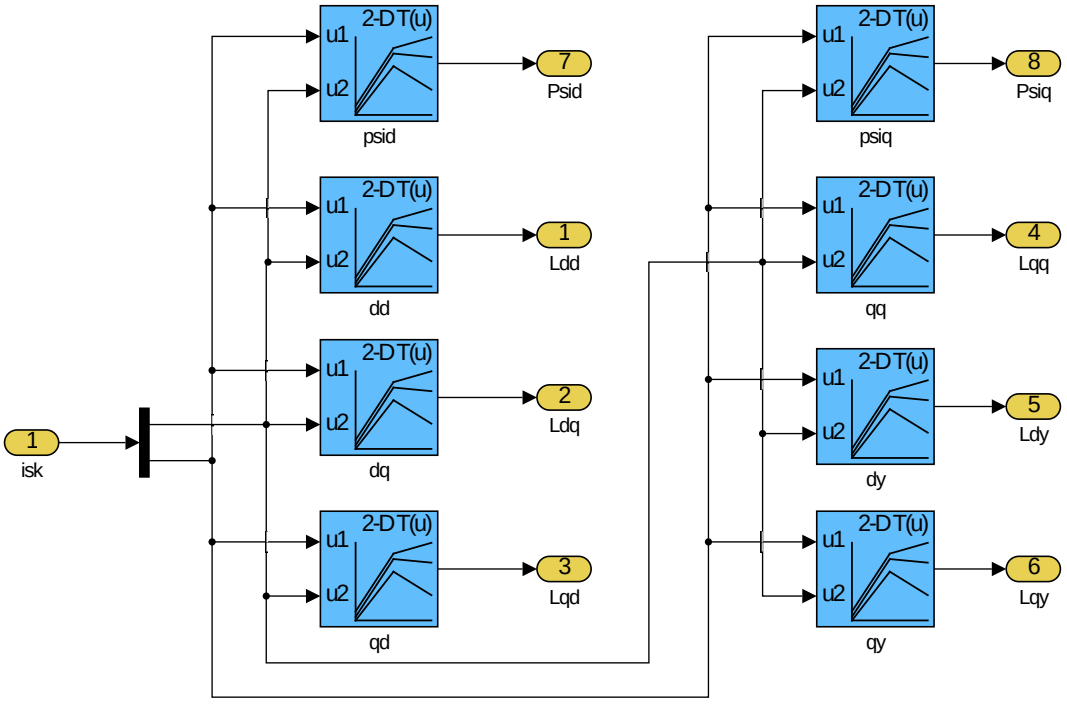

Figure C.19: Flux-linkage and Inductance Look-up Tables in Simulink.

Appendix D

Algorithms

In this appendix the some important Matlab scripts that were used to design the inductors, shape the flux-linkage-matrices, define switch vectors and MTPA current vectors are documented.

D.0.1 Bi-linear Interpolation

```
% by Peter Landsmann and Julian Kulick
function i = fcn(Psi_m,Psid,Psiq,Id,Iq)
%% 1. Initialization
P0 = [0 0]'; P1 = P0;
nd1=1; nq1=1;
Psi00 = [0 0]';
Psi01 = [0 0]';
Psi10 = [0 0]';
Psi11 = [0 0]';
%Searching Index Interval
intfound = 0;
n = length(Id);
nd0 = round(length(Id)/2);
nq0 = nd0;%round(length(Iq)/2);
%% 2. Interval Finding (by Peter Landsmann)
while intfound<2                                                    % Stop
    when interval is found
    intfound = 0;
    nd1 = nd0 + 1;
    nq1 = nq0 + 1;

    % Define vertices
    Psi00 = [Psid(nq0,nd0) Psiq(nq0,nd0)]';
    Psi01 = [Psid(nq0,nd1) Psiq(nq0,nd1)]';
    Psi10 = [Psid(nq1,nd0) Psiq(nq1,nd0)]';
    Psi11 = [Psid(nq1,nd1) Psiq(nq1,nd1)]';
```

```
% D-axis search (left/right)
% Reference is located left of the quad (if a Psi plane is considered ->
 straight line)
if      Psi_m(1) < Psi00(1) + (Psi10(1)-Psi00(1))/(Psi10(2)-Psi00(2))*(Psi_m(2)-
Psi00(2))
    if nd0>1                                                    % If
inside limits
        nd0 = nd0 - 1;
    else
        intfound = 1;
    end
% Reference is located right of the quad
elseif Psi_m(1) > Psi01(1) + (Psi11(1)-Psi01(1))/(Psi11(2)-Psi01(2))*(Psi_m(2)-
Psi01(2))
    if nd1 < n
        nd0 = nd0 + 1;
    else
        intfound = 1;
    end
% Reference is located neither left nor right of the quad => Interval
% found
else
    intfound = 1;
end

% Q-axis search (top/bottom)
% Reference is located below the quad
if      Psi_m(2) < Psi00(2) + (Psi01(2)-Psi00(2))/(Psi01(1)-Psi00(1))*(Psi_m(1)-
Psi00(1))
    if nq0>1
        nq0 = nq0 - 1;
    else
        intfound = intfound + 1;
    end

% Reference is located above the quad
elseif Psi_m(2) > Psi10(2) + (Psi11(2) - Psi10(2))/(Psi11(1) - Psi10(1))*(Psi_m
(1)-Psi10(1))
    if nq1 < n
        nq0 = nq0 + 1;
    else
        intfound = intfound + 1;
    end

% Reference is located neither above nor below the quad => Interval
% found
```

```
67      else
            intfound = intfound + 1;
69      end
    end
71

73  %% 3. Bilinear inverse interpolation (http://www.iquilezles.org/www/articles/
        ibilinear/ibilinear.htm)
    %    P = Psi00 + u(Psi01-Psi00)
75  %    Q = Psi10 + u(Psi11-Psi10)
    % Psi* = P+v(Q-P)
77  % => X = Psi*-Psi00 = A*u + B*v + C*u*v
    %
79  % Eliminate u => quadratic polynomial => find v (0..1) => calculate u
    % (0..1)
81
    % Define intermediate variables
83  X = Psi_m-Psi00;
    A = Psi01-Psi00;
85  B = Psi10-Psi00;
    C = Psi11-Psi10-Psi01+Psi00;
87
    % Define coeffecients of quadratic equation
89  c2 = X(2)*A(1)-X(1)*A(2);
    c1 = X(2)*C(1)-X(1)*C(2)+B(1)*A(2)-B(2)*A(1);
91  c0 = B(1)*C(2)-B(2)*C(1);

93  % Solve quadratic equation
    v1 = (-c1+sqrt(c1^2-4*c0*c2))/(2*c0);
95  v2 = (-c1-sqrt(c1^2-4*c0*c2))/(2*c0);

97  % Pick the solution, which is element of [0,1]
    v=0;
99  if (v1>=0 && v1 <= 1), v = v1; end
    if (v2>=0 && v2 <= 1), v = v2; end
101
    % Determine the second interpolation parameter
103 u = (X(1)-B(1)*v)/(A(1)+C(1)*v);

105 % Interpolation of the output
    id = Id(1,nd0) + u*(Id(1,nd1) - Id(1,nd0));
107 iq = Iq(nq0,1) + v*(Iq(nq1,1) - Iq(nq0,1));

109 % Output
    i = [id iq]';
```

D.0.2 Space Vector Modulation Matlab Script

```
% By Joshua Cole Mitchell 2016

function [S1, S2,S3] = fcn(v_alpha, v_beta, v_dc)
%SVPWM
%refer to http://www.diva-portal.org/smash/get/diva2:504868/fulltext01 for more info
% assume Va0 +Vb0 +Vc0 = 0, all 120 deg out of phase with each other
% Vref * Tsw = V1 * T1/Tc + V2 * T2/Tc + V0 * T0/Tc
% for sector 0 to pi/3 Vref can be located
% by converting Vref into real an imaginary parts i.e the rotated triangle version of the alpha and beta
% vectors T.. are easier to calculate

%initialise
 S1 = 0;
 S2 = 0;
 S3 = 0;

Tsw = 2;
Vref = sqrt(v_alpha^2 + v_beta^2);
theta = mod(2*pi +atan2(v_beta,v_alpha),2*pi);

if theta < pi %sec 1,2,3
   if (theta >= pi/3 &&  theta < 2*pi/3)
       sector = 2;
   else
       if (theta < pi/3)
        sector = 1 ;
       else
        sector = 3;
       end
   end
else %sect 4,5,6
  if (theta >= 4*pi/3 && theta < 5*pi/3)
    sector = 5;
  else
      if (theta < 4*pi/3)
          sector = 4;
      else
          sector = 6 ;
      end
  end
end

sigma = pi/3 - theta + ((sector - 1)/3) * pi;
gamma = theta - ((sector - 1)/3)*pi;
```

```
m = (sqrt(3) * Vref )/v_dc; % modulation index

T1 = Tsw * m * sin(sigma);
T2 = Tsw * m * sin(gamma);
T0 = Tsw - T1 - T2;

% duty cycle for each sector for upper switches. this is center aligned for less
    harmonics and noise
switch sector
    case 1
    %sector = 1;
    S1 = T1 + T2 + T0/2;
    S2 = T2 + T0/2;
    S3 = T0/2;

    case 2
    %sector = 2;
    S1 = T1 + T0/2;%T2 + T0/2;
    S2 = T1 + T2 + T0/2;
    S3 = T0/2;

    case 3
    %sector = 3;
    S1 = T0/2;
    S2 = T1 + T2 + T0/2;
    S3 = T2 + T0/2;

    case 4
    %sector = 4;
    S1 = T0/2;
    S2 = T1 + T0/2;%T2 + T0/2;
    S3 = T1 + T2 + T0/2;

    case 5
    %sector = 5;
    S1 = T2 + T0/2;
    S2 = T0/2;
    S3 = T1 + T2 + T0/2;

    case 6
    %sector = 6;
    S1 = T1 + T2 + T0/2;
    S2 = T0/2;
    S3 = T1 + T0/2;%T2 + T0/2;
end
S = 0;
```

```
Sphas = 0;
sector = sector/10;
%if S1 < 0 S1 = 0; end
%if S2 < 0 S2 = 0; end
%if S3 < 0 S3 = 0; end
 S1 = S1 - 1;
 S2 = S2 - 1;
 S3 = S3 - 1;
```

D.0.3 Maximum Torque per Ampere Matlab Script

```
%Originally by Julian Kulick 2015, adapted by Joshua Mitchell 2016
% MTPA adapted for generator mode. Note this will only produce meaningful results
    if a measured torque map is used.
%%import measured torque and flux map
load('3kw_Meausured_flux');
%% Data conditioning
% First interpolate data on a grid to match dimensions
n = 80;
isqmax = max(LUT_Psi.iq);
isdmax = max(LUT_Psi.id);
iqvec = linspace(-isqmax,isqmax,n);
idvec = linspace(-isdmax,isdmax,n);
qa = iqvec(2)-iqvec(1);
da = idvec(2)-idvec(1);
[Idi,Iqi]    = meshgrid(LUT_Psi.id,LUT_Psi.iq);%meshgrid(ivec,ivec);
[Id,Iq]      = meshgrid(idvec,iqvec);
Psi.d        = interp2(Idi,Iqi,LUT_Psi.Psid,Id,Iq,'spline');
Psi.q        = interp2(Idi,Iqi,LUT_Psi.Psiq,Id,Iq,'spline');
%clear Idi Iqi

% Define standard colors
c1 = [0.85 0.325 0.098];            % Brown:    MTPA curve
c2 = [0 0.4470 0.7410];             % Blue:     Interpolated data
c3 = [0.929 0.694 0.125];           % Orange:   Current limits

% Define interpolation area
Psid = Psi.d;
Psiq = Psi.q;
cosphi = @(Psid,Psiq,id,iq) (Psid.*iq-Psiq.*id)./(sqrt(Psid.^2+Psiq.^2).*sqrt(id
    .^2+eps+iq.^2));
Psidm = max(max(Psi.d));
Psiqm = max(max(Psi.q));

%Define MTPA grid
acc = 61;
```

```
x = linspace(0,isqmax,acc);
x2 = linspace(0,Psiqm,acc);
y = linspace(-pi/2,0,acc);

z1 = zeros(acc,acc);
z2 = zeros(acc,acc);
z3 = zeros(acc,acc);

x_mtpa_sc = [];
y_mtpa_sc = [];
ymin_mtpa_sc = [];
zmin_mtpa_sc = [];
z_mtpa_sc = [];
s_mtpa_sc = [];

% every current magnitude
for k=1:length(x)
 % every current angle
    for l=1:length(y)
        x_d = x(k)*cos(y(l));
        x_q = x(k)*sin(y(l));
        Psidtemp = interp2(Id,Iq,Psi.d,x_d,x_q,'linear');
        Psiqtemp = interp2(Id,Iq,Psi.q,x_d,x_q,'linear');
        %extract and interpolate measured torque from measured torque map
        Ttemp = interp2(Id,Iq,lut_psi_int.m,x_d,x_q,'linear');
        % Interpolated calculated Torque
        z1(l,k) = Ttemp; 3/2*p*(Psidtemp*x_q-Psiqtemp*x_d);  %%
    end

    % Add data points to OPT points
    [z1_max,z1_ind] = max(z1(:,k));
    [z2_max,z2_ind] = min(z1(:,k));

    x_mtpa_sc = [x_mtpa_sc, x(k)];
    y_mtpa_sc = [y_mtpa_sc, y(z1_ind)];
    z_mtpa_sc = [z_mtpa_sc, z1(z1_ind,k)];

    ymin_mtpa_sc = [ymin_mtpa_sc, y(z2_ind)];
    zmin_mtpa_sc = [zmin_mtpa_sc, z1(z2_ind,k)];
end

% Create curve fit object through scattered data points, set first point to 45
y_mtpa_sc = [ymin_mtpa_sc(1:end-1) -45*180/pi];          % correct bad result at |
    iss| = 0 A
z_mtpa_sc = [zmin_mtpa_sc(1:end-1) 0];          % correct bad result at |iss| = 0 A

fdata1 = fit(x_mtpa_sc(2:end)',y_mtpa_sc(2:end)','poly2','Robust','on');
```

```
80
% Execute curve fitting for defined values
82 x_mtpa_pol = x_mtpa_sc;
y_mtpa_pol = feval(fdata1,x_mtpa_pol)';
84 z_mtpa_pol = 3/2*p* ( interp2(Id,Iq,Psi.d,cos(y_mtpa_pol).*x_mtpa_pol,sin(
    y_mtpa_pol).*x_mtpa_pol).*sin(y_mtpa_pol)...
            - interp2(Id,Iq,Psi.q,cos(y_mtpa_pol).*x_mtpa_pol,sin(y_mtpa_pol).*
    x_mtpa_pol).*cos(y_mtpa_pol)).*x_mtpa_pol;
86
% Motor and Generator functionality included
88 x_mtpa_pol2 = [x_mtpa_sc(end:-1:2) x_mtpa_sc];
y_mtpa_pol2 = [-y_mtpa_pol(end:-1:2) y_mtpa_pol];
90 s_mtpa_pol2 = [-s_mtpa_pol(end:-1:2) s_mtpa_pol];
%s_mtpa_pol2 = [-s_mtpa_pol(end:-1:2) s_mtpa_pol];
92 z_mtpa_pol2 = [-z_mtpa_pol(end:-1:2) z_mtpa_pol];

94 %x_mtpa_pol2 =  x_mtpa_sc;
%y_mtpa_pol2 = y_mtpa_pol;
96 %z_mtpa_pol2 = z_mtpa_pol;

98 %x_mpf_pol2 = [x_mtpa_sc(end:-1:2) x_mtpa_sc];
% y_mpf_pol2 = [-y_mpf_pol(end:-1:2) y_mpf_pol];
100 % z_mpft_pol2 = [-z_mpft_pol(end:-1:2) z_mpft_pol];
% x_mtpv_pol2 = [x_mtpv_sc(end:-1:2) x_mtpv_sc];
102 % y_mtpv_pol2 = [-y_mtpv_pol(end:-1:2) y_mtpv_pol];
% z_mtpv_pol2 = [-z_mtpv_pol(end:-1:2) z_mtpv_pol];
104
% Plot data
106 X = meshgrid(x);
Y = meshgrid(y)';
108
figure('Name','MTPA Curve','NumberTitle','off')
110 surf(X,Y*180/pi,z1);
hold on;
112 grid off;
plot3(x_mtpa_sc,y_mtpa_sc*180/pi,z_mtpa_sc,'o','Color','white','MarkerSize',4);
114 plot3(x_mtpa_pol,y_mtpa_pol*180/pi,z_mtpa_pol,'Color','white','LineWidth',1.5);
hold off;
116 xlabel('Current magnitude $\i_s^m$ /[A]','Fontsize',12);
ylabel('Current angle $\i_s^p$ /[degrees]','Fontsize',12);
118 title('Calculated MTPA Curve','Fontsize',12);
%xlim([0,ismax]);
120 ylim([-70,-40]);
set(gca,'View',[0 90]);
122 colormap(jet);
grid on;
```

D.0.4 Measured Flux-linkage Mapping Matlab Script

```
% By Julian Kulick and Joshua Mitchell 2016
% Capture flux map for id,iq=[-imax,imax]
% Input: Measurements where x goes from min to max and down again
%        and y is increased for one step only every change of direction
%        in x.
%% 1 - start in reference
%% 2 - end in [0,0]
clc, clear, close all
% parameters
Rs = 2.4;         % stator resistance
k = 5;            % filter time constant (multiples of Ts)
th = 1;      % threshold for edge detection
mode = 1;         % 1 = cartesian, 2 = polar
p = 2;            % number of pole pairs
p_RSM = p;

%load measured data
filepath = 'C:\Users\Buddah\Google Drive\Masters\Results\Practical\2016 Sensored\3
    kW RSG 157 RPM Current Response\';

Trigger =  importdata(strcat(filepath,'trigger.dat',' '));
Id_ref = importdata(strcat(filepath,'id_ref.dat',' '));
Iq_ref = importdata(strcat(filepath,'iq_ref.dat',' '));
Id = importdata(strcat('id.dat',' '));
Iq = importdata(strcat('iq.dat',' '));
Omega = importdata(strcat('omega_m_lpf.dat',' '));
Mout = importdata(strcat('torque.dat',' '));
Udc = importdata(strcat('udc.dat',' '));
Uq = V_cal.*importdata('uq_ref.dat',' ');
Ud = V_cal.*importdata('ud_ref.dat',' ');

time = Trigger(:,1);
time_segment = (10:length(time))';%(tr(1):tr(2));
t = time(time_segment)';
idref = Id_ref(time_segment,2)';
%Iq_ref = iq_ref(100:length(time)-500);
iqref = Iq_ref(time_segment,2)';
id = Id(time_segment,2)';
iq = Iq(time_segment,2)';
ud = Ud(time_segment,2)';
uq = Uq(time_segment,2)';
mout = (Mout(time_segment,2)')./(0.96*5.56);
omega = p.*Omega(time_segment,2)';
udc = Udc(time_segment,2)';
trigger = Trigger(time_segment,2)';
plot(trigger)
```

```
% low pass filter signals
Ts = t(12)-t(11);
T1 = k*Ts;
id = filtfilt([Ts, Ts],[(Ts+2*T1),(Ts-2*T1)],id);
iq = filtfilt([Ts, Ts],[(Ts+2*T1),(Ts-2*T1)],iq);
ud = filtfilt([Ts, Ts],[(Ts+2*T1),(Ts-2*T1)],ud);
uq = filtfilt([Ts, Ts],[(Ts+2*T1),(Ts-2*T1)],uq);
omega = filtfilt([Ts, Ts],[(Ts+2*T1),(Ts-2*T1)],omega);
mout = filtfilt([Ts, Ts],[(Ts+2*T1),(Ts-2*T1)],mout);

for i =1:max(size(id(:,1)))-1
  cur_angle(i,1) = 180/pi*atan(iq(i)/id(i));
  %cur_mag(i,1) = sqrt(iq(i,2)^2+id(i,2)^2)/sqrt(2);
  volt_ang(i,1) = 180/pi*atan(uq(i)/ud(i));
  %volt_mag(i,1) = sqrt(uqref(i,2)^2+udref(i,2)^2);
  power_factor(i,1) = cos((cur_angle(i)- volt_ang(i))*pi/180);
  %if power_factor(i) > 0
  %power_factor(i) = 0;
  %end
end

% calculate flux TODO: depending on type
cur_ang = atan2(iq,id);
vol_ang = atan2(uq,ud);
PF = cos(vol_ang - cur_ang);

psid = uq./omega - Rs.*iq./omega;
psiq = -ud./omega + Rs.*id./omega;
%psid = Rs.*id./omega - uq./omega;
%psiq = -Rs.*iq./omega + ud./omega;

x = id; xref = idref;
y = iq; yref = iqref;

% elseif mode==2
%     x = atan2(iq,id);
%     y = sqrt(id.^2+iq.^2);
%     xref = roundn(atan2(iqref,idref),-4);
%     yref = roundn(sqrt(idref.^2+iqref.^2),-4);
% end

%% SEARCH DATA POINTS
% find start and stop of measurement by trigger signal
[~, tlocs] = find(diff(trigger));
%tlocs = [tlocs 928534];% 3kw fux map
%tlocs = [tlocs 1.136*10^6];% 3kw fux map 10 A rms 105 rad
%tlocs = [tlocs 1.136*10^6];% 3kw fux map 10 A rms 105 rad
```

```
% find reference changes
[~, xlocs] = find(diff(xref));
[~, ylocs] = find(diff(yref));

locs = unique([xlocs,ylocs,tlocs]);

locs = locs(locs<=tlocs(2));

% define axes vectors
xvec = [];
yvec = [];
for i=1:length(locs)-1
    l = locs(i);
    r = locs(i+1);
    xvec = [xvec,xref(ceil(l+(r-l)*0.5))];
    yvec = [yvec,yref(ceil(l+(r-l)*0.5))];
end

% create empty look up table
lut_psi.x = unique(xvec);
lut_psi.y = unique(yvec);
lut_psi.psix = zeros(length(lut_psi.x),length(lut_psi.y));
lut_psi.psiy = lut_psi.psix;
lut_psi.m = lut_psi.psix;

%% FILL FLUX MAPS
for i = 1:length(locs)-1
    l = locs(i);
    r = locs(i+1);
    xval = xref(ceil(l+(r-l)*0.5));
    yval = yref(ceil(l+(r-l)*0.5));

    [~,xi] = find(lut_psi.x==xval);
    [~,yi] = find(lut_psi.y==yval);

    % first axis is horizontal axis --> y<->x

    psid_t = roundn(mean(psid(l+ceil((r-l)*0.25):r-ceil((r-l)*0.25))),-4);
    psiq_t = roundn(mean(psiq(l+ceil((r-l)*0.25):r-ceil((r-l)*0.25))),-4);
    PF_t = roundn(mean(PF(l+ceil((r-l)*0.25):r-ceil((r-l)*0.25))),-4);
    ud_t = roundn(mean(ud(l+ceil((r-l)*0.25):r-ceil((r-l)*0.25))),-4);
    uq_t = roundn(mean(uq(l+ceil((r-l)*0.25):r-ceil((r-l)*0.25))),-4);
    psix = psid_t;
    psiy = psiq_t;
    lut_psi.psix(yi,xi) = psix;
    lut_psi.psiy(yi,xi) = psiy;
    lut_psi.ux(yi,xi) = ud_t;
```

```
    lut_psi.uy(yi,xi) = uq_t;
    lut_psi.m(yi,xi) = roundn(mean(mout(1+ceil((r-1)*0.25):r-ceil((r-1)*0.25))),-4)
    ;
    lut_psi.pf(yi,xi) = PF_t;

end

%% INTERPOLATE
n = length(lut_psi.y);
m = length(lut_psi.x);
lut_psi_eq.psix = zeros(m,m);
lut_psi_eq.psiy = zeros(m,m);
for i = 1:m
    for j=1:n
        x_temp = .25*(lut_psi.psix(i,j) + lut_psi.psix(m-i+1,j) - lut_psi.psix(i,m-
    j+1) - lut_psi.psix(m-i+1,m-j+1));
        y_temp = .25*(lut_psi.psiy(i,j) - lut_psi.psiy(m-i+1,j) + lut_psi.psiy(i,m-
    j+1) - lut_psi.psiy(m-i+1,m-j+1));

        lut_psi_eq.psix(i,j) = x_temp;
        lut_psi_eq.psix(m-i+1,j) = x_temp;
        lut_psi_eq.psix(i,m-j+1) = -x_temp;
        lut_psi_eq.psix(m-i+1,m-j+1) = -x_temp;

        lut_psi_eq.psiy(i,j) = y_temp;
        lut_psi_eq.psiy(m-i+1,j) = -y_temp;
        lut_psi_eq.psiy(i,m-j+1) = y_temp;
        lut_psi_eq.psiy(m-i+1,m-j+1) = -y_temp;
    end
end
lut_psi_eq.d(n,n) = x_temp;
lut_psi_eq.x = lut_psi.x;
lut_psi_eq.y = lut_psi.y;
lut_psi_eq.pf = lut_psi.pf;

n = 100;
ismax = max(idref);
isdmax =ismax;
isqmax = ismax;
iqvec = linspace(-isqmax,isqmax,n);
idvec = linspace(-isdmax,isdmax,n);
qa = iqvec(2)-iqvec(1);
da = idvec(2)-idvec(1);
[Idi,Iqi]    = meshgrid(lut_psi.x,lut_psi.y);
[Id,Iq]      = meshgrid(idvec,iqvec);
lut_psi_int.psix       = interp2(Idi,Iqi,lut_psi_eq.psix,Id,Iq,'spline');
lut_psi_int.psiy       = interp2(Idi,Iqi,lut_psi_eq.psiy,Id,Iq,'spline');
```

```
lut_psi_int.ux       = interp2(Idi,Iqi,lut_psi.ux,Id,Iq,'spline');
lut_psi_int.uy       = interp2(Idi,Iqi,lut_psi.uy,Id,Iq,'spline');
lut_psi_int.m          = interp2(Idi,Iqi,lut_psi.m,Id,Iq,'spline');
lut_psi_int.pf         = interp2(Idi,Iqi,lut_psi_eq.pf,Id,Iq,'spline');
lut_psi_int.x = idvec;
lut_psi_int.y = iqvec;

LUT_Psi.id = lut_psi_int.x;
LUT_Psi.iq = lut_psi_int.y;
LUT_Psi.Psid = lut_psi_int.psix;
LUT_Psi.Psiq = lut_psi_int.psiy;
LUT_Psi.m  = lut_psi_int.m;
LUT_Psi.pf = lut_psi_int.pf;

% [Idi,Iqi]    = meshgrid(LUT_Psi.id,LUT_Psi.iq);
% [Id,Iq]      = meshgrid(ivec,ivec);
 Psi.d        = lut_psi_int.psix;
 Psi.q        = lut_psi_int.psiy;
 M            =  3/2*p_RSM*(Psi.d.*Iq-Psi.q.*Id);

% Calculate inductance matrix DPsi/Di
[L.dd, L.dq]     = gradient(Psi.d,da);
[L.qd, L.qq]     = gradient(Psi.q,qa);
L.dy             = (L.dd.*L.qq-L.dq.*L.qd)./L.qq;
L.qy             = (L.dd.*L.qq-L.dq.*L.qd)./L.dd;
L.c              = (L.dd.*L.qq-L.dq.*L.qd)./L.dq;

figure();
subplot(121);
surf(lut_psi_int.x,lut_psi_int.y,lut_psi_int.psix);
xlabel('$i_s^d / A$');
ylabel('$i_s^q / A$');
title('$\psi_s^d / Wb$');
grid on;
subplot(122);
surf(lut_psi_int.x,lut_psi_int.y,lut_psi_int.psiy);
xlabel('$i_s^d / A$');
ylabel('$i_s^q / A$');
title('$\psi_s^q / Wb$');
grid on;
```

D.0.5 Fundemental Saliency Shift Mapping Matlab Script

```
% By Joshua Mitchell 2016
%%import flux map
load('Flux_Data_9600W');
```

```
%% Data conditioning
% First interpolate data on a grid to match dimensions
n = 80;
isqmax = max(LUT_Psi.iq);
isdmax = max(LUT_Psi.id);
iqvec = linspace(-isqmax,isqmax,n);
idvec = linspace(-isdmax,isdmax,n);
qa = iqvec(2)-iqvec(1);
da = idvec(2)-idvec(1);
[Idi,Iqi]    = meshgrid(LUT_Psi.id,LUT_Psi.iq);%meshgrid(ivec,ivec);
[Id,Iq]      = meshgrid(idvec,iqvec);
Psi.d        = interp2(Idi,Iqi,LUT_Psi.Psid,Id,Iq,'spline');
Psi.q        = interp2(Idi,Iqi,LUT_Psi.Psiq,Id,Iq,'spline');
%clear Idi Iqi
% calculate fundamental saliency shift.
Iss = sqrt(Id.^2+Iq.^2);
Psi_ss = sqrt(Psi.d.^2 +Psi.q.^2);
Phi_psi = atan2(Psi.q,Psi.d);
Phi_Iss = atan2(Iq,Id);
Phi_f = Phi_Iss - Phi_psi;
% rotate to current reference frame iss
Psi_ss_x = cos(Phi_f).*Psi_ss;
Psi_ss_y = sin(Phi_f).*Psi_ss;
%interpolate non-linear isotropic flux vector dq components in the iss reference
    frame
Psids = interp2(Id,Iq,Psi.d,abs(Iss),zeros(n,n),'spline');
Psiqs = interp2(Id,Iq,Psi.q,zeros(n,n),abs(Iss),'spline');
%non-linear isotropic flux vector and circulating fundamental saliency
Psi_sum_s = ((Psids + Psiqs).*(Iss./abs(Iss)))./2;
Psi_delta_nl_x = Psi_ss_x - Psi_sum_s;
Psi_delta_nl_y = Psi_ss_y;
%magnetic axis
Phi_Psi_delta = atan2(Psi_delta_nl_y ,Psi_delta_nl_x);
%calculate the shift and mod
Phi_shift = mod((2.*Phi_Iss - Phi_Psi_delta)./2 + pi/2,pi) -pi/2;
%plot shift
set(0, 'DefaultFigureRenderer', 'zbuffer'); %// this line added
figure();
hold on
%surf(Id,Iq,180/pi .*Shift.phi);
surf(Id,Iq,180/pi .*Phi_shift);
alpha(0.4)
hold off
xlabel('$i_s^d$ / [A]','Fontsize',13);
ylabel('$i_s^q$ / [A]','Fontsize',13);
zlabel('Saliency shift / [deg]');
set(gca,'XTick',(-40:10:40));
```

```
set(gca,'YTick',(-40:10:40));
%
```

D.0.6 LCL-filter Design Matlab Script

```
% By Joshua Mitchell 2016
% script to design LCL-filter for grid applications.
%% ---------------- Grid parameters ----------------
% Peak power
Pn =  3100;
% RMS phase voltage [V]
un_0 = 230;
% Peak phase voltage [V]
%u_0 = 325
u_0 = un_0 *sqrt(2);
% Peak Line to Line voltage [V]
uLL_0 = un_0 *sqrt(3);
% Base frequency [rad/s]
w_0 = 50*2*pi;
%2. Phase current,
Ip = Pn*sqrt(2)/(3*un_0);%16;
IL = Ip/sqrt(2);
u_DC_ref = 600;%600
u_DC = u_DC_ref;
C_DC = 5e-4;
% ---------------- LCL Filter parameters ----------------
Zb = uLL_0^2/Pn;
Cb = 1/(w_0*Zb);
ka = 0.05; %max power factor variation from grid is 20%
Lb = Zb/w_0;
Lmax = Lb*0.1;

%% ---------------- filter design ----------------
% Formulate design space and plot graphs
x = 0.05; %percentage
n1 = 100;
Ld = linspace(0.0005,Lmax,n1);
r = linspace(0.01,5,n1);
[ri,Ldi]    = meshgrid(r,Ld);%meshgrid(ivec,ivec);
ka1 = 1./(abs(1 + ri.*(1-(Cb*(f_PWM*2*pi)^2).*Ldi.*x)));
Igmax = Pn*sqrt(2)/(3*un_0); %amps

 figure();
 subplot(2,2,1)
 surf(ri,Ldi,ka1);
 xlabel('r'); % x-axis label
```

```
ylabel('Li'); % y-axis label
zlabel('ka');
xlim([0,3]);
ylim([0,0.03]);
zlim([0,0.3]);
subplot(2,2,2)
surf(ri,Ldi,ka1);
xlabel('r'); % x-axis label
ylabel('Li'); % y-axis label
zlabel('ka');
xlim([0,3]);
ylim([0,0.03]);
zlim([0,0.3]);
set(gca,'View',[0 0]);
subplot(2,2,3)
surf(ri,Ldi,ka1);
xlabel('r'); % x-axis label
ylabel('Li'); % y-axis label
zlabel('ka');
xlim([0,3]);
ylim([0,0.03]);
zlim([0,0.3]);
set(gca,'View',[0 90]);
subplot(2,2,4)
surf(ri,Ldi,ka1);
xlabel('r'); % x-axis label
ylabel('Li'); % y-axis label
zlabel('ka');
xlim([0,3]);
ylim([0,0.03]);
zlim([0,0.3]);
set(gca,'View',[90 0]);

%Calculate individual parameters ripple current

deltaIlmax = 0.06*Igmax; %for 10% ripple

%ka_int = interp2(ri,Ldi,ka1,r,L1,'spline');

%Ideal VSC inductor
Li = u_DC_ref/(6*f_PWM*deltaIlmax);

%grid inductor within the limit of Lmax
Lg = Lmax - L1;

% Grid Ripple current
ripple = (u_DC_ref/(6*f_PWM*(L1)))/Igmax;
```

```
% limit of base capacitor
C1 = Cb*0.05;
C_delta = C1/3;

% set ripple percentage
ka = 0.05;

%ideal calculate grid side inductance
Lg2 = (sqrt(1/ka^2) + 1)/(C1*(2*pi*f_PWM)^2);

%checks
r = Lg2/Li;
k = 1/abs(1 + r*(1 - Li*C1*(f_PWM*2*pi)^2));
ka_int = interp2(ri,Ldi,ka1,r,Li,'spline');

%Resonant frequency
Wres = sqrt((Li + Lg2)/(Li*Lg2*C1));
Fres = Wres/(2*pi);

%Resonant frequency damping
Rc = 1/(3*Wres*C1);
Rc_delta = Rc*3;

%inductor resistance estimates
R1 = 1;
R2 = 0.2;

L_F = Li + Lg2;
R_F = R1 + R2;
T_F = L_F/R_F;

%some bode plots
H_lcl =tf([1],[Li*C1*Lg2 0 L_F  0 ]);
H_dlcl = tf([C1*Rc 1],[Li*C1*Lg2 C1*Rc*L_F (L_F) 0]);
H_LC = tf([1/(L_F*C1)],[1 Rc/L_F 1/(L_F*C1)]);
H_L = tf([1/L_F],[1 L_F]);

figure();
bode(H_dlcl,{1,10e6});
legend('dLCL','Location','northeast');
legend('boxoff');
xlim([0,10e6]);
grid on

%
```

D.0.7 Inductor Design Matlab Script

```
%% By Joshua Mitchell 2016
% script to design the dimensions , turns cross sectional area of the
% Inductor for the LCL and LC filter
%Design inductor having a given inductance L,which carries worst-case current Imax
    without saturating.
%Based on Al data for a E80/38/20 EE core
%1. Applied voltage,
VL = 230;% volts;
%2. Line current,
IL = 9;
Ip = sqrt(2)*IL;%16;
%3. Line frequency
f = 50;% hertz.;
%4. Current density,
J = 300;%amp/cm2
%5. Efficiency goal,
Ne = 90;% efficeicny percentage
%6. Magnetic material = Silicon
%7. Magnetic material permeability,
um = 1550;%1500; %ue
%8. Flux density,
Bac = 0.32;%1.4;%Tesla
%9. Window utilization,
Ku = 0.4;
%10. Waveform factor, for sinusoid
Kf = 4.44;
%11. Temperature rise goal,
Tr = 50;%degrees
%1. Core Number = E80/38/20
%2. Magnetic Path Length,
MPL = 15.2;% cm
%3. Core Weight,
Wtfe = 676;% grams
%4. Mean Length Turn,
MLT = 15.0;%14.8;% cm
%5. Iron Area,
Ac = 3.90;%6.13;% cm2
%6. Window Area,
Wa = 3.66;%4.84;% cm2
%7. Area Product,
Ap = 29.7;% cm4
%8. Core Geometry,
Kg = 4.93;% cm5
%9. Surface Area,
At = 213;% cm2
%10. Winding length,
```

```
G = 3.81;% cm
%11. Lamination tongue,
E = 2.54;% cm
%13. core Al
Al = 882;%4150;% nH ungapped 882nH gappeg 5mm
u0 = 4*pi*1e-7;%  H/m magnetic field constant
Pr = 1.724e-6; %resistivity of copper in ohm cm
VA = VL*IL; %watts
%initialise
Inductance=0;
Turns=0;
gaplength=0;
corenumber=0;
wirediameter=0;
Ploss=0;
Trise=0;
%initial L
Core_num_i = 1;
n_i = 1;
Lg = 0.002; % air gap
e = 1;


for j = linspace(0.001,Lf,1000)

    L_f = j;
    Inductance(e) = j;

    for i = 0:100
    Aw = Ku*Wa/n_i;
    R = Pr*n_i*MLT/Aw;
    Kgl = ((Pr *L_f^2 * Ip^2)/(Bac^2*R*Ku))*1e8;
    Ac_req = 1e4*(u0*L_f*Ip^2)/(Bac^2*Lg*3); % air gap lenght multiplied by 3
    bevcause there are 3 gaps
    Al_cal = (10*Bac^2*Ac_req^2)/(L_f*Ip); % nH
    Core_num = ceil(Ac_req/Ac);
    Core_num = ceil(Al_cal/Al);
    Ac_new =  Core_num * Ac;
    F = (1 + (Lg/sqrt(Ac_new)) * log10(2*G/Lg));
    n_f = sqrt(L_f*Lg/(0.4*pi*Ac_new*F*1e-10));
    n_i = n_f;
    end

    %Assign values to table variables
    Aw = Ku*Wa/n_f;
    R = Pr*n_f*MLT/Aw;
    Kgl = ((Pr *L_f^2 * Ip^2)/(Bac^2*R*Ku))*1e8;
```

```
    Kg = (Ac_new^2*Wa)/(MLT);
93  Wire_D = sqrt(4*Aw/pi); %in cm
    Wire_D = Wire_D*10;%in mm
95  Pcu = R*IL^2;
    P_gap = 0.155*E*3*Lg*f*Bac^2;
97  At_new = At*Core_num;
    P_tot = P_gap + Pcu;
99  Surf_A_W_D = P_tot/At_new ;
    T_rise = 450*(Surf_A_W_D)^0.826; %degrees
101 Rs(e) = R;
    AW(e) = Aw*10^2;
103 Kg_ratio(e) = Kg/Kg1;
    A_l(e) = Al_cal;
105 Turns(e)= n_f;
    gaplength(e) = Lg;
107 corenumber(e) = Core_num;
    wirediameter(e) = Wire_D;
109 Ploss(e) = P_tot;
    Trise(e) = T_rise;
111 n_i =450;
    e = 1+e ;
113 end

115 % print table
Al_cal,n_f,Lg,L_f,Core_num,Wire_D,Pcu,T_rise;
117 table(Inductance',Rs',Turns',gaplength',corenumber',wirediameter',Ploss',Trise',...
    'VariableNames',{'Inductance','Resistance','Turns','gaplength_m','corenum','
    Wire_D_mm','Ploss','Trise'})
```

Appendix E

Filter-Inductor Design and Manufacturing

In this appendix the design process for filter inductors is detailed.

E.1 Inductor Design Process

All the inductors used in this project, for filter and cable emulation purposes, were designed using the K_g method [123]. K_g is known as the core geometrical constant and represents the effective electrical size of a particular magnetic core. It takes into account the geometry of the core as well as its electrical properties and is formulated using four constraints.

• Constraint 1 : The Turns Ratio

$$NI_{max} = B_{max} A_c \Re_g = \frac{B_{max} l_g}{\mu_0}, \tag{E.1}$$

where N is the number of turns, I_{max} is the maximum peak current in the wire, l_g is the air-gap, A_c is the core area in cm^2, $\Re_g$ is the air-gap reluctance and μ_0 is the permeability of the air-gap. The core reluctance, $\Re_c$, is usually ignored because $\Re_c \ll \Re_g$ and is thus negligible in the calculations. This benefits the design because $\Re_g$ does not change drastically with temperature and thus helps the inductor to resist saturation with temperature increase. B_{max} is the magnetic flux in Tesla and is chosen to be less than saturation flux density B_{sat}.

• Constraint 2: Specific Inductance

$$L = \frac{N^2}{\Re_g} = \frac{\mu_0 A_c N^2}{l_g}, \tag{E.2}$$

• Constraint 3: Fill factor

$$K_u W_A \geq N^2 A_w, \tag{E.3}$$

where W_a and MLT are functions of the core geometry. K_u is the fraction of the core window area W_A that is filled by copper. A typical value for a simple low-voltage inductor is $K_u = 0.5$. Mechanical limitations that cause K_u to be less than 1:

• Round wire does not stack perfectly thus K_u is reduced by a factor of 0.7 to 0.55
• Wire insulation reduces Ku by 0.95 to 0.65 (depending on wire size and type of insulation)
• Bobbins use up some window area
• Additional insulation may be required between windings

• Constraint 4: Wire Resistance

$$R = \rho \frac{l_b}{A_w} = \rho \frac{N^2 MLT}{A_w}, \tag{E.4}$$

where ρ is the resistivity of the conductor material (copper at room temperature is $1.724e10-6\Omega cm$), l_b is the length of the wire, and A_w is the wire bare area. MLT (mean-length- per-turn of the winding) is a function of the core geometry. The quantities A_c, W_A and MLT are generally found from the core datasheet, I_{max}, B_{max}, μ_0, L, K_u, R, and ρ, are design specifications and N, l_g, and A_W, are unknowns. K_g is a value that combines the above equations to describe the effective electrical size of magnetic cores. K_g derived by eliminating the three unknowns:

$$K_g = \frac{A_c^2 W_A}{MLT} \geq \frac{\rho L^2 I_{max}^2}{B_{max}^2 R K_u}. \tag{E.5}$$

Core manufacturers specify the equivalent inductance A_L in mH obtained with $N = 1000$ for various air-gap values. A_L is used to relate the desired inductance L to N, core geometry and the desired current rating in eqs. (E.6) and (E.7).

$$A_L = \frac{10 B_{max}^2 A_c^2}{L I_{max}}, \tag{E.6}$$

$$L = A_L N^2 10^{-9}, \tag{E.7}$$

where L is in Henry and A_c is in cm^2. It was found that the inductance equations were particularly inaccurate in the presence of an air gap. This is due to the fact that

the K_g method equations do not account for fringing flux. The presence of fringing flux decreases the total reluctance of the magnetic path which results in a higher inductance value than the value calculated by equation (E.2). Using (E.8) for the fringing factor F, L is then be recalculated using (E.9) [124]. An additional fringing flux factor must be included into the calculation of L.

$$F = 1 + \frac{l_g}{\sqrt{A_c}} log_{10}(\frac{2G}{l_g}), \tag{E.8}$$

$$L = \frac{N^2}{R_g F 1e^{10}}, \tag{E.9}$$

where G is the winding length. Note the inclusion of the $1e^{10} mm = 1cm$ conversion factor in (E.9). The inductor power loss and temperature rise can also be estimated using the following equations:

$$P_{cu} = RI_{rms}^2, \tag{E.10}$$

$$P_{gap} = 0.155 E L_g f B_{max}^2, \tag{E.11}$$

$$P_{tot} = P_{gap} + P_{cu}, \tag{E.12}$$

$$T_r = 450(\frac{P_{tot}}{A_t C_n})^0.826, \tag{E.13}$$

where P_{cu} and P_{gap} are the copper and air-gap core loses respectively, E is the lamination tongue, A_t is the core surface Area in cm^2, T_r is the temperature rise of the inductor and C_n is the total number of cores used. A Matlab Script was written to compute these equations see appendix for details.

The following parameters in table E.1 where used in the design of the inductors for the LCL-filter.

It was found that there was ≈ 8 % deviation in number of turns, an inductance deviation of 2.7 % and a deviation in RMS current saturation 0.1 %. The above equations were thus useful in providing a guideline for number of cores and turns before winding. This greatly increased the manufacturing and testing time of the cores since winding formers and bobbins could be made to exact specifications and not trial and error.

Table E.1: Core design parameters.

Supply Parameters	Value	Units
Phase voltage	230	V_{RMS}
Rated power	5	kW
Line current	7.2464	I_{RMS}
Fundamental frequency	50	Hz
Inductor Parameters		
Core Number	E80/38/20	
Current density, J	300	A/cm^2
Flux density, B_{ac}	0.32	$T, tesla$
Window utilization, K_u	0.4	
Sinusoid waveform factor, K_f	4.44	
Temperature rise, T_r	50	$\circ C$
Inductance factor, A_L	882	$nH/1000N$
Magnetic field constant, μ_0	$1.2566e^{-06}$	μ_f
Core window area, A_c	3.9	cm^2
Resistivity of copper ρ	$1.724e^{-6}$	Ωcm
Magnetic Path Length, MPL	15.2	cm
Core Weight, Wtfe	676	$grams$
Mean Length Turn, MLT	15.0	cm
Window Area, W_A	3.66	cm^2
Area Product, A_p	29.7	cm^4
Core Geometry, K_g	4.93	cm^5
Surface Area, A_t	213	cm^2
Winding length, G	3.81	cm
Lamination tongue, E	2.54	cm

Table E.2: Calculated inductor design values.

Parameters	Inductors					
	L_i	L_g	L_f	150 m $L_{DC,cable}$	450 m $L_{DC,cable}$	450 m $L_{AC,cable}$
$L[mH]$	25.4	2.71	2.0	6.73	22.44	22.44
$R[\Omega]$	0.82	0.39	0.024	0.081	0.27	0.27
N	215	148	37	68	124	124
$l_g[mm]$	4	4	2	2	2	2
core no.	6	1	6	6	6	6
Wire $\phi[mm]$	0.93	1.12	2.25	1.66	1.23	1.23
$Current[A, RMS]$	6.0	6.0	9.0	9.0	9.0	9.0
$P_{loss}[W]$	27.41	13.05	1.96	6.55	21.8	21.8
$T_{rise}[^\circ]$	18.83	44.82	2.13	5.78	15.60	15.60

List of References

[1] P. H. Tran, "Matlab / simulink implementation and analysis of three pulse-width-modulation (PWM)," Master of Science, Boise State University, 2012.

[2] S. Rolland and B. Auzane, "The Potential of small and medium Wind Energy in Developing Countries," *Alliance for Rural Electrificaion*, p. 12, 2012.

[3] S. Gsanger and J. Pitteloud, "2015 small wind world report summary," *Wolrd Wind Energy Association (WWEA)*, 2015.

[4] Z. Alnasir and M. Kazerani, "Performance comparison of standalone SCIG and PMSG-based wind energy conversion systems," *Canadian Conference on Electrical and Computer Engineering*, pp. 1–8, 2014.

[5] F. Blaabjerg, "Future on power electronics for wind turbine systems," *IEEE Journal of Emerging and Selected Topics in Power Electronics*, vol. 1, no. 3, pp. 139–152, 2013.

[6] W. E. Leithead, "Dependence of performance of variable speed wind turbines on the turbulence , dynamics and control," *IEE Proceedings-C*, vol. 137, no. 6, pp. 9–11, 1990.

[7] E. Muljadi, C. P. Butterfield, and P. Migliore, "Variable speed of generators with rotor-speed feedback in wind power," *Wind Energy Symposium*, no. 15 ASME, 1996.

[8] S. Arnaltes, "Comparison of variable speed wind turbine control strategies," *Pro- ceedings of the International Conference on Renewable Energies and Power Quality*, vol. 1, no. 1, pp. 80–85, 2000.

[9] E. Muljadi, K. Pierce, and P. Migliore, "Control strategy for varaible-speed stall-regulated wind turbines," *American Control Conference*, pp. 1710–1714, 1998.

[10] J. Chen, J. Chen, and C. Gong, "New overall power control strategy for variable-speed fixed-pitch wind turbines within the whole wind velocity range," *IEEE Transactions on Industrial Electronics*, vol. 60, no. 7, pp. 2652–2660, 2013.

[11] L. Bisenieks, D. Vinnikov, and G. Ilya, "New converter for interfacing PMSG based small-scale wind turbine with residential power network," *7th International Conference-Workshop Compatibility and Power Electronics*, no. July, 2011.

[12] A. M. Eltamaly and H. M. Farh, "Maximum power extraction from wind energy system based on fuzzy logic control," *Electric Power Systems Research*, vol. 97, pp. 144–150, 2013.

[13] A. D. Hansen and L. H. Hansen, "Wind turbine concept market penetration over 10 years (1995-2004)," *Wind Energy*, vol. 10, no. 1, pp. 81–97, 2007.

[14] A. Luna, P. Rodriguez, R. Teodorescu, and F. Blaabjerg, "Low voltage ride through strategies for SCIG wind turbines in distributed power generation systems," in *PESC Record - IEEE Annual Power Electronics Specialists Conference*, 2008, pp. 2333–2339.

[15] H. Li and Z. Chen, "Overview of different wind generator systems and their comparisons," *IET Renewable Power Generation*, vol. 2, no. 2, pp. 123–138, 2008.

[16] H. Polinder, J. A. Ferreira, B. B. Jensen, A. B. Abrahamsen, K. Atallah, and R. A. McMahon, "Trends in wind turbine generator systems," *IEEE Journal of Emerging and Selected Topics in Power Electronics*, vol. 1, no. 3, pp. 174–185, 2013.

[17] A. Boglietti and M. Pastorelli, "Induction and synchronous reluctance motors comparison," *Proceedings - 34th Annual Conference of the IEEE Industrial Electronics Society, IECON 2008*, pp. 2041–2044, 2008.

[18] W. T. Villet and M. J. Kamper, "Position sensorless control of a reluctance synchronous wind generator drive with an LC inverter filter," *Electric Power Components and Systems*, vol. 43, no. 8-10, pp. 1051–1061, 2015.

[19] J. J. Germishuizen, F. S. van der Merwe, K. van der Westhuizen, and M. J. Kamper, "Performance comparison of reluctance synchronous and induction traction drives for electrical multiple units," *Conference Record of the 2000 IEEE Industry Applications (IAS) Annual Meeting and Conference*, vol. 1, pp. 316–323, 2000.

[20] A. Boglietti, A. Cavagnino, M. Pastorelli, and A. Vagati, "Experimental comparison of induction and synchronous reluctance motors performance," *Annual IEEE Industry Applications Society (IAS) Meeting*, vol. 1, pp. 474–479, 2005.

[21] C. M. Hackl, M. J. Kamper, J. Kullick, and J. Mitchell, "Current control of reluctance synchronous machines with online adjustment of the controller parameters," in *to be published in Proceedings of the 2016 IEEE International Symposium on Industrial Electronics (ISIE 2016)*, 2016.

[22] W. T. Villet, M. J. Kamper, P. Landsmann, and R. Kennel, "Hybrid position sensorless vector control of a reluctance synchronous machine though the entire speed range," *15th International Power Electronics and Motion Control Conference, EPE-PEMC 2012 ECCE Europe, Novi Sad, Serbia*, pp. 1–7, 2012.

[23] P. Landsmann, R. Kennel, H. W. De Kock, and M. J. Kamper, "Fundamental saliency based encoderless control for reluctance synchronous machines," *The XIX International Conference on Electrical Machines (ICEM)*, no. Oct, 2010.

[24] R. Teodorescu, M. Liserre, and P. Rodríguez, "Grid converters for photovoltaic and wind power systems," in *JohnWiley & Sons, Ltd, The Atrium, Southern Gate, Chichester,West Sussex, PO19 8SQ, United Kingdom*, 2011, pp. 237–287.

[25] "Solacity, a wind turbine report," http://www.solacity.com/docs/Warwick%20Wind%20Trials%20Report.pdf, accessed: 01/12/2015.

[26] "Solacity, a wind turbine report," http://www.solacity.com/docs/BEST%20turbine%20trial%20report.pdf, accessed: 01/12/2015.

[27] "Wipo Wind Power, small scale wind turbine company," http://www.wipo-s^{b}windpower.com/, accessed: 03/12/2015.

[28] "Kestrel, small scale wind turbine company," http://www.kestrelwind.co.za/, accessed: 01/12/2015.

[29] "Windturbinestar, small scale wind turbine company," http://www.windturbinestar.com/, accessed: 01/12/2015.

[30] "Bergey, small scale wind turbine company," http://www.bergey.com/, accessed: 03/12/2015.

[31] "Calla-Glory, small scale wind turbine company," http://www.callaglory.com/, accessed: 03/12/2015.

[32] "Fortis Wind Energy, small scale wind turbine company," http://www.fortiswindenergy.com/, accessed: 03/12/2015.

[33] "Gaia-wind, small scale wind turbine company," http://www.gaia-s^{b}wind.com/, accessed: 03/12/2015.

[34] "GHRE Power, small scale wind turbine company," http://www.ghrepower.com/en/, accessed: 03/12/2015.

[35] "Hopefull Energy, small scale wind turbine company," http://www.hopefulenergy.com/, accessed: 03/12/2015.

[36] "Qingdao Windwings Wind Turbine, small scale wind turbine company," http://www.qdfzy.com/en/, accessed: 03/12/2015.

[37] "Ventera Wind, small scale wind turbine company," http://www.venterawind.com/, accessed: 03/12/2015.

[38] C. Dirscherl, C. Hackl, and K. Schechner, "Pole-placement based nonlinear state-feedback control of the DC-link voltage in grid-connected voltage source power converters: A preliminary study," in *Proceedings of the 2015 IEEE International Conference on Control Applications*, 2015, pp. 207–214.

[39] ——, "Explicit model predictive control with disturbance observer for grid-connected voltage source power converters," in *Proceedings of the 2015 IEEE International Conference on Industrial Technology*, 2015, pp. 999–1006.

[40] K. Schechner, F. Bauer, and C. M. Hackl, "Nonlinear DC-link PI control for airborne wind energy systems during pumping mode," in *Airborne Wind Energy: Advances in Technology Development and Research*, R. Schmehl, Ed. Springer-Verlag, 2016.

[41] D. Le Gouriérès, *Wind power plants: theory and design*, 1st ed. Oxford: Pergamon Press, 1982.

[42] C. Thumthae and T. Chitsomboon, "Optimal angle of attack for untwisted blade wind turbine," *Renewable Energy*, vol. 34, no. 5, pp. 1279–1284, 2009.

[43] "Mragheb, turbine aerodynamics," http://mragheb.com/NPRE%20475%20Wind%20Power%20Systems/Aeorodynamics%20of%20Rotor%20Blades.pdf, accessed: 13/12/2014.

[44] "hyperphysics," http://hyperphysics.phy-s^{b}astr.gsu.edu/hbase/pber.html, accessed: 13/12/2014.

[45] B. Neammanee, S. Sirisumrannukul, and S. Chatratana, "Development of a wind turbine simulator for wind generator testing," *International Energy Journal*, vol. 8, no. 1, pp. 21–28, 2007.

[46] H. Kojabadi, L. Chang, and T. Boutot, "Development of a novel wind turbine simulator for wind energy conversion systems using an inverter-controlled induction motor," *IEEE Transactions on Energy Conversion*, vol. 19, no. 3, pp. 547–552, 2004.

[47] A. D. a.D. Hansen, C. Jauch, P. Sørensen, and F. Iov, *Dynamic wind turbine models in power system simulation tool DIgSILENT*, 2003, vol. 1400, no. August.

[48] J.-p. Du Plooy, "Development of a Converter-Fed Reluctance Synchronous Generator Wind Turbine Controller," no. March, 2015.

[49] Olimpo Anaya-Lara, N. Jenkins, J. Ekanayake, P. Cartwright, and M. Hughes, *Wind energy generation: modelling and control*, 2009.

[50] "Futurenergy, small scale wind turbine company," http://www.futurenergy.co.uk/10kwturbine.html, accessed: 11/5/2015.

[51] "Eaglepower, small scale wind turbine company," http://www.eaglepower.co.uk/, accessed: 11/5/2015.

[52] "Macrowindturbine, small scale wind turbine company," http://www.macrowindturbine.com/MW400.html, accessed: 11/5/2015.

[53] "Gaia-wind, small scale wind turbine company," http://www.gaia-s^{b}wind.com/events-s^{b}and-s^{b}news/small-s^{b}wind-s^{b}turbine-s^{b}image-s^{b}gallery/, accessed: 11/5/2015.

[54] "Professor R. Teodorescu, Research activities in wind power, aalborg university," http://www.jst.go.jp/sicp/ws2012_denmark/presentation/presentation_21.pdf, accessed: 11/5/2015.

[55] "Windpowermonthly, article," http://www.windpowermonthly.com/article/1211056/close-s^{b}vestas-s^{b}v164-s^{b}80-s^{b}nacelle-s^{b}hub, accessed: 11/5/2015.

[56] K. Fischer, T. Stalin, H. Ramberg, J. Wenske, and R. Karlsson, "Investigation of converter failure in wind turbines," *Elforsk*, vol. 58, no. 12, p. 69, 2012.

[57] B. Rabelo, W. Hofmann, and M. Glück, "Emulation of the static and dynamic behaviour of a wind-turbine with a DC-machine drive," in *PESC Record - IEEE Annual Power Electronics Specialists Conference*, vol. 3, 2004, pp. 2107–2112.

[58] L. A. C. Lopes, J. Lhuilier, A. Mukherjee, and M. F. Khokhar, "A wind turbine emulator that represents the dynamics of the wind turbine rotor and drive train," *PESC Record - IEEE Annual Power Electronics Specialists Conference*, vol. 2005, pp. 2092–2097, 2005.

[59] M. Monfared, H. Madadi Kojabadi, and H. Rastegar, "Static and dynamic wind turbine simulator using a converter controlled dc motor," *Renewable Energy*, vol. 33, no. 5, pp. 906–913, 2008.

[60] A. Bouscayrol, X. Guillard, and P. Delarue, "Hardware-in-the-loop simulation of a wind energy conversion system using energetic macroscopic representation," *Industrial Electronics Society, 2005. IECON 2005. 31st Annual Conference of IEEE*, vol. 0-7803-925, pp. 2523–2528, 2005.

[61] J. Yaoqin and W. Zhaoan, "Experimental Study of Control Strategy for Wind Generation System," *Power electronics specialist conference*, pp. 1202–1207, 2007.

[62] R. G. D. Oliveira, "Development of a wind turbine simulator for wind energy conversion systems -experimental results," *9th Brazilian Electronics Conference*, vol. 9, no. 1, pp. 313–318, 2011.

[63] R. Teodorescu, F. Iov, and F. Blaabjerg, "Flexible development and test system for llkW wind turbine," *Design*, 2003.

[64] W. Hu, Y. Wang, X. Song, and Z. Wang, "Development of wind turbine simulator for wind energy conversion systems based on permanent magnet synchronous motor," *Electrical Machines and Systems, 2008. ICEMS 2008. International Conference on*, pp. 2322–2326, 2008.

[65] W. Li, D. Xu, W. Zhang, and H. Ma, "Research on wind turbine emulation based on DC motor," *ICIEA 2007: 2007 Second IEEE Conference on Industrial Electronics and Applications*, no. 3, pp. 2589–2593, 2007.

[66] A. D. Diop, E. Ceanga, J. L. Rétiveau, J. F. Méthot, and A. Ilinca, "Real-time three-dimensional wind simulation for windmill rig tests," *Renewable Energy*, vol. 32, no. 13, pp. 2268–2290, 2007.

[67] F. Martínez, S. de Pablo, and L. C. Herrero, "Fixed pitch wind turbine emulator using a DC motor and a series resistor," *13th European Conference on Power Electronics and Applications*, pp. 1–9, 2009.

[68] A. G. G. Rodríguez, A. G. Rodríguez, and M. B. Payán, "Estimating wind turbines mechanical constants," *Renewable Energy & Power Quality Journal*, vol. 1, no. 5, pp. 9–11, 2007.

[69] J. K. Kostko, "Polyphase reaction synchronous motors," *Journal of the American Institute of Electrical Engineers*, vol. 42, no. 11, pp. 1162–1168, 1923.

[70] R. A. Trubenbach, A. T. Mackay, and M. J. Kamper, "Performance of a reluctance synchronous machine under vector control," *Power Electronics Specialists Conference*, pp. 803 – 808, 1993.

[71] J. Slootweg, S. de Haan, H. Polinder, and W. Kling, "General model for representing variable speed wind turbines in power system dynamics simulations," *IEEE Transactions on Power Systems*, vol. 18, no. 1, pp. 144–151, 2003.

[72] A. Pathan, A. Schilli, J. Johansson, L. Vehviläinen, A. Larsson, and J. Hutter, *Tracking environmental impacts in global product chains: rare earth metals and other critical metals used in the cleantech industry*, 1st ed. Copenhagen: Norden, 2013.

[73] S. Buso and P. Mattavelli, "Digital Control in Power Electronics," *Synthesis Lectures on Power Electronics*, vol. 1, no. 1, pp. 1–158, jan 2006.

[74] C. Dirscherl, C. Hackl, and K. Schechner, "Modellierung und Regelung von modernen Windkraftanlagen: Eine Einführung *(available at the authors upon request)*," in *Elektrische Antriebe – Regelung von Antriebssystemen*, D. Schröder, Ed. Springer-Verlag, 2015, ch. 24, pp. 1540–1614.

[75] L. Vidyarthy and K. P. Singh, "A comprehensive analysis of space vector pulse width modulation for 3-phase voltage source inverter (VSI)," *International Journal of Engineering Research & Technology*, vol. 1, no. 6, pp. 1–7, 2013.

[76] K. Ma, "Power electronics for the next generation wind turbine system," Phd, Aalborg University., 2013.

[77] Abb, "ABB wind turbine converters Increased turbine output for creating the perfect wind economy."

[78] C. Busca, A.-I. Stan, T. Stanciu, and D. I. Stroe, "Control of Permanent Magnet Synchronous Generator for large wind turbines," *IEEE International Symposium on Industrial Electronics*, pp. 3871–3876, 2010.

[79] H. W. De Kock, "Position sensorless and optimal torque control of reluctance and permanent magnet synchronous machines," PhD, University of Stellenbosch, 2009.

[80] W. Baik, M. Kim, N. Kim, and D. Kim, "An optimal efficiency control of reluctance synchronous motor using neural network with direct torque control," *Iecon'03.*, pp. 1590–1595, 2003.

[81] H. W. De Kock, "Dynamic control of the permanent magnet assisted reluctance synchronous machine with constant current angle," MSc, University of Stellenbosch, 2006.

[82] F. J. W. Barnard, "Position sensorless control of a transverse-laminated reluctance synchronous machine," no. December, 2014.

[83] L. Xu, X. Xu, T. a. Lipo, and D. W. Novotry, "Vector control of a synchronous reluctance motor including saturation and iron loss," *IEEE Transactions on Industry Applications*, vol. 27, no. 5, pp. 977–985, 1991.

[84] D. Schröder, *Elektrische Antriebe - Regelung von Antriebssystemen*, 4th ed. Berlin Heidelberg: Springer-Verlag, 2015.

[85] W. T. Villet and M. J. Kamper, "Design of a reluctance synchronous machine for saliency based position sensorless control at zero reference current," *Proceedings of the IEEE International Conference on Industrial Technology*, pp. 301–306, 2013.

[86] J. Kulick, "Simulations and control of a small-scale wind turbine system with reluctance synchronous generator," MSc thesis, Control of reneawable energy systems research group, Techincal Universisty of Munich (TUM), Germany, 2015.

[87] S.-J. Kang, J.-I. Ha, and S.-K. Sul, "Position controlled synchronous reluctance motor without rotational transducer," *Industry Applications Conference, 1998. Thirty-Third IAS Annual Meeting. The 1998 IEEE*, vol. 1, pp. 671–676 vol.1, 1998.

[88] F. J. W. Barnard, M. J. Kamper, and W. T. Villet, "Hybrid active-flux and arbitrary injection position sensorless control of reluctance synchronous machines," *International Symposium on Power Electronics, Electrical Drives, Automation and Motion (SPEEDAM)*, no. 3, pp. 1146–1151, 2014.

[89] S. Ichikawa, M. Tomitat, S. Doki, and S. Okuma, "Sensorless control of synchronous reluctance motors based on an extended EMF model and initial position estimation," *IECON'03. 29th Annual Conference of the IEEE Industrial Electronics Society*, vol. 3, no. 4, pp. 16–25, 2003.

[90] S. C. Agarlita, I. Boldea, and F. Blaabjerg, "High frequency injection assisted "active flux" based sensorless vector control of reluctance synchronous motors, with experiments from zero speed," *IEEE Energy Conversion Congress and Exposition: Energy Conversion Innovation for a Clean Energy Future, ECCE 2011, Proceedings*, pp. 2725–2732, 2011.

[91] W. T. Villet, "Critical evaluation and application of position sensorless control techniques for reluctance synchronous machines," PhD, University of Stellenbosch, 2014.

[92] T. Frenzke, "Impacts of cross-saturation on sensorless control of surface permanent magnet synchronous motors," *Proc. of Power Electronics and Applications, 2005 European Conference on*, pp. 1–10, 2005.

[93] A. Piippo, M. Hinkkanen, and J. Luomi, "Sensorless control of PMSM drives using a combination of voltage model and HF signal injection," *Conference Record - IAS Annual Meeting (IEEE Industry Applications Society)*, vol. 2, no. 3, pp. 964–970, 2004.

[94] H. Zhu, X. Xiao, and Y. Li, "A simplified high frequency injection method for PMSM sensorless control," *IEEE 6th International Power Electronics and Motion Control Conference*, vol. 3, pp. 401–405, 2009.

[95] E. Capecchi, P. Guglielmi, M. Pastorelli, and A. Vagati, "Position-sensorless control of the transverse-laminated synchronous reluctance motor," *IEEE Transactions on Industry Applications*, vol. 37, no. 6, pp. 1768–1776, 2001.

[96] R. Lagerquist, I. Boldea, and T. Miller, "Sensorless-control of the synchronous reluctance motor," *IEEE Transactions on Industry Applications*, vol. 30, no. 3, 1994.

[97] A. Piippo, J. Salomaki, and J. Luomi, "Signal injection in sensorless PMSM drives equipped with inverter output filter," *IEEE Transactions on Industry Applications*, vol. 44, no. 5, pp. 1614–1620, 2008.

[98] Z. Yaou, Z. Wansheng, and K. Xiaoming, "Control of the permanent magnet synchronous motor using model reference dynamic inversion," *WSEAS TRANSACTIONS on SYSTEMS and CONTROL*, vol. 5, no. 5, pp. 301–311, 2010.

[99] F. J. W. Barnard, W. T. Villet, and M. J. Kamper, "Hybrid active-flux and arbitrary injection position sensorless control of reluctance synchronous machines," *International Symposium on Power Electronics, Electrical Drives, Automation and Motion (SPEEDAM)*, vol. 51, no. 3, pp. 1146–1151, 2014.

[100] W. T. Villet and M. J. Kamper, "Design and performance of compensated reluctance synchronous machine drive with extended constant power speed range," in *2012 IEEE Energy Conversion Congress and Exposition, ECCE 2012*, 2012, pp. 4330–4337.

[101] J. K. Steinke, "Use of an LC filter to achieve a motor-friendly performance of the PWM voltage source inverter," *IEEE Transactions on Energy Conversion*, vol. 14, no. 3, pp. 649–654, 1999.

[102] J. He, G. Y. Sizov, P. Zhang, and N. a. O. Demerdash, "A review of mitigation methods for overvoltage in long-cable-fed PWM AC drives," *IEEE Energy Conversion Congress and Exposition: Energy Conversion Innovation for a Clean Energy Future, ECCE 2011, Proceedings*, no. 1028348, pp. 2160–2166, 2011.

[103] J. Salomaki, M. Hinkkanen, and J. Luomi, "Sensorless control of induction motor drives equipped with inverter output filter," *IEEE Transactions on Industrial Electronics*, vol. 53, no. 4, 2006.

[104] Danfos, *Output filters design guide*, 2010.

[105] E. B. Nielsen, "Control of LC-filter connected PMSM Using Internal State Estimator," Aalborg University, Aalborg, Tech. Rep., 2014.

[106] J. Dannehl, C. Wessels, and F. W. Fuchs, "Limitations of voltage-oriented PI current control of grid-connected PWM rectifiers with LCL filters," *IEEE Transactions on Industrial Electronics*, vol. 56, no. 2, pp. 380–388, 2009.

[107] A. Reznik, "Analysis and design of a smart-inverter for reneawable energy interconnection to the grid," MSc, Colorado School of Mines, 2012.

[108] A. Barbosa, G. A. Junior, and P. Barros, "Symmetrical optimum based PI control redesign," *Anais do XX Congresso Brasileiro de Automática*, pp. 1143–1149, 2014.

[109] B. C. Parikshith and V. John, "Higher order output filter design for grid connected power converters." *Fifteenth National Power Systems Conference (NPSC), IIT Bombay*, pp. 614–619, 2008.

[110] R. Xu, L. Xia, J. Zhang, and J. Ding, "Design and research on the LCL filter in three-phase PV grid-connected inverters," *International Journal of Computer and Electrical Engineering*, vol. 5, no. 3, pp. 322–325, 2013.

[111] A. Reznik, M. G. Simoes, A. Al-Durra, and S. M. Muyeen, "LCL filter design and performance analysis for grid-interconnected systems," *IEEE Transactions on Industry Applications (IAS)*, vol. 50, no. 2, pp. 1225–1232, 2014.

[112] Standards Coordinating Committee 21, *IEEE Standard for Interconnecting Distributed Resources with Electric Power Systems*, 2003.

[113] International Electrotechnical Commission, "Electromagnetic compatibility (EMC) Part 3-6: Limits-Assessment of emission limits for the connection of distorting installations to MV, HV and EHV power systems," *IEC 61000-3-6*, 2008.

[114] M. Hojabri and M. Hojabri, "Design, application and comparison of passive filters for three-phase grid-connected renewable energy systems," *Journal of Engineering and Applied Sciences (ARPN).*, vol. 10, no. 22, pp. 10 691–10 697, 2015.

[115] H. W. Low, "Control of grid connected active converter," MSc, Norwegian University of Science and Technology, 2013.

[116] J. Mühlethaler, M. Schweizer, R. Blattmann, J. W. Kolar, and A. Ecklebe, "Optimal design of LCL harmonic filters for three-phase PFC rectifiers," *IEEE Transactions on Power Electronics*, vol. 28, no. 7, pp. 1–12, 2013.

[117] H. G. Jeong, D. K. Yoon, and K. B. Lee, "Design of an LCL-filter for three-parallel operation of power converters in wind turbines," *Journal of Power Electronics*, vol. 13, no. 3, pp. 437–446, 2013.

[118] X. Zong, "A single phase grid connected DC / AC inverter with reactive power control for residential PV application," MSc., University of Toronto, 2011.

[119] M. Liserre, C. Klumpner, F. Blaabjerg, V. G. Monopoli, and A. Dell'Aquila, "Evaluation of the ride-through capability of an active-front-end adjustable speed drive under real grid conditions," in *IECON Proceedings (Industrial Electronics Conference)*, vol. 2, 2004, pp. 1688–1693.

[120] J. Suul and M. Molinas, "Tuning of control loops for grid connected voltage source converters," *IEEE International Conference on Power and Energy (PECon 08)*, no. PECon 08, pp. 797–802.

[121] M. N. Ibrahim, P. Sergeant, and E. M. Rashad, "Synchronous reluctance motor performance based on different Electrical steel grades," *IEEE Transactions on Magnetics*, vol. 51, no. 11, pp. 1–4, 2015.

[122] M. J. Kamper, F. S. Van Der Merwe, and S. Williamson, "Direct finite element design optimisation of the cageless reluctance synchronous machine," *IEEE Transactions on Energy Conversion*, vol. 11, no. 3, pp. 547–553, 1996.

[123] R. W. Erickson and D. Maksimovic, *Fundamentals of Power Electronics*, 2nd ed. New York: Springer, 2001.

[124] C. W. T. McLyman, *Transformer and Inductor Design Handbook*, 3rd ed. New York: Marcel Dekker inc., 2004.